

FORMATION AND MODIFICATION OF *A_g* ATOMIC POINT CONTACTS

Der Fakultät für Mathematik und Physik
der Gottfried Wilhelm Leibniz Universität Hannover
zur Erlangung des Grades
Doktor der Naturwissenschaften
Dr. rer. nat.
genehmigte Dissertation

von

M. Tech. Atasi Chatterjee

geboren am 03.11.1987 in Durgapur, Indien

2019

Referent: Prof. Dr. Herbert Pfnür (Leibniz University Hannover, Germany)

Erster Korreferent: Prof. Dr. Peter Lemmens (Technische Universität Braunschweig, Germany)

Zweiter Korreferent: Prof. Dr. Christoph Tegenkamp (Technische Universität Chemnitz, Germany)

Tag der Promotion: 08.07.2019

Dedicated to my father
Ranendra Kumar Chatterjee (1944 – 2008)

I miss you a lot and wish you could be with us !!!

Abstract

There is the hope that *Molecular electronics* would enable the fabrication of ultra-small sized functional molecular circuits. However, since this is currently not easily possible using the conventional Si technology, this branch of nano-technology requires significant understanding of the various physical processes that take place on the atomic scale which are governed by quantum mechanical principles. Quantum mechanics introduces uncertainties in the behaviour and, therefore, the investigation of atomic and molecular junctions is not very straightforward. Many approaches have been developed to fabricate such junctions in a reliable way, but nevertheless, there still exists a lack of reproducibility amongst measurements. Similarly, along with the increasing miniaturisation demands, not only smaller circuits are desired, but their efficiency and performance also suffers from the increased current densities and local heating. Therefore, while investigating atomic/molecular junctions the approach within this thesis was two-fold: (a) better understanding of the mechanism of electromigration (EM) within nano-structures and (b) fabrication of reproducible atomic point contacts using EM in ultra-thin Ag structures.

In this thesis, an unique set-up consisting of a 4-tip SEM/STM UHV chamber was used to perform EM measurements on nano-structures. Multiple Ag nano-structures were fabricated on a Si substrate using a two-step lithography process and presence of the in-situ SEM enabled easy navigation from one nano-structure to the other. The tips were used for contacting the structures and a feedback controlled electromigration (FCE) mechanism was used to control the voltage between them during the EM process. Significant effort was devoted on the development and integration of the EM set-up within the 4-tip SEM/STM UHV chamber in order to establish an in-situ fabrication and characterisation technique of atomic/molecular junctions.

Ag bow-tie shaped structures with a centre width between 100-200 nm were investigated at ℓN_2 temperatures and the in-situ characterisation of the structures was performed before and after EM. Ultra-thin Ag structures deposited on Si exhibited a granular nature with an average grain size of Ag grains between 30-40 nm. Therefore, the smallest constriction consisted of more than one grain, which when subjected to EM, led to a complex structure formation. It was observed from the conductance curves that even though these structures depict conductance quantisation while thinning during EM, they could not be re-used for repeatable opening and closing of atomic junctions. This observation led to the conclusion that in order to fabricate reproducible atomic junctions, structure widths below the size of one single grain must be used. To reduce the centre widths below 30 nm, focused ion beam (FIB) patterning was employed, to reliably shape the centre constriction to widths below 20 nm. This extra nano-structuring step allowed precise in-situ local control on the morphology of the structures, which served as a step forward in defining the geometry of the atomic junctions and also improved the reproducibility of the EM technique. EM on these structures produced very well defined conductance plateaus which could be re-opened multiple times, suggesting that atomically precise metallic point contacts were generated. Hence, this dissertation addresses one of the very complex issues in molecular electronics i.e. reproducible fabrication of atomic contacts.

Furthermore, CO molecule(s) were adsorbed on these point contacts. Being one of the very simple asymmetric molecules, CO served as a good candidate to understand the role of

chemisorption on such junctions. Time-resolved current measurements showed bi-stabilities that were dependent on bias voltages. Conductance could be reproducibly changed between two states just by changing the operating voltage suggesting even the simplest molecular junction possesses the capability to function as switches, or memory devices. In the present case, the exact mechanism behind this behaviour has not been completely comprehended, but few possibilities have been outlined. Hence, this thesis also provides intriguing results on electrical properties of chemisorbed Ag atomic contacts.

Keywords: Electromigration, nano-structuring, atomic point contacts, CO molecule, Ag

Kurzzusammenfassung

Es besteht die Aussicht, dass *molekulare Elektronik* die Herstellung von funktionell ultrakleinen molekularen Schaltkreisen ermöglichen könnte. Da dies derzeit mit der herkömmlichen Si-Technologie nicht ohne weiteres möglich ist, erfordert dieser Zweig der Nanotechnologie auch ein umfassendes Verständnis der verschiedenen physikalischen Prozesse auf atomarer Skala. Diese Prozesse unterliegen quantenmechanischen Prinzipien im Sub-Nanometer-Bereich. Aufgrund der Quantenmechanik und der damit eingehenden Unsicherheiten im Verhalten, ist die Untersuchung von atomaren und molekularen Verbindungen nicht einfach. Es wurden zwar viele Ansätze entwickelt, um derartige Übergänge auf zuverlässige Weise herzustellen, trotzdem besteht immer noch ein Mangel an Reproduzierbarkeit zwischen Messungen. Neben den steigenden Anforderungen an die Miniaturisierung sind nicht nur kleinere Schaltkreise erwünscht, sondern auch ihre Effizienz und Leistungsfähigkeit leiden unter erhöhten Stromdichten und lokaler Erwärmung. Daher wurden bei der Untersuchung von atomaren/molekularen Verbindungen in dieser Arbeit zwei Ansätze verfolgt: (a) das Verständnis des Mechanismus der Elektromigration (EM) innerhalb von Nanostrukturen zu verbessern und andererseits (b) die Herstellung reproduzierbarer atomare Punktkontakte unter Verwendung von EM in ultradünnen Ag-Strukturen zu erreichen.

Um EM-Messungen an Nanostrukturen durchzuführen wurde im Rahmen dieser Arbeit ein einzigartiger Aufbau bestehend aus einer 4-Spitzen-STM/SEM-UHV-Kammer benutzt. Vielfache Ag Nanostrukturen wurden mit Hilfe eines zweistufigen Lithographieprozesses hergestellt, während das vorhandene in-situ SEM die einfache Positionierung der Messspitzen auf der jeweiligen Nanostruktur gestattete. Ein rückkopplungsgesteuerter Elektromigrationsmechanismus kontrollierte die Spannung zwischen den die Strukturen berührenden Spitzen. Erheblicher Aufwand wurde getrieben zur Entwicklung einer EM-Anordnung in der 4-Spitzen-STM/SEM-UHV-Kammer um sowohl die Herstellung von atomaren oder molekularen Kontakten zu gewährleisten als auch deren in-situ Charakterisierung.

Ag-Strukturen mit einer bogenförmigen Verengung, die eine Breite im Zentrum zwischen 100 - 200 nm aufwies, wurden bei ℓN_2 -Temperaturen untersucht und eine in-situ Charakterisierung der Strukturen wurde vor und nach der EM durchgeführt. Auf Si abgeschiedene ultradünne Ag-Strukturen zeigten eine nanokristalline Struktur mit einer durchschnittlichen Größe der Ag-Nanokristalle zwischen 30 und 40 nm. Daher bestand die kleinste Einengung aus mehr als einem Kristall, was unter der Einwirkung der EM zu einer komplexen Struktur- bildung führte. Anhand von Leitfähigkeitskurven wurde beobachtet, dass diese Strukturen zwar die Leitfähigkeitsquantisierung während des Ausdünnung durch der EM zeigten, diese jedoch nicht für das wiederholbare Öffnen und Schließen von atomaren Kontakten verwendet werden konnten. Diese Beobachtung führte zu dem Schluss, dass zur Herstellung reproduzierbarer atomarer Verbindungen Strukturbreiten unterhalb der Größe eines einzelnen Kornes verwendet werden müssen. Um die Breite im Zentrum unter 30 nm zu reduzieren, wurde eine Strukturierung mit fokussiertem Ionenstrahl (FIB) eingesetzt, die sehr zuverlässig Strukturen unter 20 nm Breite im Zentrum der Verengung erzeugte. Dieser Fertigungsschritt ermöglichte eine präzise lokale Kontrolle der Morphologie der Strukturen, die einen Schritt in Richtung definierter Geometrie von atomaren Kontakten bedeuteten. EM auf diesen Strukturen erzeugte sehr gut definierte Leitfähigkeitsplateaus, die mehrmals wieder geöffnet werden konnten, was darauf hindeutet, dass präzise atomare metallische Punktkontakte erzeugt wurden. Die-

se Dissertation spricht also eines der sehr komplexen Themen molekularer Elektronik an, nämlich die reproduzierbare Herstellung von atomaren (Punkt-)Kontakten

Darüber hinaus wurden an diesen Kontakten CO-Moleküle adsorbiert. Als eines der einfachsten asymmetrischen Moleküle war CO ein guter Kandidat, um die Rolle der Chemisorption an solchen Verbindungen zu verstehen. Zeitaufgelöste Strommessungen zeigten Bistabilitäten, die von den Vorspannungen abhängig waren. Die Leitfähigkeit konnte reproduzierbar zwischen zwei Zuständen einfach durch Ändern der Betriebsspannung geschaltet werden. Dies legt nahe, dass selbst die einfachsten molekularen Verbindungen die Fähigkeit besitzen, als Schalter oder Speicherelemente zu fungieren. Im vorliegenden Fall konnten für den exakten Mechanismus nur einige mögliche Szenarien skizziert werden, er ist jedoch noch nicht verstanden. Diese Dissertation enthält also auch spannende Ergebnisse zu den elektronischen Modifikationen von atomaren Silberkontakten durch Chemisorption.

Schlagwörter: Elektromigration, Nanostrukturierung, atomare Punktkontakte, CO Moleküle, Ag

Acronyms

2DEG	2 dimensional electron gas.....	37
AFM	Atomic force microscope.....	4
C-AFMBJ	Conducting probe atomic force microscopy break junctions	4
DI	De-ionised.....	48
EBL	Electron beam lithography	4
EDX	Energy dispersive x-ray.....	91
EM	Electromigration	4
EMBJ	Electromigrated break junctions.....	4
FCE	Feedback controlled electro-migration.....	7
FEM	Finite element method	127
FIB	Focused ion beam	4
FPGA	Field programmable gate array	29
HOMO	Highest occupied molecular orbital	10
HRTEM	High resolution transmission electron microscope	38
HV	High voltage	52
ICCG	Incomplete Cholesky Conjugate Gradient.....	128
IETS	Inelastic electron tunneling spectroscopy.....	16
LDOS	Local density of states.....	43
LT	Low temperature.....	28
LUMO	Lowest unoccupied molecular orbital	10
MBE	Molecular beam epitaxy	53
MCBJ	Mechanically controllable break junctions.....	4
MIBK	Methyl isobutyl ketone	53
MMA	Methyl methacrylate	52
MTTF	Mean time to failure	24
NMP	N methyl pyrrolidone.....	51
PCG	Preconditioned Conjugate Gradient	128
PMMA	Poly methyl methacrylate	52
RT	Room temperature	9
SAM	Self assembled monolayer.....	14
SC1	Standard cleaning1	48
SC2	Standard cleaning2	48
SEM	Scanning electron microscope.....	19
SERS	Surface enhanced Raman spectroscopy.....	11
SPA-LEED	Spot profile analysis low energy electron diffraction.....	55
SPMBJ	Scanning probe microscopy break junctions.....	4
STM	Scanning tunneling microscope	4
STMBJ	Scanning tunneling microscopy break junctions	4

TEM	Transmission electron microscope	8
TM	Thermal migration	8
UHV	Ultra-high vacuum	42

Contents

1	Introduction	1
1.1	The need for molecular electronics	2
1.2	Molecular electronics: A concise overview	3
1.3	Techniques to fabricate atomic-sized electrodes and molecular junctions	4
1.3.1	Scanning Probe Microscopy Break Junctions (SPMBJ)	4
1.3.2	Mechanically Controllable Break Junctions (MCBJ)	6
1.3.3	Electromigrated Break Junctions (EMBJ)	7
1.4	Single molecular junction properties apart from electronic transport	8
1.4.1	Mechanical properties and mechanical characterisation	9
1.4.2	Thermoelectric properties	9
1.4.3	Optical properties and opto-electronic characterisation	10
1.4.4	Spintronics and Quantum interference	12
1.5	Functionalities of single molecular junctions	13
1.5.1	Switches	13
1.5.2	Rectifiers	15
1.6	Challenges and Open Questions	16
1.6.1	In-situ Characterisation setup	16
1.6.2	Lack of reproducible atomic and molecular junctions	17
1.6.3	Integration and Commercialization	17
1.7	Objectives and Outline of this dissertation	18
2	Theory of electromigration (EM) and atomic point contacts	21
2.1	Physics of EM	22
2.1.1	Blech Length	23
2.1.2	Blacks'law and Mean Time to Failure (MTTF)	24
2.1.3	Wire width	24
2.1.4	Micro-structure	25
2.2	EM: a serious issue in thin films	26
2.3	EM in nano-meter sized electrodes for generation of point contacts	28
2.4	Transport properties through metallic point contacts	30
2.4.1	Classical Maxwell's theory	31
2.4.2	Semi-classical Sharvin's approximation for ballistic contacts	33
2.4.3	Scattering approach : Landauer's formula	34
2.5	Conductance of atomic sized metal contacts	36
2.5.1	Conductance quantisation	37
2.5.2	Mechanism of atomic contact formation	40
2.5.3	Conductance histograms	42
2.5.4	Local density of states in atomic contacts	43
2.6	Conductance of metal-molecule junction	44

3	Materials and Methods	47
3.1	Sample Preparation	48
3.1.1	Photo-lithography processing steps for contact pads fabrication	48
3.1.2	Electron beam lithography (EBL) of the nano-structures	51
3.1.3	Focused ion beam (FIB) patterning on the nano-structures	54
3.2	4-tip SEM/STM UHV chamber	55
3.2.1	High resolution SEM in combination with multi-tip STM	56
3.2.2	Standard contacting procedure	57
3.2.3	EM setup	58
4	EM and morphological changes in Ag nano-wires	61
4.1	EM: A brief overview	62
4.2	EM in Ag nano-wire structures	63
4.3	EM in notched Ag nano-wire structures	65
4.4	Theoretical simulations of EM and thermal migration (TM) in Ag nano-wires	67
4.4.1	Modelling of the nano-wire structure	67
4.4.2	Geometries simulated	70
4.5	Simulation results of the Ag nano-wire	70
4.5.1	Temperature profile	71
4.5.2	Current density profile	72
4.5.3	Temperature gradient profile	73
4.5.4	EM Mass Flux	74
4.5.5	TM Mass Flux	74
4.5.6	EM Mass Flux Divergence	75
4.5.7	TM Mass Flux Divergence	76
4.6	Conclusion	77
5	EM in bow-tie structures	79
5.1	Bow-tie structures	80
5.2	Structure formation in bow-tie structures by EM	80
5.3	Formation of tunnelling contacts by EM	82
5.4	Electrical measurements	83
5.4.1	Conductance traces	84
5.4.2	Statistical analysis	85
5.5	Fourier transform of experimental conductance histograms	87
5.6	Conclusion	90
6	Fabrication of atomic point contacts using FIB patterned structures	91
6.1	Fabrication of different geometries for local morphology control using FIB . .	92
6.1.1	FIB line structuring	93
6.1.2	FIB Elliptical structuring	94
6.2	EM in FIB structures	94
6.2.1	EM in line structured samples	94
6.2.2	EM in ellipse structured samples	95
6.3	Energy dispersive x-ray (EDX) measurements in FIB structures	96

6.4	Electrical measurements	97
6.4.1	Conductance traces of ellipse structures	97
6.4.2	Statistical analysis	99
6.5	Conclusion	102
7	Modification of atomic point contacts by CO adsorption	103
7.1	Introduction to molecular junction measurements	104
7.2	Experimental details	104
7.2.1	Fabrication of Ag atomic contacts with defined geometry	104
7.2.2	CO adsorption	106
7.2.3	Time resolved current measurements of Ag-CO junction: CO switch	109
7.3	Possible scenarios: CO switch	113
7.3.1	Switching between adsorption sites	113
7.3.2	Local changes in bond angles thereby modifying electronic states	113
7.3.3	Number of molecules	116
7.4	Conclusion	116
8	Summary and Outlook	119
8.1	Summary	119
8.2	Outlook	119
I	Appendix	121
A	Experimental Techniques	123
A.1	Electron Microscopy	123
A.1.1	Scanning electron Microscope (SEM)	123
A.1.2	Energy dispersive x-ray (EDX)	126
A.2	Finite element analysis	127
A.2.1	Finite element method (FEM)	128
A.2.2	ANSYS	128
A.2.3	Equations used in the simulation	129
A.3	Fast current measurement (FCM) setup	130
A.4	Data Treatment	133
B	Bibliography	137
C	Publications	167
	Curriculum Vitae	169
	Acknowledgements	171

Chapter 1

Introduction

*Nano-technology is manufacturing
with atoms*

William Powell

In this introductory chapter, the main motivation behind molecular electronic measurements would be set. Though the field of molecular electronics is still in its fundamental and experimental phase, nevertheless, the extensive on-going research can fairly improve the chances of realizing a commercial molecular electronic technology.

Starting with a brief introduction of molecular electronics and its importance, the different methods used to construct measurement test-beds for molecular testing will be explained whilst detailing the advantages and disadvantages of each technique. Apart from electronic transport, studies highlighting the optical, mechanical, thermoelectric as well as the spin properties of single molecule junctions would be detailed next, to provide the readers with a broader insight into this interdisciplinary field. After introducing the several ways to measure different properties of the system, two important molecular functionalities are introduced as examples (switches and rectifiers). Towards the end of this chapter, the different challenges and open questions that continue to exist in this field are discussed. Finally, the chapter concludes with the objectives of this dissertation along with a chapter-wise outline at the end.

1.1 The need for molecular electronics

The long-standing problem of electronic circuit miniaturization is nearing its limit. Moore's law defines that the number of transistors on an integrated circuit doubles every two years. This prediction by Gordon Moore was used to estimate the long term requirements in the research and development areas and it has proved to be accurate over several decades. Nevertheless, in the last 40 years, the size of transistors have shrunk from $10\mu\text{m}$ to 5nm (in present research devices) [1]. With this demand of miniaturization, the number of transistors on an integrated circuit would have to reach 32 billion by the year 2020: meaning, the size of one transistor needs to go down even further. Over the years, the down-scaling of electronic devices not only concentrated on the size of the device but also on the efficiency and its overall performance.

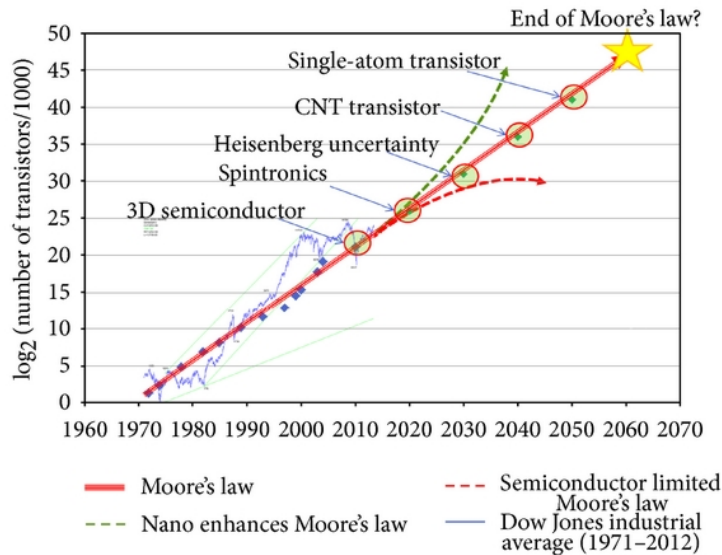


Figure 1.1: The red bold line depicts the conventional Moore's law whereas the red dashed line marks the limit of the semiconductor Moore's law. Nano-technology enhances the Moore's law which is marked with a green dashed line showing the ultimate miniaturisation as a single-atom transistor. Adapted from [2]

Nevertheless, Moore's law is approaching its limit. Downscaling at this rate is extremely difficult with the present lithographic technologies. This is because the resolution with present lithographic techniques is still one order of magnitude higher than the approximate size of a single molecule. It has already become challenging to reproducibly fabricate structures below 20nm . Furthermore, when the size approaches a certain range (below 10nm), quantum mechanical principles dominate the behaviour of such devices. Moore's law is depicted in Figure 1.1 [2]: showing the semiconductor limited Moore's law and nano enhancing Moore's law until the limit of a single atom transistor.

The smallest possible entity by definition is an atom. A molecule is the smallest stable functional entity that can be used as a device. To meet the limits of Moore's law, the smallest miniaturisation possible/feasible is by designing electronic components using atoms

and (or) molecules. Functional electronic components made out of atoms and molecules can be the ultimate smallest size that can be realized. Hence, *Molecular electronics*, which deals with the fabrication and realisation of integrated devices using atoms and molecules become important. The present Si technology cannot get closer to atomic scale resolution that molecular electronics can achieve, making it one of the promising fields of the present research.

After the discovery of the properties of a metal-semiconductor junction, the functionalities such as diodes and transistors could be realised based on the fact that the mechanism of current flow in metals and semiconductors is different. The present semiconductor technology is based on devices made out of Si. The band-gap of Si is a bulk property and one or few atoms of Si would behave differently as compared to the bulk. This fact is the reason why transistors below 10 nm made out of Si is no longer reliable. This brings in the uncertainties related to quantum mechanical principles. In a similar manner, transport through any metal-molecule junction would behave differently. Therefore, it is necessary to investigate the transport properties of various metal-molecule junctions. Furthermore, interfacing issues with existing electronic technology would be another challenge. Hence, the field of molecular electronics brings in a lot of future prospects to solve the miniaturization problems (which has reached a saturation now) along with its challenges to circumvent the uncertainties. Therefore, it is necessary to develop a better understanding of the underlying physics to overcome the uncertainties within this area of research. This will also allow steps forward to the ultimate miniaturization issues.

1.2 Molecular electronics: A concise overview

As briefed slightly in the previous paragraph, it is the study of using molecules to construct the building blocks of an electronic circuit. Such studies, in the future will enable smaller electronic circuits that could have the possibility to replace today's conventional electronic circuitry. It deals with both experimental as well as theoretical studies mainly concentrating on charge transport through single molecules between atomically spaced metallic electrodes. The intrinsic properties of a free molecule in a vacuum can get completely altered or significantly changed when it is placed between electrodes. It is also important to understand the reasons behind the modification of the intrinsic molecular properties in the presence of the electrodes.

In reality, a molecule can be characterised by a discrete set of molecular orbitals. Because of the coupling between the metal and the molecule, there is a broadening of the molecular orbitals close to the interface. This results in some charge transfer between the two, further shifting the molecular orbitals with respect to the Fermi level of the metal. When an external bias is applied, further re-organisation of charge takes place. These are known as interface effects which only influences the junction properties over a few nano-meters. In such a scenario, the properties of the bulk material are almost un-affected. On the other hand, for *Molecular electronics*, this interface is the prime element of the complete device. Hence, the chemical nature of the bond as well as the electrode-molecule geometries, very much influences the final properties.

For the first time in the year 1974, Aviram and Ratner [3] suggested that a molecule can behave as a rectifier. Since then this idea has served as a vision for future molecular electronics.

Contemporarily, experiments on single molecular layers were conducted by Kuhn et al. [4]. Then in the 1980s, the development of scanning tunneling microscope (STM) and atomic force microscope (AFM) both from IBM Zurich Laboratory, quickly became outstanding tools for visualising molecules and measuring their properties, making this field of research more realistic. After that around the 1990s and beginning of 2000, first attempts to measure single molecule conductance was made by the groups of Mark Reed and James Tour [5, 6].

Measuring the electrical conductance through single molecules and the integration of molecular devices to the existing technology is not very easy. There are basically three most important primary challenges. First amongst them is the fabrication of sub nano-meter spaced atomically precise electrodes and second, having one functional molecule reliably bonded between those atomically precise electrodes. The proper functionality of the molecular junction heavily depends on the fluctuations of the electrode-molecule interface, which is the third aspect. Electrode fabrication and molecular functionalities are challenges that have still not been optimized even though various techniques have been developed. Fluctuations in electrode molecule coupling still remains a very serious issue. Within the introduction, the different techniques used for fabrication of ultra-small electrode gaps and molecular junctions will be first discussed, followed by the several molecular properties that can be measured in addition to electronic transport. Towards the end of the introductory chapter, some functionalities such as switches and rectifiers are mentioned followed by open questions and challenges. This discussion helps to understand the present state of the art with existing open questions that need to be addressed.

1.3 Techniques to fabricate atomic-sized electrodes and molecular junctions

There are different techniques to fabricate sub nano-meter spaced electrodes [7–10]. The three most important and well established ones are mechanically controllable break junctions (MCBJ), scanning probe microscopy break junctions (SPMBJ) and electromigrated break junctions (EMBJ). Apart from these, there have been many other attempts to fabricate such electrodes. These include angle deposition [11, 12], electromigration (EM) while metal deposition [13, 14], electrochemical approach [15, 16], shadow evaporation [17], photo-lithography with pattern size reduction [18], nano-imprint lithography [19], adhesion lithography [20], self aligned nano-lithography [21], focused ion beam (FIB) milling [22–26] and electron beam lithography (EBL) [27, 28]. None of these approaches could be established as full-proof techniques. The main issue in these techniques is primarily the reliable formation of atomic point contacts in a controllable manner. The existing established break junction methods will be discussed in detail in the following subsections.

1.3.1 Scanning Probe Microscopy Break Junctions (SPMBJ)

Basically, this technique involves the formation of a metal-molecule-metal junction between a conducting substrate and a metallic tip (scanning probe). The molecules can be either in vacuum or in liquid and can either be present in the solution before the formation of the junction or can be evaporated in-situ under vacuum. SPMBJ [29–33] is mainly of two types - scanning tunneling microscopy break junctions (STMBJ) and conducting probe atomic

force microscopy break junctions (C-AFMBJ). The working mechanism between both the techniques, STMBJ and C-AFMBJ is slightly different. In the case of STMBJ, there is a tunnelling current between the conducting substrate and the metallic tip, where both are in close proximity but not in direct physical contact [9]. On the other hand in C-AFMBJ, an external circuit is used to apply current between the conducting substrate and the metallic tip which are in direct physical contact. The strength of this technique lies in the fact that it can perform high resolution imaging of the molecule in contact but nevertheless it is very challenging. Figure 1.2 [30, 32] shows an example each for both types of SPMBJ i.e. STMBJ and C-AFMBJ.

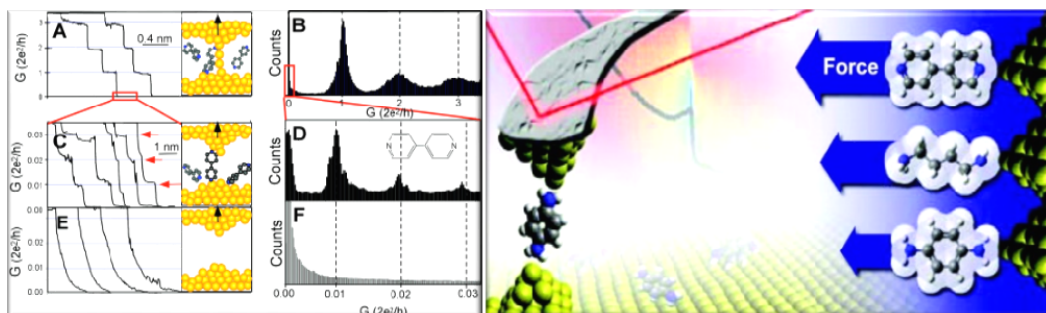


Figure 1.2: Left: STMBJ illustration reproduced from [30]. Here a Au tip is used to create the junction with a gold substrate on the other side. Conductance plateaus show formation of a successful metallic junction. Right: C-AFMBJ illustration reproduced from [32]. Image shows a pictorial representation of the technique.

Such a technique can be used to perform repetitive measurements by bringing the tip in and out of contact with the substrate containing molecules. This enables the collection of a huge amount of traces with statistical analysis and simultaneous imaging possibilities. Such methods are very sensitive to the tip shape and to the roughness of the substrate. The molecular orientation can change according to the space availability and shape of electrode tips. Other disadvantage of such an approach is that it suffers from huge thermal and mechanical instabilities that do not allow stable measurements for prolonged period of time as compared to the other methods described below.

Now that the technique is described with its general limitations and advantages, it must be understood that the actual realisation of a molecular junction with this technique is complicated. The method itself describes the formation of a metallic junction using a tip and a substrate, which to some extent introduces randomness in the configuration of electrodes. The atomic configuration of a tip in contact with the substrate definitely would not be exactly identical to the atomic configuration of the substrate electrode. This introduces some asymmetry between both sides. Now, if a molecule is introduced in between the two electrodes, it can have several possible binding sites due to the asymmetric configuration of the electrodes. This can already be noticed in the cartoons (A and C) in Figure 1.2. This can cause misinterpretation between the transport data of molecules. Without the confirmation of well-defined electrode configurations, analysis of molecular junction becomes tricky and the reliability of the technique becomes totally dependent on statistics.

1.3.2 Mechanically Controllable Break Junctions (MCBJ)

In this technique, the thinning of a metallic wire (notch-induced) or a well-defined lithographically patterned metallic nano-wire (on a substrate) is carried out by placing the sample between two supports and simultaneously pushing the sample from underneath using a pushing rod. As the name suggests, the approach here is very similar to SPMBJ with the difference lying in the way the electrodes are moved. In SPMBJ, the tip is directly moved with piezo-actuator displacements, whereas in MCBJ (Figure 1.3), the substrate bending is performed by the piezo-activated pushing rod. This vertical displacement of the pushing rod introduces the horizontal inter-electrode separation in the lithographically defined metallic free-standing nano-wire structure. With nano-meter scale precision of the pushing rod displacements, sub pico-meter electrode displacements can be achieved. This method is known for its outstanding mechanical stabilities and ultra-precise control of electrode gaps at the angstroms level. These are the two important differences between MCBJ and SPMBJ (mechanical stability and control of gap sizes). MCBJ is quite robust in these two aspects.

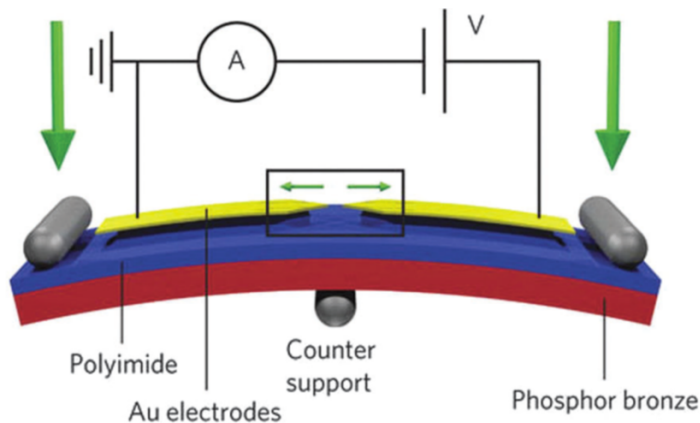


Figure 1.3: MCBJ illustration reproduced from [34]. The different parts of the set-up is labelled giving an impression of the role of various parts.

MCBJ was first introduced by Moreland et al. [35] and Muller et al. [36]. The first illustration of MCBJ for molecular junctions was demonstrated by Reed et al. [5]. While the advantages of this method have already been pointed out, the main disadvantages include insufficient information about the exact local shape and configuration of the electrodes as well as at the vicinity of the molecular junction. This method can be performed in liquid as well as in vacuum and molecules can be deposited before breaking the junction in solution or can be deposited in-situ under vacuum after breaking the junction. As there is no control on the number of molecules within the gap or in the vicinity, the MCBJ method always needs additional simulation studies or other experimental support to explain the data and possible molecular configurations. The limitation of both the discussed techniques (SPMBJ and MCBJ) regarding well-defined starting configuration of electrodes is quite similar. SPMBJ still has some control on the number of molecules being bridged between the junction but on this aspect MCBJ takes a back-seat. The definition of electrode molecule geometries is very important for the reliable functioning of molecular junctions.

1.3.3 Electromigrated Break Junctions (EMBJ)

This method is an electrical form of MCBJ. In EMBJ, (Figure 1.4), the mechanical forces in the case of MCBJ are replaced by electrical forces in EMBJ. A lithographically patterned metallic nano-structure with a well-defined nano-constriction at the centre is subjected to voltage ramps that produce high current densities at this constriction (due to geometry). Due to high current densities, electron wind forces dominate over the field forces at the centre, forcing material movement against the direction of current flow. In Figure 1.4, (a figure similar to [37]) it can be noticed that a hillock (accumulation of material) appears along the direction of electron flow. The removal of material from the other electrode produces a void (size of the void can be controlled) on the other side. By controlling the current carefully, sub nano-meter separation between the two electrodes can be achieved. This is the most versatile property of this technique that does not require any complicated set-up or designated electronics in order to fabricate point contacts. The only control one needs to monitor is the current and in principle, atomically precise control on the fabricated electrodes can be possible. EM process is accompanied by other competing processes (discussed later) which makes it critical and difficult to control the gap sizes. Nevertheless, efforts have been made to optimise the process.

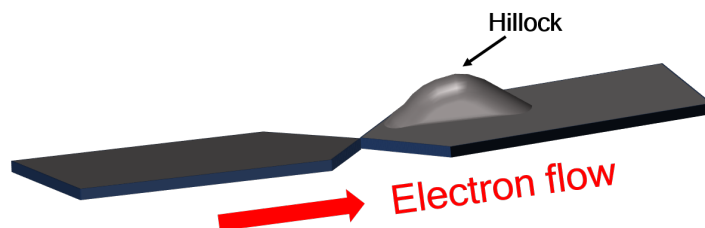


Figure 1.4: This is a model representation of a Ag bow-tie nano-structure subjected to EM. The direction of the electron flow determines the material movement. A hillock marks the material accumulation by EM.

EM possesses the capability to control the atomic configuration of electrodes as the process involves atom by atom movement (reverse of an electrochemical method). It has another advantage with respect to molecular measurements i.e. the field enhancement at the gaps. A molecule can be trapped easily due to the field enhancement at point contacts. The only limitation of such a technique is the difficulty to re-use the already electro-migrated junctions (once broken) whereas it is possible to mechanically open and close junctions in case of MCBJ. For performing statistics using EM, multiple junctions need to be tested. In this regard, there have been attempts for the parallel fabrication of nano-gaps using this technique [38, 39]. EM technique is also very advantageous for fabricating three terminal device configurations for molecular electronic applications [40].

EMBJ method was first reported by Park et al. [41] for fabricating electrodes with nano-scale separation. Since then, many investigations were performed. Another major development to control the EM technique was reported using a feedback control instead of individual ramps, known as feedback controlled electro-migration (FCE) [42–46]. Different types of feedback parameters were used in order to make the EM process more controllable and reproducible [47, 48]. Furthermore, modification of the 2-terminal configuration EM to a

4-terminal configuration EM set-up [49] was also reported as a better version to control the process. Other off-springs of this method include field-emission induced EM [50–57]. It has to be understood that there is a very close relation between EM and thermal migration (TM). Temperature gradients are developed during the flow of current through a constricted structure. This close relation between EM and the several other temperature related competing processes led to different attempts to estimate the TM effects on the process of EM and calculation of temperature gradients within the structure [58–61] during the process. In-situ transmission electron microscope (TEM) imaging [61–68] was also carried out to observe the gap formation by EM in real-time.

1.4 Single molecular junction properties apart from electronic transport

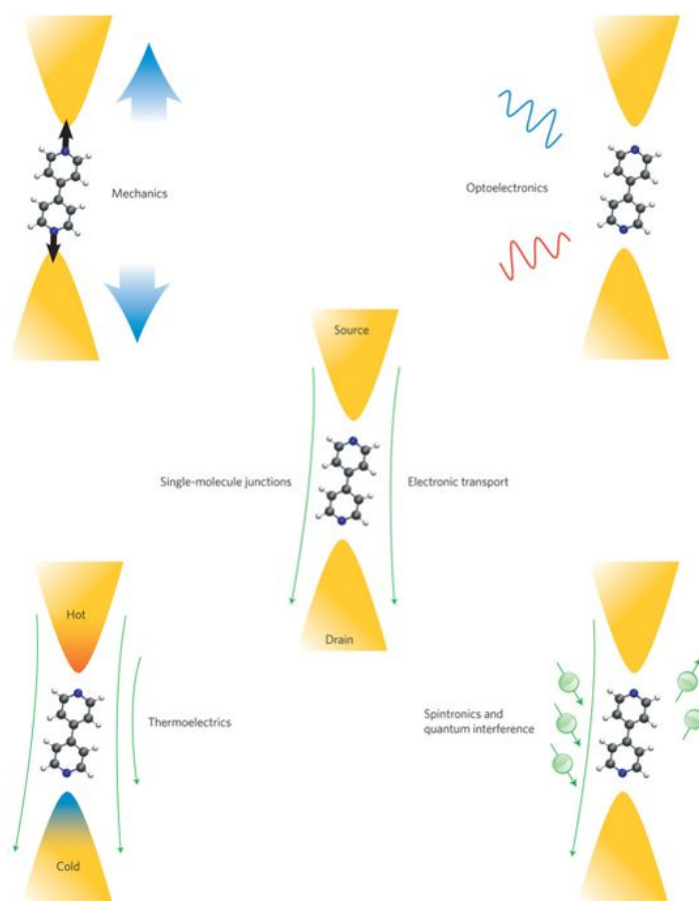


Figure 1.5: Illustration reproduced from [69]. This overview illustration shows the capability of molecular electronics and a wider perspective apart from electronic transport.

After the introduction of the different well-known techniques used to fabricate metallic electrodes and molecular junctions, this section focuses on the different characteristics of a single molecular junction. Apart from electronic transport, investigation of several other

properties of the molecular junctions are presently being carried out in order to complement electronic characterisation. For example, optical, thermal, mechanical and spin properties are being explored (Figure 1.5). The following subsections briefly deal with the importance of each of these properties and their contribution to the overall understanding of a metal-molecule-metal junction at the atomic scale.

1.4.1 Mechanical properties and mechanical characterisation

Electronic transport measurements of single molecule junctions alone, are not able to provide any direct structural information about the junction. Direct imaging of atomically resolved mono-atomic Au wires has been performed [70] to correlate structural information with electronic properties. However, this technique is not suitable for molecular junction investigations. In this regard, simultaneous electronic and mechanical measurements of the single atomic junctions can provide significant information about the structure of these junctions [71]. Rubio et al. [72] carried out the first simultaneous measurements of force and conductance of Au point contacts and similarly Tao and co-workers [73] demonstrated similar measurements at room temperature (RT) which is a widely accepted method today.

The most important information from such measurements is the relation between the force and the current measured. Ternes et al. [74] could realise the theoretical prediction that force and tunnelling current scales similarly with distance, experimentally. The similarity in the exponential decay of current and short-range forces with increasing distance between the electrodes with almost the same decay constant gives an indication that the same orbital likely controls both the parameters. Measurements using the static AFM mode [73] demonstrated the feasibility of measuring bond rupture forces and correlate them with the linker groups and the backbone of the molecule. The works of Wagner et al. [75] and Aradhya et al. [76] showed direct quantification of the contribution of Van der Waals forces on molecular junctions. In all these measurements discussed, the junction conductance was the primary signature and the mechanical forces were considered to be the secondary property. However for non-conducting molecules, which also form junctions mechanical force measurement may be the primary signature. This new avenue of force measurements on single molecule junctions serves a potential way to mechanochemistry [69].

1.4.2 Thermoelectric properties

It is a long-standing issue to experimentally measure the thermal heating within the metallic nano-wire and atomic contacts. Several theoretical simulations have been performed to estimate the temperature profile of the nano-constrictions formed using different techniques but there is still not enough experimental information available. On these lines, there are some important works from the group of Reddy and co-workers [77]. They developed a technique to probe the temperature with nano-meter resolution, which they named as scanning thermal microscopy [78]. Using this technique they estimated the temperature profile during EM of nano-wires [59] and correlated it with simulations. Scanning thermal microscopy functions as a thermocouple tip (Figure 1.6) used to measure the temperature profile of an electro-migrated structure 100 nm away from the cathode connecting the nano-wire. Correlation of the temperature calculations and extrapolations within the nano-wire with the simulations suggest that the asymmetry in the temperature profile is attributed to the phe-

nomenon of material transfer during EM. Such developments help to gain deeper insights on the in-accessible measurements, such as in-situ temperature measurement during EM.

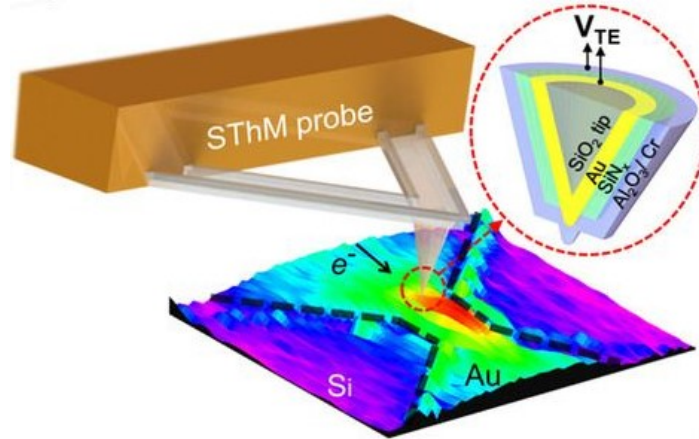


Figure 1.6: Figure reproduced from [59] Model representation of a scanning thermal microscopy setup. This depiction shows how the tip (thermocouple) was used as the tool for estimating the temperature of a local nano-structure subjected to EM.

Several experimental techniques were proposed recently to measure thermo-power and Seebeck coefficient (S) in point contacts. Ludoph et al. [79] were the first to experimentally measure S in Au point contacts via thermoelectric measurements of molecular junctions. Similarly, Reddy et al. [80] used an STM geometry to quantify S in molecular junctions. They reported that a positive S increased with increasing molecular length. Such measurements allowed an understanding of the transport mechanisms involved therein. For example, Venkataraman and co-workers [81] showed that amine-terminated molecules conduct through the highest occupied molecular orbital (HOMO) but pyridine terminated molecules conduct through the lowest unoccupied molecular orbital (LUMO). A variety of molecular junctions has been used to measure S , which involves hole and electron transport [82–84]. Changing the functional groups changes the value of S indicating the direct influence of the chemical structure on the thermoelectric properties. Yee et al. [85] showed n-type fullerene molecules could help to generate high thermo-power values. This can help in future molecular device fabrication and technologically benefit to convert waste heat for useful purposes.

1.4.3 Optical properties and opto-electronic characterisation

Optical properties influencing electronic transport in molecular electronic devices is an interesting field known as molecular optoelectronics [69]. However, the fundamental mismatch lies in the optical and molecular length scales where the former is in micro-meter scale. In spite of this mismatch, there are two main motivations of such studies being crucial and helpful in the understanding of the working of molecular electronic devices. They are: (a) sub nanometer spaced metallic electrodes serve as excellent candidates for local field enhancement of plasmons [86, 87]. Using Raman spectroscopy characterisation of these local structures can be performed [88–91] (b) for many molecules, light serves as an external stimulus for switching and other properties. Ward et al. [92] demonstrated simultaneous electrical and optical

measurements on electro-migrated Au molecular junctions and obtained Raman signals that could be used in identifying junction structures [93, 94]. Later they extended this work to obtain information on vibrational and electronic heating in molecular junctions [95]. Similarly Liu et al. [96] combined Raman spectroscopy along with STMBJ and performed simultaneous optical and conductance measurements on Au STM break junctions. Both the studies by Ward et al. and Liu et al. found striking differences between Raman spectra of conducting and broken molecular junctions. These findings clearly show that optical measurements can help in understanding the effect of local structure on transport properties [97].

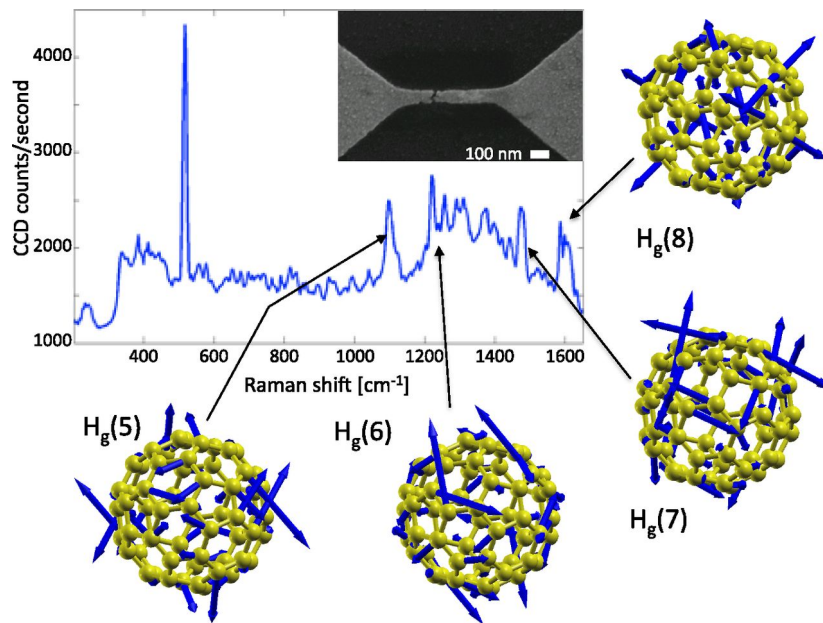


Figure 1.7: Figure reproduced from [98] Raman Spectra of C_{60} molecule between an electromigrated junction. The respective values are marked as contributions from the different configurations of the molecule.

Surface enhanced Raman spectroscopy (SERS) is becoming increasingly common as optical measurements are helpful in providing valuable molecular information [98–100]. Figure 1.7 depicts a fullerene molecular junction which is fabricated by EM. The different peaks in the Raman spectra attribute to the different rotational configurations of the C_{60} molecule. Such studies demonstrate the possibilities to directly locate molecules within the gap. There are also examples of combined SERS on MCBJ [101] and SERS on EM junctions [102]. Ho and co-workers [103, 104] showed a measurement of differential conductance as well as photon emission simultaneously on individual molecules using STM. In this method they used an insulating layer between the molecules and the metallic layer so that the radiated photons are not quenched by the metal and the molecular fingerprint information is present in the emitted photons. Berndt et al. [105] studied plasmon mediated emission in metallic electrodes. However, the main challenge in these electro-luminescence studies compared to Raman studies is to find the correct combination of insulator and molecule making it quite uncommon.

The second motivation behind optical studies of molecular junctions is the use of light as a

stimulus for controlling the transport of molecular junctions. There are examples of molecules that can be switched between different isomers in presence of light [106–108]. Although a large number of molecules are known to switch in solution in presence of light, contacting them with metallic electrodes have shown alteration in switching properties. Light can be coupled to nano-scale electrodes, and being able to couple plasmons with molecular electronic devices can be a new dimension for nano-fabrication of transmission lines and optical antennas [69, 109, 110].

1.4.4 Spintronics and Quantum interference

Miniaturisation using molecular electronics cannot be complete without involving quantum mechanical concepts [111]. Keeping this in mind, the ability to control electronic and nuclear spins within molecular electronic devices can be helpful to realise new functionalities. Experimental works from the groups of McEuen, Ralph [112] and Park [113] demonstrated spin transport and Kondo effect for the first time. After these breakthroughs, Kondo effect was studied in other single molecule junctions as well [114, 115]. This effect is not only restricted to molecular junctions but has also been observed in bare Au junctions [116]. Not only that, Kondo effect was also observed in ferromagnetic Ni electrodes [117]. Sordan et al. demonstrated the Coulomb blockade effect in electro-migrated break junctions [118].

Spintronics can serve as the mechanism for future molecular electronic storage devices [119]. Experiments have been carried out with three combinations i.e magnetic molecules and non-magnetic electrodes, non-magnetic molecules and magnetic electrodes, and magnetic electrodes and magnetic molecules [69]. Such trials have helped in understanding the spin-dependent transport of electrons. Electronic spins are coupled to the electrodes, which makes it even more challenging. On the other hand, nuclear spins are very weakly coupled to the surroundings. There are studies by Vincent et al. [120] where they propose a new way to read out the nuclear spin of a Tb atom in a single molecule device. The studies mentioned above not only help in understanding the magnetic properties of single molecules and atoms but also can help to design future memory and logic devices using single molecules [69].

Quantum interference appears due to the wave nature of electrons, when the device length is of the order of the phase coherence length of electrons. This effect can decrease or increase the conductance value depending on the position of the functional groups. In fact, this can open up new pathways for controlling various device operations such as switching [121]. Theoretical efforts to understand this can be found in these references [122–125]. It was reported that quantum interference not only modifies the transmission spectrum but also affects intra-molecular electron transfer paths and in special cases can flow mainly through space rather than through molecular bonds [126]. It was suggested that electron-phonon coupling in molecules can quench quantum interference effects [127]. Experiments confirming the theoretical predictions of quantum interference affecting the transmission spectra have recently been performed [128, 129].

Though the concept is very simple, it is not easy to realize such concepts experimentally in a reliable manner. In a simple conductance superposition experiment [130], two molecules were investigated, where a conductance enhancement of a factor of 4 was expected. However, even in such a simple experiment, conductance enhancement of a factor of 3 was obtained instead of 4. This shows that molecular junctions cannot be easily treated as scaled-down

versions of mesoscopic devices. Furthermore, systematic research is needed for the better understanding and realization of such concepts. Nevertheless, the existing knowledge and experience are also important to design future molecular electronic devices.

1.5 Functionalities of single molecular junctions

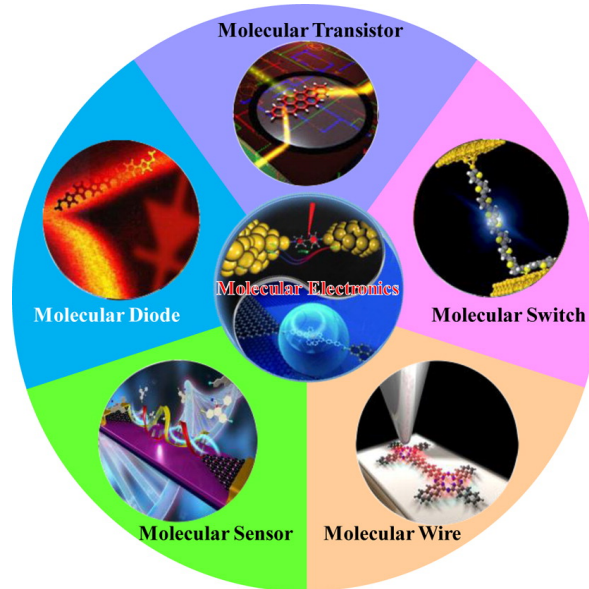


Figure 1.8: Illustration reproduced from [131]. The figure illustrates the several electronic components that can be realised using the concept of molecular electronics.

Now that the popular techniques for fabrication of molecular junctions with respective advantages and limitations, as well as the properties that could be measured with these molecular junctions apart from the electronic properties are discussed, now some examples of real functionalities leading to the actual applications will be described. Many different functionalities have been realized using molecules, namely transistors, diodes/rectifiers, switches, sensors, wires, etc. An illustration shown in Figure 1.8 shows all of them. Two interesting functionalities are discussed below in detail i.e switches and rectifiers.

1.5.1 Switches

A switch is an attractive molecular functionality that has been studied over the years. In a switch, the conductance changes between two or more states. The low conductance state is referred to as the OFF position and high conductance state is referred to as the ON position. There are several ways in which such functionality can be realised. Changes in conductance states can be achieved in several ways (a) using stable molecular isomers (b) inducing conformational changes within same molecules (c) oxidation and reduction states of the molecule (d) changing the metal molecule interface coupling (e) attaching and detaching a molecule between electrodes and (f) by in-situ chemical reaction of the molecule. All the mentioned states of the molecule can be realised using different stimuli like UV and visible

light, electric field, heat, and current. Furthermore, metal-molecule interface coupling and inter-electrode gap distances can be tuned using mechanical forces from MCBJ and STMBJ.

Single molecule switches using isomers have been reported using the diarylethene molecules where the open isomer closes under the irradiation of UV light leading to a complete current path along the molecule. On the other hand, the closed isomer opens the ring under visible light irradiation, breaking up the current path into two [132]. The conductance of closed isomer is higher than that of the open form. Other examples of single molecule switches using photochemical reactions have also been reported [133, 134].

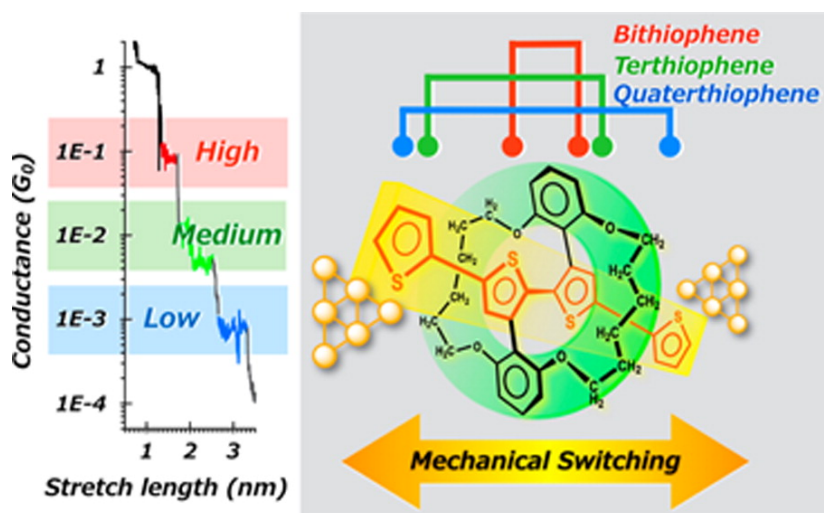


Figure 1.9: Illustration reproduced from [135]. The illustration depicts the length dependence on the conductance. The mechanical switching between anchoring sites changes the effective length and consequently the conductance changes.

Regarding switching by conformational changes, the first example of single molecule switches based on this mechanism was in phenylene ethynylene oligomers in matrices of alkane-thiolate self assembled monolayer (SAM) [136]. The origin of switching was attributed to the conformational changes of the monolayers. During STM imaging of the topographic profile of the molecules, the active molecules protruded out of the SAM in the high conductance state, whilst in low conductance state, the height relative to the SAM was lower. An example of stereo-electronic switching behaviour in single molecule junctions can be found in the works of Su et al. [137].

Another mechanism for single molecule switches is based on interface coupling [138]. Here the single molecule switching can be controlled by controlling the strength of metal molecule coupling using mechanical forces. Mechanically controlled binary switching has been seen in alkanedithiols, oligoenes as well as pyrazines. For example, in pyrazines [139], conductance between high and low states changed by moving the electrodes. By tuning the gap distances, anchoring positions in the same molecule can be changed, as reported by Miguel et al. [140]. Similar experiments using this mechanism of dynamically controlling the anchoring sites using STMBJ were carried out with oligothiophene [135]. The mechanical elongation and compression of the junction led to switching between three conductance states (changing length by mechanically changing anchoring sites) as shown in Figure 1.9. The longer molecule

quarterthiophene corresponds to the lowest conductance showing the length dependence.

Switching in an octanethiol single molecule junction using STMBJ was successful by controllable attachment and detachment of the molecule by adjusting the voltage between the tip and the substrate. The most recent mechanism, which involves an in-situ chemical reaction to control the anchoring positions of the single molecule, was realized by Huang et al. [141].

1.5.2 Rectifiers

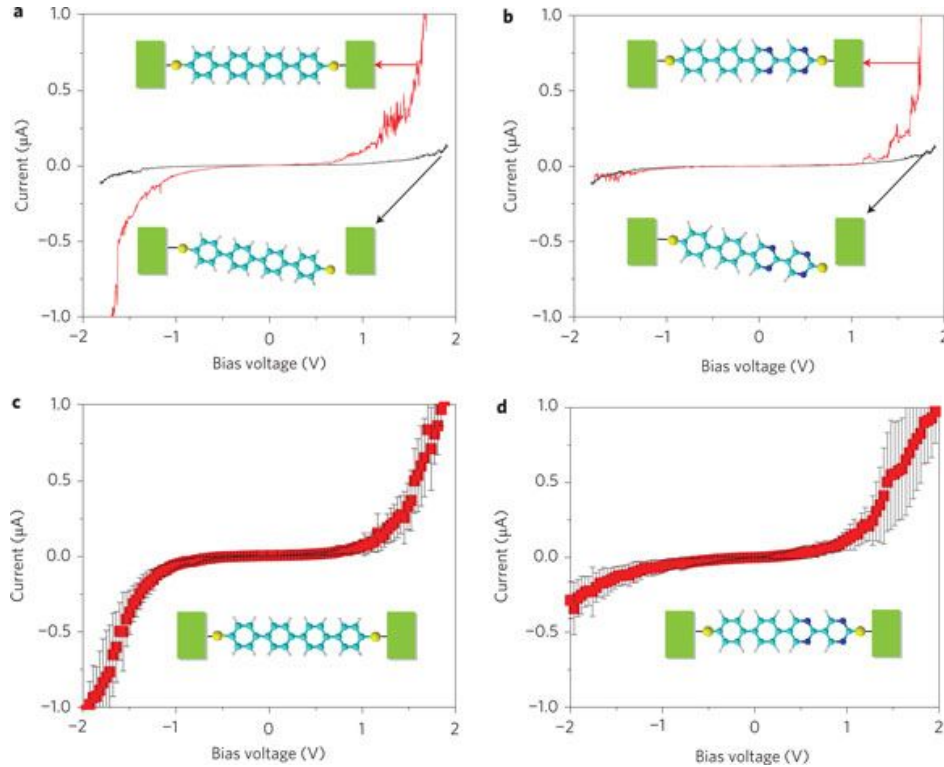


Figure 1.10: Figure reproduced from [142] (a) I-V characteristics of a symmetric molecule. (b) I-V characteristics of asymmetric molecule. (c) Average of 30 curves for symmetric molecules. (d) Average of 50 curves of asymmetric molecules.

Rectification is one of the very important basic functionalities required for future molecular device fabrication. This was proposed theoretically by the famous works of Aviram and Ratner[3]. In 1997, Metzger et al. reported experiments where a molecular diode was realised using monolayers of $C_{16}H_{33}Q-3CNQ$ with the Al layer below and Mg electrode coating on the top [143]. When the mismatch between the energy levels gets reduced by applying an external voltage in one particular polarity, and vice versa happens on the reversal of the polarity (i.e. the energy level difference increases), rectification can be realised in such a case. From this, it is easy to understand in terms of molecular electronics that an asymmetric electrode molecular interface can give rise to such a phenomenon. Asymmetric electrode molecule interface could be realised in three possible ways (a) asymmetric molecules [142, 144, 145] (b) asymmetric electrodes [146] and (c) inconsistent interface coupling [147, 148] on either side.

Experiments have been reported using both MCBJ and STM techniques to realise single molecular diodes/rectifiers using the three ways mentioned above. An example of an asymmetric molecule exhibiting rectifier behaviour is dipyrimidinyl-diphenyl covalently bound to Au electrodes with thiol bonds [142]. As a control experiment, the symmetric version of the same molecule showed no rectification (see Figure 1.10). Here, the molecule dipyrimidinyl-diphenyl was used in the STMBJ technique. The asymmetric configuration was controlled by a selective de-protection strategy. Using MCBJ technique, dipyrimidinyl-diphenyl have also been reported with diode like characteristics [149].

A single molecular diode has been reported using a DNA molecule [150], where the native DNA molecule did not exhibit any rectification but a DNA-coralayne single molecule junction showed high rectification ratios. In the second case of rectification, using asymmetric electrodes, either a normal symmetric molecule or an asymmetric junction itself without any molecule should serve the purpose due to the inherent property of work function mismatch. The first experiment with such an attempt was performed with a monolayer of hemiquinone attached to the surface of Au/Ag (anode) on mica with a Pt tip (cathode) [146]. A similar study was reported for phthalocyanines bound to highly oriented pyrolytic graphite (HOPG) [151]. The third mechanism to obtain rectifier like properties requires an inconsistent metal molecule interface. This was achieved in different ways by different groups. By using two electrodes of the same metal and symmetric molecules, the symmetry was broken by exposing different electrode areas to an ionic solution of molecules which exhibited rectification properties [152]. Another similar example is with an asymmetric molecule $C_{16}H_{33}Q-3CNQ$ between Au substrate and tip. Here, the Au substrate and the tip was functionalised with the same functional groups to achieve symmetric end contacts. Rectification disappeared in the case of the planar molecule, whereas rectification was observed when the molecule was twisted out of the plane [153].

After introducing the concepts, it is important to analyse the further developments needed and the areas of ambiguities already existing in the literature. As the field of molecular electronics is governed by quantum mechanics, the functioning of the final device can be affected substantially by uncertainties of the molecule-metal interface. The topic of the next section would be to identify the open questions and existing challenges that need serious attention in order to have a proper functional molecular device.

1.6 Challenges and Open Questions

1.6.1 In-situ Characterisation setup

Molecular electronic studies and techniques involve sub-nm spaced electrode fabrication and transport through a molecule between them. All existing methods to characterise molecular junctions are indirect measurements. Until now it has not been possible to directly measure a single molecule between two electrodes. This would directly solve many issues. For example, inelastic electron tunneling spectroscopy (IETS) measurements can be used to identify cis and trans isomers on exposure to irradiation [154] from vibrational fingerprints. This cannot be performed in-situ, during the switching of the molecule between the electrodes from one isomer to the other. There have been some in-situ TEM investigations of the EM thinning process [61–66, 68], but TEM technique itself requires ultra-thin sample preparation. It would

be very interesting if in-situ STM could be performed simultaneously during the EM thinning while measuring the conductance at the same time, to observe the generation of single atomic point contacts. Though there have been TEM imaging attempts on electro-migrated contacts (not possible in all samples), in-situ STM while thinning has not been achieved till today due to technical and interference issues. EM creates an un-even structure due to material transport, and it is difficult to perform STM on a rough surface at the atomic scale. These existing limitations do not allow direct information to be obtained from the structures. From the existing indirect measurements and theoretical simulations, only partial information can be obtained.

Apart from in-situ imaging techniques, a unique setup to measure in-situ properties such as electronic, mechanical, optical as well as thermal, all in one setup would have the capability to provide significant information on the functioning of molecular junctions.

1.6.2 Lack of reproducible atomic and molecular junctions

As already briefed earlier, the presence of a molecule between electrodes alters the molecular energy levels. Not only that, the functioning of such devices becomes extremely sensitive to the atomic configuration of both the molecule and electrodes along with their interface. Firstly, very well-defined electrodes (atomically precise) should be fabricated. This would solve the ambiguities in the local arrangement of atoms within the electrode and ensure reproducible contact geometries. Secondly, one particular method has to be standardised for the creation and characterisation of molecular junctions. This is because such measurements depend significantly on the mechanism involved during the fabrication as well as on several external parameters (foreign particle, radiation, electric fields, temperature changes, etc.). For example, junctions fabricated using self-diffusion of metal atoms can lead to completely different geometries and conductance values as compared to the junctions produced by mechanical pulling. Variation amongst different techniques is bound to happen in such a delicate field where the mechanism of formation is responsible for the final result.

Even though individual working groups have achieved a high standard of reproducibility, there are still variations between groups even experimenting with the same molecules using different techniques or electrodes. Such an ambiguity between techniques, electrodes, and molecules does not allow reproducibility in fabricating even the simplest junction.

1.6.3 Integration and Commercialization

The ultimate requirement of all these complex procedures is to integrate it with the existing circuitry. Though there has been extensive research on how to realize such devices and finding new functional molecules for the future, there has been considerably limited research focus on the integration strategies of the molecular electronic devices with the present electronic circuitry. Some challenges in this regard include parallel fabrication of nano-scale electrodes and proper connection with the macroscopic electronics. Existing functional devices involve SAMs. They are very fragile and not suitable for practical packaging purposes. Another practical challenge is the size compatibility. The size of existing technology and molecular technology needs a reliable interfacing platform. Not only that, the switching processes with molecules occur at much faster time-scales and at very small currents. This is also another serious issue. Other problems include: any commercial assembly should have the possibility to

be disassembled, which is quite difficult with molecular devices and lastly, molecular devices are sensitive to the environment, after incorporating in real devices, the functionality and efficiency should not be affected. In these aspects, nothing significant has been achieved so far.

To make this a commercial technique, there are several issues which need to be addressed. First how to manufacture a large number of nano-gap electrodes with an atomically precise configuration and how to precisely insert functional molecules in them so that all of them are equally addressable. Here come the problems of interference and cross talk which also have to be taken into account. As has already been reported by many, the immediate environment plays a huge role in the proper functioning of the device, multiple single molecule devices integrated into one chip may show different behaviour than the one tested without the others.

1.7 Objectives and Outline of this dissertation

The above-mentioned challenges and open questions need an in-depth physical understanding of the processes and technologies to realise them. Here in this thesis, the objective is to address the first two challenges (lack of reproducible atomic point contacts and requirement of an in-situ set-up) reported in the previous section. Firstly, a unique setup is proposed and developed for molecular measurements which possess the capabilities of in-situ imaging and characterisation of a metallic as well as a molecular junction. This technique also has provisions to be expanded in the future so that several properties can be measured simultaneously within one set-up. Secondly, the lack of reproducibility in atomic point contacts has been addressed here using the mechanism of EM. Despite the fact that a lot of effort was devoted to the process of EM to fabricate atomic point contacts, several unresolved issues remained in this field. These were mainly due to two reasons. First, as long as very strict controls on the starting size and local microstructure of the metallic structure are not performed, it is unlikely that after the process of thinning, the electrode geometries will be reproducible. This is one of the key issues that has been addressed in this thesis. Second, the relation of geometry, gradient, and temperature on the final process of EM was identified and the mechanism of atomic point contact formation using EM was identified. Finally, after addressing these two major issues, the functionality of the set-up and these atomic point contacts were tested with in-situ adsorption of CO molecules. The molecules exhibit a switching behaviour that can be tuned with voltages. Therefore, this dissertation helps in the development and understanding of two challenging aspects in the field of molecular electronics as well as tests the functionality of the developed system.

In this chapter, a brief motivation to the need for molecular electronics and its meaning has been discussed. With the discussion of techniques used to fabricate molecular junctions, various properties of molecular junctions and some molecular functionalities, the present state-of-the-art and the possible developments that can be made, were identified. This chapter ends with the description of the existing open questions followed by the objectives that were addressed in this dissertation. The remaining thesis is organised as follows.

Chapter 2: This focuses on the theoretical concepts and models needed to interpret the observations in this thesis. These include the classical Maxwell's formula, the semi-classical Sharvin's formula and the Landauer's formula following the scattering approach explaining

the conductance of single atomic point contact. Electrical measurements of an atomic point contact using conductance plateaus and histograms as well as, an understanding of the mechanism responsible for plateaus (in traces) and peaks (in histograms) is discussed. This chapter concludes with a brief explanation of the conductance of a molecular junction.

Chapter 3: This discusses the experimental materials and methods. All details of the sample preparation, software and hardware integration to the 4-tip scanning electron microscope (SEM)/STM chamber is described.

Chapter 4: Here, experiments with long Ag nano-wire structures and their simulations are detailed. This work has been published in *Journal of Physics Condensed Matter*. From this chapter, the crucial parameters playing an effective role in the process of EM could be identified and further experiments were performed based on these results.

Chapter 5: This focuses on the experiments with the bow-tie structures at low temperatures. Structure formation and importance of the granular layer will be pointed out. Fourier transform of the conductance histograms in the bulk regime suggested breaking along principal crystallographic directions. In these still mesoscopic (100-200 nm) structures, Fourier transform analysis could help identify the mechanism of EM.

Chapter 6: Based on the above finding FIB structuring was carried out to ensure one grain boundary at the narrowest constriction of these bow-tie structures. This pre-structuring before EM could help to achieve atomic point contacts with great reproducibility using EM. All details of FIB structuring and formation of atomic point contacts using EM and different EM pathways followed during the process are described in this chapter. Findings from this chapter are already published in *Applied Physics Letters*.

Chapter 7: Explains the modification of these point contacts by CO adsorption. Conductance of atomic point contacts could be modified by in-situ CO adsorption experiments. Ultra-fast current measurements were performed to observe the dynamics of the contact formation in presence of CO. Bi-stabilities were observed and millisecond re-arrangements of the molecule decorated Ag contacts are described in this chapter.

Chapter 8: This chapter summarises the various findings of the thesis and provides a broad future outlook from the present know-how.

Chapter 2

Theory of electromigration (EM) and atomic point contacts

Here in this chapter theoretical concepts of electromigration (EM) and metallic point contacts will be presented. In the beginning, an overview of the EM process in metals is discussed with the general concepts known over the years such as the mean time to failure, Black's law, Blech length and the micro-structural know-how in case of polycrystalline metals. After the general description, the main focus will be on the several attempts of EM in nano-meter sized contacts. This gives an insight into the various ways that it can be controlled and used for atomic point contact generation. This is followed by the theory behind the transport properties of metallic point contacts. The classical Maxwell's law will be explained first, followed by the semi-classical Sharvin's law which takes into account the quantisation of conductance. The Landauer's formula (using scattering approach) details the conductance of point contacts in ballistic contacts. The conductance of atomic point contacts obtained from various experiments is discussed next. Conductance quantisation, conductance histograms and the mechanism of contact formation are also described towards the end of this chapter. Finally this chapter ends with the discussion on the conductance of molecular junctions.

2.1 Physics of EM

EM is the transport of metal atoms in a biased condition because of momentum transfer from the collisions between conducting electrons and atoms constituting the metal. This transfer of momentum has been originally proposed independently within a semi-classical ballistic model by Fiks (1959) and by Huntington and Grone (1961) [155] and the quantum mechanical model by Bosvieux and Friedel (1962) [156]. There were many modifications and refinements on this topic which have been reviewed by Sorbello (1975) [157] and later in 1985 by Verbruggen [158].

Considering the electrons inside a metal, when no current is flowing through it, the electrons can be considered to be at rest. Although electrons inside the metal are always under a motion but the ‘averaged’ electron can be treated as an imaginary entity having the average momentum of all the electrons that are equally distributed in all directions. This imaginary entity can be considered at rest. Therefore, even though the electron is not at rest, the vector sum of momenta is zero. When current is passed through the metal, this averaged electron is accelerated by the electric field until it suffers a collision with a defect. On collision, the momentum gained from the field is transferred to the defect which is the so-called electron wind. This causes material migration. “Material migration” is a common term for various material transport processes in solids. These are (1) material migration due to temperature gradients, (2) chemical diffusion depending on concentration gradients, (3) material migration due to mechanical stress, and (4) material migration occurring due to an external electrical field. This material migration caused by an electrical field is known as EM [159]. The expression for the net mass flux is given below, as J

$$J = DC \left(\frac{z^* e \rho j}{kT} - \Omega \frac{\partial \sigma}{\partial x} \right) \quad (2.1.1)$$

where D is the thermally activated diffusion coefficient, C is the concentration of diffusing atoms, kT is the average thermal energy, z^* is the net effective charge, e is the electronic charge, ρ is the resistivity, Ω is the activation volume and σ is the hydrostatic component of the mechanical stress. The first term in the Equation 2.1.1 represents the force due to EM and the second term in this equation (2.1.1), represents the stress gradient generated due to a flux divergence. When the forces due to EM and stress gradient are equal, i.e. both the terms in the Equation 2.1.1 are equal to each other, net mass flux (J) becomes zero causing no failure from EM. This is known as the Blech condition which will be described in a separate subsection.

For polycrystalline materials, the grains are oriented in different directions. When current passes through such a material, there is an interaction between electrons and metal ions within the material. Atoms near the grain boundaries suffer from this electron wind as the electrons experience a force that directs them to move in the direction of electrons. Therefore, there are two kinds of forces on the individual metal ions inside the conductor. A direct force (F_{field}) which is the force on a positive metal ion in the presence of an electric field. The second one is known as the electron wind force (F_{wind}) resulting from the momentum transfer from the conduction electrons to the metal ions. Electron wind force direction is against the direction of conventional current flow (Figure 2.1).

The figure shows a conductor made of Ag material and the different forces acting on Ag ions constituting the conductor. The motion of an atom in one direction is accompanied by

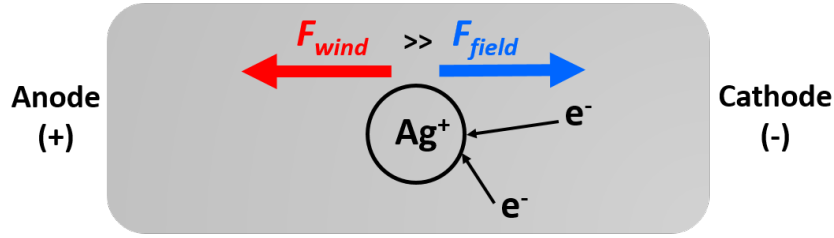


Figure 2.1: Schematic depicting two forces acting on the metal ions constituting the material. F_{wind} is towards the anode and F_{field} is towards the cathode [159].

the motion of a vacancy in the opposite direction. This is true irrespective of whether the diffusion mechanism is in the lattice, at the grain boundary or at some other interface. Thus, at the anode, one can expect the accumulation of material (hillocks) and similarly, depletion of material (voids) can be observed at the cathode. Grain boundaries are the weakest points within the whole lattice, and there is a lack of symmetry around the grain boundary within the lattice. Hence, when a metal is subjected to current for an extended period, the metal atoms gain sufficient energy to cross the grain boundaries, and migrate along the direction of electron flow, leading to accumulation of material (hillocks) at the anode and depletion of material (void) at the cathode. Such transfer of material due to EM led to short circuit and open circuit failures. Stress gradients that oppose the EM force generate both tensile and compressive stress. Tensile stress is generated at sites of positive flux divergence (void), whereas compressive stress is generated at a negative flux divergence (hillock). Failure due to EM was a major reliability issue for integrated circuits which demanded serious attention and various models were developed to understand and control them. Very briefly, some of the important concepts/models which could explain EM in the micro-meter sized interconnects will be first described before moving on to the discussion of EM in thin films and using this mechanism as a constructive tool to fabricate atomic junctions.

2.1.1 Blech Length

This is a condition derived from Equation 2.1.1, which provides an approximate limit on the conductor length that is susceptible to EM failures at a particular current density. A mechanical stress build-up creates an opposite migration process which reduces or even compensates the effective material flow towards the anode. When mass flux J (in Equation 2.1.1) is zero,

$$\frac{\partial \sigma}{\partial x} = \frac{z^* e \rho j}{kT\Omega} \quad (2.1.2)$$

this limiting condition is obtained. This condition expressed in Equation 2.1.2, is the Blech condition. It is named after Ilan Blech [160]. From this condition, Blech length can be calculated. Blech length is referred to as the minimum length (or lower length limit) of the conductor at which EM can take place. Conductors below this threshold length are not victims of EM. Blech length is calculated by integrating over the stress profile of Equation 2.1.2. Conductors with lengths greater than Blech length (l_{Blech}) are susceptible to EM failures. This is usually expressed in the form of Blech product given below,

$$\frac{(\sigma_{\max} - \sigma_0)\Omega}{z^*e\rho} = j l_{\text{Blech}} \quad (2.1.3)$$

When the product of the current density and the length of the conductor (Blech product) is lower than a particular threshold value which is defined or can be calculated from Equation 2.1.3, the conductor is free from EM failures [161]. This product is a constant value that depends only on material constants (Equation 2.1.3) and denotes that higher the current densities, shorter should be the conductor lengths in order to prevent EM.

2.1.2 Blacks'law and Mean Time to Failure (MTTF)

The failure of a particular part within an integrated circuit caused by EM can result in the failure of the entire circuit operation [159]. At the end of the 1960's, a physicist named J. R. Black developed an empirical model to estimate the mean time to failure (MTTF) of a wire, taking into consideration the process of EM [162]. The expression of MTTF proposed by the physicist is given in the Equation 2.1.4 below,

$$MTTF = \frac{A}{j^n} \exp\left(-\frac{E_a}{k_B T}\right) \quad (2.1.4)$$

where A is a constant based on the cross-sectional area of the conductor, j is the current density, E_a is the activation energy, k is the Boltzmann constant, T is the temperature and n is a scaling factor (usually set to 2 according to Black). Therefore, the current density and the temperature values are the factors influencing the design process of the conductor suffering from EM. From Equation 2.1.4, MTTF is inversely proportional to the square of current density ($n=2$). The factor was set to 2 as metallization schemes did not take into account the effect of a refractory layer. If the failure occurred due to the expansion of pre-existing voids or voids that are formed in a shorter time compared to the total failure time, the current exponent in the above equation was considered close to one. If $1 < n < 2$, the most probable reason for failure was due to the combination of nucleation and growth. If $n > 2$, failure was most likely due to Joule's heating induced temperature gradients. Another important aspect of this equation is that the current density term and the temperature term both are on the same side of the equation. Hence, the reliability of a conductor due to high temperatures must be accompanied by decreasing current densities. This is not easy to visualise.

2.1.3 Wire width

Since current density developed within the conductor is an important factor governing EM and current density depends on the current and the effective cross-sectional area, therefore the width of the conductor plays a major role in the process. The larger the width of the conductor, the lower is the current density produced. The lower the current densities, the higher is the resistance to EM. However, there is also a lower limit to this width below which it is again resistant to EM. If the width of the conductor/inter-connect line is below the grain size of the metal layer, it becomes completely immune to EM even if the current density increases. This type of arrangement is called a bamboo microstructure where the grains lie perpendicular to the current flow and therefore limit the damage by EM. Figure 2.2 shows the relation between the width of the metallic section and the bamboo structure [159].

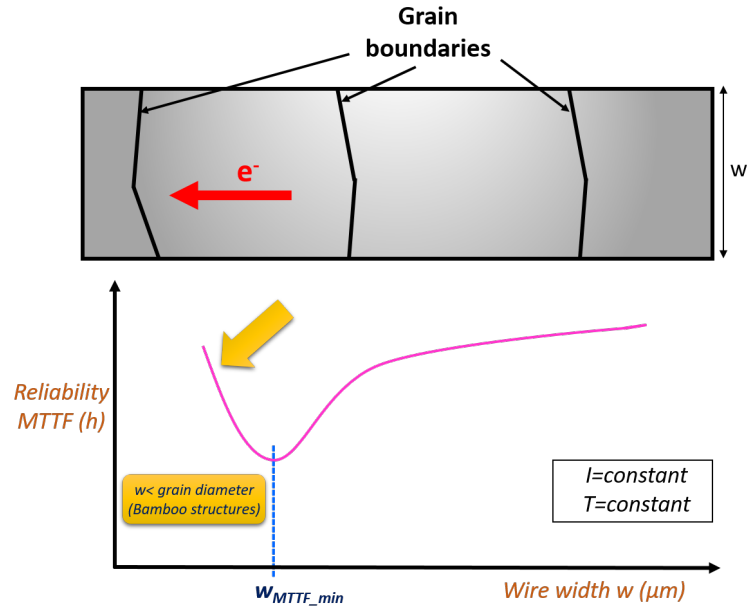


Figure 2.2: Schematic depicting the bamboo grain structure which is oriented at right angles to the direction of the electron flow and permits limited grain boundary diffusion [159].

2.1.4 Micro-structure

The micro-structure of a metallic conductor and the arrangement of the grains within the metallic structure affects the atomic transport by EM. Depending on the deposition technique and other related factors, the grain structure of the metallic layer can vary from one position to the other. The previous subsection shows the dependence of the structure width on the process of EM but the grain distribution also matters significantly. The existence of triple points can change the region of accumulation depending on the crystallographic orientation of the grains at the triple point. Figure 2.3 shows two images. Figure 2.3 (a) depicts a normal triple point location. The two different cases that may be present at the triple point is demonstrated in Figure 2.3 (b). It shows the region of depletion is due to a negative flux divergence and region of accumulation is because of a positive flux divergence. This also determines the exact microscopic location of voids and hillock formations within a metallic interconnect.

Similarly, transition from a coarser grain structure to a finer one and vice versa can also affect the mass accumulation and void formation. In Figure 2.4 the transition from the fine grain structure to the coarse grain structure can be clearly seen. This denotes a region of mass accumulation as there are more number of grain boundaries in a finer grain structure as compared to a coarser one. Figure 2.4 also shows the transition from a coarse grain structure to a finer structure. This leads to a mass depletion or a void prone location.

Concluding this section, it must be pointed out that, EM dependence on the local microstructure of the metal using the above-mentioned theories is valid for micro-meter thick lines. It was already introduced in the first chapter that, as long as the bulk behaviour of the

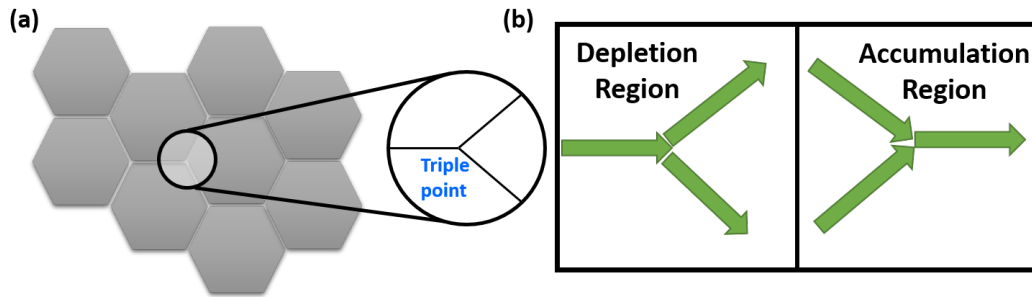


Figure 2.3: (a) Schematic of a triple point grain boundary. (b) Two possible directions of the grains at the triple point showing the region of depletion (void) and region of accumulation (hillock).

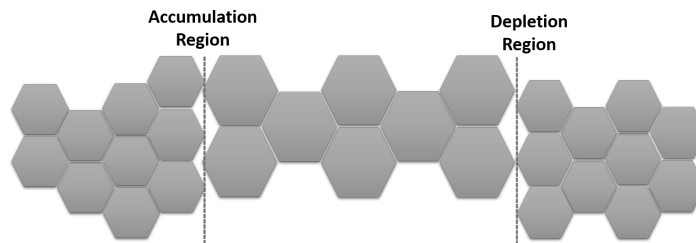


Figure 2.4: Schematic for grain structure distributions showing transitions between fine grain structure and coarse grain structures and vice versa. Positions of mass accumulation and mass depletion denotes the respective hillock and void prone areas. ¹

material is important, the interface effects do not really affect the overall performance. Now, the miniaturisation demands a transition of the micro-electronics to the nano-electronics, where the length as well as the width of the interconnects are below 100 nm. These consequences of the scaling down demand the understanding of EM induced transport of material in the nano-scale. This is the subject of the next section. This would provide the basis to understand the importance of EM at the nano-scale.

2.2 EM: a serious issue in thin films

Presently EM is of practical as well as of academic interest, as microelectronic devices employ thin films as circuit elements, which when subjected to high current densities can suffer EM damages. On the other hand, due to the increasing demands of miniaturisation, circuits are becoming smaller and denser. This automatically amounts to large heat generation and power dissipation values in these circuits. The current densities in micro-meter lines can be 2-3 orders of magnitude higher than the current densities in bulk metallic lines, but the underlying Si in microelectronic circuits provides excellent heat dissipation without excess damage due to Joule's heating. At these high orders of magnitude of current densities, EM

¹Source:https://www.doitpoms.ac.uk/tlplib/electromigration/flux_1.php

becomes very important.

The other aspect, which has increased the demands of EM studies, is the fabrication of nano-gap electrodes using this technique. There have been many attempts to use this technique to create sub nano-meter spacings between electrodes for molecular electronic applications [41–46]. Using the electron-wind and feedback mechanism to control the electron wind and thermal gradients, many theories have been proposed to understand the mechanism of EM within micro and nano-lines [163–167]. This requires the understanding of the interplay of EM forces and thermal migration (TM) forces at different temperatures. Not only these two forces but accompanying stress gradients and interface stresses generated due to these fields play a significant role.

These dynamic effects are difficult to predict using simulations but temperature gradients can at least be calculated in simulations. Temperature gradients within the sample or at the interface, the dynamic changes in temperature in the presence of current needs to be considered within the simulations in order to calculate reasonable estimates. This aspect is practically impossible to realise experimentally, since measuring the temperature inside the structures while current is flowing through them is not an easy task. Even if one uses a scanning tunneling microscope (STM) tip having a thermocouple material to measure the temperature on the sides of the structure [59], still the temperature at the centre where one expects the changes to occur, cannot be measured correctly as the field to tunnel an extra tip will affect the EM process. Therefore direct measurements are not possible in such a situation. Only estimations using theoretical simulations or extrapolations using some formulas have been performed [58, 60, 61]. There is still a lack of a proper model that can be used for different metals and at different substrate temperatures, for calculating the dynamic profile of the temperature within the nano-wire during EM. This ambiguity exists because till date no strict controls on the starting size and distribution of the grains at the narrowest constriction have been performed before the structures are subjected to EM experimentally. Interface effects are not considered in theoretical simulations as well as defects and imperfect electrode geometries are rarely incorporated in simulations. This gives rise to a huge difference between the simulated geometries and the real geometries as well as simulated temperature gradients and actual dynamic temperature changes within the sample. These are the main reasons why many un-resolved questions still exist.

EM causes material transfer, which changes the local geometry of the structure. The narrow constriction experiences a higher current density as compared to the remaining structure, which leads to local heating of the structures. Both temperature, as well as the geometry of the structure, contributes to the measured resistance of the structure. Therefore, it is very important that the feedback control which is used to perform EM has the capability of taking into consideration these complex counter-active phenomena. When strict controls on the microstructure of the sample before EM is performed and proper feedback is setup to control the process, reliable atomic contacts can be generated. In the next section, a brief description of how EM process has been used to generate atomic contacts so far will be briefly reviewed. Both theoretical and experimental attempts will be discussed in order to understand the present status and further developments required.

2.3 EM in nano-meter sized electrodes for generation of point contacts

Park et al. [41] in 1999 demonstrated the fabrication of nano-meter spaced Au electrodes by EM technique. These nano-meter spaced electrodes were tested for molecular applications by inserting CdSe nano-crystals between them. This study was one of the very first attempts towards application of EM technique for molecular electronic studies. In the same year analysis of failure mechanisms of Au nano-wires under applied current was reported by Durkan and his group [168]. The publication reported that the failure current densities depend on the length and width to a certain extent and the failure is an interplay of poly-granular and trans-granular EM as well as local heating and grain mobility. A few years later, Au electrodes were prepared with nano-meter spacing using a large dc bias employing the EM technique at room temperature (RT) [169]. This method was reported as a simple fabrication scheme to study the transport properties of nano-particles between metallic electrodes. In 2005, Strachan et al. [42] demonstrated a controlled way of EM in Au nano-structures in ambient conditions. It was reported that the formation of nano-gap takes place through three regimes: a bulk regime which then approaches a few-atoms regime and finally the tunnelling regime. A very different mechanism was proposed by Umeno and co-workers [170] regarding the mechanism involved during EM. Their claims suggested that the peak voltage obtained from the histogram of critical voltages coincided with the self-diffusion barrier of metal atoms, indicating EM in very small junctions is due to the self-diffusion of metal atoms driven by the microscopic kinetic energy transfer from a single conduction electron to a single metal atom. Hadeed et al. [171] used EM to create 1-2 nm nano-gaps by utilizing the interplay between EM and Joule's heating without using any feedback. Gardinowski from our group [172] showed switching nano-meter contacts on ultra-thin Ag structures. It was observed that the gaps could be opened at low temperature (LT) and could be closed by thermal annealing to RT. A new mechanism was proposed by Hoffmann et al. [173] which involved nano-contact formation by thermally assisted EM of Au nano-wires. This was obtained by maintaining constant power at the nano-contact. It can be noted that different groups propose different mechanisms within their structures claiming different ways of controlling EM to fabricate nano-meter gaps. As high current densities from EM leads to Joule's heating, temperature estimations became a serious issue during the these developments.

Esen et al. [60] investigated the temperature within the Au nano-wire during EM neglecting the heat conduction to the oxide surface and assuming contacts as heat sinks. Assuming all the power is generated at the centre of Au nano-wire, still, the temperature was estimated to be less than 290 K. The same group reported studies of different device geometries using a special design [44]. They concluded that roughly a constant temperature is maintained during EM and it is a temperature controlled process instead of a bias controlled one. There were several ambiguities existing in this field especially considering the temperature estimation within the nano-wires during EM. In this regard, Trouwborst et al. [58] estimated the temperature of the nano-wire to be almost independent of the substrate temperature. They claimed that EM occurs at a threshold temperature of 450 K - 460 K irrespective of the temperature of the sample (LT or RT). This suggests that thermal diffusion or gradient does not play a significant role. This estimation of temperature is higher than the temperature reported by Esen and group [60]. The ambiguity does not end here. Taychatanapat and

group [61] calculated the temperature to be much higher than the previous two studies. They estimated temperatures of 1625 K for Au nano-wires which is much larger than the melting point of Au. In 2014, a publication from Jeong et al. [59] characterised nano-meter scale temperature fields during the process of EM. This study reported a direct measurement of temperature using a thermocouple tip, 100 nm away from the cathode. With the combination of this challenging experiment and theoretical simulations using COMSOL, they could confirm that EM occurs at temperatures lower than the melting point of metal and voids accumulating at the cathode causes both local hot spots and asymmetric temperature distributions. All these attempts to calculate the temperature within the nano-wire during EM show a wide variation between each other. As it is very difficult to measure the temperature in-situ during EM, temperature control was indirectly implemented by preventing thermal runaway. This was performed by using feedback control on the EM process.

Open circuit EM can lead to thermal runaway and uncontrolled EM. With the incorporation of feedback, these problems were resolved to some extent. This concept of feedback controlled electro-migration (FCE) was introduced by Shih et al. [46]. This was one of the first attempts regarding the use of feedback. Dong et al. [48] used a new type of feedback parameter to control the process. They observed that the relative current noise increased more than two orders of magnitude as compared to the resistance. This large change in the current noise was the reason for them to use it as a feedback parameter. FCE was also reported by Campbell and Knobel [45]. Motto and group [43] also fabricated nano-gap structures with a very simple feedback mechanism that allowed to control the EM process. All attempts using a software-feedback could not be faster than a few milliseconds. At LT, metal migration is slower in comparison to RT. Hence, such software feedback might already be enough to control the process. For practical applications, controlling the process at RT needs a much faster feedback process. Wu and co-workers [49] reported that a four-terminal set-up is necessary that combines a fast hardware analog feedback along with a slow software digital feedback to maintain a constant voltage over the junction and control the formation of nano-gaps reliably. In 2015, Kanamuru and his colleagues reported an ultra-fast FCE process using a field programmable gate array (FPGA). This ultra-fast device with faster response times (μs) is another way to overcome the time consuming slow software feedback using Keithley which in the order of milliseconds.

To identify the most effective feedback parameter amongst all reported parameters, and methods to improve the feedback algorithm, some theoretical simulations were performed. Demarchi and group [167] performed an electro-thermal modelling of EM induced gap fabrication. They developed a model that was verified for different nano-wire geometries and it was used to control the feedback voltage. In 2012, another theoretical modelling to fabricate nano-gap was reported from the group of Demarchi [164]. They calculated numerical atomic flux and could relate them with experimental atomic fluxes so that the feedback algorithm could be improved.

EM structures possess the possibility to be expanded in the form of devices. Van der Zant and group fabricated three-terminal molecular devices using EM [40, 174]. Regarding the requirement of a large number of structures, for testing purposes of EM, parallel fabrication of nano-gaps [38, 39] was reported where FCE was used to fabricate a large number of nano-gap in one single step. These developments show that EM has the potential to be one of the powerful techniques for fabricating nano-gaps on a large scale if controlled properly.

Here, the important controls are summarised. It is not clear until today, which mechanism exactly governs EM at the nano-scale even though several studies were reported. In most of the studies, the material was Au. This is because of few reasons: (a) The starting width of the structures and grain distribution is not identical in all reported experiments (no uniformity) and (b) the exact temperature cannot be measured and controlled. From the existing literature, it is clear that FCE can control the process much better than open circuit EM. For RT measurements, software feedback to control EM having response times in milliseconds can be harmful to the structures as metal diffuses at a much faster rate at RT than the feedback control can respond. For LT measurements, ultra-fast feedback may not be necessary as the diffusion of metal atoms happens at a reduced rate as compared to RT. This suggests that an efficient feedback control (depending on the temperature of the sample) can balance the temperature by preventing thermal runaway and can control EM to fabricate atomic contacts. Nevertheless, strict control on the local grain structure of the sample prior to EM is equally important.

2.4 Transport properties through metallic point contacts

Conductance of a macroscopic conductor can be explained using Ohm's law. Ohm's law relates the conductance with the geometrical parameters of the conductor. The conductance G is inversely proportional to the length L of the conductor and directly proportional to the cross sectional area A . It can be expressed as follows

$$G = \frac{\sigma A}{L} \quad (2.4.1)$$

where σ is the conductivity of the metallic conductor.

Even though Ohm's law describes the value of conductance at the macroscopic scale, the origin of this conductance lies at the atomic scale (motion of electrons). At the end, the conductance description means how do the electrons travel within the conductor [175]. Assuming a metallic conductor at absolute zero, a perfect ordering of the lattice atoms is expected. In reality, this is not true. Imperfections, grain boundaries as well as impurities are always present within a metal lattice that scatter the electrons flowing through the conductor [175, 176]. This means that the electrons can travel fixed distances before they are scattered at any of these irregularities.

There are two scattering mechanisms: Inelastic scattering and elastic scattering. Inelastic scattering is defined as a mechanism in which energy transfer takes place during the scattering event. Examples of inelastic scattering include electron scattering with other electrons or electron scattering with phonons (lattice vibrations). Elastic scattering involves no energy transfer during the scattering process. Electron scattering with the metal ions within the lattice is an example of elastic scattering. Metal ions being heavy, no energy transfer takes place and the phase of the electron is also preserved. Nevertheless, the scattering mechanism depends on the mean free path of the electron in that system. The elastic mean free path l is the average distance traversed by an electron between two elastic scattering events.

In mesoscopic physics different transport regimes can be identified according to the length of the conductor. When the length L of the conductor is greater than the elastic mean free path l , then the electron undergoes elastic and inelastic scattering as it travels through the

sample. This is known as the diffusive transport regime and it is mainly seen in macroscopic systems. On the other hand if L is smaller than l , the transport regime changes from diffusive to ballistic. In ballistic regime, electron momentum is constant and is only limited by the scattering at the boundaries of the sample. Figure 2.5 shows the two transport regimes [71, 176].

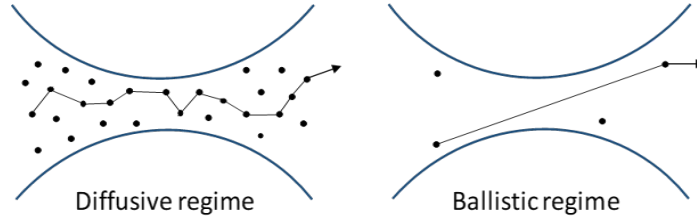


Figure 2.5: Schematic showing the two different transport regimes (a) Diffusive transport regime (b) Ballistic transport regime.

When the dimensions of the conductor is smaller than the mean free path l , the Ohm's law is no longer valid. Sharvin calculated the conductance of a conductor that has a dimension smaller than the mean free path l but much larger than the De-Broglie wavelength of the electron λ_F . Such a regime is not completely classical because it is below l and not completely quantised because it is larger than Fermi wavelength of the electron λ_F . This is a semi-ballistic transport regime [175]. For atomic-sized conductors, the width of the conductor (W) is comparable to the Fermi wavelength of the electron λ_F . In a fully ballistic channel, width W and height H of the channel both are of the same order as Fermi wavelength, λ_F . Therefore, such a conductor is completely in the quantum ballistic regime [175]. This was calculated by Landauer.

In this section, the classical Maxwell's theory [177] of diffusive transport and semi-classical Sharvin's formula [178] will be first introduced. Following this, the scattering approach for electron transport in quantum coherent structures (Landauer's formula) [179] will be described. At these small length scales, the wave nature of the electrons becomes influential.

2.4.1 Classical Maxwell's theory

As already explained above and as everyone is familiar with the very basic Ohm's law, when current I is passed through a metallic conductor with conductivity σ , a voltage drop occurs across the conductor, due to the resistance offered by the conductor in the path of the current flow [71]. In the micro-scopic explanation of Ohm's law, current density j and local electric field E is related as given below. At each point of the material, j is proportional to E . The microscopic form of Ohm's law is then written as follows, [177]

$$j(r) = \sigma E(r) \quad (2.4.2)$$

The electric field E satisfies the Poisson's equation and the boundary conditions specify that the current density component normal to the surface of the conductor must be zero. Maxwell tried to calculate the conductance of a point contact, where the contact was modeled as a

constriction with hyperbolic geometry. In a hyperbolic geometry, an analytical solution can be obtained using oblate spheroidal co-ordinates (η, ν, ϕ) as x , y and z given below,

$$\begin{aligned}x &= a \cosh \xi \cos \eta \cos \psi \\y &= a \cosh \xi \cos \eta \sin \psi \\z &= a \sinh \xi \sin \eta\end{aligned}$$

where $2a$ is the distance between the foci, and $(0 \leq \xi \leq \infty)$, $(-\pi/2 \leq \eta \leq \pi/2)$, $(\pi \leq \psi \leq \pi)$ considering η is a constant surface (See Figure 2.6).

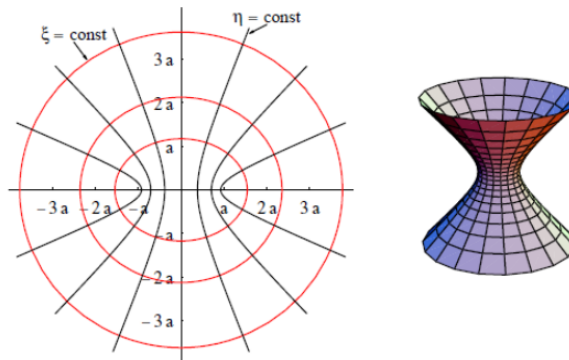


Figure 2.6: Oblate spheroidal co-ordinates. Reproduced from [71].

The constriction can be then defined by $\eta = \eta_0 = \text{constant}$. Therefore the radius of the narrowest part in the constriction is given by $r_0 = a \cos \eta_0$. Considering charge neutrality within the metal, Poisson's equation can be reduced to the Laplace form,

$$\nabla^2 V(r) = 0 \quad (2.4.3)$$

where $V(r)$ is the electrostatic potential. Anticipating solution depends on ξ only, equipotential surfaces are ellipsoids, and satisfying the boundary conditions, solution is given by

$$V(\xi) = -\frac{V_0}{2} + \frac{2V_0}{\pi} \arctan(e^\xi) \quad (2.4.4)$$

V_0 is the voltage drop at the constriction.

Then calculating the total current using Ohm's law, integrating over the total constriction, and finally dividing by V_0 , the total conductance of the constriction can be expressed as G_M which is the known as the Maxwell's conductance. (See [71, 177])

$$G_M = 2a\sigma(1 - \sin \eta_0) = 2r_0\sigma \frac{1 - \sin \eta_0}{\cos \eta_0} \quad (2.4.5)$$

In the limiting case of $\eta_0 = 0$, the contact conductance simply reduces to an orifice of radius a or of a non-conducting plate separating two metallic half spaces where the conductance reduces to

$$G_M = 2a\sigma = 2a/\rho \quad (2.4.6)$$

where resistivity of the material is ρ .

This relationship in Equation 2.4.6, is valid only when the radius a is larger than the electron mean free path l . When a is comparable to l , then the approximations by Sharvin [178] needs to be taken into account. The conductance proposed by Maxwell is related to material resistivity ρ , which in turn depends on l . Whereas, Sharvin's conductance G_S is independent of mean free path l [180] (details in the next sub-section). The transition from Maxwell's conductance G_M to Sharvin's conductance G_S was studied by Wexler [181] using a Boltzmann approximation. From transmission electron microscope (TEM) investigations [180], the experimental conductance could be reasonably fitted using a mean free path length of 3.8 nm and the Wexler's interpolation formula in Au point contacts [181].

2.4.2 Semi-classical Sharvin's approximation for ballistic contacts

When the dimensions of the contact are much smaller than the mean free path l , but larger than the Fermi wavelength of the electron λ_F , in such semi-classical constrictions, Ohm's law could no longer be used [175]. Sharvin [178] first proposed the conduction through this type of contacts [71]. Sharvin considered the two electrodes as electron reservoirs separated by an orifice. The model used by Sharvin is depicted in Figure 2.7.

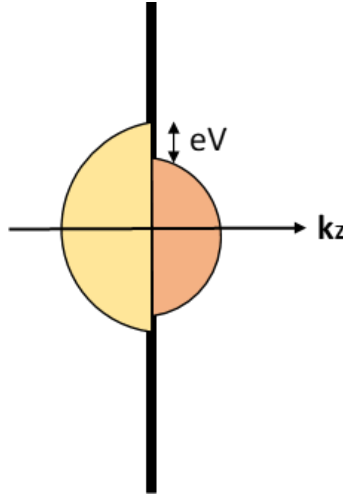


Figure 2.7: Model to calculate the Sharvin's conductance. A circular orifice separates the two electron reservoirs. The energy difference between two electron reservoirs is eV .

There is a large potential gradient near the contact, which accelerates the electrons within a short distance. This semi-classical expression of the current density is written as

$$j(r) = \frac{2e}{L^3} \sum_k v_k f_k(r), \quad (2.4.7)$$

where $f_k(r)$ is the semi-classical distribution function and denotes the occupation of state k at position r and v_k is the electron group velocity. In the absence of collision events,

on application of voltage V , the right moving states occupy an energy eV higher than the left moving states, resulting to a total current density, $j = e\langle v_Z \rangle \rho(\epsilon_F) eV/2$ where $\rho(\epsilon_F) = mk_F/\pi^2\hbar^2$ is the density of states at the Fermi level and $\langle v_Z \rangle = \hbar k_f/2m$ is the average velocity in the positive z-direction. The total current is obtained by integrating over the contact and the conductance is called as Sharvin's conductance [178]. This is given by,

$$G_S = \frac{2e^2}{h} \left(\frac{k_F a}{2} \right)^2 \quad (2.4.8)$$

where h is Planck's constant, k_F is the Fermi wave vector, and a is the contact radius. Sharvin's conductance does not depend on the material properties or geometrical parameters like conductivity σ or length L but only depends on electron density. To incorporate quantum mechanics, wave nature of the electrons enters by considering Fermi distribution function.

The voltage drop is concentrated on a length scale of the order of a near the contact. The power $P = IV$ is completely converted into the kinetic energy of the electrons that enter ballistically into the second electrode [71]. Here, energy relaxation of the electrons is not taken into account as this model is semi-classical and not completely a quantum model. Here, it is considered that energy dissipation takes place far away into the contacts by scattering with phonons. In reality, there is a slight inelastic scattering taking place near the contact as well [71].

2.4.3 Scattering approach : Landauer's formula

When transport experiments are performed on meso-scale devices, (atomic-sized constriction) the meso-scopic conductor is connected to macroscopic electrodes that allows passing currents through them. In experiments, these contacts serve as the connection or a bridge between the measurement device (tips,cables) and the real nano-meter sized metallic structures. These electrodes are in thermal equilibrium (temperature of the sample) and have a definite chemical potential. They act as electron reservoirs or heat sinks [71].

The scattering approach relates the transport properties (conductances) with the transmission and reflection probabilities for the charge carriers incident on the sample. In this type of approach, there exists two assumptions. First, the phase-coherence is assumed to be preserved on the entire sample and second, the inelastic scattering is restricted to the electron reservoirs only. In spite of these assumptions, this approach has been very successful in explaining many experimental results on meso-scopic devices.

The conductor can be modelled as a scatterer connected to the electron reservoirs by perfect leads (Figure 2.8). Within these leads, the electrons propagate as plane waves along the longitudinal direction, while due to the lateral confinement, the transverse momentum of the electrons is quantized. Similar to the normal wave-guide problem, the quantized momentum in the transverse direction defines a set of incoming and outgoing modes on each lead. (N_α is the number of modes on lead α). In reality, perfect leads do not exist. This is an assumption within the scattering approach to simplify the formalism. Even though perfect leads are assumed, using perfect leads does not affect the results as long as sufficiently large number of modes is considered.

Another construction simplifying the scattering approach is that there exists a "perfect" coupling between the leads and the electron reservoirs. Assuming the perfect coupling be-

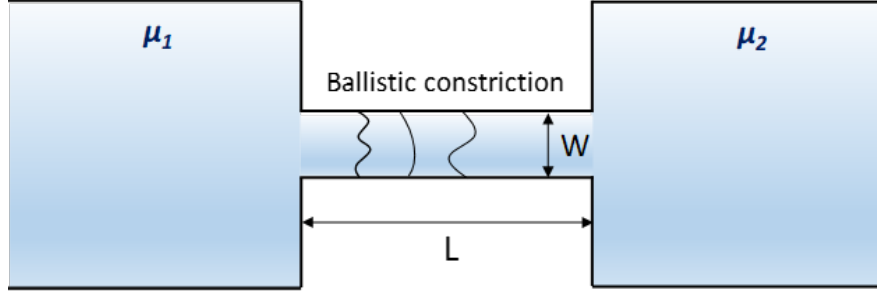


Figure 2.8: Schematic of a ballistic channel of length L , width W and height H . The channel is connected to electron reservoirs on both sides with electrode potentials μ_1 and μ_2 . The confinement of electrons are in y and z directions.

tween electrodes and leads, the distribution of the incoming modes becomes fixed, which is determined by the Fermi distribution on the corresponding electrode. Similarly, all the outgoing modes on the leads are transmitted into the receiving electrode. Therefore the boundary conditions on the incoming and outgoing modes become very simple. The last assumption to make the formulation simple is that the sample is just a perfect one-dimensional conductor, having a single mode occupied.

Now, the expression for current and conductance using the scattering approach is calculated here [179]. As the dimensions of the conductor are close to the Fermi wavelength λ_F , all the electron wavelengths are not allowed [175]. Assuming voltage V is applied across the two electrodes, the population of the mode moving from left to right can be described by Fermi distribution function f_L on the left electrode and the population of the mode moving from right to left can be described by Fermi distribution function f_R on the right electrode. The current is written as,

$$I = \frac{e}{L} \sum_{k\sigma} v_k (f_L(\epsilon_k) - f_R(\epsilon_k)) \quad (2.4.9)$$

$$I = \frac{e}{\pi} \int dk v_k (f_L(\epsilon_k) - f_R(\epsilon_k)), \quad (2.4.10)$$

where L is the length of the conductor and σ is the electron spin. As this is a one-dimensional system, the density of states is $\rho(\epsilon) = 1/v_k \hbar$ and the current can be written as [71]

$$I = \frac{2e}{h} \int (f_L(\epsilon) - f_R(\epsilon)) d\epsilon \quad (2.4.11)$$

The factor 2 in the above equation is due to spin-degeneracy. At absolute zero, $f_L(\epsilon)$ and $f_R(\epsilon)$ are step functions. They are equal to 1 below $\epsilon_F + eV/2$ and $\epsilon_F - eV/2$ energies. Their values are 0 above this energies. Thus the expression leads to $I = GV$, where $G = 2e^2/h$. This shows that a perfect single mode conductor between two electrodes has a finite resistance which is $12.9\text{k}\Omega$ ($h/2e^2$) which is totally different from macroscopic leads where a perfect conductor has almost zero resistance. This finite resistance is due to the resistance at the interface of the leads and the electrodes.

Now discussing the same scattering problem in a two-terminal configuration, the amplitudes of the incoming and the outgoing waves are related by an energy dependent scattering matrix. This matrix is given by,

$$\hat{S} = \begin{bmatrix} \hat{s}_{11} & \hat{s}_{12} \\ \hat{s}_{21} & \hat{s}_{22} \end{bmatrix}$$

where $\hat{s}_{\alpha\beta}$ is a $N_\alpha \times N_\beta$ matrix whose components $(\hat{s}_{\alpha\beta})_{mn}$ are the ratio between the outgoing amplitude of mode n and lead α and incoming amplitude of mode m and lead β .

$$\hat{S} = \begin{bmatrix} \hat{r} & \hat{t}' \\ \hat{t} & \hat{r}' \end{bmatrix}$$

where r denotes reflection and t denotes transmission. In a single mode case, the current is given by the difference between the incoming and outgoing states. Using the elements in the scattering matrix the current expression can be written as follows, [71]

$$I_{m\alpha} = \frac{2e}{h} \int_{-\infty}^{\infty} d\epsilon \left[\left(1 - \sum_n |\hat{r}_{mn}|^2 \right) f_\alpha - \sum_{\beta \neq \alpha} \sum_n |\hat{t}_{mn}|^2 f_\beta \right] \quad (2.4.12)$$

Performing the above summation of all the modes, total current of lead 1 is given as

$$I_1 = \frac{2e}{h} \int_{-\infty}^{\infty} d\epsilon \left[\left(N_1 - R_{11} \right) f_1 - T_{12} f_2 \right] \quad (2.4.13)$$

where $R_{11} = Tr(\hat{r}\dagger\hat{r})$ and $T_{12} = Tr(\hat{t}\dagger\hat{t})$ and taking N_1 as $N_1 = T_{12} + R_{11}$, the current expression reduces to

$$I_1 = \frac{2e}{h} \int_{-\infty}^{\infty} d\epsilon T_{12} (f_1 - f_2). \quad (2.4.14)$$

From this above equation, the linear conductance is given by,[71]

$$G = \frac{2e^2}{h} \int_{-\infty}^{\infty} d\epsilon \left(-\frac{\delta f}{\delta \epsilon} \right) T_{12}, \quad (2.4.15)$$

which at $T = 0$ reduces to the very well known Landauer's formula [179] given by

$$G = \frac{2e^2}{h} T_{12}, \quad (2.4.16)$$

where $G_0 = 2e^2/h = 77.5\mu S$ and for $T_{12} = 1$ that is conductance of a single channel, G reduces to this value which is known as quantum of conductance.

2.5 Conductance of atomic sized metal contacts

Already described in the above section, the linear conductance of atomic sized conductors G can be described in terms of the Landauer's expression [71, 179]

$$G = \frac{2e^2}{h} \sum_n \tau_n, \quad (2.5.1)$$

where τ_n describes the transmission probability of the conduction channels of the metal. In metal nanowires, the number of atoms in the contact is directly proportional to the width of the contact [175].

Since the sub-band splitting in the case of metals is approximately 1 eV, considering the diameter of one Au atom as 2.5 Å, and Fermi wavelength is of the order of the atomic diameter, indicates the presence of a very small number of modes [71, 175]. When an experimental condition of τ equals to 1 up to N number of modes can be achieved, then the conductance value can be expressed as integer times the quantum of conductance, G_0 . The actual number of transmission modes depends on the valency of the metal [176]. It has been observed for noble metals like Cu, Ag, and Au, s -orbital is responsible for conduction of current [175, 182], hence transmission is 1 for these metals.

Fermi wavelength in metals (λ_F) is approximately 5 Å. To resolve the splitting of 1 meV between the quantum modes, cooling to l He temperatures is required in 2 dimensional electron gas (2DEG) experiments. On the other hand, the mode splitting in metals ($2\pi^2\hbar^2/m\lambda_F^2$) is 1 eV, which is 3 orders of magnitude higher and can easily be observed in RT. The relevant number of conduction channels in a single atom contact can be approximated as $N = (k_F a/2)^2$. For Cu, this value equals to 0.83 (very close to 1) suggesting single atom contacts have a single conductance channel [71].

The local atomic configuration is responsible for the absolute conductance value which can often deviate from exact multiples of conductance quantum. These give rise to non-integer conductance values in experiments where quantisation of quantum modes is observed. Transmission probabilities of the quantum modes are critically influenced by the wave function match between electrons within the contact and the wave function within the leads. The atomic picture of the contact and the composition of the electronic quantum modes are inter-related.

2.5.1 Conductance quantisation

To investigate this conductance quantization mentioned theoretically in the above sections, experiments of breaking a metallic contact using break junction techniques became very prominent since the last 3 decades. The electron transport measurements attracted a huge amount of funding and interest with the hope towards atomic scale electronics. A break junction experiment necessarily requires a specially designed metallic contact structure with a well defined constriction at the centre and broader leads towards the end which is then pulled apart on both the sides. There are different ways of realising it (mechanically, electrically, etc.) as already introduced in the first chapter. While the structure is pulled apart, the metal atoms are slowly retracted from each other at the centre and various structural rearrangements take place until only a few atoms are bridging the centre. Just before the breaking, the conductance of monovalent metals is always close to $G_0 = 2e^2/h = 77.5\mu S((12.9k\Omega)^{-1})$. This property has been observed for monovalent metals (Cu, Ag, Au and alkali metals Li, Na and K). For sp and sd -metals the plateaus are normally less regularly spaced, and the last plateau before tunnelling mostly is a factor of two or more away from G_0 .

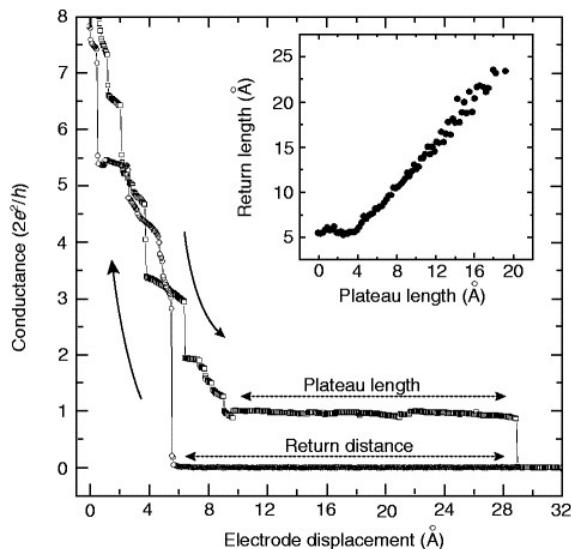


Figure 2.9: Reproduced from [183]. Conductance plateaus of a Au break junction in a MCBJ set-up at 4.2 K. In this case pulling of Au electrodes led to formation of single atom thick Au chains minimum 4 atoms long and with a maximum of upto 8 atoms long, confirming it acts as a 1D quantised wire.

As a very good example of stepwise conductance plateaus, Figure 2.9 is shown here [183]. This plot shows two traces where the opening and closing of Au contact are shown. The conductance plateaus decrease stepwise with a very well defined and stable $1 G_0$ plateau. They also report that these stable plateaus obtained are results of a particular atomic configuration developed during the process. It has also been observed experimentally that each curve does not repeat in exact detail because it depends on the exact atomic positions at that time. This is expected since the structural arrangement of the atoms cannot be controlled and during each experiment, the contact evolves through a different sequence of structures [71, 184]. Even though different traces vary from each other (Figure 2.9), the trend remains the same.

The theoretical formula by Landauer [179] predicts that the number of channels into which the electrons scatter should be well-defined integers, but this may always not be the case as non-integer values are very common and can occur due to back-scattering on defects and irregular structural arrangements, etc. Non-integer values not only occur in the case of MCBJ and EM techniques where it is not possible to control the local geometry of atoms, but have been observed in the case of electrochemical fabrication methods [185, 186] also. Li et al. [186] found that the non-integer conductance values are not stable for very long times as compared to integer multiples. This may be related to the stabilisation of the contact by filling of quantum modes or due to the formation of multiple single atom Au wires pointed out by Ohnishi et al. [70] using high resolution transmission electron microscope (HRTEM) studies. Ohnishi and co-workers directly measure the relationship between electron transport and structures of single Au atomic chain(s) and confirmed that the conductance of a single atomic chain is $2e^2/h$ [70].

As already clear from Figure 2.9, Au forms stable metallic chains with a value of a single

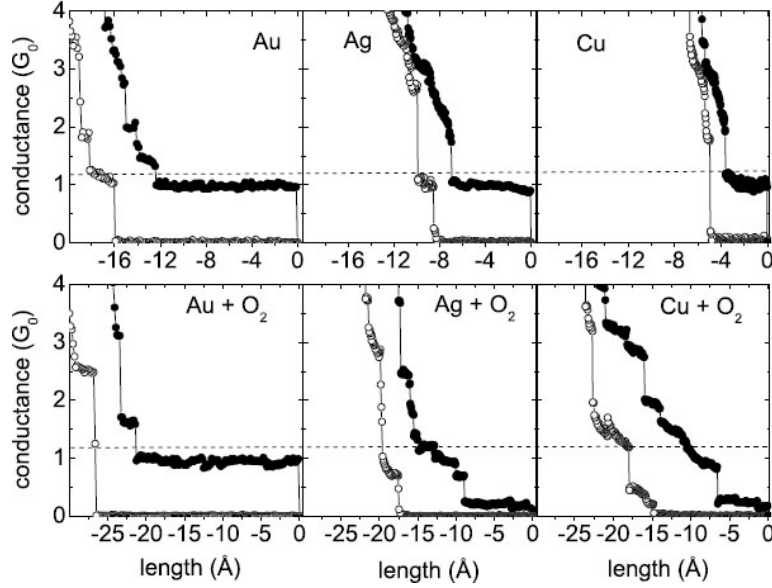


Figure 2.10: Reproduced from [187]. Conductance plateaus of Au, Ag and Cu before and after introduction of oxygen. Closed black dots are while opening the junction and open white circles are closing curves.

conductance quantum. This behaviour has not been observed in Ag and Cu which are isoelectronic noble metals. This suggests that the properties of Au that are absent in other noble metals are responsible for this effect. In Au, surface studies show, the (110) surface shows a missing-row reconstruction where every second row of atoms is absent and (100) surface possesses a quasi-hexagonal reconstruction. These surface reconstructions are absent in $4d$ elements like Pd, Rh, and Ag but they are present in $5d$ elements like Au, Ir, Pt. Very similar chain formation was also found with Ir and Pt in MCBJ experiments [188]. For Pt, the last conductance plateau was above $1 G_0$ and was found to be less smooth than Au. Smit et al. [188] found no chain formation for Pd, Rh, and Ag suggesting that the above-mentioned reason is a related phenomenon. This result shows a difference in properties between $4d$ and $5d$ elements revealing the balance between s and d electrons as an important parameter for bonding in atomic chains.

The last interesting feature that is observed in conductance plateaus are the sub- G_0 plateaus. As mentioned in the previous paragraph, the reason of atomic chain formation is attributed to the difference in the balance between s and d orbitals. It is therefore expected that chemisorption of specific adsorbates, which can modify this balance in the $4d$ metals could induce chain formation in such metals. Similar experiments were performed where Au, Ag and Cu was subjected to oxygen adsorption and a change in the conductance plateaus was observed [187]. There was not much difference in the conductance plateau of Au when oxygen was incorporated but a significant difference in the conductance plateau of Ag and Cu was observed (Figure 2.10). When oxygen was introduced, the $1 G_0$ plateau in Ag and Cu were not pronounced but abruptly dropped to sub- G_0 values ($0.1 G_0$ for Ag and $0.2 G_0$ for Cu). Another study of Ag point contacts [189] confirmed by cross-correlation technique

that two additional features at $0.4 G_0$ and $1.3 G_0$ could be assigned to oxygen atom between the Ag-Ag atomic point contact in series and Ag-Ag single atomic contact with oxygen in parallel respectively.

2.5.2 Mechanism of atomic contact formation

Quantization of conductance as interpreted by experimentalists was shortly introduced above. To understand the experimental data and the exact mechanisms involved, either the experimental findings need to be complemented with similar theoretical simulations or direct real-time imaging experiments are necessary. This subsection is briefly devoted to the understanding of the atomic contact formation mechanism by different direct and indirect methods. One of the most direct ways to visualise such atomic contact formation is the HRTEM method [190–199]. In this method, thinning takes place exclusively by atomic diffusion [200] between two nearby holes drilled in a thin metallic film and not by external mechanical or current forces. This is the main difference between this method (only direct method) and the other methods (indirect).

Simulation studies (indirect method), take into account the mechanism of elongation to break the contact [200] instead of diffusion. Molecular dynamics (MD) and density functional theories (DFT) are the most frequently used techniques. Molecular dynamics simulations do not take atomic diffusion processes into consideration. Even then, the results obtained using this method at LT matches well with experiments, as atomic diffusion is almost absent in LT. Not only the stretching (mechanism) is an important parameter, but the direction in which the stretching is considered in simulations is also important. This directional dependence can only be directly observed in a TEM experiment. From the TEM experiment of Ag nano-wires (Figure 2.11), this difference of thinning in the different crystallographic directions, can be observed [192].

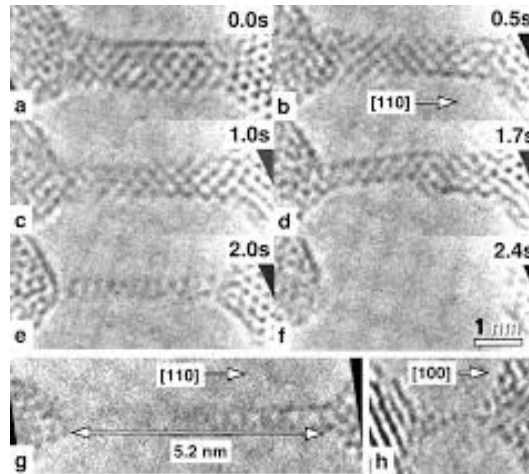


Figure 2.11: Reproduced from [192]. (a-f)HRTEM images of Ag nano-wires in (110) direction over time (g)Rod like (110) Ag structure (h) Linear atomic chain when one apex is along (100).

Rodrigues et al. [192] used a 5 nm thick polycrystalline Ag film (grain size 50-100 nm). In-

situ HRTEM images of atomically thin Ag films (Figure 2.11) [192] depict rod-like nano-wire structures in (110) direction whereas Ag(111) nano-wires tend to break abruptly preventing the formation of atomic chains. Rod-like Ag (110) nano-wires were the most frequent observed morphology. Ag nano-wires only favoured suspended Ag atomic chains, when at least one of the apexes was oriented along (100) direction. Before these Ag experiments were reported, similar experiments in 5 nm thick polycrystalline Au film (grain size 50-100 nm) were carried out by the same group [191]. They reported HRTEM investigations of Au nano-wires where they observed the evolution of Au nano-wire with sliding apexes. Au nano-wires were generated in 3 principal directions and also between grains with different orientations. Au(100) grains mostly formed atomic chains, whereas rod-like nano-wires were prominent for (110) grains. The behaviour of both metals appeared to be similar. From these investigations, the difference in behaviour related to the thinning in various crystallographic directions becomes clear.

From several calculations, it has been seen that the values of bond breaking forces are different from one metal to the other and their respective crystallographic orientations when atomic contacts are formed. This is because the most preferred orientation has the highest bond-breaking values [200]. To identify suitable metals for point contacts, several estimation parameters were followed. All the parameters were a measure of the strength of bonding in one-dimensional (1D) structure in comparison to a crystal structure. Higher the ratio between the two, most suitable it is for atomic point contacts.

TEM method takes 1 minute as a rule for the formation of atomic contact, which for molecular dynamics simulation is almost impossible to simulate (maximum 20 fs) [200]. It was shown in experiments, that nano-contact formed using self-diffusion took 15 s whereas by elongation it could be as small as 0.01 s [200]. Moreover, conductance values differ depending on the mode of formation also observed in experiments [201]. All these differences suggest that the mechanism of atomic contact formation depends on the thinning process. With these issues in mind, the kinetic Monte Carlo method was created, which takes into account both atomic diffusion as well as elongation into calculations. Comparing the molecular dynamics calculations with those of Monte Carlo simulations showed, the latter method takes into account the internal atoms whereas the molecular dynamics only involves surface atoms [200].

The conductance of these atomic contacts depends very much on the number of atoms present in the contact area and their respective positions. There have been theoretical studies of conductance histograms (details in the next subsection) showing the effect of the number of atoms on conductance. Now, concentrating on the transition from the bulk regime of the metallic conductor to the few atoms regime, several theories have been proposed. Contacts having a larger initial cross-section, gradually undergo a series of changes, i.e removal of geometric shells followed by removal of electronic shells finally approaching the few atoms regime. This has been discussed thoroughly in MCBJ measurements for alkali metal [202] and noble metals [203]. Similarly, the opposite effect is observed in the case of electrochemical techniques where the shells are constructed one by one [204]. Obermair et al. [204] studied Ag shell filling effects by the electrochemical method relating the conductance with crystallographic facet growth of the Ag crystal. Yanson and group [205] suggested a model based on the semi-classical Sharvin's formula, that could explain the square root of conductance is proportional to the radius of the contact. Obermair et al. [204] found excellent agreement of

shell filling effects correlating Sharvin's formula and experimental conductance values.

2.5.3 Conductance histograms

Conductance quantisation is observed as well-defined conductance plateaus within the conductance traces. However, the conductance values at which plateaus are obtained, slightly vary between different measurements of the same technique and may have different quantisation values with different techniques. This is because the exact conductance value depends on the exact electrode configuration. Fluctuations due to external parameters such as purity of the material, environmental effects (ambient or ultra-high vacuum (UHV)), temperature, impurity or contamination, backscattering of electrons and parallel tunnelling paths can lead to deviations [71]. By constructing conductance histograms, these fluctuations can be averaged out and the most preferred conductance values appear as dominant peaks. From experiments it has been seen that for noble metals like Au, histogram peaks are obtained at $1 G_0$, $2 G_0$, $3 G_0$, etc. whereas for alkali metals Na, K, etc. the series continues like 1-3-5- G_0 . For transition metals like Nb, Pt, Rh, etc. a broad feature is seen well above $1 G_0$, i.e between 1.5-2.5 G_0 . For *sp*-metals like Al, the first peak lies just below $1 G_0$, approximately around $0.8 G_0$ [71].

The peak structure obtained in the experimental conductance histograms provides valuable information on the most preferred conductance values. As discussed in the previous subsection, the mechanism of thinning determines the final atomic configuration and consequently the conductance values as well. Despite enormous attempts to understand the transport properties of metallic nano-structures, the origin of these peaks in the histograms is still an open question [206]. There is variance in peak values from experiment to experiment and between research groups, which shows the underlying origin of histogram peaks is not very simple and straightforward. To explore the important factors determining the histogram peak structure and how these factors alter the peak structures in conductance histograms, theoretical simulations of conductance histograms were performed. Hasmy et al. [207] simulated atomic configuration histograms on Al nano-contacts to study the effect of temperature and various crystallographic orientations of the metal on the simulated histograms. Peak structures of conductance histograms were found to be prominent and sharp at LT as compared to increased temperatures. This already suggests that temperature is one of the factors determining the peak resolution in the conductance histograms. Secondly, the calculated minimum cross-section histograms in the various crystallographic directions revealed different peak structures proving that conductance histograms are sensitive to the crystallographic orientations as well. Another similar study on Au contacts using molecular dynamics and tight binding model calculations [208] provides some crucial information on the dynamics of atomic point contact formation and another important factor related to the interpretation of conductance histograms. Correlating the minimum cross-section histograms with conductance histograms (constructed theoretically), it was observed that contacts with different radii could have similar conductance values. Additionally, the peak at $1 G_0$ does not necessarily signify a contribution from one atom at the minimum cross-section. Similarly, Pauly et al. [206] tried to study the origin of experimentally observed conductance histograms for different types of metals (*s*-type, transition metal, ferromagnetic and a *sp*-type metal). They found that not only the different atomic orbitals contribute to the electronic transport

channels but also the mechanical properties give rise to certain favourable structures which are then finally reflected in the conductance histograms.

2.5.4 Local density of states in atomic contacts

It is difficult to get an idea about the local density of states in atomic contacts from the already available experimental methods. As much information cannot be obtained from experiments, simulation studies are used. To find the relationship between the contact structure and its electronic properties, Stepanyuk et al. [209] calculated the local density of states (LDOS) for atoms of a Cu contact for contracted, stretched and intermediate states. It was observed that the LDOS for p -electrons remained almost unaltered whereas the LDOS of s and d electrons showed significant changes.

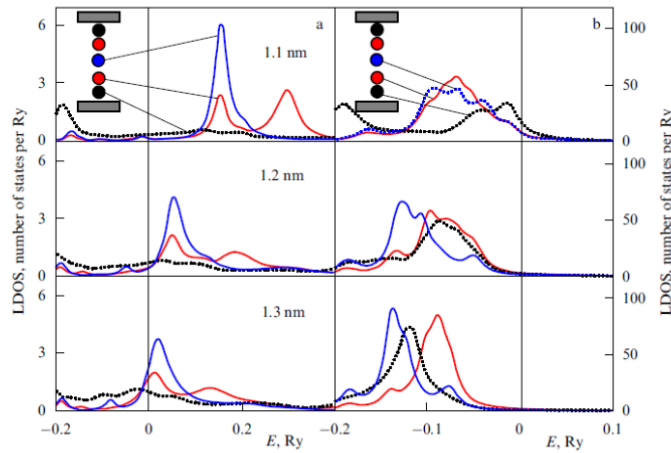


Figure 2.12: Reproduced from [200]. (a) LDOS of s -electrons (b) d -electrons in Cu atoms of a 5 atom contact and inter-electrode distances 1.1 nm, 1.2 nm and 1.3 nm. Red, blue and black curves correspond to LDOS of the internal atom between the central and terminal atom, central atom and terminal atom respectively.

In Figure 2.12, the LDOS of s and d -electrons for atoms in a Cu atomic contact subjected to elongation is depicted [200]. The charge density of s -electrons was reported to be higher which is responsible for the enhanced conductance of nano-contact before rupture. On the other hand, the LDOS of d -electrons for the atoms of a contracted Cu contact was close to the Fermi level and were smeared due to presence of strong inter-atomic interactions [200]. As the distance between the electrodes was increased, d and s states shifted towards lower energies (Figure 2.12). The overall behaviour suggests that s -electrons play a significant role in the stretched state and d -electrons play a dominant role in the contracted Cu atomic contacts. The same behaviour was observed for other metallic atomic contacts of similar configuration e.g Au. To sum up, changes in the LDOS at the Fermi level are related to changes in the length of the atomic contact which strongly affects the final conductance.

Now that the conductance of atomic point contact formation, its mechanism of formation, conductance quantisation and conductance histograms have been discussed, now the conductance of a molecular junction will be briefly introduced.

2.6 Conductance of metal-molecule junction

The integral part of a molecular junction is the metal-molecule interface. Just because the complete device is in the nano-meter scale, the behaviour of this interface becomes very important. The overall functionality, reproducibility, and stability depend on this interface. Therefore, a basic understanding of a metal molecule interface is essential.

A single molecule possesses a discrete set of energy levels. When it is brought in contact with a metal surface, the position of the molecular orbitals get re-normalised (due to screening of metal) and the resulting image charges reduce the highest occupied molecular orbital (HOMO)-lowest unoccupied molecular orbital (LUMO) gap bringing the orbitals closer to the Fermi level of the metal. The direction of the charge transfer depends on the actual value of the Fermi level of the metal and the alignment of the molecule [182]. If the HOMO of the molecule is closer to the metal Fermi energy, then electrons from the HOMO are transferred to the Fermi level of the metal. On the other hand, if LUMO of the molecule is closer to the metal Fermi energy, then electrons from the Fermi level of the metal are transferred to the LUMO of the molecule. The conductance of the molecule nearby the electrodes is strongly affected by this charge transfer. The electronic states of the metals overlap with the molecular orbitals of the molecule leading to a hybridised wave function over the whole junction. This is known as the broadening of the molecular energy levels.

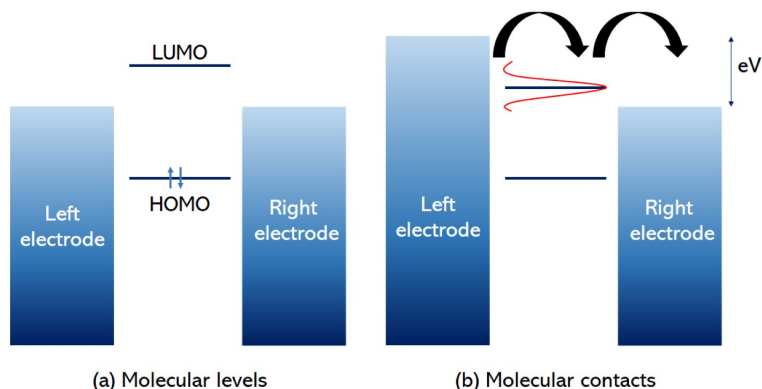


Figure 2.13: Illustration depicting the two electrode potentials and the molecular orbitals between them. Two different situations are shown (in presence and absence of bias). (a) Schematic showing no coupling between molecular levels and electrodes i.e no biasing (b) Representation of the same molecular levels and electrodes under applied bias and broadening.

In Figure 2.13 two different scenarios are shown. (a) The first case is a hypothetical case where no broadening is shown. The molecular levels below the Fermi energy are fully occupied. In the absence of an electric field, the molecular levels are not broadened and no electrons flow between the electrodes. The second case (b) depicts a junction in the presence of an electric field, there is a transfer of electrons from right electrode to the left electrode which shifts their potentials by $eV/2$ each. The molecular orbitals get broadened as charge redistribution leads to hybridisation of orbitals. When the bias is enough to align a molecular level between the electrode potential of the two electrodes, the flow of current takes place

[175].

Considering the molecular energy level can be expressed as a single level ϵ , the number of electrons occupying this level at temperature T and electrochemical potential μ can be expressed as a Fermi-Dirac distribution. The current through such a junction can be expressed as,

$$I = \frac{2e}{\hbar} \frac{\tau_1 \tau_2}{\tau_1 + \tau_2} [f(\epsilon, \mu_1) - f(\epsilon, \mu_2)]. \quad (2.6.1)$$

where τ_1 and τ_2 are the coupling factors between two electrodes and μ_1 and μ_2 are the electrochemical potentials of each electrode.

Considering the broadening of the molecular energy level, the density of states of this broadened energy level cannot be expressed any more by a single level Dirac energy function ϵ . The broadened density of states can be expressed as a Lorentzian function, [175]

$$D(E) = \frac{\frac{\tau}{2\pi}}{(E - \epsilon)^2 + (\frac{\tau}{2})^2} \quad (2.6.2)$$

where ϵ is the energy level of the molecule without any broadening. Therefore, the total current through the molecule considering the Lorentzian shaped density of states of the molecule is given as [175]

$$I = \frac{2e^2}{h} \frac{\tau_1 \tau_2}{(E - \epsilon)^2 + \frac{(\tau_1 + \tau_2)^2}{4}} \quad (2.6.3)$$

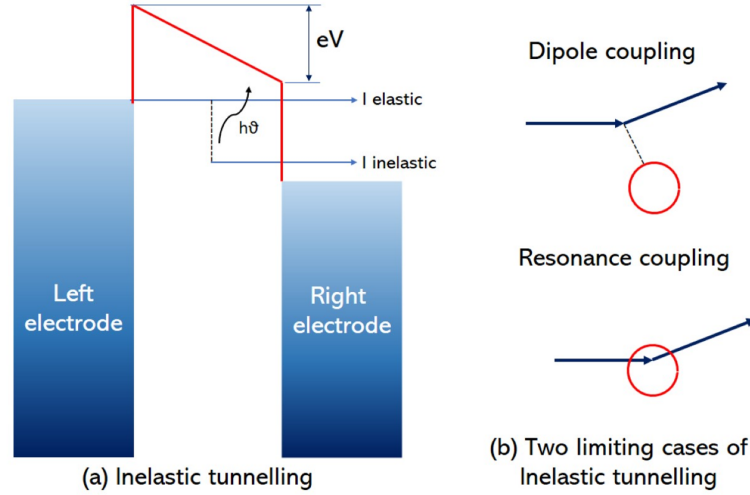


Figure 2.14: Illustration showing the mechanism of inelastic tunnelling. (a) Inelastic tunnelling showing the photon excitation process (b) Two limiting cases of inelastic tunnelling.

In Figure 2.14 a schematic shows the electrode potentials as well as the inelastic tunnelling. When the applied bias voltage is higher than the molecular vibrational energy, an inelastic path is created. The electron excites the molecule and loses its energy before it is transferred to the opposite electrode. In Figure 2.14(b) two limiting cases of dipole and resonance

coupling is demonstrated [175]. In the case of dipole coupling, momentum change is due to an electron approaching and the energy from the electron can be exchanged to the molecule. In the case of resonance scattering, an electron can be trapped temporarily in a molecular orbital.

Chapter 3

Materials and Methods

This chapter deals with the details of sample preparation and the experimental setup used for the measurements. It was already introduced in the first chapter that, it is difficult to perform multiple measurements on the same junction using electromigration (EM) method unlike in mechanically controllable break junctions (MCBJ). Hence, one of the primary requirements was to fabricate a large number of nano-structures on each sample. To meet this requirement, the samples were fabricated using a two step lithographic process. Photolithography was performed to fabricate the Ag contact pads and electron beam lithography (EBL) to pattern the Ag nano-structures in between the contact pads. These contact pads were used for contacting the tips of the 4-tip scanning electron microscope (SEM)/scanning tunneling microscope (STM) and establish a robust contact with the structures. Neither any wiring nor any chip carrier method was used. This unique set-up provided an increased flexibility to test many structures on the same sample without breaking vacuum and the presence of in-situ SEM helped to navigate easily from one structure to the other. The sample preparation, 4-tip SEM/STM set-up and the in-house developed LabVIEW program for controlling EM that was integrated to the 4-tip SEM/STM are the contents of this chapter. Some parts of this chapter have been reproduced from [210].

3.1 Sample Preparation

A two-step lithography was used to fabricate the contact pads and the Ag nano-structures on Si (100) substrate. Low-doped Si substrates ($1000 \Omega\text{cm}$ at 300K) were used, as they are insulating at temperatures below 150 K [172] which is a pre-requisite for an EM experiment. Ag metal was chosen due to several reasons. First, chemical flexibility of Ag is higher as compared to Au [172] and very little studies have been performed on Ag. On the other hand, Au has been widely used in molecular experiments due to its inert quality and easy handling benefits. Another reason to use Ag on Si was its epitaxial growth on hydrogen terminated Si(100) at low temperature (LT) around 100 K [211]. At LT, Ag forms a Schottky barrier to the substrate, keeping the structure well isolated from the bulk Si [212].

The idea was to be able to contact the STM tips on the Ag contacts to create a robust contact between the Ag nano-structures and the tips. Even though Ag on Si was deposited at LT and the know-how that epitaxially Ag wets the hydrogen-terminated Si (100) surface, even then, it was found out that the Ag deposited contacts directly on hydrogen-terminated Si (100) surface was not robust enough to allow proper electrical contact. The metallic Ag contacts turned out to be too soft as compared to the STM tips. This resulted in removal of Ag when the tip was used for contacting. The STM tips could not contact the metallic layer as it could easily touch the Si layer. This means that there was no proper wetting of Ag on Si and an adhesion layer was required. Ti adhesion layer was used before Ag deposition in order to create electrically robust Ag contacts on Si (100) surface. This helped in reduction of the lattice mismatch between Ag and Si to allow good quality Ag contacts on Si (100) surface that could be probed with STM tips.

3.1.1 Photo-lithography processing steps for contact pads fabrication

This section will describe the step by step processes that were followed during the photolithography process. For a pictorial representation, Figure 3.1 is provided. This figure shows the steps involved from spin coating of the photo-resist to lift off after deposition of metal. The other details about solution concentrations, time and temperature of separate steps are described in the text.

Cleaning of the Si wafer

Initially, before the standard steps of lithography is started, the Si(100) wafers are cleaned with standard RCA cleaning technique. Initially the wafer is immersed in Piranha solution ($5\text{ l H}_2\text{O}$, $4\text{ l } 96\% \text{ H}_2\text{SO}_4$, $1\text{ l } 30\% \text{ H}_2\text{O}_2$) for 10 min at 110°C followed by rinsing in de-ionised (DI) water ($6 \text{ M}\Omega\text{cm}$). Then a 1% HF ($1.96\text{ l H}_2\text{O}$, 40 ml of 50% HF) dip is carried out for 60sec followed by rinsing in DI water ($6 \text{ M}\Omega\text{cm}$). Then the standard cleaning1 (SC1) is performed in $8\text{ l H}_2\text{O}$, $1.6\text{ l } 30\% \text{ NH}_3$, $1.6\text{ l of } 30\% \text{ H}_2\text{O}_2$ for 10 min in 70°C followed by rinsing in DI water ($6 \text{ M}\Omega\text{cm}$). After this step, standard cleaning2 (SC2) is carried out in $8\text{ l H}_2\text{O}$, $1.6\text{ l } 37\% \text{ HCl}$, $1.6\text{ l of } 30\% \text{ H}_2\text{O}_2$ for 10 min in 70°C followed by rinsing in DI water ($6 \text{ M}\Omega\text{cm}$). Finally the wafer is rinsed in a spin dryer with hot $\text{N}_2(5.0)$. This is followed by the pre-clean before lithography with 1% HF($1.96\text{ l of H}_2\text{O}$, 40 ml of 50 % HF) dip for 50 sec followed by rinsing in DI water ($6 \text{ M}\Omega\text{cm}$). Again the wafer is rinsed in a spin dryer with hot $\text{N}_2(5.0)$ thereafter.

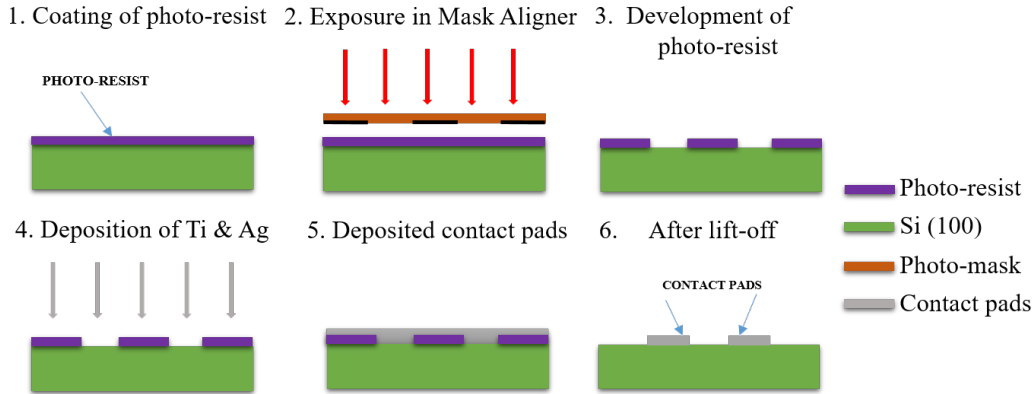


Figure 3.1: The step by step process of photolithography is shown starting from coating of the photo-resist till the lift off to achieve the contact pads according to the designed mask.

Spin coating

The first step is the spin coating of the photo-resist. The complete wafer is spin coated with a negative lift off photo-resist NloF 2020 at 4000 U/min for 50 sec followed by a soft-bake on a hotplate at 100 °C for 120 sec. The soft bake is required to remove any bubbles that may have formed during the spin coating process.

Exposure

The exposure is carried out in a mask aligner at 10 mW/cm² for 4 sec. This is followed by a post-bake at 110 °C for 60 sec. The mask for photolithography is shown in Figure 3.2. The green areas are photo-transparent and white ones are opaque to light. After exposure of a negative resist, re-polymerisation of the exposed areas take place (here green areas). The resist in these areas stay back after the development process.

Development

Thereafter it is developed in the developer solution (AZ 826) for 90 sec at room temperature (RT) followed by rinsing in DI water (6 MΩcm). Finally the wafer is rinsed in a spin dryer with hot N₂(5.0). As already mentioned before, the photo-resist in the green areas (in Figure 3.2) stays back and the photo-resist from the white portions is removed after development.

Deposition

The next step is the deposition of the metallic contact pads. Upon deposition, the metal is deposited directly on Si (100) in the white areas (Figure 3.2) which eventually forms the contact pads on Si. In the green portions, the metal is also deposited, but above the photo-resist and not directly on Si. These green areas (photo-resist and metal on top) are removed in the lift off step. Ti (5 nm) is deposited followed by Ag (50 nm) for creating robust contacts. The deposition is carried out inside an ultra-high vacuum (UHV) chamber by electron-beam deposition.

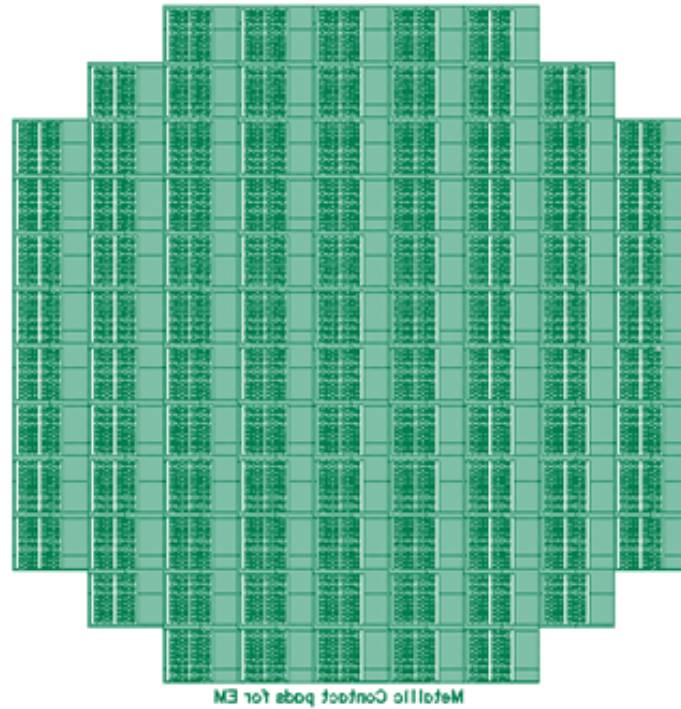


Figure 3.2: The image shows the patterned mask that has been used for the photo-lithographic process for preparing contacts for small structures. The green areas are transparent to light and the white areas are opaque to light. This is designed for a negative lift off resist so that the contacts are on the white areas after lift off.

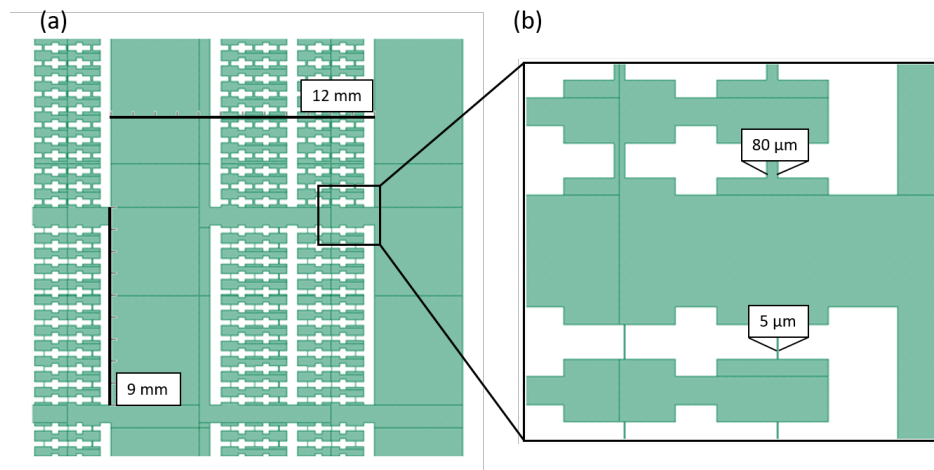


Figure 3.3: (a) Magnified image of Figure 3.2 to show the size of the small samples that are obtained from the whole wafer. (b) Shows a magnified area between two small samples to depict two differently sized contact pads in two different samples. The larger contact is $80\ \mu\text{m}$ and the smaller one is $5\ \mu\text{m}$.

Lift off

The final step is the lift-off process. This is performed by immersing the wafer in N-methylpyrrolidone (NMP) at 80 °C for 4-6 min in an ultrasonic bath followed by rinsing in DI water (6 MΩcm). Finally the wafer is rinsed in a spin dryer with hot N₂(5.0).

The photo-lithographic mask was designed in such a fashion that, after cutting the whole wafer into small pieces (12 mm x 9 mm), each small piece contains 72 small contacts (See Figure 3.3) for EBL structures. To increase flexibility, the mask was designed with two different contact sizes. Half of the wafer could be cut into small pieces (12 mm x 9 mm) which had 80 μm spaced contacts and the remaining half could be cut into small pieces (12 mm x 9 mm) having 5 μm spaced contacts. (Figure 3.3).

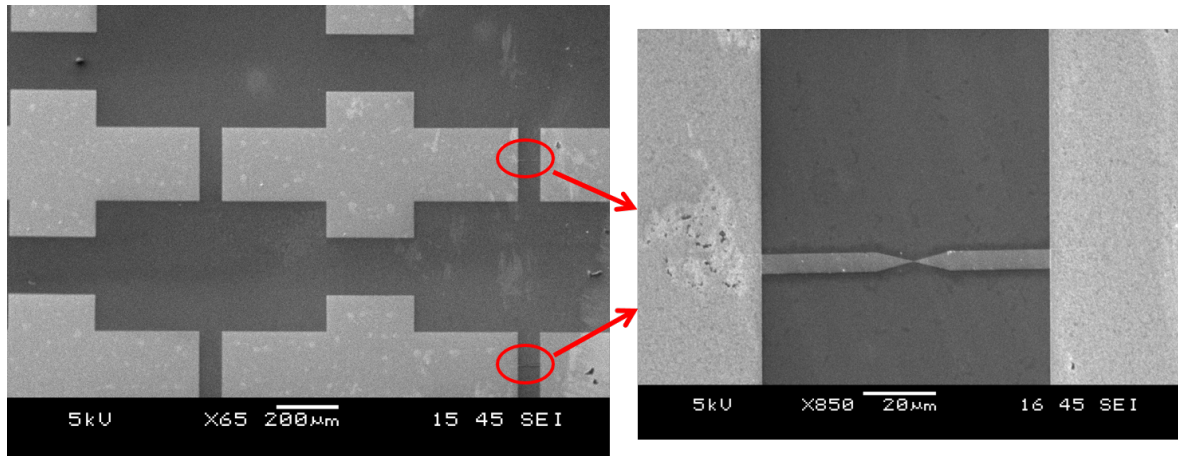


Figure 3.4: Overview Left: SEM image of the 80 μm spaced contact pads. Right: A 100 μm EBL patterned structure between the contacts. One small sample (12 mm x 9 mm) has 72 such contacts.

Finally after the lift off step, the whole wafer was spin coated with two layers of electron beam resist (details in the next sub-section) for patterning the small structures between contacts. The whole Si wafer was then cut into small pieces (12 mm x 9 mm) before performing EBL. The coating of the electron beam resist was carried out before cutting the whole wafer into small samples in order to ensure uniform thickness of the electron beam resist on all the small sample pieces. The SEM image of the contact pads (see figure Figure 3.4) gives an overview of the larger contact and the bridging structures (prepared by EBL) therein.

3.1.2 Electron beam lithography (EBL) of the nano-structures

EBL comprises of essentially five steps - spin coating, exposure, development, deposition of metal and finally the lift off. All the steps are described in details below. Figure 3.5 shows the step by step processes involved.

Spin coating

The electron beam resist is coated onto the whole wafer by spin coating. The thickness of the resist obtained after spin coating depends on several parameters (concentration of resist, molecular weight of the resist and the rotational speed during coating). First, the whole wafer was placed on a CONVAC spin coater on which it was held by a vacuum chuck. Initially 2 ml of methyl methacrylate (MMA) resist was dispensed on the sample for coating of the first layer. The resist was allowed to spread uniformly at 500 rpm for 5 sec and the rotational speed was then ramped up to 4500 rpm for 45 sec. This recipe was optimised by coating MMA at different combinations of speed and time. After coating with MMA, the wafer was baked on a hot-plate at 150 °C for 90 sec. The actual thickness was measured with an ellipsometer after coating. In this way, an uniform layer of 210 nm MMA could be achieved. Then the subsequent poly methyl methacrylate (PMMA) layer was spin coated with a rotational speed of 4000 rpm for 50 sec to achieve a 180 nm layer. This layer was baked at 180 °C for 90 sec. These baking processes are important to eliminate the bubbles inside the coated resist. The purpose of using a double layer resist was to get an undercut after development, which facilitates easy removal of the resist during lift off.

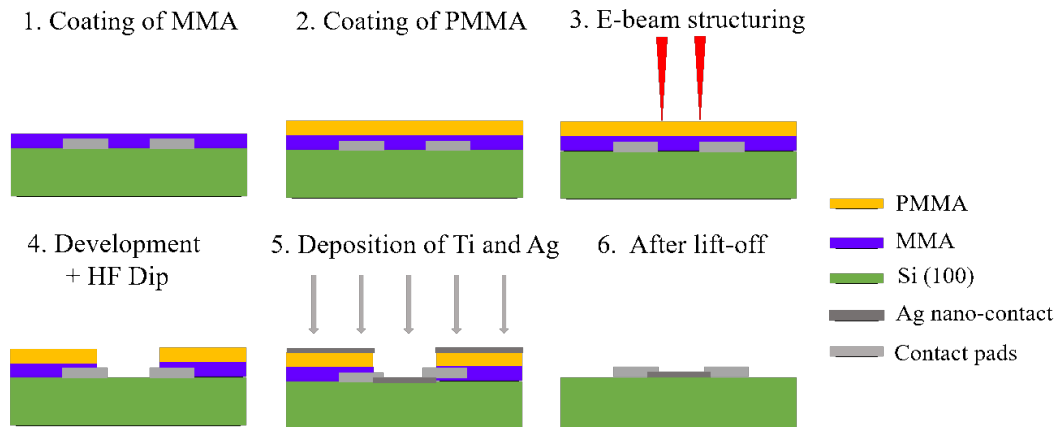


Figure 3.5: This image shows the steps involved in the EBL process for a better understanding.

Exposure

The spin coated wafer was cut into 12 mm by 9 mm pieces before performing EBL. They were mounted on a JEOL SEM 5900 and pumped down to a vacuum of 5×10^{-7} mbar. The structures were designed using Raith lithographic software (Raith ELPHY Plus). For EBL, an acceleration voltage of 30 kV was used. Initially, the high voltage (HV) was switched on for an hour to get a stationary current. After an hour, the alignments were performed to maximise the current.

In the next step, the sample coordinates (UVW) were directly correlated with the stage co-ordinates (XYZ). After this, a marker was focused and stigmation was adjusted. This position was used for performing write field alignments so that the electron beam moves accurately and corresponds to the length defined by the coordinates. Write field alignment

was carried out starting with a lower magnification to a higher magnification so that the beam is focused on all magnifications. For writing $100\ \mu\text{m}$ long structures, 800 X magnification was used which corresponded to $100\ \mu\text{m}$ write field. This helped the whole structure to be written in one write field. For smaller writing fields like $10\ \mu\text{m}$, 8000 X magnification could be used.

Now the desired structure along with the preferred position on the sample was written with an electron dose of $320\ \mu\text{C}/\text{cm}^2$. The time gets calculated automatically by the software according to the dosage and length of the structure. Experiments were carried out to find out the optimum dosage to achieve a center width of $100\ \text{nm}$ - $200\ \text{nm}$ reproducibly.

Development

The next step is to develop the above written structures. This was performed in a mixture of methyl isobutyl ketone (MIBK) and isopropanol with a ratio of 1:3 for 50 sec to dissolve the exposed resist at RT. This development process was terminated by immersing the sample in isopropanol for 15 sec. PMMA being a positive resist, the resist from the exposed regions (written structure) was removed after development. The samples were dipped in 1% HF solution for 15 sec till no drops are seen to stick on the sample. This additional HF dip was carried out to ensure a H-passivated surface after the development and before metal deposition. At the end, the samples were N_2 dried and immediately transferred to the load lock of the UHV chamber in order to prevent any oxides and adsorbates on the surface prior to deposition.

Deposition

The sample was loaded in the molecular beam epitaxy (MBE)UHV chamber under a base pressure of 1×10^{-10} mbar. 1 nm of Ti was deposited as a wetting layer before deposition of Ag. 5 nm - 25 nm of Ag was deposited right after the Ti layer without breaking the vacuum. The thickness of the different metal deposition steps were monitored by a calibrated quartz crystal micro-balance. After deposition the samples were taken out for the lift off process. The metal was deposited on the exposed areas directly on Si.

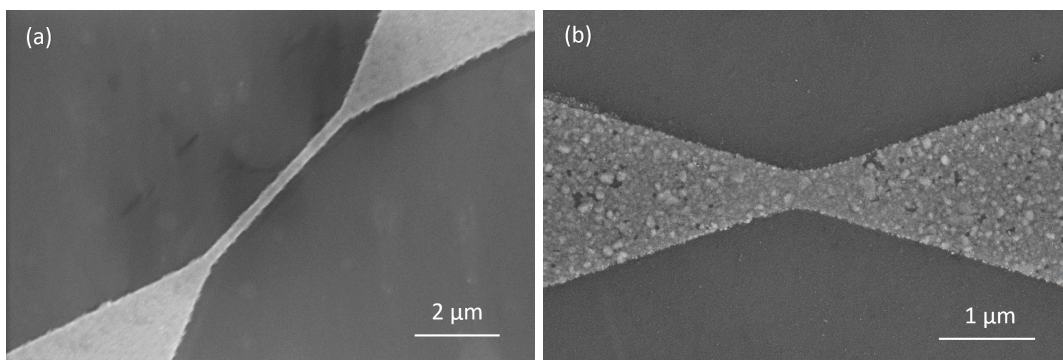


Figure 3.6: Overview of structures in the SEM a) Ag nano-wire structure (25 nm Ag on 1 nm thick Ti buffer layer between Ag and Si(100) substrate), b) bow-tie structure with a 5 nm thick Ag layer on 1 nm thick Ti buffer layer.

Lift off

Lift off was performed by dipping the samples in acetone for 1 hr at RT followed by 20 min in 50 °C to remove the electron beam resist and the unwanted metal from the unexposed areas of the sample surface. The samples were blow dried in N₂ and were immediately transferred to the SEM chamber for observation, focused ion beam (FIB) processing, subsequent storage and measurements. Figure 3.6 depicts the SEM images of EBL patterned nano-structures after the lift off.

3.1.3 Focused ion beam (FIB) patterning on the nano-structures

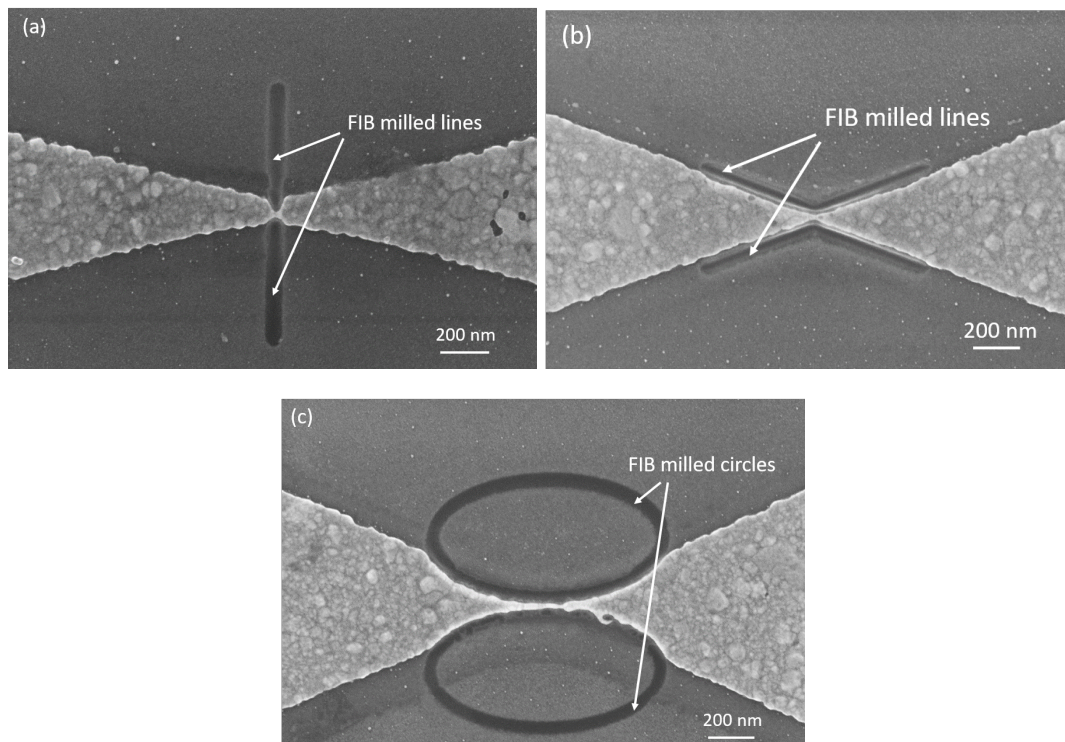


Figure 3.7: Overview of FIB processed structures in the SEM a) 500 nm lines were drawn from both sides to reduce the centre cross-section. b) triangular pattern structure c) circles were patterned using FIB to make a smooth structure and avoid sharp gradients

As seen from Figure 3.6, the centre constriction of the structures patterned using EBL was between 100 and 200 nm and it was necessary to reduce the centre width to one order of magnitude below. The reasons behind this necessity will be evident in the following chapters. This reduction of the central width was possible by performing local FIB milling at the centre. FIB milling was performed using a Carl Zeiss SEM/FIB Auriga system. This method uses a highly focused Ga ion-beam for milling the structure. SEM along with FIB was an excellent combination to identify the local grain structure and perform FIB accordingly to ensure one grain at the narrowest constriction. Several geometries were tried as shown in Figure 3.7 in

order to meet the pre-requisites of an ideal structure prior to EM. These requisites will be evident as the following chapters are discussed.

3.2 4-tip SEM/STM UHV chamber

The EM experiments were performed inside an UHV chamber, as cooling the samples using liquid N_2 down to 100 K was important to suppress the thermal migration (TM). Moreover, Ag being sensitive to the ambient conditions, could not be stored or measured in an ambient STM. Additionally, it was necessary to carry out the fabrication of atomic point contacts and measurement of molecules in an ultra-clean environment under UHV conditions in order to rule out the effect of adsorbates and impurities. The SEM was used to navigate between various structures and electrical conductance measurements were carried out by contacting the individual structures using the STM tips. The base pressure of the system was around 3×10^{-10} mbar. A diagram of the UHV chamber is shown in Figure 3.8. The chamber comprises of two parts: a preparation and an analysis chamber. Both these parts are provided with load lock chambers in front of the main chamber which allow the change of samples and replacement of tips without compromising the UHV conditions.

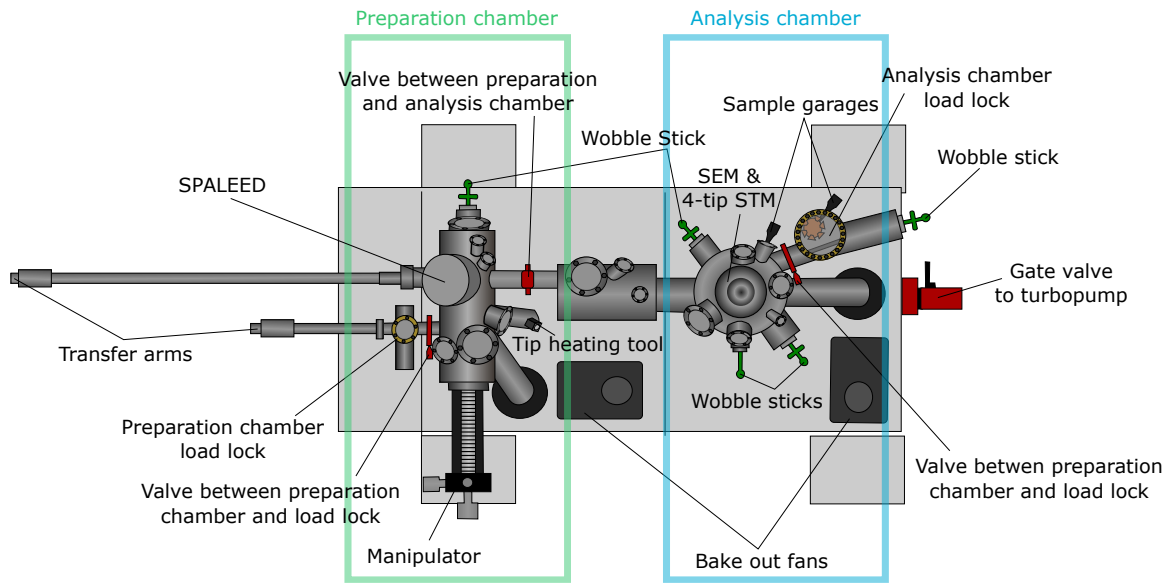


Figure 3.8: Schematic of the 4 tip SEM/STM UHV chamber from Omicron. The chamber is divided into two parts: The preparation chamber and the analysis chamber. The 4-tip STM in combination with a high resolution SEM is present in the analysis chamber.

The preparation chamber has several evaporators, gaseous inlets for molecular gas adsorption experiments and a spot profile analysis low energy electron diffraction (SPA-LEED) to check the quality of the samples before analysis. Samples can also be heated either via direct current or via a backside filament in the preparation chamber. Additionally, samples can be cooled down to 100 K on a separate stage using liquid N_2 . The temperature is controlled by an infrared pyrometer (LUMASENSE IG 140, accuracy in probed temperature region $\pm 5^\circ C$) and

the emissivity coefficient ϵ is calibrated in a feedback controlled manner with respect to the Si substrate. A sample garage allows the storing of up to six samples inside the preparation chamber.

For the EM experiments, the samples were transferred into the analysis chamber, which is separated from the preparation chamber by a gate valve. Inside the analysis chamber, a 4-tip STM in combination with a high resolution SEM allows the exact positioning of STM tips and contacting of nano-structures. During transport measurements, the sample stage can be cooled with liquid He or liquid N₂ to a temperature of 25 K and 100 K respectively. The tips can not be cooled directly and hence they can only cool while they are in tunneling contact. The garage inside the analysis chamber has ten spaces for holding samples and tips.

3.2.1 High resolution SEM in combination with multi-tip STM

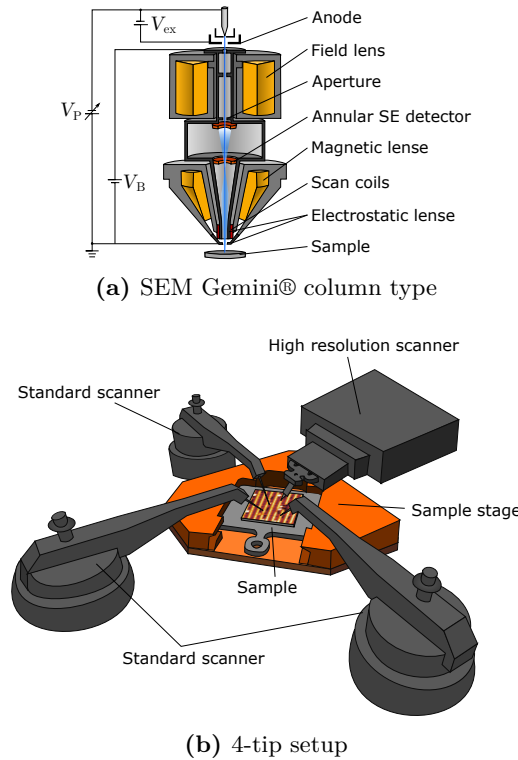


Figure 3.9: (a) Cross sectional view of the principal setup of the Gemini® SEM type (adapted from [213]).
 (b) Schematic overview of the 4-tip STM setup used for the transport experiment (adapted from [214]).

A schematic overview of the high resolution SEM and 4-tip STM setup is depicted in Figure 3.9. The SEM is a Gemini® type SEM from Carl Zeiss AG. The electrons are emitted by hot field emission from a sharp filament which is heated to around 1200 K when a strong electrostatic field is applied to it. In comparison to cold field emission, much higher emission currents and beam stability can be achieved. This results in an improved image quality at lower accelerating voltages. A further enhancement of the image quality as compared to other

SEM is achieved in this type of SEM by an additional voltage, known as booster voltage (cf. V_B in 3.9(a)). This additional voltage maintains a high beam energy throughout the whole column. Just shortly prior to striking the sample, the electrons are decelerated to the chosen primary beam energy. Due to this, aberration is minimized and the diameter of the beam is only a few nano-meters. The aberration correction is especially important in this set-up because of the relatively large working distances of around 1.5 cm needed for operating the 4-tip STM. Using this set-up, the Gemini® type SEMs are proven to have a resolution of 4 nm.

The 4-tip STM set-up consists of four individual STM scanners. For each individual STM tip, a feedback controller is provided in order to move the tip independently on the sample surface with nano-meter precision and to gently contact the surface during transport measurements. A schematic drawing of the set-up is shown in figure 3.9(b). There are three standard scanners and one high resolution scanner. The three standard scanners are mainly used just for transport measurements but can also perform STM. The high resolution scanner is specially designed to perform atomically resolved STM scans. It has better protection against vibrations which can be used to resolve sample surfaces with atomic precision. All the tips used in transport experiments and STM trials were electrochemically etched W tips, prepared in-house, using a well established standard recipe [215]. The tips were pulsed by voltage pulses (between 10 - 20 V for 1 - 50 ms) to clean and condition them prior to transport or STM measurements.

3.2.2 Standard contacting procedure

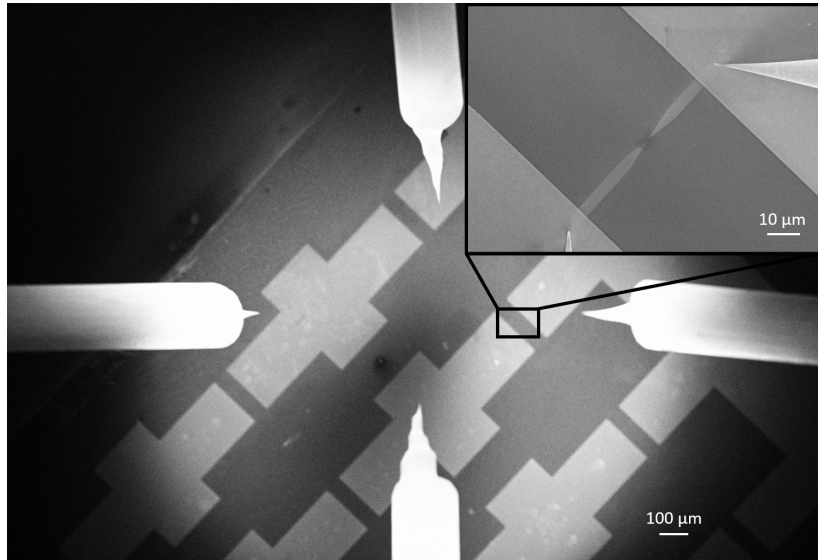


Figure 3.10: Overview of the contacts and the nano-structures as seen with SEM. Inset: Magnification of the small rectangle, where two tips were used to contact the nano-structure for EM experiments. The centre of the nano-structure under investigation is located between the small tip-shaped structures and is shown in detail in Figure 3.6.

Figure 3.10 shows an example of how the overall sample looks like under SEM. The larger

contact pads (patterned with photolithography) can be clearly identified. The inset shows the small structure (patterned with EBL) between the large contact pads. The resolution in this image is not sufficient to clearly see the dimensions at the centre of the nanowire structure (refer to Figure 3.6). Two out of the four available tips were used for contacting the nano-structure.

Sourcing and probing of current and voltage is done by means of a Keithley sourcemeter via a switch-box. First, the tips are positioned carefully on the contact pads on either sides of a small nano-structure by the help of the SEM. Then, the STM feedback loop is used to approach the tip to the specified tunnelling current. For transport measurements, the feedback loop is turned off and the tips are brought in contact with the sample surface in 0.1 nm steps. If the substrate is conductive, a voltage is applied between the sample ground and the approaching tip. Contacts are considered to be reliable as soon as the measured current jumps from 10^{-10} A (the noise level with blanked SEM beam) to about 10^{-7} A. Then the EM experiments were performed using the in-house developed feedback controlled electro-migration (FCE) program (described in the next subsection).

3.2.3 EM setup

This subsection describes the principle of FCE. This is an in-house developed LabVIEW program that was created in order to have a fully automated process of EM. This program is very similar to the existing FCE programs [42, 43]. The main principle is to slowly provide the structure with successive voltage ramps by simultaneously measuring the conductance. There are two feedback loops within the program (Figure 3.11) [216].

The main principle is to slowly provide the structure with successive voltage ramps by simultaneously measuring the conductance. There are two feedback loops within the program. These feedback loops operate by comparing the change in conductance with the threshold value. The threshold values of conductance change for both the feedback loops can be entered manually within the program. The feedback loops work in such a manner that, if the measured change in conductance exceeds the threshold, the ramp is reduced by a voltage factor, and vice versa. The appropriate voltage increment or decrement in both the loops can be controlled by changing the voltage factor. Similarly, voltage factor for both the feedback loops can also be entered manually in the program. Another useful parameter is the ramp speed that can be specified by the user. Since a higher ramp speed makes the process faster in the beginning, initially a higher ramp speed is desirable. Whereas when a few atoms regime is reached, the ramp speed can be lowered accordingly to avoid uncontrolled EM.

Now the main algorithm will be discussed. The main algorithm is represented by two feedback loops which run until a relative difference between the measured resistance and a previously measured resistance occurs. Figure 3.11 represents the flowchart for the FCE program. The difference between both the feedback loops is that the first loop has a fixed comparative resistance (R_0) whereas in the second feedback loop, the comparative resistance (R_i) changes every time the loop is running. The comparator resistance in the first loop only changes when the resistance check in the first loop is true, consequently, a lower voltage is supplied. Hence, the first feedback loop controls the total increase of resistance by controlling the junction temperature. This should avoid the thermal runaway.

The second feedback loop controls the speed of momentary resistance increment. If the

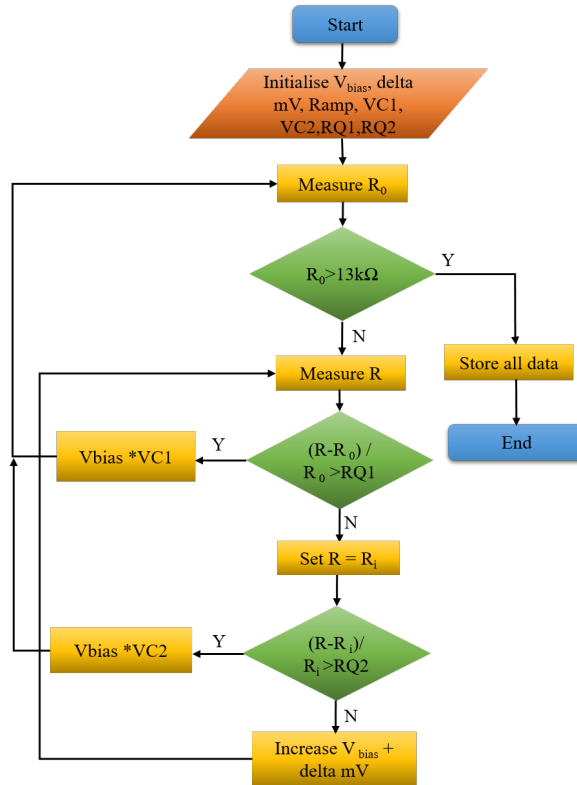


Figure 3.11: Flowchart of the FCE program

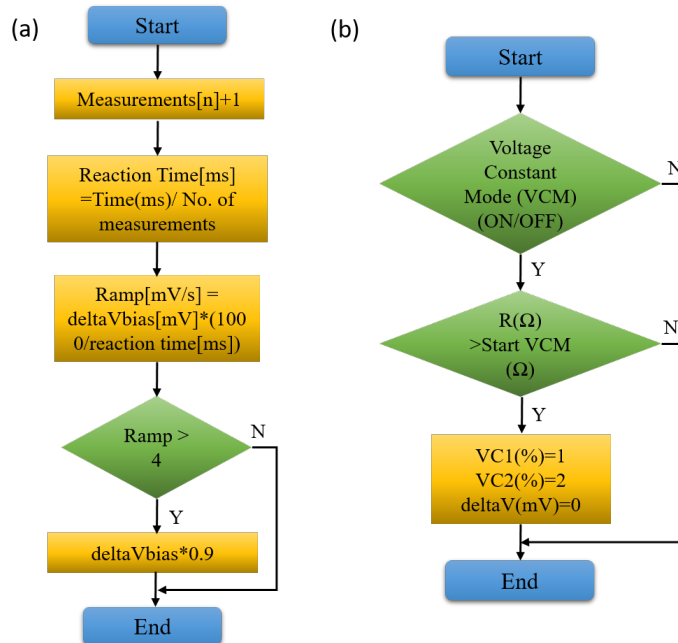


Figure 3.12: (a) Subflowchart for ramp speed calculation (b) Subflowchart for VCM mode

resistance increase is too fast, structural changes due to EM could be the reason. Uncontrolled EM can lead to destructive stresses causing surface tension effects and uncontrolled melting of the wire. The function of the second feedback loop is to prevent the formation of large gaps by uncontrolled EM. The ramp speed (flow chart in Figure 3.12(a)) shows that the voltage increase by δV does not happen faster than a fixed threshold which is the ramp speed. Figure 3.12(b) represents the flowchart for the VCM. This mode can be used to perform constant voltage measurements. It sets the δV to zero and the voltage factors to one [216].

If the relative change of resistance is higher than a threshold value, then the resistance check is set to true. A lower value of the resistance change than the threshold is false. If resistance check is true (Y), the programmed voltage is decreased by a constant factor (VC1), see Figure 3.11. When the resistance check is false (N), the second resistance check starts. If the second check is also false (N), the programmed voltage is increased by a fixed increment (δV). See Figure 3.12 for more details on the δV calculation and actual ramp speed. If the second resistance check is true (Y), then the voltage is decreased by another constant value (VC2).

Chapter 4

EM and morphological changes in Ag nano-wires

In this chapter, electromigration (EM) as a structuring tool is investigated in Ag nano-wires (width 300 nm, thickness 25 nm) on a Si(100) substrate inside a ultra-high vacuum (UHV) 4-tip scanning electron microscope (SEM)/scanning tunneling microscope (STM) chamber. As mentioned in the previous chapter, the Ag nano-wires were fabricated using a two-step lithographic process on a Si substrate. Controlled EM was performed with the help of a home-built feedback controlled electro-migration (FCE) LabVIEW program, also described in the previous chapter. The program controlled the voltage between the tips during EM. Morphological changes were captured using the SEM and real-time movement of material due to EM was observed. These experiments were performed at room temperature (RT), where the role of thermal migration (TM) could not be neglected. Here an effort to understand the effect of geometry and temperature of the nano-wires on the EM process has been made by taking help from simulation of similar structures. Furthermore, notched Ag nano-wires were also experimented. A new type of wire-like structure formation was observed for the notched nano-wires suggesting the simultaneous action of EM and TM is responsible for structure formation. Some contents of this chapter have been published in [210].

4.1 EM: A brief overview

The phenomenon of EM is the motion of particles induced by electric currents or fields. The so-called direct force is responsible for the movement of atoms in a strongly inhomogeneous electric field due polarization and bond rupture. The wind force, on the other hand, describes the movement of atoms by electron scattering and momentum transfer at defects. Depending on the effective mass of the electrons, it can have either sign along the direction of the electric current. For a positive effective mass, the wind force is responsible for material transport from cathode to anode, thereby creating voids at the cathode and hillocks at the anode. On the other hand, thermal migration (TM), i.e., the diffusion of atoms due to the thermal gradient, also plays an effective role, since current flow through a metallic wire with finite resistance is always accompanied by local heating. The combination of both processes is responsible for failure of integrated circuits, which has been studied over decades [217–220].

Most reliability studies performed earlier aimed at micro-meter wide interconnect lines [43, 165]. With the ongoing miniaturization of microelectronic circuits, also the interconnects got finer and narrower. Since EM depends on current densities, EM effects become more important due to the inherent increase of current densities needed in such wires [220]. On the other hand, in increasingly small structures EM is not only important as a failure mechanism. It can also be used for the controlled generation of nano-meter sized gaps suitable for molecular electronics [41, 42]. Furthermore, these nano-gaps gained wider interest in context with the strong field enhancements achievable in nano-gaps of metallic structures. Thus local Raman spectroscopy becomes feasible [95, 221] and plasmons can be efficiently coupled to such nano-structures [222–225].

Interestingly Ag and Ag alloys have been suggested recently as possible replacement for Au and Cu ultra-fine wires [226], although Ag wires show large effects of EM. In recent studies [227, 228] the main mechanism was identified as void formation by granular fracture at grain boundaries [227–230]. It was also shown that the microstructure of the metallic wire is locally responsible for the shape of the void [231].

Phenomenologically the overall effect of EM can be described as a thermally assisted transfer of electron energy (and momentum) to individual atoms (wind force) [229, 232], but the issue of relative contributions is still under debate, although detailed theories have been developed [217, 233–236]. Contrary to polycrystalline material, for single crystalline Ag wires surface diffusion turned out to play the dominant role rather than grain boundary diffusion [237]. In this case a net mass transport opposite to the electron flow direction, i.e. in the direction of the conventional current was found [238, 239].

Already from these few examples it is obvious that the understanding of EM is far from being complete. Further detailed studies would help to deepen this understanding so that EM can be better controlled inside nano-wires, but can also be reliably used for the formation of nano-gap structures.

As it is shown in this chapter, EM at RT not only forms voids and hillocks, but also formation of new wire-like structures with different geometries was observed. Here, the effect of TM and EM in Ag nano-structures (fabricated ex-situ using a two-step lithographic process) is studied. The planar structures on Si(100) are contacted using a 4-tip SEM/STM set-up and the morphological changes during voltage application is observed. In addition, simulation studies of the Ag nano-wire structures (similar to experiments) were carried out

in order to estimate the effect of geometry and temperature. This helped to find out the relative contributions of EM and TM to the mechanism of structure formation.

4.2 EM in Ag nano-wire structures

Figure 4.1 shows the centre of the Ag nano-wire used for EM experiments. A current of 15 mA was passed through a 10 μm long Ag nano-wire with a width of approximately 300 nm and a thickness of 25 nm, corresponding to a current density of $2 \times 10^8 \text{A}/\text{cm}^2$. Cluster formation after current was applied for 7 mins is demonstrated in Figure 4.1(b), which finally leads to the formation of a large void at the cathode, (after 15 mins) as observed in Figure 4.1(c), which was taken after the wire was broken. This clearly shows that the material moved from the void and condensed as clusters on the anode side. Exactly at this location void formation was predicted by the simulations as discussed at the end of the chapter.

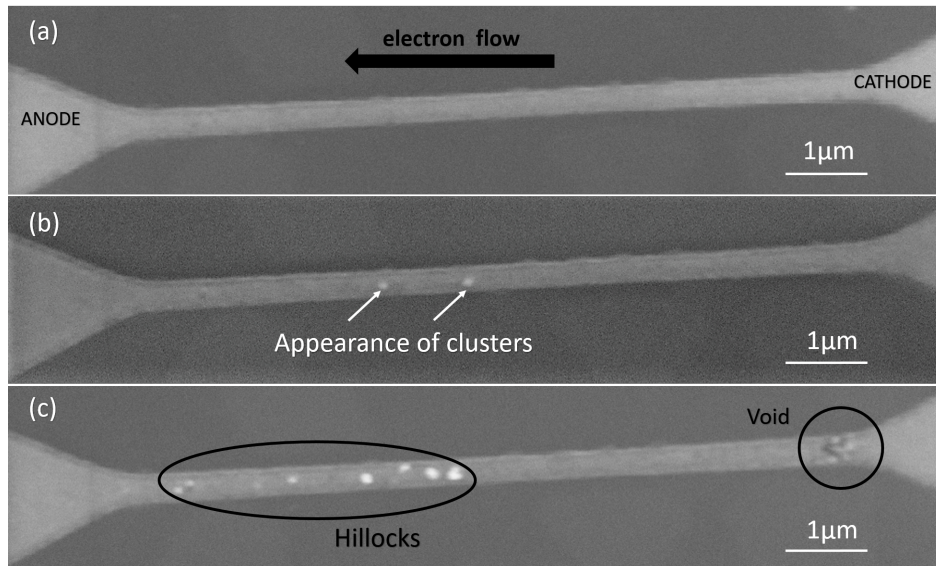


Figure 4.1: Structural evolution of a Ag nano-wire (width 300 nm, height 25 nm) when passing a current of 15 mA from left to right. (a) no current applied. (b), after 7 min and (c) after 15 min of current application. Clearly seen is the formation of Ag islands on the left part of the wire and of a cluster of voids close to the right end of the wire.

A more detailed evolution of resistance as a function of time is seen in Figure 4.2. The final measured resistance after this step (not shown in Figure 4.2) was 11.8 k Ω , i.e. close to the resistance of a single point contact. However, as the inset of the same figure shows, there is an evolution of a granular structure at the void. Therefore, the interpretation of this resistance as a single point resistance is most likely not accurate, but is rather the result of a combination of the local resistances of the grain boundaries involved in the multiple atomic contacts constituting the void. These observations have some similarity with those of Stöffler et al. [240]. The authors claim that the metallic contact must be partially broken, together with single or few contacts in parallel [241]. Accepting this interpretation, the fluctuations seen in the resistance must be due to a series of local changes of configurations.

They occasionally result in sudden larger jumps of resistance, as also seen in Figure 4.2. In most cases, these local transient configurations with higher resistance are not stable, and the resistance goes back to the value before the jump.

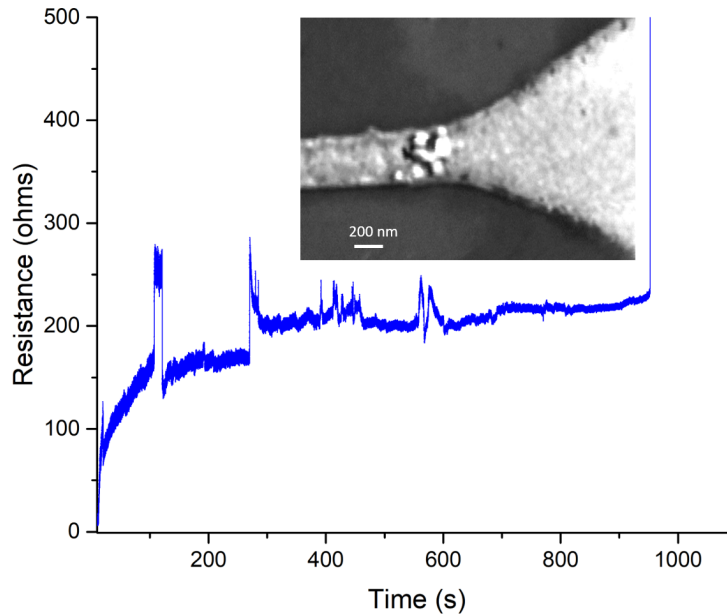


Figure 4.2: Resistance versus time during EM of the Ag nano-wire of Figure 4.1. In this time window the voltage was ramped linearly from 0.1 mV to 3.2V. Inset: SEM image of the void structure at the cathode.

Apart from the void formation at the location predicted by simulation, there is further evidence that EM is the dominant mechanism for the net material transport here. It occurs along the direction of motion of the *electrons*, i.e. opposite to the current direction, indicating it is unidirectional, as expected for EM. For the competing process of TM, however, a symmetric distribution of material is expected, driven by temperature gradients. The largest temperature gradient is between the nano-wire and Si interface, but it cannot lead to material transport, as Ag does not form silicides close to RT. The gradient along the wire, however, is essentially symmetric with respect to the wider part of the structure and has the hottest point in the middle of the wire. If this was the reason, material accumulation on either sides of the nano-wire away from the centre must have taken place, contrary to the observations here. On the other hand, simulations reproduce the effect that the electron-wind force pushes material from cathode to anode uni-directionally with a maximum divergence close to the junction where the cross-section changes.

Looking closer to the distribution of the material from the voids, it is found to be condensed at a distance of 5 to 9 μm away from the void (Figure 4.1(c)). Interestingly, the maximum temperature in the centre of the wire had to be passed by the migrating particles, i.e., most of the diffusion happened *along*, and not opposite to the thermal gradient. This migration

can again only be accomplished by electron wind forces. The fairly large distances involved here require correspondingly long diffusion lengths and the absence of scattering at these length scales. On the other hand, the condensation process is a sign of a local decrease in temperature and an increased probability for atomic collisions in order to form stable and immobile Ag islands. Although the temperature gradient is the same on both sides of the centre, condensation takes place only on the anode side confirming again that electron wind forces are stronger than the thermal diffusion in this situation. Also this finding matches the results of the simulations, where TM under very similar condition as those in the experiment was found to be orders of magnitude smaller than EM.

In summary, it can be concluded that EM is the dominant mechanism of Ag transport in these still meso-scopic nano-structures at RT and at current densities of the order of 10^8 A/cm². In these structures material transport occurs predominantly at locations with large gradients of resistance, e.g. at sudden changes in cross section of the wire. The granularity, which plays an important role for smaller structures (see below), does not seem to have a significant influence on the void and hillock formation by EM, since the results are in very good qualitative agreement with the simulations that use only a continuum description for the material.

4.3 EM in notched Ag nano-wire structures

The experiments described above on long Ag nano-wires, which revealed the dominance of EM even close to RT, showed that material transport is highest close to the location with the highest current density and susceptible to current gradients. However, the chance to get multiple contacts within a structure formed by EM is still very large. Therefore, for the formation of smaller contacts or even single atomic point contacts, the location of the thinning process had to be better defined, (e.g. by a more local increase of the current density). For this reason, notched nano-wires were tested. Interestingly, a new wire-like structure formation was observed close to the notch. Although varying in detail from experiment to experiment, the general phenomenon turned out to be reproducible in several samples.

As an example, the structural evolution over time of a notch made with an STM tip into a 1 μ m wide and 25 nm thick Ag wire is shown in Figure 4.3, starting with the structure shown in Figure 4.3(a). The notch reduced the cross section to about one third. Clusters started to develop near the notch after passing a current of 15 mA through the structure for 30 min (see Figure 4.3(b)). Since the resistance did not increase, the current was slowly increased to a maximum of 20 mA (current density $\approx 10^9$ A/cm²). Instead of breaking up the structure, the material was reorganized into a narrower wire-like structure, which can be observed (Figure 4.3(c)) after 60 min. The process was stopped after 120 min (Figure 4.3(d)).

This phenomenon of new structure formation cannot be due to EM alone, but must be a combined effect of EM and TM. Here the generation of the notch, which accumulates material in the vicinity of the notch, must be considered, too. Though the width of the nano-wire is reduced (see Figure 4.3(a)), an excess material is piled up near the notch in a shape that is far from an equilibrium configuration. Thermal annealing, induced by the current heating of the wire, causes thermal diffusion in order to achieve a more regular form. Only thermal gradients, however, would not form wires from clusters. This diffusion seems to be directed by EM so that several small clusters also try to join the bigger structure and to form a wire,

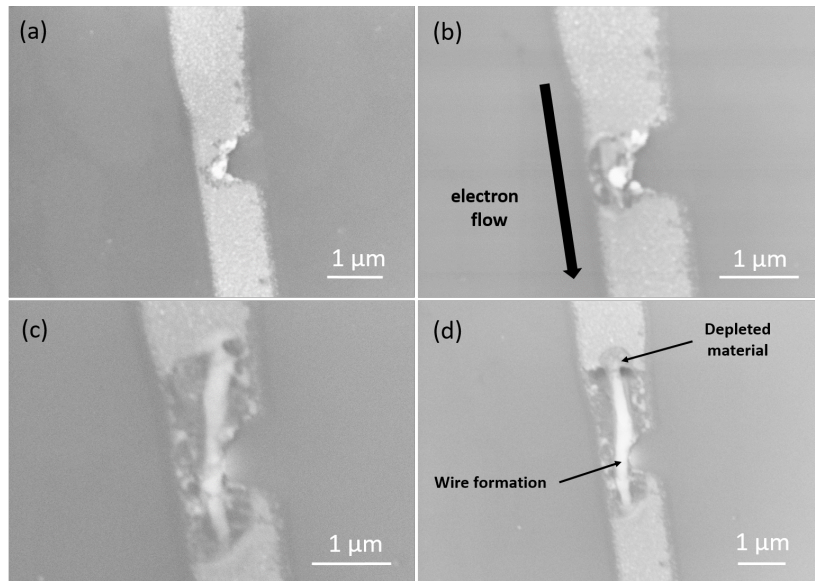


Figure 4.3: Wire with indentation generated with an STM tip. Current was passed from bottom of the structure to top. Signs of EM are visible. The combination of TM and EM leads to formation of a crystalline wire with a width of 200nm.

as seen in Figure 4.3(b).

On the other hand, active material transport caused by EM can also be discriminated, e.g. at the top end of the thin wire in Figure 4.3(d) and by the asymmetric extension of the depleted zones above and below the notch. This means that EM brings additional material from the broad structure into the wire. In other words, the electron wind force depletes material on the cathode side as well as from the edges of the broad structure and accumulates it into the thin wire. TM is responsible for structural round-off and for redistribution of the material from higher temperature regions (near the notch) to both sides of the notch, thus also assisting in wire formation. Similar phenomena have also been observed quite recently [172, 232].

Concluding from both the sections above, it can be noticed that nano-wire structures are susceptible to gradients and EM experiments show that at these sharp gradients, void formation is expected. The EM process does not rely only on gradients but it is one of the factors which has to be considered. Initially void and cluster formation was observed on cathode and anode sides respectively but when notched wires were experimented on expecting a void at the notched area, a completely different structure formation was observed. As both types of structures (nano-wire type and notched nano-wire type) were subjected to EM at RT, from these experiments, the effect of geometry and structural gradients on the final process is significantly clear. Moreover creation of a notched wire by an STM tip leads to accumulation of extra material on the nano-wire at one particular position disturbing the equilibrium. Therefore to study the effect of EM on similar structures, experiments on bow-tie structures were carried out which is the content of the next chapter. Besides geometry and gradient, other important factors affecting EM in nano-structures are temperature and layer thickness which play a crucial role. To understand the effect of interplay of these factors, theoretical

simulation studies of these nano-wire structures were performed.

4.4 Theoretical simulations of EM and thermal migration (TM) in Ag nano-wires

Theoretical simulations of Ag nano-wires subjected to EM at RT and results obtained from these simulations are discussed in this section. These simulations were performed by Tianlin Bai from the group of Dr. Ing. Kirsten Weide-Zaage. The relation between experiments and simulations will be discussed here.

The simulation of EM and TM of a homogeneous Ag film on the Si substrate is based on a continuum description of heat flow, diffusion, thermally assisted EM, and EM-induced stress [160, 162, 242]. The finite element program ANSYS has been used to model the process within the nano-structure (details in Appendix). Initially, a steady state analysis or static simulation is carried out, beginning with the iterative thermal-electrical simulation. For each node of the finite element mesh, the differential equations are solved. The detailed differential equations are provided in the Appendix. The simulations yield estimates of maximum temperature, current density and temperature gradient profiles within the nano-structures. Using them, EM and TM flux distributions as well as flux divergences were calculated. Different nano-wire geometries have been simulated to understand the effect of geometry on the EM process. In this section, a short description of the mesh model and the material parameters used in the simulations will be provided first, which will be followed by the results obtained from the simulations.

4.4.1 Modelling of the nano-wire structure

To understand the migration phenomenon inside the nano-wires and to find out the best geometry for producing atomic sized gaps using EM, geometry modelling is a very important step in the simulation. By calculating the different physical parameters of interest using the boundary conditions and material parameters, a finite element model with an adequate mesh is created.

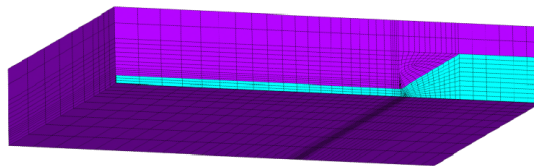


Figure 4.4: Reproduced from [243]. Model of the mesh structure showing the Si substrate and the Ag nano-wire. The violet block is the substrate and light blue area is the quarter of the nano-wire. The lengths and angles are marked in the figure which will be clear in the following paragraphs.

A mesh is considered to be ideal and correct when the output of the calculated parameters does not change with changing the number of nodes. The lowest number of nodes at which the

output parameters start to become constant is chosen. Figure 4.4 shows the mesh structure of a quarter of the nano-wire and the substrate.

Due to the symmetry of the nano-wire, the simulation could be optimized by choosing a simplified model and corresponding boundary values. Using valid boundary values, the simulation results of the simplified model are consistent with the results of original model. This method also minimizes the amount of time it takes to build the model and calculate the results. Here, due to symmetry reasons, a quarter of the entire structure is used as the model of the nano-wire (Figure 4.5). The mesh model of this quarter of the nano-wire is shown in Figure 4.5(a) and a magnified image of the same is shown in Figure 4.5(b). Figure 4.5(b) depicts the difference in the mesh construction at the critical positions of the nano-wire from the other parts of the nano-wire. Areas of quick changes in cross-section are most crucial and more number of nodes gives a better result. This shows that the mesh construction is fully optimised.

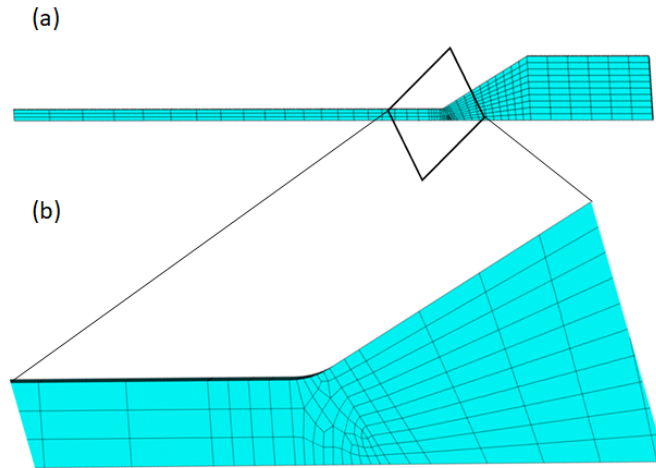


Figure 4.5: Model of the mesh structure showing only quarter of the nano-wire. (a) Quarter nano-wire mesh structure depicts the number of nodes within the mesh varies depending on the position. (b) Magnified picture showing only the mesh structure of the angular portion. The number of nodes gets dense at the junction [243].

As explained above, the model had to be constructed depending upon the experimental parameters of interest. For the simulations, the length of the nano-wire (L_1), the thickness of the nano-wire (L_3) and the angle at which the nano-wire meets the remaining structure (A_1) was varied. The width of the nano-wire (L_2), width of the whole structure (L_4) and the thickness of the silicon substrate (L_5) were kept constant. The L_1 was varied from $1\ \mu\text{m}$, $2\ \mu\text{m}$, $5\ \mu\text{m}$ to $10\ \mu\text{m}$. A_1 was varied from 10° , 30° , 45° to 90° . L_3 was set to two values of $25\ \text{nm}$ and $10\ \text{nm}$. The constant parameters used were L_2 , which was $250\ \text{nm}$, L_4 , which was $25\ \mu\text{m}$ and L_5 was $500\ \mu\text{m}$. See Figure 4.6 for the details. Figure 4.6 shows the complete nano-wire in white and the quarter of the nano-wire shaded in blue. Such a quarter was used as a mesh as shown above.

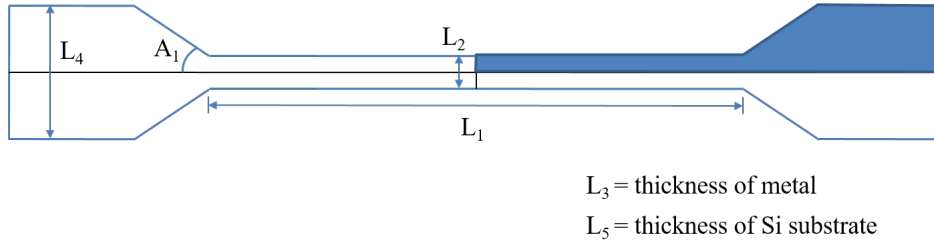


Figure 4.6: The complete nano-wire along with the nomenclature of the different geometrical parameters that are used in the simulations are depicted.

Boundary values

From the model just described above, constant values used (L_2 , L_4 and L_5) were already listed. The two boundary conditions used are the applied current (I) and the substrate temperature (T_{surf}). For the thermal-electrical simulations of the quarter of the nano-wire, the applied current was set to 7.5 mA, and the substrate temperature to 300 K. As the applied current during experiments was 15 mA, due to symmetry reasons, the quarter of the real nano-wire was simulated using 7.5 mA

Material Parameters

Material parameters and boundary values play an important part in the completion of the simulation models. In order to obtain accurate simulation results, the definition of material parameters should be as precise as possible and boundary conditions must be kept consistent with the actual experimental conditions. The material parameters that were used for the simulations are discussed here. Joule's heating cannot be ignored in this simulation. The temperature strongly varies with the position, especially along the nano-wire. Therefore, the definition of the relationship between temperature and material properties is necessary. The change of thermal conductivity and specific resistance of test materials is considered in the simulation process.

$\kappa(\text{W/cm.K})$	200 K	300 K	400 K	500 K	600 K	700 K	800 K	900 K
Ag	4.30	4.27	4.20	4.13	4.05	3.97	3.89	3.82

Table 4.1: Thermal conductivity at different temperatures for Ag (from ref.[244])

Thermal conductivity characterizes the ability of a material to conduct heat. When the electrical conductance is given, the thermal conductivities of electrical conductor can be calculated with the help of the Wiedemann-Franz's law. The thermal conductivity, κ , for Ag at various temperatures is given in Table. 4.1. The specific electrical resistance ρ is given in Table. 4.2 for the range between 200 K to 900 K.

Lastly, the material constants of Ag is provided here in a tabular format (Table 4.3) [242]. The different parameters such as activation energy (E_A), diffusion coefficient (D_0) etc. for Ag at RT can be found in this table. These values were used during the simulations.

ρ ($\Omega \cdot \mu\text{m}$)	200 K	300 K	400 K	500 K	600 K	700 K	800 K	900 K
Ag	0.010	0.016	0.022	0.029	0.035	0.042	0.049	0.056

Table 4.2: Specific electrical resistance at different temperatures for Ag (from ref. [245])

Property	Ag
Z^*	-21
N_0	5.85×10^{10}
D_0 (cm^2/s)	1.71
Q (eV)	-0.0867
E_A (eV)	0.58

Table 4.3: Material parameters for Ag (ref.[242])

4.4.2 Geometries simulated

Here, the various combinations of geometrical parameters simulated are laid down in Table 4.4. As there were four variables for L_1 and A_1 each and two variables for L_3 , hence there were 32 combinations to be simulated. The Table 4.4 shows the number of each model so that it is easy to refer to the results [243].

L1	10°	30°	45°	90°
1 μm	1:L3=25nm 2:L3=10nm	3:L3=25nm 4:L3=10nm	5:L3=25nm 6:L3=10nm	7:L3=25nm 8:L3=10nm
2 μm	9:L3=25nm 10:L3=10nm	11:L3=25nm 12:L3=10nm	13:L3=25nm 14:L3=10nm	15:L3=25nm 16:L3=10nm
5 μm	17:L3=25nm 18:L3=10nm	19:L3=25nm 20:L3=10nm	21:L3=25nm 22:L3=10nm	23:L3=25nm 24:L3=10nm
10 μm	25:L3=25nm 26:L3=10nm	27:L3=25nm 28:L3=10nm	29:L3=25nm 30:L3=10nm	31:L3=25nm 32:L3=10nm

Table 4.4: Layout of the model numbers for different simulations

4.5 Simulation results of the Ag nano-wire

From the Table 4.4, the different parameter combinations with their respective model numbers can be seen. It shows 32 model geometries and each of this geometry was simulated for seven different parameters. The parameters simulated were, *temperature profile*, *current density profile*, *temperature gradient profile* (all three within the nano-wire as well as from the bulk to the nano-wire) and *EM mass flux*, *TM mass flux*, *EM mass flux divergence*, *TM mass flux divergence* within the nano-wire. Now it is practically impossible to show the profiles of all the models (32) for all parameters (7) which amounts to 224 profiles. Therefore, all seven simulations for only one model where $L_1 = 10\mu\text{m}$, $L_3 = 25\text{nm}$, $A_1 = 30^\circ$ (model no.27) is presented here. This model is chosen for the discussion of the results as this is the geometry

which is discussed in the experimental section [243].

4.5.1 Temperature profile

Figure 4.7 shows the spatial temperature distribution within the wire. This is a cross-sectional view of the quarter nano-wire. The blue areas show minimum temperature and red areas show the maximum temperature. The maximum increase of temperature (around 11 K) along the wire was found to be at the centre of the nano-wire, similar to what has been seen in refs. [43, 165]. This trend of the temperature profile within the nano-wire with maximum temperature at the centre of the nano-wire and lower towards the wider parts of the structure is observed for all the simulated models.

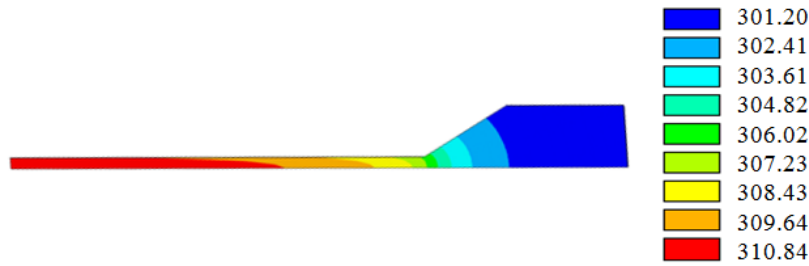


Figure 4.7: Spatial temperature profile for geometry $L_1 = 10\mu\text{m}$, $L_3 = 25\text{nm}$, $A_1 = 30^\circ$, and boundary conditions $I = 7.5\text{mA}$ and $T_{surf} = 300\text{K}$. L_2 , L_4 and L_5 are kept fixed as mentioned before. Units in K.

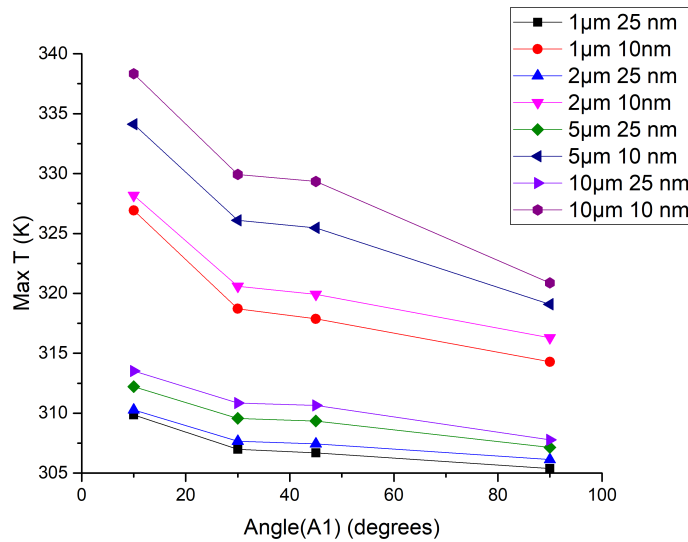


Figure 4.8: Temperature plots for $I = 7.5\text{mA}$ and $T_{surf} = 300\text{K}$ for combinations of L_1 (left column of table) and L_3 (right column) as a function of A_1 . L_2 , L_4 and L_5 were kept fixed.

In Figure 4.8 the maximum temperatures at various combinations of L_1 and L_3 as function of A_1 , is plotted to see the effect of the geometry on the maximum temperature. Though

the temperature profiles are very similar for all tested structures, the dependence of the maximum temperature on the geometry can be well spotted. Firstly, the maximum temperature scales inversely with layer thickness. All the structures with a thickness of 25 nm (L_3) have maximum temperatures lower than 315 K whereas the structures with a thickness of 10 nm (L_3) have maximum temperatures higher than 320 K. Secondly, the maximum temperature decreases with an increase in the angle(A_1). The influence of (L_1) on the maximum temperature is comparatively less dramatic than L_3 and A_1 .

4.5.2 Current density profile

Figure 4.9 shows the current density distribution for the same geometry mentioned above. Current density vectors (in units of $A/\mu m^2$) are plotted (as arrows) within the quarter of the nano-wire.

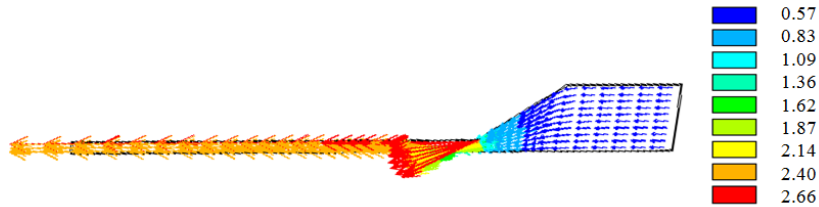


Figure 4.9: Current density distribution for the same geometry and boundary conditions as in Figure 4.7. Units in $A/\mu m^2$.

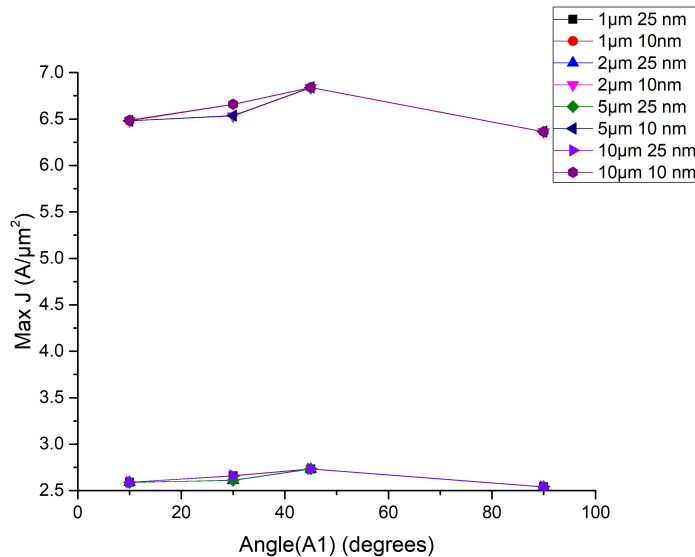


Figure 4.10: Maximum current density plots for $I = 7.5$ mA and $T_{surf} = 300$ K for combinations of L_1 (left column of table) and L_3 (right column) as a function of A_1 . L_2 , L_4 and L_5 were kept fixed.

Again the blue arrows (Figure 4.9) signify lower densities and red arrows signify higher current densities. It can be noted that the current density turned out not to be uniformly

distributed, but it is maximal at the edges where the nano-wire joins the wider part of the structure (similar to ref. [43]). The maximum current density at this position calculated for this geometry was $2.66 \text{ A}/\mu\text{m}^2$.

Figure 4.10 shows the maximum current densities plotted for the geometries indicated in the box, to observe the effect of geometry on the current densities. The maximum current density is dramatically inversely proportional to the L_3 i.e layer thickness. For 10 nm films, the current density value is 3 times the value which is obtained for the 25 nm films. The influence of L_1 and A_1 stays the same (not very crucial dependence).

4.5.3 Temperature gradient profile

Figure 4.11 shows the spatial distribution of the temperature gradient for the same geometry as Figure 4.7.

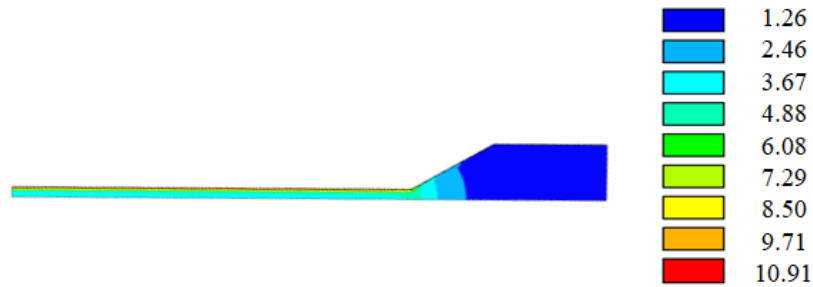


Figure 4.11: Spatial temperature gradient distribution nano-wire for the same geometry and boundary conditions as in Figure 4.7 Units: $\text{K}/\mu\text{m}$.

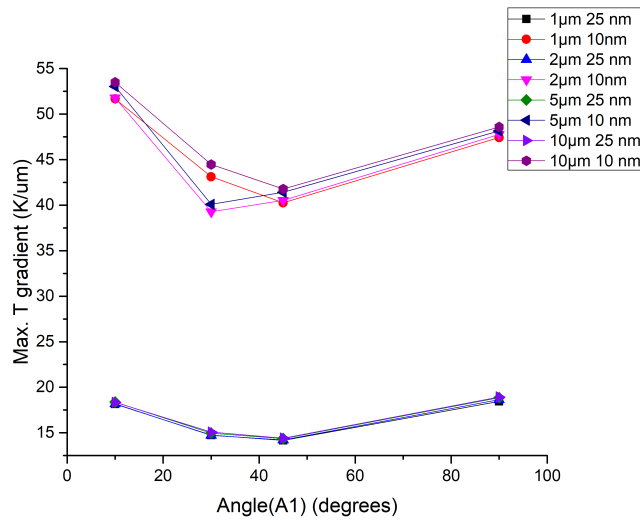


Figure 4.12: Maximum temperature gradients for $I = 7.5 \text{ mA}$ and $T_{surf} = 300\text{K}$, for combinations of L_1 (left column of table) and L_3 (right column) as a function of A_1 . L_2 , L_4 and L_5 were kept fixed.

Along the nano-wire (Figure 4.11), it is maximal at the junction where nano-wire meets the wider part of the structure. The temperature gradient is given in units of $K/\mu\text{m}$. The maximum value for this geometry was found to be $10.9 K/\mu\text{m}$. The temperature gradient profile within the bulk is not shown here. The temperature gradient points from the substrate towards the nano-wire.

Finally the maximum temperature gradient for all geometries is plotted in Figure 4.12. The maximum temperature gradient is roughly 3 times higher in 10 nm films compared to 25 nm films, as expected. Another important finding from this plot is that the minimum temperature gradient is for angles around 40° . Nevertheless, the length L_1 and angle A_1 have a limited impact on the temperature distributions, whereas the main sensitivity is to the layer thickness L_3 .

From simulations of the above profiles, it can be summarised that the effect of layer thickness plays a vital role. The values of maximum temperature gradient and maximum current density are three times larger for thinner (10 nm) films. The effect of length of nano-wire (L_1) is significantly less on these parameters. Temperature decreases with the angles, whereas current density reaches its maximum value for angles around 45° and the temperature gradient is always minimum at these angles.

4.5.4 EM Mass Flux

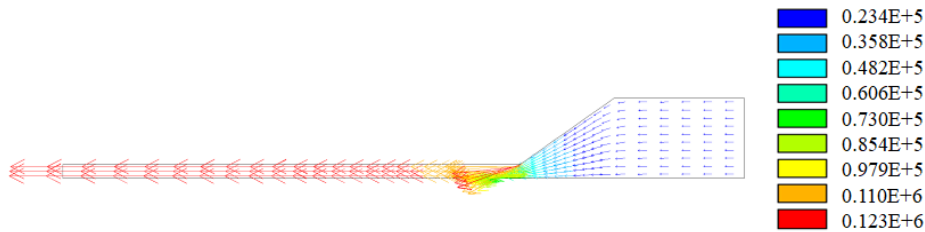


Figure 4.13: EM mass flux distribution in units of $\text{atoms}/(\mu\text{m}^2\text{s})$ for the same geometry and boundary conditions as in Figure 4.7

Figure 4.13 depicts the EM mass flux distribution within the metallic nano-wire. The EM mass flux vector is shown as arrows with the same colour coding. The mass flux is highest at the junction between wire and the wider part of the structure, as well as at the centre of the nano-wire leading to a divergence mainly at the former location. This is the contribution from the wind force. The EM mass flux is mainly directed along the flux of electrons, i.e. opposite to the (technical) current direction. Material transport seen in the experiments was also in the same direction. The EM mass flux values under these current densities was found to be of the order of 0.2 to 1×10^5 atoms per $\mu\text{m}^2\text{s}$.

4.5.5 TM Mass Flux

Figure 4.14 depicts the TM mass flux distribution within the metallic nano-wire. Red arrows indicate a higher TM mass flux as compared to the blue arrows. It is directed from the centre of the nano-wire towards the wider part of the structure. This is the direction which is opposite to the direction in which the material transport takes place in the experiments. The

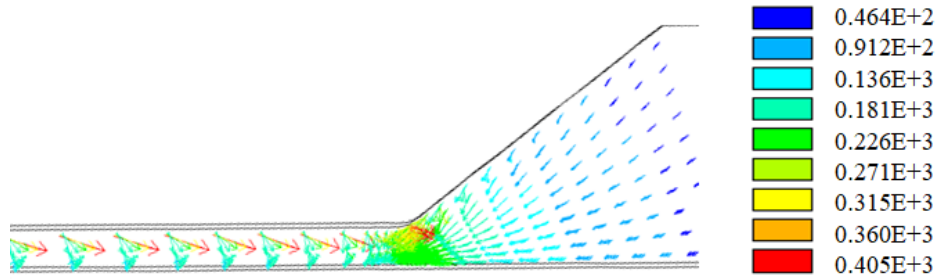


Figure 4.14: TM mass flux distribution in units of atoms/ $(\mu\text{m}^2\text{s})$ for the same geometry and boundary conditions as in Figure 4.7

TM mass flux has been found to be three orders of magnitude lower (up to 4×10^2 atoms per $\mu\text{m}^2\text{s}$) than EM mass flux distribution. Keeping both the factors in mind, i.e. the magnitude and the direction, it is certain that in Ag nano-wires with similar geometry, EM flux plays a dominant role over the TM flux at RT which is responsible for the transport of material from the cathode to the anode.

4.5.6 EM Mass Flux Divergence

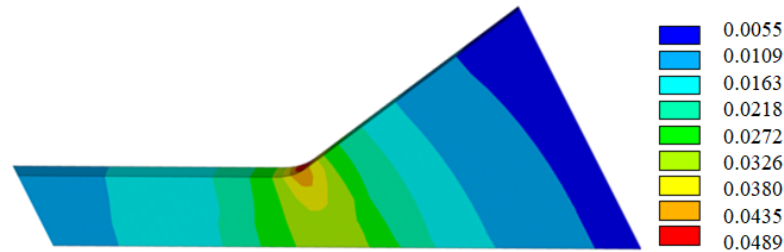


Figure 4.15: EM mass flux divergence in units of atoms/ $(\mu\text{m}^3\text{s})$ for the same geometry and boundary conditions as in Figure 4.7

Figure 4.15 shows the spatial distribution of the EM mass flux divergence within the metallic nano-wire. From Figure 4.15, it is clear that the maximum value of EM mass flux divergence is at the junction of the nano-wire and its wider part compared to other parts of the nano-wire. The maximum value of EM divergence which is colored in red, has a value of 0.0489 atoms/ $\mu\text{m}^3\text{s}$ for this geometry. This is not surprising since the highest current densities have been observed at these abrupt changes of cross section. According to the migration theory, a positive mass flux divergence results in the formation of a void, whereas a negative value promotes the growth of a local hillock.

4.5.7 TM Mass Flux Divergence

Figure 4.16 shows an analogous distribution for the divergence of TM mass flux within the metallic nano-wire from the interface (bottom in this case) to see the effect. As seen in Figure 4.16, the maxima of the EM and of the TM mass flux divergence coincide closely in space. The maximum value of TM mass flux divergence is $0.0087 \text{ atoms}/(\mu\text{m}^3\text{s})$ for this geometry.

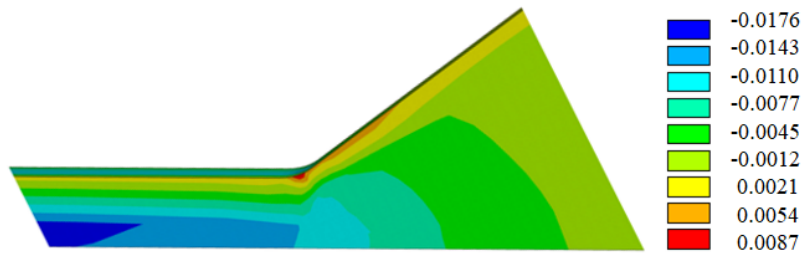


Figure 4.16: Spatial distribution of the TM mass flux divergence in units of $\text{atoms}/(\mu\text{m}^3\text{s})$ for the same geometry and boundary conditions as in Figure 4.7

Comparing the mass flux divergences of both the migration processes, (Figure 4.15 and 4.16), the EM driven divergence is at least an order of magnitude larger, which means that TM is not dominant at the highest current densities of this study. However, TM can generally not be neglected at RT.

Another interesting aspect of these divergence distributions is, though the maximum is at the same position, the divergence is completely different. The EM mass flux divergence (Figure 4.15) is within the wire, whereas the TM mass flux divergence is mainly due to the gradient between the substrate and the wire. As this gradient is not physically explainable, i.e Ag does not diffuse into Si, therefore this effect can be neglected.

When flux divergence is positive, a void is generated. As seen in Figures 4.15 and 4.16, the flux divergence indeed is positive and maximal at the end of the nano-wire. In agreement with this prediction, formation of voids at this position has been observed experimentally. The mass flux of EM towards the centre of the wire is counteracted by TM since the thermal gradient points in the direction away from the center of the wire towards the contacts on both sides. The formation of voids at one end of the wire indicates that EM is dominant.

From the above simulations, a qualitative and quantitative idea on how the process may evolve within the nano-structure can be inferred. The estimates of temperature and mass flux are indeed useful to estimate the effects of geometry on them. The positive EM mass flux divergence within the wire and 3 orders higher magnitude of EM mass flux over TM mass flux in the direction observed in the experiments certainly prove that for this geometry, at RT, the void formation at the cathode is dominated by the EM process.

4.6 Conclusion

Experiments on meso-scopic, but very thin Ag nano-structures at RT, showed that material transport at current densities between 10^8 and 10^9 A/cm² is mainly caused by the electron wind force, i.e. by momentum transfer due to scattering of electrons, whereas TM plays no significant role. Although the granular structure of these films contribute to the resistivity, it is not important for the formation of voids at the cathode and the accumulation of Ag clusters near the anode, as shown by a comparison with continuum simulations. This shows that the interplay between EM and TM is a complex phenomenon and is greatly affected by temperature, initial geometry of the nano-structure and the layer properties. The local enhancement of current densities and of temperature at locations of quick changes of cross sections indicate enhanced scattering probabilities of electrons. This results in a local enhancement of resistance. Therefore, these locations are a source of local instabilities, i.e. void formation, as also observed from non-zero divergences in agreement with our experiments. From these observations, in order to form atomic point contacts using EM, the most important factors influencing the process turns out to be the control of local geometry and temperature. In the next chapter, bow-tie structures (single narrow constriction) are experimented instead of long nano-wire structures and 100 K temperatures are used for better expected results.

Chapter 5

EM in bow-tie structures

After the experimental investigations of the Ag nano-wire structures combined with continuum simulations in the last chapter, the effect of geometry and layer thickness of the local structures on the process of electromigration (EM) was understood. As it was found out that the void formation took place at sudden changes of cross-section with local enhancement of resistance, bow-tie structures with only one constriction at the centre were fabricated in contrast to the nano-wire-type structures (shown in Chapter 4). The idea behind the bow-tie structures was to localise the smallest constriction in order to create atomic point contacts at this position. Using electron beam lithography (EBL), structures with a central width of 100-200 nm could be reproducibly generated. These structures were subjected to a feedback controlled electro-migration (FCE) at 100 K with the aim of generating atomic point contacts. Electrical characterization showed conductance plateaus, demonstrating the conductance quantisation phenomena. From scanning electron microscope (SEM) observations, a complex structure formation at the centre, when subjected to high current densities, after first cycle of EM opening was observed. The mechanism of thinning within these structures was identified from the Fourier transform analysis of the conductance histograms constructed from the conductance traces. Some parts of this chapter have been used for a manuscript that has been submitted.

5.1 Bow-tie structures

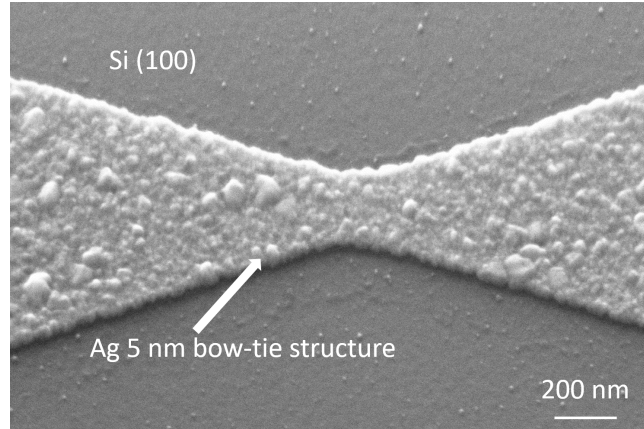


Figure 5.1: SEM image of a bow-tie Ag nano-structure written by EBL with a centre constriction of approximately 200 nm 5 nm thick and 1 nm Ti adhesion layer.

Figure 5.1 shows an SEM image of the centre of a bow-tie structure. The as produced bow-tie structure is granular in nature. Grains between 30 nm - 50 nm in the Ag layer can be identified from the image. From the discussions in the last chapter, it was clear that the locations of quick changes in cross sections are the most vulnerable places where the effect of EM can be strongly seen. Therefore these structures were prepared in order to restrict the position of the atomic point contacts strictly to the centre. These 5 nm thick Ag films on Si substrate were very susceptible to sulphide contamination in ambient conditions. Hence they had to be stored under ultra-high vacuum (UHV) after lift-off with minimum delay. These samples were cooled to 100 K for EM measurements to avoid any thermal migration (TM) effects. The structures were fabricated between the contact pads, and the contact pads were used to cool down the tips to 100 K which took several hours. Once the shrinking reduced, a stable contact between the tip and the structure was established via the contact pads. This robust contacting procedure was essential before the EM measurements at 100 K could be started.

5.2 Structure formation in bow-tie structures by EM

In a typical experiment on a bow-tie shaped sample with a constriction width of 300 nm and a film thickness of 5 nm, a maximum current of 14 mA was passed through it at 100 K. Figure 5.2, shows this bow-tie structure of Ag on Si with 1 nm Ti adhesion layer after EM. The local granular structure with more than one single grain at the narrowest constriction when subjected to high current densities leads to this kind of complex structure even at 100 K.

Figure 5.2 shows such a typical structure formation with several small filaments and one main wire. One can notice the asymmetry in the amount of material that has been transported. The right side of the constriction is comparatively more depleted as compared to the left side, where most of the material is accumulated as bright filaments joining the remaining part of the nano-structure. This uni-directional movement of material is a typical

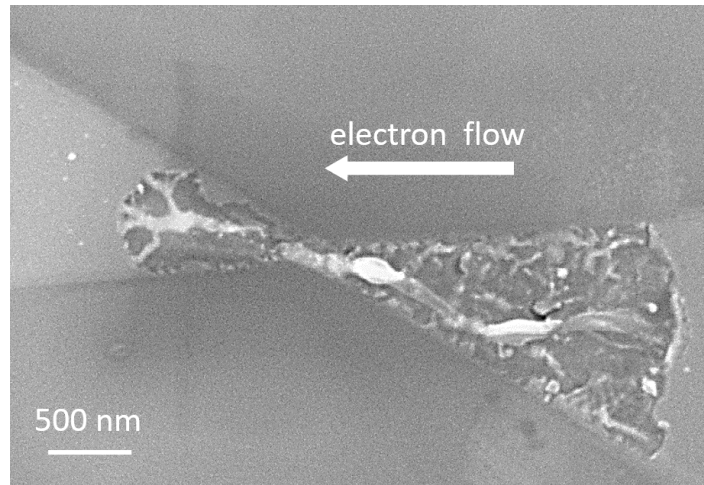


Figure 5.2: Electro-migrated Ag bow-tie structure (thickness 5 nm) after passing a current of 14 mA for 30 min at 100 K.

characteristic of EM which distinguishes it from the TM that would have had symmetric sides.

This questions the role of TM: From the known (lowest) activation energy for hopping migration of Ag on Ag surfaces [246], and the estimates of local heating in these structures at the known current densities ($\Delta T \leq 50$ K), TM should be at least 7 orders of magnitude slower than at room temperature (RT). Hence TM should not play any role in these cooled down structures. This finding still leaves several possibilities open for the underlying mechanism: The many local irregularities within the wires of Figure 5.2 suggest that TM is strongly reduced, in agreement with the estimates from simulations, but local heating to much higher temperatures than estimated by formation of transient local constrictions cannot be excluded. Even EM alone may be able to form such structures in the granular film. If there is still assistance from TM for EM, the barriers must be much smaller than for TM alone.

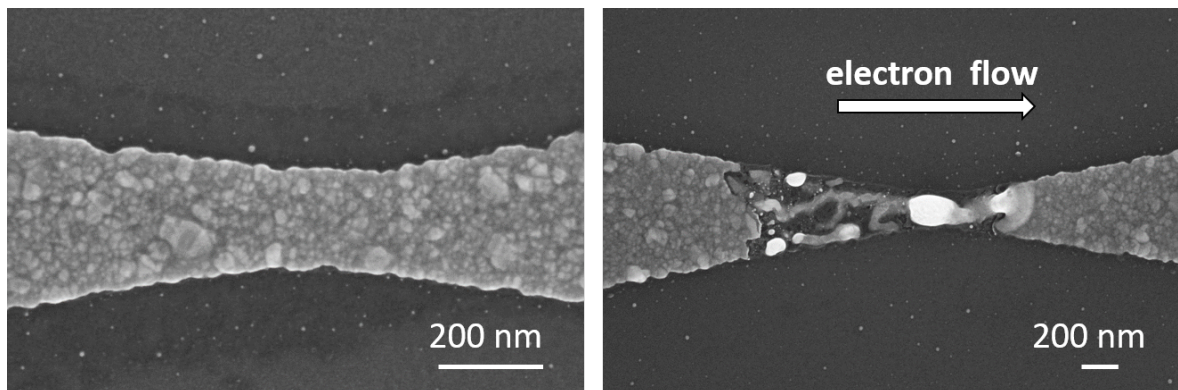


Figure 5.3: Left: SEM image of the centre of a 5 nm thick and 200 nm wide structure before it has been subjected to the EM process. The image shows the granularity of the structure. Right: SEM image of the structure after the EM process.

As already mentioned, the TM effects are reduced by cooling the sample with ℓN_2 to about 100 K. The left side of Figure 5.3 shows the granular Ag film with a centre constriction of 180 nm. A densely packed array of grains of size 30-40 nm in these 5 nm thick Ag films can clearly be distinguished. This granular structure becomes significant, as explained next. The right side of Figure 5.3 shows an SEM image after passing a current of 14 mA corresponding to a current density of $2 \times 10^{13} \text{A/m}^2$ at 100 K using the FCE algorithm. These current densities are exactly one order of magnitude higher than the values required at RT [210], indicating the dominance of EM at these low temperature (LT). When subjected to such *high current densities*, the structure breaks up into a new complicated arrangement (Figure 5.3). The formation of a large cluster on the right side of the smallest constriction and simultaneously a single wire on the left side could be identified. This wire is much thinner than that formed at RT and has an irregular shape. The latter property indicates *strong reduction of TM*. Altogether this *asymmetric material transport* along the direction of electron flow proves that EM is the primary cause of this structure formation.

Even though the initial width of the structures shown above (Figure 5.2, Figure 5.3) are different (by an order of 2), still there is a complicated structure formation in both cases. The probable reason for such a structure formation is the granular nature of the contact material. It is the contact resistance between individual grains that determines the overall resistance in these structures[247]. This contact resistance can be quite high so that there are several possibilities to exceed the critical current density for EM when only a few junctions still exist in the cross section of the wire. In structures between 100-200 nm in width, there are indeed several grains present in the smallest constriction. These grains are only weakly coupled by the grain boundaries so that these boundaries have relatively large resistances compared to the interior of the grains. The weak coupling between Ag grains result in focusing of the current to even smaller cross sections, and the local position of contact areas at the grain boundaries define the starting points of EM. As a result, thinning by EM starts simultaneously at several grain boundaries. Since the granular structure of the material is prone to local variations in resistance, it is difficult to control and restrict the starting point of EM to one in 100-200 nm constrictions. Therefore, in these structures a *randomness in structure formation* in the vicinity of the smallest constriction was always observed. The local grain structure cannot be controlled which introduces random wire and cluster formation. As long as the narrowest width of structures is much wider than the average grain size of the Ag film, it is very likely that EM can start simultaneously at several locations within the network of grain boundaries at the smallest constriction.

5.3 Formation of tunnelling contacts by EM

Step-wise plateaus in resistance are observed once resistances higher than $3 \text{ k}\Omega$ ($4G_0$) is reached. Such quantised plateaus have not been observed while performing the RT measurements (Chapter 4). From these well-defined conductance plateaus with values of $4G_0$, $3G_0$, $2G_0$, and G_0 , it can be confirmed that conductance quantisation takes place in these bow-tie structures at 100 K. This quantized conductance is a characteristic for ballistic electronic transport through junctions consisting of only very few atoms. The details of these conductance traces will be discussed in the next section. These conductance plateaus were obtained during the first EM cycle but when the same structure was electro-migrated again,

conductance quantisation was not observed. Similarly, quantised plateaus did not appear after annealing as well. This fact corroborates with the SEM investigations just reported. From SEM investigations, a complex structure formation was observed after the first EM cycle which changed the local morphology of the granular structure. This modified granular structure (once formed) did not allow repeatable opening of these junctions. Hence this is the most likely reason for the absence of conductance quantisation on repetition.

To understand the reason responsible for the local resistance of the grains seems to be a crucial factor. It has been reported by [240] that sputtered metal layers have smoother surfaces than e-beam deposited layers. The local microstructure of the metallic nano-structures and the contact resistance between grains varies from structure to structure and sample to sample. Local microstructural arrangement and their contact resistance plays a role on the observance of conductance quantisation while thinning using EM. This was observed when structural breakdown of similar nano-structures by EM [240] was reported. The build-up of hillocks was due to the thermally assisted diffusion of metal under the influence of EM forces, i.e., the wind force arising from the momentum transfer from electrons to atoms and from the electrostatic forces. In the present experiments, similar observations were made. Participation of multiple grains within the narrowest constriction led to the step by step conductance quantisation to a few atoms (atomic chains formed) for the first time. After switching off the current, local temperature gradients was responsible for the changes in local surface morphology making it unsuitable for further reproducible results.

After understanding the absence of conductance quantisation on repetition and its link to the structure formation that are morphologically more stable (formed by remaining TM or the local temperature increase due to high current densities on granular structure), now the conductance quantisation (formation of tunnelling contacts) will be discussed. Single atomic chains or single atomic point contact configuration are the two most possible scenarios which can lead to such characteristic conductance plateaus. The plateaus at decreasing integer multiples suggest thinning of the structure with removal of atoms one by one. Depending on the local structural details, long chains as well as short lived single atom contacts both can contribute to quantisation. As the centre width is 100-200 nm, it is difficult to attribute one certain geometry to the conductance value. However, several such weak points may exist and finally one of them develops as an atomic chain. This can be the case in some experiments, where resistance dropped from 22k Ω - 36k Ω to 4-6k Ω after switching off the current for several minutes. This phenomenon indicates evidence that EM generates structures that are far from equilibrium. Considering both SEM and conductance measurements, competition and re-arrangement between local grains complicates the process. These wide structures tend to form fibular structures where no systematics in structure formation exists, neither the exact position can be controlled. Even then, conductance quantisation was observed and atomic chains could be fabricated which proves that these bow-tie structures at 100 K are better candidates as compared to nano-wire-type structures in RT.

5.4 Electrical measurements

Statistical analysis of the conductance plateaus (by constructing conductance histograms) was performed to find out the most preferred conductance values for these structures. The next section concentrates on the Fourier transform analysis of these conductance histograms

which sheds a light on the thinning mechanism of these still meso-scopic structures.

5.4.1 Conductance traces

Here, the electrical characterization of the bow-tie junctions measured at ℓN_2 temperatures will be reported. The initial resistance was typically $50 - 100 \Omega$. In line with works of Motto et al. [43] a similar FCE set-up (described in Chapter 3) for stabilizing EM was used, that allowed to increase current in small steps.

For the EM process, a starting voltage of 5-10 mV was applied and was ramped up at a speed of 4 mV/s while simultaneously measuring the resistance. When the resistance between two measurements changed by more than a preset value (1.5 to 3%), the voltage ramp was stopped and the voltage was slightly reduced. Beginning at the reduced voltage, a new ramp was started only after the resistance was stable for at least 100 ms. Abrupt changes of resistance occurred at critical current densities of $5 \pm 2 \times 10^{13} \text{ A/m}^2$, as already mentioned, and at voltages between 0.8 V and 1.5 V, depending on the actual structure. Once the resistance reached the k Ω -range, clear resistance plateaus became observable. This procedure was continued till the resistance reached more than 20 k Ω . If EM was stopped before the first significant current drop (i.e. at 0.5 to 0.8V), recovery of the initial resistance occurred and no structural changes took place.

This procedure allows to test stability of a particular structure characterized by a certain value of resistance. Even at constant currents, the structures were prone to step by step thinning as also reported by researchers from other groups [42]. Obviously, the current-induced forces reduce the activation energy not only for the last step, i.e break of the chain -, as reported by Yang et al. [248].

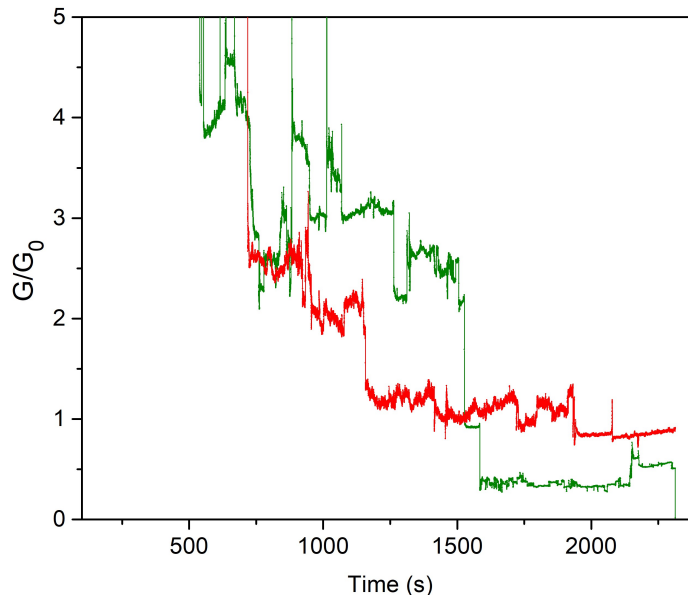


Figure 5.4: Conductance traces during EM of bow-tie structures at 100 K as a function of time. Two sample traces are shown while breaking the structure for the first time. Electrical measurements show conductance plateaus that vary from structure to structure and noise levels that vary between plateaus of same measurement.

Typical plateaus in resistance become first visible with a characteristic resistance around $4k\Omega$ (conductance close to $3G_0$, precise values vary from structure to structure). Further EM results in a second plateau close to $6k\Omega$ to $8k\Omega$, and to a final step at 13 to $20k\Omega$. Such conductance traces are shown in Figure 5.4. The red and the green trace are representatives of two different bow-tie structures. These finite steps in conductance are characteristic for ballistic quantum transport of electrons through contacts that are only a few atoms wide [70, 249]. Exact integer multiples of the conductance quantum G_0 are expected only for a transmission probability, $T = 1$. Since T depends on the local geometry of the contacts, it can in general be smaller than 1 [250].

Two main observations from these plateaus are: (a) Plateaus of conductance: The precise values of conductance plateaus vary between different opening cycles, since they depend on the local contact geometry at the atomic scale [191]. Structures produced by EM can locally be far away from an equilibrium configuration [251]. Therefore, relaxation processes involve not only the contact itself, but also its immediate environment. These relaxations are most likely the main reason for the quasi-continuous small changes in conductance within one plateau, also seen in Figure 5.4. They may also be responsible for occasional jumps to higher conductance values. (b) Fluctuations: These are not due to experimental imperfections, since the amplitude of these fluctuations change abruptly from one plateau to the other within the same measurement. Such an example can be seen when the fluctuation becomes typically very small at the lowest conductance plateau close to $1G_0$ in the green plot. Similarly, in the red trace the noise level around $0.9G_0$ is again less than that of $3G_0$ and $2G_0$.

5.4.2 Statistical analysis

To find out the conductance values that occur most frequently, histograms of conductance traces of these bow-tie structures were constructed. Statistical analysis is commonly performed for mechanically controllable break junctions (MCBJ) studies [252] and very rarely implemented in case of EM break junctions[253]. Histograms provide the best way to determine the most probable conductance values obtained within a set of samples.

A histogram plot between 0 and $5G_0$, constructed with 20 conductance traces of bow-tie structures is shown in Figure 5.5. The histogram for higher G_0 values is shown later (Figure 5.6). Such a plot turns out to be useful to determine the dominant channels participating in the transport along with the sub- G_0 channels. Two most prominent peaks in the conductance histogram are at $0.6G_0$ and $0.9G_0$ (Figure 5.5) followed by a much broader peak at $1.4G_0$. To obtain the exact values of the peaks, a gaussian multiple peak fitting is performed on the histogram. The three most dominant peaks below $5G_0$ are marked in pink ($0.6G_0$), green ($0.9G_0$) and blue ($1.4G_0$).

The possibility of parallel contacts cannot be ruled out completely as concluded from the SEM investigations. When parallel conductance channels are present, then the conductance values corresponding to the summation of these channels should be an indication of the same. Herein, also such a case was observed. The summation of $0.6G_0$ and $0.9G_0$ is close to $1.4G_0$ which is also observed. This observation combined with fact that resistance value drops to lower values in some cases as mentioned in the previous section suggests possibility of multiple weak links and competition between multiple tunnelling contacts.

Figure 5.5 is plotted upto $5G_0$ where the contribution from the thicker sections is not

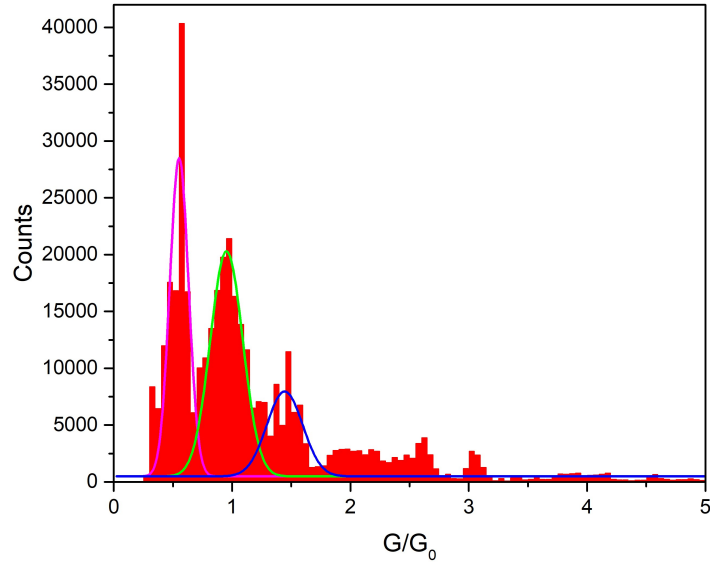


Figure 5.5: Histogram of conductance traces collected during breaking of 100-200 nm bow tie structures. The histogram is calculated using a bin size of 0.05. The peaks are fitted to obtain the exact values of the maxima as well as the width of the peak show the stability of a particular configuration.

shown. For conductance values below $5 G_0$ the maximum counts is 40,000, whereas higher G_0 values have much lower counts. It would have been difficult to determine the dominant peaks at thicker sections if the same plot was used to plot the higher conductance values as well.

Figure 5.6, shows the histogram peaks between $2 G_0$ and $25 G_0$ for the same 20 conductance traces. This conductance histogram starts at $2 G_0$ in order to avoid the pure ballistic regime and show only the semi-classical region. In Figure 5.6 peaks at $2.1 G_0$, $2.6 G_0$, $3.0 G_0$, $3.8 G_0$, $4.2 G_0$, $4.6 G_0$, $14.5 G_0$, $15 G_0$, $16 G_0$, $18 G_0$, $20.5 G_0$ and $21 G_0$ is observed. These are the different metastable configurations attained during thinning of the structure from the bulk regime to few atoms regime. The abrupt jump from $14.5 G_0$ to $4.6 G_0$ is a clear indication of the same. Such configurations (metastable states) are characteristic of the EM process, which are not commonly observed in a MCBJ experiment. Recently this has also been observed for EM experiments in Cu nano-contacts[251].

In order to understand the thinning mechanism, Fourier transform analysis of this conductance regime is performed below. The semi-classical Sharvin's formula is an approximation for contacts approaching the ballistic regime which was briefly introduced in Chapter 2. The next section details that, frequencies obtained in the Fourier transform analysis of experimental conductance histograms can be very closely related to the frequencies calculated from the semi-classical approximation of Sharvin's formula (eqs. 2.4.8). Keeping this idea in mind, the Fourier transform analysis of the conductance histogram above $2 G_0$ should provide some valuable information on the thinning mechanism and preferred orientations.

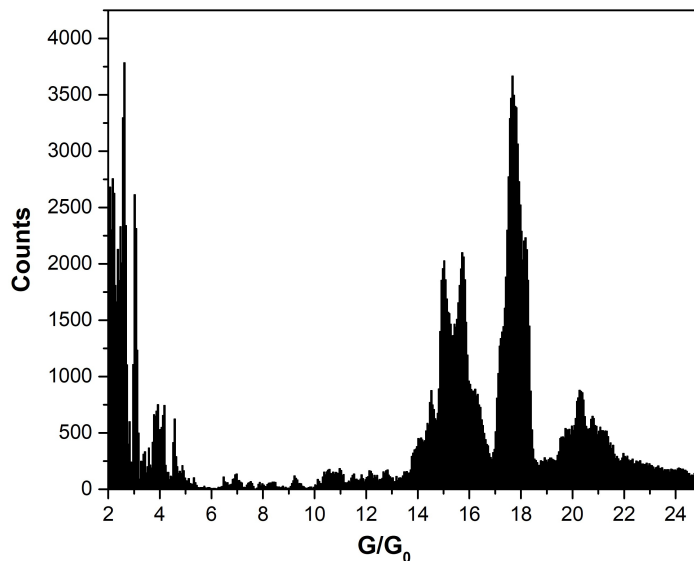


Figure 5.6: Histogram of conductance traces between $2G_0$ and $25G_0$. This region excludes the strong peaks at $0.6G_0$, $0.9G_0$ and $1.4G_0$ to show the conductance quantization above $2G_0$ which is the semi-ballistic to bulk regime.

5.5 Fourier transform of experimental conductance histograms

This analysis is performed on the conductance histograms that covers the semi-classical regime. Fourier transform provides information on the various frequencies present within the conductance histogram peak structure. The frequency spectrum (Fourier transform) would represent peaks at positions that correspond to the spacing between the peaks in the conductance histogram. Correspondingly, such a spectrum would provide information on the crystallographic orientations of the grains involved in the thinning process (within the few atoms regime). This can help to understand the re-organisation of the nano-structure from the bulk regime to a few atoms. The theory behind this Fourier analysis is described here briefly.

One of the ways of direct observation of real time atomic junction formation is the high resolution transmission electron microscope (HRTEM) investigations of metallic nano-contacts (explained in Chapter 2). These in-situ measurements could be very well correlated with the theoretical simulations of conductance histograms performed for different metals [206–208]. The HRTEM investigations was also useful to understand the relation between the simulations (calculated using Sharvin’s formula) and the Fourier transform of experimental conductance histograms [251, 254, 255] (relation of periods obtained from Sharvin’s formula).

In Au nano-wires, Yanson et al. [254] observed atomic size oscillations within the frequencies obtained from the Fourier transform of conductance histograms obtained from a MCBJ experiment. The authors reported that the observed periods in the conductance histograms could be explained by the atomic discreteness along the principal crystallographic directions. These frequencies are obtained from the Sharvin’s formula for an fcc crystal structure. The

nano-wire conductance according to this formula for a circular cross section area A within the semi-classical limit is given by [71, 254],

$$g = \frac{G}{G_0} = \pi A - (\pi A)^{1/2} + 1/6 \quad (5.5.1)$$

$$G = gG_0 = G_0 \left[\left(\frac{k_F R}{2} \right)^2 - \frac{k_F R}{2} + 1/6 \right] \quad (5.5.2)$$

Fermi wavelength $\lambda_F = 2\pi/k_F$.

The cross-sectional area A is expressed as λ_F^2 assuming electrons are confined by boundaries [254] and considering a spill out of $0.34 \lambda_F$ beyond that, then the last two terms in eqs. 5.5.1 can be neglected. This brings in a linear relationship between A and g ($\Delta g = \pi \Delta A$). Considering fcc packing in direction perpendicular to the three principal directions (111), (100), and (110), 2-dimensional unit cells can be identified. The area of the unit cells in (111), (100), and (110) direction is $\sqrt{3}/2a^2$, a^2 and $\sqrt{2}a^2$ respectively. Here a is the lattice constant. If one by one atom increment is considered then the conductance would scale $\Delta g_{111} : \Delta g_{100} : \Delta g_{110} = 0.87:1:1.41$. This describes the spacing between conductance values for thinning in the principal directions. Similarly the inverse of above values should appear in the Fourier transform of such a conductance histogram where spacing between G values correspond to a specific direction. The calculated periods in the three principal directions are $\Delta g_{100}=0.96$, $\Delta g_{111}=0.83$, $\Delta g_{110}=1.36$. The inverse of these periods correspond to the frequencies in the Fourier transform as $(\Delta k_F R)^{-1}$. The frequencies obtained from eq. 5.5.1 and eq. 5.5.2 for an fcc crystal structure are $0.8 G_0^{-1}$, $1 G_0^{-1}$ and $1.3 G_0^{-1}$ corresponding to three principal crystallographic directions (110),(100) and (111) respectively [254].

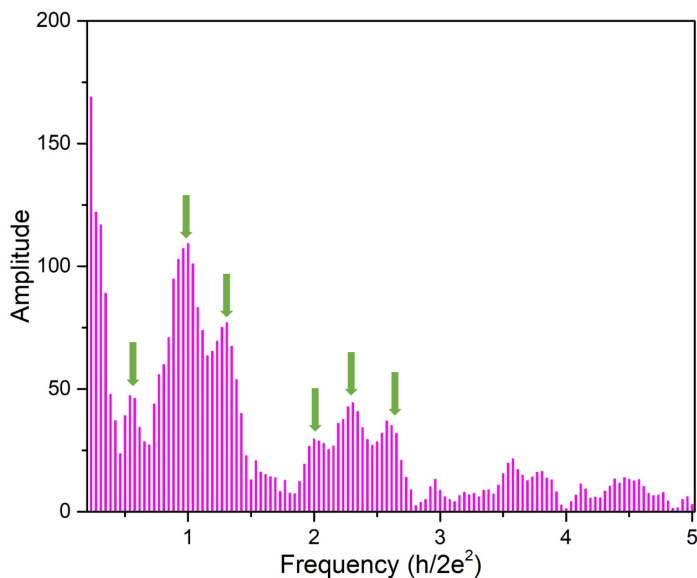


Figure 5.7: Fourier transform of the histogram section between $2.0 G_0$ and $15 G_0$ showing most prominent frequencies at $1.0 G_0^{-1}$ and $1.3 G_0^{-1}$. The next prominent ones are $0.6 G_0^{-1}$, $2.1 G_0^{-1}$, $2.3 G_0^{-1}$ and $2.6 G_0^{-1}$.

The Fourier transform of the conductance histogram of the present experiments in bow-tie structures between $2 G_0$ and $15 G_0$ is presented in Figure 5.7. The most dominant frequencies are $1 G_0^{-1}$ and $1.3 G_0^{-1}$. These two values at $1 G_0^{-1}$ and $1.3 G_0^{-1}$ indicate thinning mostly occurs along (100) and (111) directions during EM. These frequencies match the values obtained from the semi-classical Sharvin's formula just discussed above [254]. The correlation is realistic since for diameters larger than 2.5 nm, the core of the nano-wire has a fcc crystalline structure [256]. Similar observations were reported in the Fourier spectrum of experimental conductance histograms between $1.2 G_0$ and $15 G_0$ of Au nano-wires [254] from a MCBJ experiment. For Au nano-wires [254], these two frequencies were accompanied by a third prominent frequency at $0.8 G_0^{-1}$. The Fourier transform (Figure 5.7) in this case does not show a peak at this value. A peak at $0.8 G_0^{-1}$ in the Fourier transform corresponds to (110) direction. This clearly distinguishes the fact that in these bow-tie structures, contribution from (110) is absent. It can also be concluded that in a Au MCBJ experiment, conductance histograms reflect thinning in all major crystallographic directions, but in Ag EM experiments only grain directions (100) and (111) contribute to atomic contact formation.

This matches with the findings of HRTEM [192], where it was reported that Ag mostly forms rod-like structures for (110) directions. In-situ HRTEM studies of Ag [192] also showed that atomic chains are only possible when at least one grain is oriented in (100) direction. Above calculation of periods from the Sharvin's formula estimates a frequency of $1 G_0^{-1}$ is a contribution from (100) direction. Therefore in these structures, the dominant $1 G_0^{-1}$ frequency indicate thinning in this particular direction. Combining both the facts, HRTEM studies (states atomic chains are only possible when at least one grain is (100)) and dominant frequency from the Fourier transform of the histogram ($1 G_0^{-1}$ corresponds to thinning in (100)) indirectly proves that the frequency at $1 G_0^{-1}$ (Figure 5.7) corresponds to atomic chain formation in these electromigrated bow-tie Ag structures.

Similar studies were also reported for Al nano-contacts [255]. These experiments were performed by pulling apart commercially purchased Al wires, a process similar to MCBJ. Fourier analysis of the conductance histograms (constructed from breaking traces at constant voltages) revealed similar results. Recently in 2017, similar atomic discreteness analysis (using Fourier transform) was performed from conductance histograms of electro-migrated Cu nano-contacts [251]. In these studies, ratio of periods obtained from the Fourier transform of experimentally obtained conductance histograms scaled to the crystallographic frequencies (calculated from Sharvin's formula), meaning that conductance histogram peaks correspond to the thinning along the crystallographic directions even for EM. Contributions from all crystallographic directions can be present in the conductance histograms constructed from experimental datas (other than direct observation e.g HRTEM and simulations), as it is practically impossible to have well-defined orientation of nano-wires for experiments [207]. The contribution from different crystallographic orientations can only be segregated in theoretically simulated conductance histograms.

Other peak frequencies in the Fourier analysis (Figure 5.7) are at $0.6 G_0^{-1}$, $2.1 G_0^{-1}$, $2.3 G_0^{-1}$ and $2.6 G_0^{-1}$. The frequency at around $0.6 G_0^{-1}$ in this case has also been observed before, by Mares et al. [203] and Yanson et al. [257]. This frequency was attributed to the oscillating frequency of a diametric orbit. This frequency was observed to be very prominent for Ag, less prominent in Cu and absent in Au as observed by the authors of [203]. These numbers are calculated from a semi-classical expansion where the geometry is described

by stable clusters. These clusters have diameters for which a bouncing electron wave traveling along a closed classical path within the spherical cluster obeys the Bohr-Sommerfeld quantization condition. The frequency at $0.6 G_0^{-1}$ is a contribution of diametric orbit for cylindrical systems. When a spherical system is considered, contribution from triangular and square orbits are dominant which is not the case here.

Frequencies around $2.3 G_0^{-1}$ corresponds to an approximate spacing of $0.47 G_0$ in the conductance histogram. These values are expected for stable Ag dimers [203]. The final observation is the shell effect that can also be seen in the Ag structures using EM. Shell effects were observed by Mares et al. [203] for noble metals Cu, Ag and Au. They report in their article, Fourier transform of the conductance histograms show the electronic shell effect for these metals. This can be identified by the main peak in the Fourier transform at $1 G_0^{-1}$. The dominant frequency at this value has been obtained for Au and Cu also and is a characteristic of electronic shell filling.

5.6 Conclusion

In this chapter, the EM experiments in bow-tie structures with 100-300 nm central widths at 100 K was demonstrated. Structure formation into a filamentous form as well as cluster-wire formation was observed. Structure formation at 100 K seems to be fully governed by EM, and TM seems to be negligible. Conductance measurements depicted perfect conductance quantisation when thinning for the first time. On repeating, well defined plateaus were not observed. This observation along with SEM investigations, suggests that formation of multiple weak links within the 100-200 nm constriction takes place during EM. Granular nature of the contacts does not allow them to be a reliable candidate for repeatable single atomic point contact fabrication. Therefore, the identification of a single conductive channel was not possible as long as the narrowest width of the structures was much wider than the average grain size. Nevertheless, different preferred conductance values were obtained from the conductance histograms of these rather wide (100-200 nm) bow-tie structures. Fourier transform of these conductance histograms and its relation to the (i) well-known semi-classical Sharvin's formula as well as (ii) HRTEM studies of Ag was used to understand the thinning mechanism from the bulk regime to the atomic chain formation regime. Not only the thinning and preferred crystallographic orientations were identified from the frequencies, but also the electronic shell effect in Ag nano-wires was observed. In order to fabricate reproducible point contacts, focused ion beam (FIB) structuring was performed on these bow-tie structures. The details of this nano-structuring, and the restriction on the number of grains at the narrowest width for a more precise control of the EM process at that grain boundary are the contents of the next chapter.

Chapter 6

Fabrication of atomic point contacts using FIB patterned structures

Herein a systematic way to precisely locate atomic point contact formation using an unique combination of focused ion beam (FIB) and electromigration (EM) is reported. By characterizing and manipulating the conductive properties of single Ag nano-grain boundaries with EM, atomic point contacts could be generated at well defined locations with extreme reliability in ultra-thin (5 nm) and ultra-small (minimum width 16 nm) Ag nano-structures, deposited on hydrogen terminated low-doped Si(100) samples. Single contacts were always obtained once the smallest constriction of the structures was below the average grain size of the Ag films and competing thermal migration (TM) was suppressed. This helps to localise the position of a single point contact and even the thinning could be identified from energy dispersive x-ray (EDX) analysis. These ultra-thin and laterally open structures on Si provide complete accessibility for local characterisation of the molecular junction. Statistical analysis of the conductance measurements gives an insight to the various metastable conductance states that are formed during the process. Parts of this chapter have been reproduced from this publication [258].

6.1 Fabrication of different geometries for local morphology control using FIB

The bow-tie shaped nano-structures having a centre width between 100 nm to 200 nm, extensively discussed in the previous chapter had multiple grains as well as grain boundaries within this narrowest constriction. As a result, when these structures were subjected to high current densities during the EM process, due to the participation of several grains, a complex structure formation took place (discussed in Chapter 5). This structure formation was dependent on the local granular arrangement of the metallic layer hence was difficult to control.

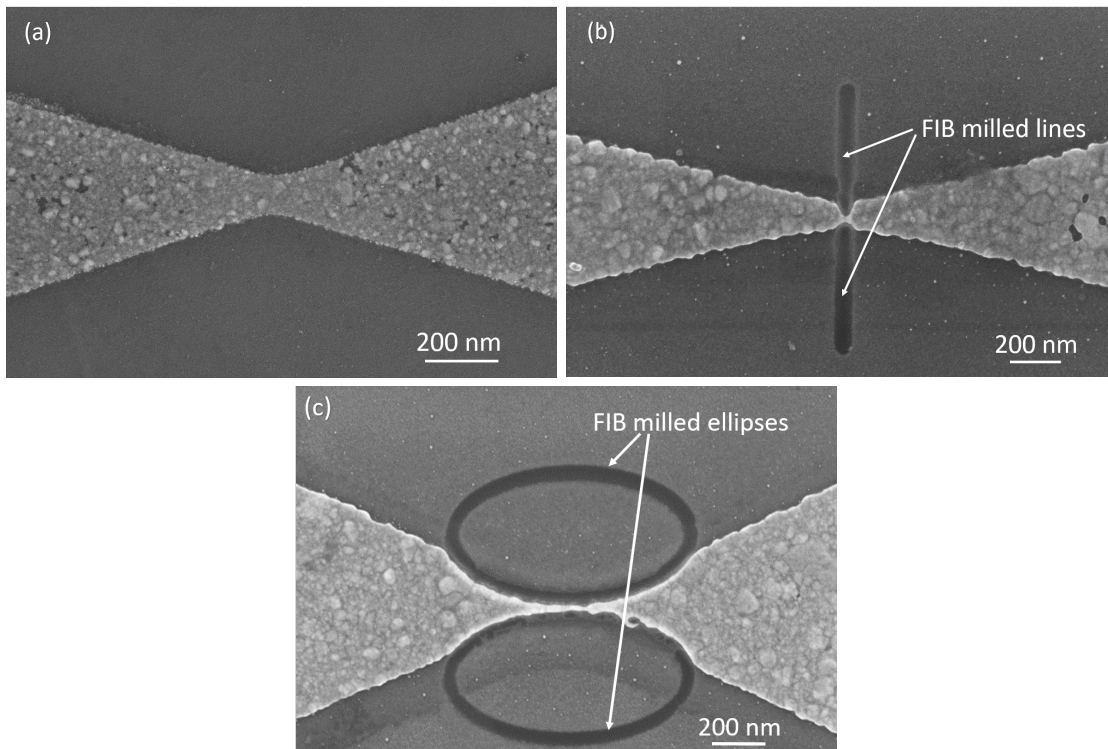


Figure 6.1: Overview of tested structures (SEM): (a) Example of bow-tie structure with a 5 nm thick Ag layer on 1 nm thick Ti buffer layer, (b) bow-tie structure processed with FIB by etching two lines (dark grey) with the ion beam down to a narrowest width of 20 nm, (c) FIB-processed bow-tie structure generated by etching two ellipses with the ion beam. The narrowest width was reduced to 16 nm.

To locally control this granular structure, FIB structuring with the aim to avoid multiple grain boundaries at the narrowest constriction was performed. Additionally this aim had to be matched with the observation that EM is very susceptible to gradients in cross sections (Chapter 4) and in electrical resistance [210]. Therefore, a balance is required between the two. For this reason, two structural extremes of FIB structuring have been performed on the bow-tie structures. Figure 6.1 depicts three images. Figure 6.1(a) shows the normal bow-tie structure without any FIB structuring. The two types of FIB structuring are shown as (i) line structuring: an abrupt narrowing (Figure 6.1(b)) and (ii) elliptical structuring: a very gradual variation of the cross section (Figure 6.1(c)). Both structures yielded a narrowest

constriction between 10-20 nm which was sufficient to ensure one single grain at the smallest constriction i.e. it was below the typical grain size of the Ag layer. The two structuring styles differ from each other in (i) gradient with the remaining structure and (ii) the number of grains at the smallest constriction. In Chapter 3, another type of FIB structuring was shown (triangular pattern structure). The triangular pattern is an intermediate structure between the line and ellipse structuring. The results after EM of triangular patterned structures were similar to line structured samples therefore only the two extreme cases are discussed here.

6.1.1 FIB line structuring

The reason for FIB structuring (as already explained earlier) was to reduce the width of the local structure to ensure one grain at the smallest constriction. The first type of structuring was a FIB line structuring (See Figure 6.1(b) and Figure 6.2). This was performed by patterning lines with the Ga beam at 30 kV acceleration voltage and 1 pA current. 500 nm long lines were patterned from either sides in a direction perpendicular to the length of the structures at the vicinity of the centre with the aim to create a Ag bridge of 10-20 nm. The diameter of the Ga ion beam depends on the focusing conditions, approximately 50 nm at a typical dosage of $0.1 \text{ nC}/\mu\text{m}^2$ was used to pattern these structures.

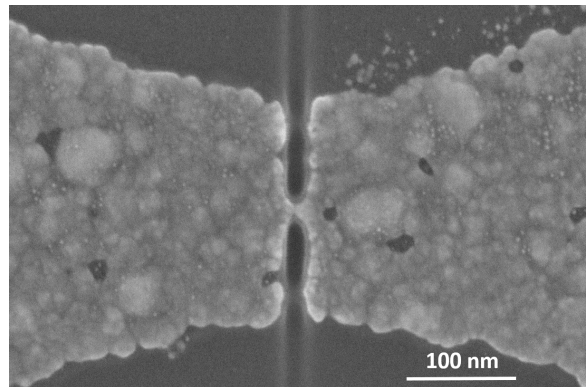


Figure 6.2: SEM image of a FIB line patterned structure with an initial width of 200 nm. The white Ag structure has a narrow bridge of 20 nm which corresponds to a single grain.

The ion-beam dosage and the distance between the two lines was varied to optimise the final width of the Ag bridge, so that it is below the grain size of a single Ag grain. The whole process before and after the structuring could be very well controlled with the visualisation using the SEM. This helped us to observe the local grain structure at the centre and accordingly adjust the dosage as well as distance between the lines. Resistance measurements on the structures and outside the structures were performed to make sure that the samples are not doped with Ga. It could be confirmed that at such low dosages, Ga did not introduce any changes in resistance before and after the FIB structuring within the samples.

The starting width of the structures being one order of magnitude higher than the desired width, the line structuring could generate structures where the remaining structure body (apart from the centre) was separated only by 50-100 nm on both sides (Figure 6.2). This introduced a huge gradient in the vicinity of the cross-section especially when the initial width of the structures before FIB structuring is larger than 150 nm. .

6.1.2 FIB Elliptical structuring

The second type of patterning that was performed is the elliptical grooves. As already discussed, that the aim of having single grains at the narrowest width needed to be accompanied with also having smooth gradients in cross-section, the later requirement could not be fulfilled by performing line structuring. In Figure 6.2 the presence of huge gradients from a width of >100 nm abruptly to 20 nm can be observed clearly.

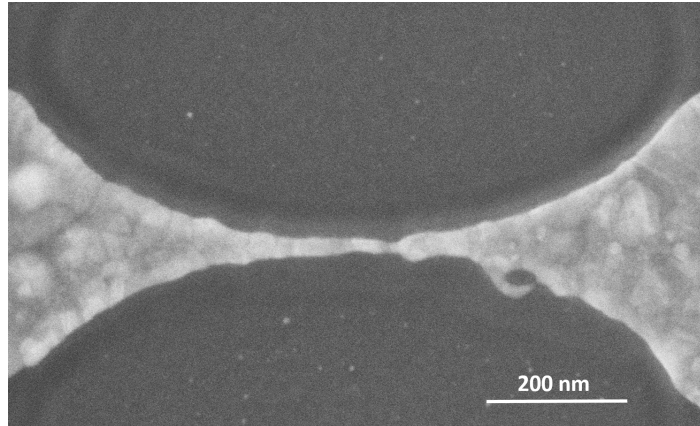


Figure 6.3: SEM image of a FIB ellipse structuring with an initial width of 110 nm. The white Ag structure has a smooth variation of grain sizes with the narrowest grain of 16 nm at the centre position .

For generating a smooth gradient within the centre and a gradual variation of the width, elliptical grooves were patterned on both sides of the centre (see Figure 6.1(c)). Figure 6.3 shows a magnified version of Figure 6.1(c). Here, the gradual variation of grain sizes can be identified clearly for a length of approximately 300 nm. Similar acceleration voltage of 30 kV and an ion-beam current of 1 pA was used for structuring. Again by varying ion beam dosages and the distance between the ellipses, the size of the Ag bridge at the centre-most location could be optimised. The best structures were obtained with a dosage of $0.1\text{-}0.2\text{ nC}/\mu\text{m}^2$ without any doping issues.

6.2 EM in FIB structures

6.2.1 EM in line structured samples

Figure 6.4 shows SEM images of two different line patterned structures (similar to Figure 6.2) after EM. The difference in the two structures is the starting width. The structure on the left side is wider (200 nm) at the centre than the structure on the right (100 nm) before patterning is performed. But after patterning, the centre constriction is reduced to 20 nm ensuring only one grain boundary exists at the smallest constriction for both the line patterned structures. This step already introduces an abrupt gradient (already discussed) where the cross-section suddenly drops from few hundreds of nano-meters to few tens of nano-meters. The detrimental effect of this abrupt gradient after EM can be spotted in Figure 6.4 and has a two-fold effect. First, there is a huge amount of material transfer from the cathode to

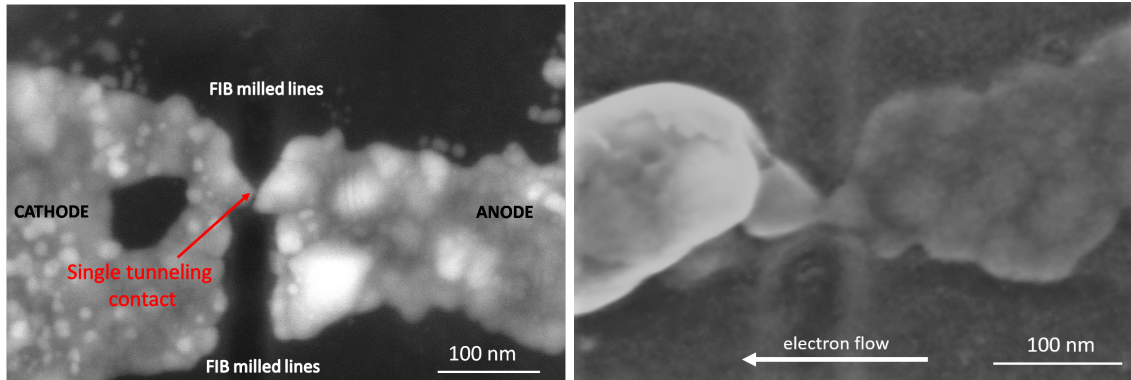


Figure 6.4: SEM images of two FIB line patterned structures after EM. Left: Initial width of 200 nm before line patterning and after subjecting to EM. Right: Similar patterning on a structure of initial width 100 nm, after EM. Note the accumulation of material due to high gradients.

the anode side and second, this huge transfer of material can lead to multiple contacts after repeated cycles of EM or after annealing. Apart from the centre grain, the material within the remaining structure is separated only by 50-100 nm (along the line). This distance can be easily overcome by thermal diffusion when repeated EM cycles are carried out leading to local temperature gradients, since at low temperature (LT) the usual TM is suppressed. This reduces the overall stability of the structure. Therefore, line structured samples were not the most suitable candidates for fabrication of reproducible atomic point contacts. The difference in EM behaviour of the ellipse structured samples where abrupt gradients are not present in comparison to line patterned samples will now be discussed.

6.2.2 EM in ellipse structured samples

The second type of FIB structuring with elliptical grooves, as shown in Figure 6.1(c) and Figure 6.3 yields smooth gradients of the overall cross section, with a formation of a chain of single grains of varying sizes. In such a structure, the (electrically) weakest grain boundary cannot be determined a priori, but due to the small variation in cross section amongst adjacent grains, only a small amount of material is transported during EM in order to create a point contact. SEM image of such a structure before (Figure 6.5(a)) and after EM is shown in Figure 6.5(b). The bright white spot in Figure 6.5(b) denotes the accumulation of Ag along the direction of electron flow. Several grain boundaries are visible clearly but the thinning can be observed at the narrowest grain boundary.

It can be seen that smooth gradient allows less material transport as compared to the abrupt gradients in line structuring. Even after repeated EM cycles, repeatable structures with similar conductance values were obtained in contrast to line structuring where it was prone to multiple tunnelling contacts after the first cycle and no stable conductance values could be obtained. Therefore, from the SEM investigations of these ellipse structured samples, neither a complex structure formation which occurred for the bow-tie structures without structuring, nor a significant amount of material transfer which took place in case of line structured samples, could be observed, which leads to an unstable morphology. Atomic point

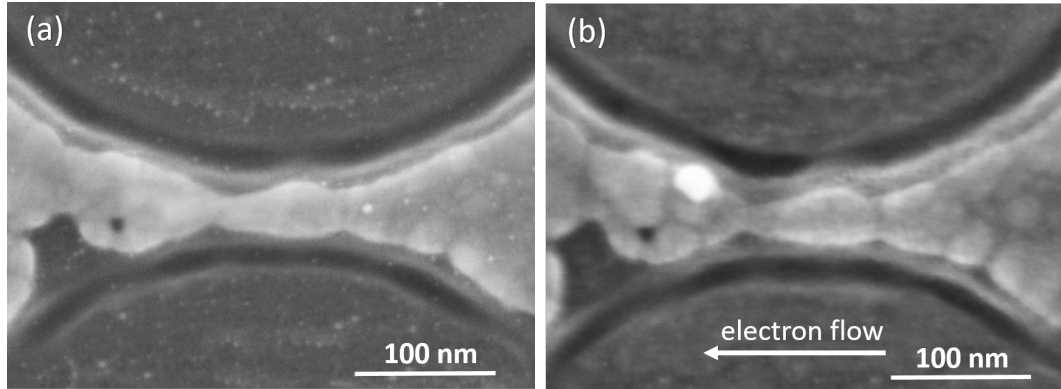


Figure 6.5: SEM images of a Ag nano-structure, 5 nm thick and 20 nm wide, after FIB structuring (dark ellipses). (a) before EM, (b) after passing a current of 5 mA in the direction indicated by the white arrow for 6 min.

contact cannot be visible in SEM images but apart from the bright material accumulation spot and thinning of the narrowest grain boundary, no other distortions were observed within the structure concluding that the electrical conductance corresponds to atomic point contacts. It was reproducible and identical values of conductance could be obtained after repeated opening and closing of the junctions at 100 K. The details of conductance measurements are discussed later in this chapter confirming that ellipse structured samples are the ideal candidates for atomic point contact fabrication.

6.3 Energy dispersive x-ray (EDX) measurements in FIB structures

Figure 6.6 depicts the spatial distribution of EDX intensities of Ag (blue) and Si (green) as an overlay mapping for both the types of structures - line structuring (right part of Figs. 6.4) and elliptical structuring (right part of Figs. 6.5). No EDX measurements were performed before EM experiments. The high concentration of Ag at the anode and depletion of Ag at the cathode is clearly visible in both images of Figure 6.6, where, a large amount of material transport is visible in the line patterned structure, which is strongly reduced in the structures patterned with ellipses. For the elliptical structure, in spite of the existence of several grain boundaries in the thinnest part, the thinning occurs only at one of the grain boundaries, as can be clearly observed from the image (right image in Figure 6.6).

EDX signals of Ga and Ti along with other related impurities like O, C and S were recorded. The signals obtained were below the instrument measurement sensitivity. Such trace amounts of Ga, Ti do not play a significant role in EM experiments. They were neither visible at the narrowest grain nor in the vicinity.

From these results it can be concluded that EM properties can be better controlled on a structure with smooth gradients. The thinning occurs at the grain boundary with the minimum width. Thus multiple junctions can be excluded. As a consequence the stepwise plateaus in the conductance measurements described in the next section, must correspond to the quantized resistance of atomic point contacts.

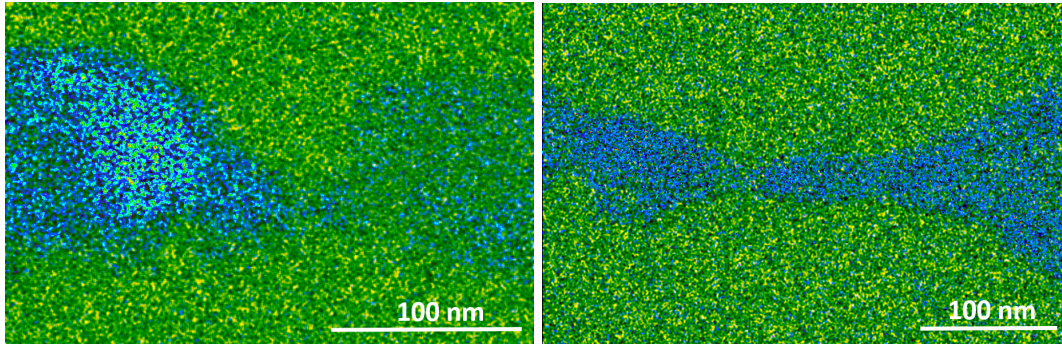


Figure 6.6: Spatial distribution of EDX intensities with Ag (blue) and Si (green) for two different types of structuring extremes described above. Left: EDX image after EM of a line structured sample which is shown in the right part of Figure 6.4. Strong asymmetric Ag distribution on both sides of line structuring with accumulation of Ag on the left side of the narrowest constriction and depletion on the right side very similar to the observation in the SEM image (right part of Figs. 6.4). Right: EDX image after EM of an ellipse structured sample shown in right part of Figure 6.5. Thinning of the narrowest grain boundary can be clearly identified by lower Ag counts similar to a reduced contrast at this particular location in the SEM image (right part of Figure 6.5).

6.4 Electrical measurements

Now in this section, conductance measurements of the ellipse-structured samples will be reported. The EM breaking was performed in a similar manner as discussed in Chapter 5 for the bow-tie structures. The same feedback controlled electro-migration (FCE) program was used which allowed to obtain step by step conductance plateaus on the way to conductance quantum (G_0). The conductance plateaus are described in details below.

6.4.1 Conductance traces of ellipse structures

Conductance traces recorded during EM breaking are a result of the thinning process that takes place electrically. Therefore, the plateaus obtained in the traces represent stable atomic configurations for a particular duration. A jump from one conductance plateau to the other indicates a release in the strain developed within the atomic arrangement corresponding to the previous plateau.

In Figure 6.7, a single conductance trace is depicted as a function of time. Looking to the conductance plateaus it can be observed that close to $3G_0$, $1.5G_0$, and $0.7G_0$, stable steps are visible. This is referred to as conductance quantization. These finite steps in conductance are characteristic for ballistic quantum transport of electrons through contacts that are only a few atoms wide [70, 249]. Exact integer multiples of the conductance quantum G_0 are expected only for a transmission probability, $T = 1$, but in most cases $T < 1$ is observed, since T depends, among several further parameters, on the local geometry of the contacts, and in this particular case, on scattering at the grain boundary.

From the measurements, (Figure 6.7) fluctuations are observed. These are not due to experimental imperfections, since the amplitude of these fluctuations changes abruptly from one plateau to the other within the same measurement. Here the fluctuation becomes typically

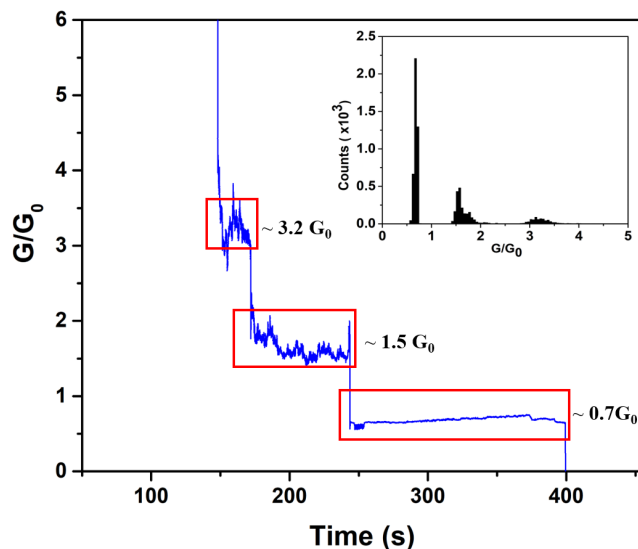


Figure 6.7: Conductance as a function of time during ramping the applied voltage at 4 mV/s at a single FIB-processed bow-tie structure shown in Figure 6.5. The voltage at the first plateau was about 1.1 V. The step-by-step thinning of the grain boundary during EM process is captured in the well defined plateaus. Inset: Conductance histogram derived from this measurement.

very small at the lowest conductance plateau close to $1 G_0$ ($0.7 G_0$). This means that this configuration is more stable than the plateaus with higher conductances. Since near $1 G_0$, only a single atom still makes the contact, there exists little flexibility in terms of atomic motion without breaking the contact. Therefore, the atom can at best vibrate, which has little effect on the local conductance. This property is also clearly observed in the peak-narrowing when plotting histograms (see inset of Figure 6.7). Hence it can be concluded that the fluctuations seen in Fig 6.7 are due to the fluctuating atomic rearrangements in the vicinity of the constriction.

Plateaus below G_0 have often been reported [189, 259, 260] and are also found here. These values do not necessarily mean that impurity particles bridge the atomic gap. However, in view of the relatively high reactivity of Ag and the necessary processing steps under ambient conditions, contributions of atomic impurities to conductance cannot be excluded as well. Along these lines, similar sub- G_0 values as obtained here were reported, e.g., for oxygen-induced atomic chains [188] and for Ag contacts with oxygen atoms either in series or in parallel to the metallic contact [189, 259]. Not only vacancies and oxygen impurities, but also impurities like carbon and nitrogen from the environment can play some role in conductance measurements [261]. Atoms like oxygen or sulphur form strong bonds with Ag and thus reduce the electron density close to the Fermi level, which makes small tunnelling gaps likely in presence of such an atom in the junction. Since the bond lengths are well defined, the appearing tunnelling resistances also have well defined values. Therefore, sub- G_0 conductance features can be attributed to either special metastable contact configurations of Ag or to the inclusion of single atoms like oxygen, carbon, or water introduced by the sample processing steps [262].

The precise values of conductance plateaus vary between different opening cycles, since they depend on the local contact geometry at the atomic scale [191]. Structures produced by EM can locally be far away from an equilibrium configuration [251]. Therefore, relaxation processes involve not only the contact itself, but also its immediate environment. These relaxations are most likely the main reason for quasi-continuous small changes in conductance, also seen in Figure 6.7. They may also be responsible for occasional jumps to higher conductance values.

6.4.2 Statistical analysis

Statistically analysing the conductance traces of several structures, allows the possibility to look for common features by constructing histograms. Peaks in such a histogram would represent the most preferred conductance values. These values represent stable atomic configurations. Such a histogram also filters out the metastable values occurring in a single conductance trace which may be characteristic of some local defects of that particular junction. The conductance plateaus show up as peaks in the probability distribution with some variance, since each trace is a characteristic of the local contact geometry of that junction.

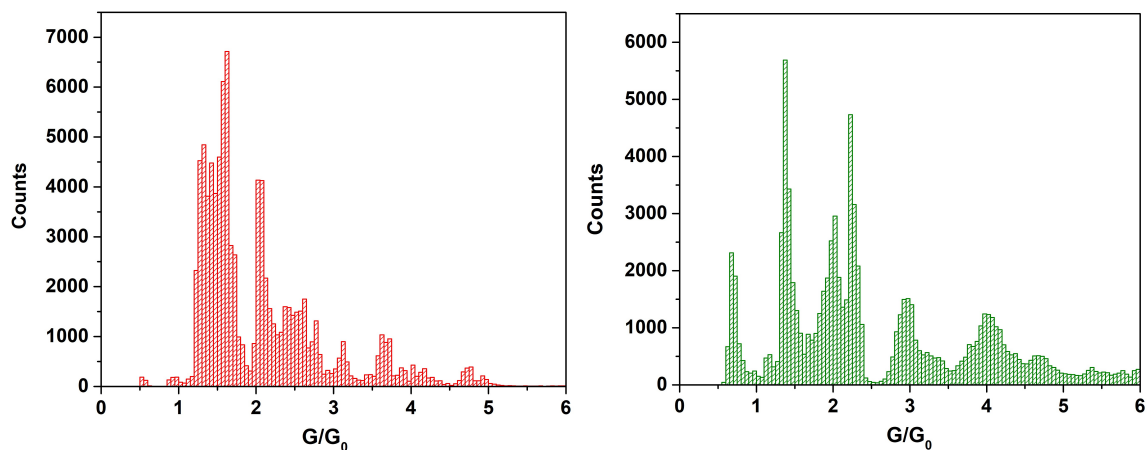


Figure 6.8: Two histograms constructed using two different sets of conductance trace data. Left: Red dashed histogram without conductance plateaus at $0.7 G_0$. Right: Green dashed histogram with conductance plateaus at $0.7 G_0$. The similarities as well as differences in the peak positions of both the histograms can be spotted.

After looking at the conductance traces of several structures, the conductance traces could be segregated into two sets of data. First set of data does not have a plateau at $0.7 G_0$, whereas the other set has a sub- G_0 plateau (at $0.7 G_0$) similar to the conductance trace shown in Figure 6.7. Figure 6.8 shows two separate histograms of conductance traces of these two data sets. There are significant differences between the two histograms. The right part of the Figure 6.8 showing a green dashed histogram contains a clear peak at $0.7 G_0$. This peak at $0.7 G_0$ is absent in the left histogram (red dashed) of the Figure 6.8. While the right histogram exhibits very clear peaks at 0.7 , 1.4 , 2.1 , 2.3 , 3 and $4 G_0$, only peaks at 1.4 , 2.1 and close to $3 G_0$ are common in the left histogram. Further peaks in the left histogram at 1.6 , 2.5 and $3.6 G_0$ are not present in the right series. From these results it seems that the contact

formation by EM follows different pathways with differing preferred shapes. Also kinetics may play a role as well. These preferred shapes may be influenced by impurity atoms (e.g right histogram), where the $0.7 G_0$ value also appears.

The complete histogram combining both the data sets (in Figure 6.8) is shown in Figure 6.9. These conductance traces were obtained during opening of 13 ellipse-structured contacts (see Figure 6.9) and several clear as well as sharp maxima particularly at values below $3 G_0$ can be identified.

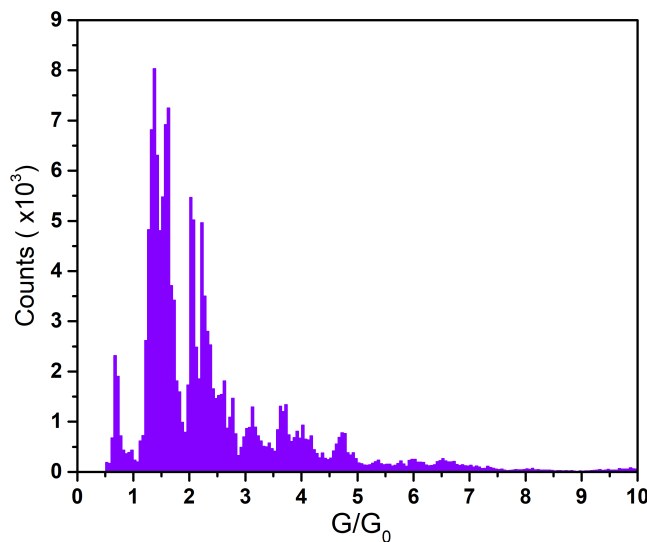


Figure 6.9: Histogram constructed with conductance traces of 13 samples with FIB structuring (ellipses) and with a bin size of $0.05 G_0$.

Discrete peaks (in units of G_0) are visible at 0.7, 1.4, 1.6, 2.1, 2.3, 2.6, 3.1 and 3.7. This series ended for almost all scans close to 1.3 (more than 90% of our experiments) before complete opening of the contact, while a minority showed a very well-defined conductance plateau at $0.7 G_0$. It was observed that certain values are coupled: the value at 0.7 appeared together with 1.3, 2.1 and 2.3 with high probability, whereas 1.6 and 2.6 were minimal under these conditions Figure 6.8. This finding shows that EM follows different pathways favouring local and metastable configurations, which can also be impurity-induced [251]. It could be further concluded from these results that relaxation processes involve not only the contact itself, but also its immediate environment.

Upon repeated cycles of warming up to room temperature (RT) and opening at 100 K, only the plateau close to $1.3 G_0$ remains observable in all cases, but the value at $0.7 G_0$ disappeared. Therefore, the former can be identified with the formation of a single atomic point contact, whereas the later seems indeed to be impurity-induced. There has been studies of Ag junction with and without atomic oxygen incorporation [263], which suggest Ag-O-Ag conductance value to be approximately $0.4 G_0$. Such existing studies, as well as the reason that $0.7 G_0$ value disappeared after repeated opening, demonstrates that this sub- G_0 value is impurity related. Here, it is interesting to compare the striking differences observed between the measurements of bow-tie structures (reported in Chapter 5) and FIB structured samples reported here. Sharp peaks at $0.6 G_0$ and $0.9 G_0$ were observed in case of bow-tie structures

with a rather broad peak at $1.4 G_0$. The peak at $0.9 G_0$ (in bow-tie structures) was never observed in ellipse structured samples. Secondly, a rather broad peak at $1.4 G_0$ (in bow-tie structures) suggests higher instability in the configuration whereas the $1.4 G_0$ peak here is relatively sharp and well defined. Therefore, conductance values close to $1.3-1.4 G_0$ can be assigned as a characteristic to single point contact, only observable in ellipse structured samples.

Finally it can be pointed out that non-integer values of conductance in units of G_0 are very common, in agreement with calculations [264]. The preferred crystallographic orientation of Ag on Si(100) at LT has been reported to be in (111) direction [211], but Ag (111) rarely forms linear atomic chains at LT [188, 197]. When a nano-wire breaks abruptly instead of atomic chain formation, the well-defined integer plateaus may not be observed [192, 197, 265]. Instead, abrupt jumps occur in non-integer values, as seen in most of the curves reported here. Non-integer values of conductance in units of G_0 for Ag contacts were also seen in ultra-high vacuum (UHV)-mechanically controllable break junctions (MCBJ) measurements [197]. Similarly dynamic high resolution transmission electron microscope (HRTEM) investigations showed that Ag (111) nano-wires are prone to abrupt rupture instead of forming atomic chains [192]. Xie et al. [185] calculated ideal Ag crystalline nano-junction geometries assuming two fcc clusters connected by an Ag-Ag bridge in (111) direction, and correlated them with the non-integer plateaus obtained in electrochemically formed Ag atomic contact. From Chapter 5, it can be noted that the frequencies obtained from the Fourier transform analysis of the conductance traces of the bow-tie Ag structures show prominent evidence that (100) and (111) grains are primarily participating in the thinning process. There was no peak suggesting the directional dependence of (110) grains in these structures. HRTEM investigations in Ag nanowires [192] also confirm this fact. Similarly, non-integer values of conductance were also observed in simulation studies by Pauly et al. [206] where stability of Ag (100) nanowire structures were presented.

The quantized values obtained in the present experiments of contact generation by EM have little overlap with those obtained with Ag electrodes in break junction experiments [266] and with electrochemically generated atomic Ag contacts [185]. Only values at 0.9 and $2.7 G_0$ were observable in MCBJ measurements [266]. This comparison with by EM indicates that impurities and/or metastable structures by EM probably play a more important role than usually assumed. These effects are not prominently captured in a MCBJ experiment.

For the single crystalline and for the well annealed structures investigated in ref. [185], only conductance values close to integer multiples of G_0 were observed, in agreement with simulation studies [185, 264], whereas deviations from integers were attributed to extended and local defects [192, 197, 265]. Contrary to the thinning of a (locally) single crystalline material, as, e.g., in an electrochemical cell, the junction created by EM is between two Ag grains with different crystallographic orientations. Although locally preferred directions of atomic motion [188, 197, 211] on individual grains may still exist, the junction will most likely not be formed by atoms that connect the two grains on regular crystal positions. Following the above argumentation, the formation of a junction at an extended defect explains the non-integer values of conductance observed here. On the other hand, there are clearly metastable configurations that are selected by the EM process with high preference, as seen in Figure 6.9.

6.5 Conclusion

In this chapter, FIB structuring was discussed as a very important pre-requisite for fabrication of metallic point contacts using EM, which was employed to reduce the centre constriction below the size of a single grain of the prepared Ag layers. Two different structuring shapes were experimented to find the best candidate suitable for EM in terms of material transfer and overall reliability. From EM observations under SEM, the ellipse structured samples turned out to be the most reliable and reproducible candidate for point contacts. Conductance measurements suggested that repeated opening and closing of contacts at 100 K was possible in these structures. Different metastable configurations of the electro-migrating contact was captured in the the form of peaks within the histogram. Two different EM pathways could be identified which indicates that, depending on the local atomic re-arrangement, the absolute conductance values differ, but in both cases, a peak at $1.3 G_0$ was obtained, which could be attributed to the formation of atomic point contacts.

Modification of atomic point contacts by CO adsorption

In this chapter, the functionality of the as-prepared Ag atomic point contacts have been tested by in-situ adsorption of CO molecule(s) on these junctions. Abrupt changes in conductance values were obtained after dosing the chamber with CO molecule(s) prior to which the junctions were electro-migrated to form atomic contacts. Conductance values dropped by an order of magnitude below the starting conductance value (conductance quantum G_0). This sudden drop of conductance provides the very first signature of CO-modified Ag atomic contacts. Specially customised time-resolved current measurements were performed to understand the dynamics of the molecular junction. Bi-stabilities in conductance states were observed with the ultra-fast time resolved set-up. On further investigation of these bi-stabilities at different voltages, it was observed that the switching between two conductance states were activated at specific voltages only. These findings indicate that, there were complex/metastable processes taking place even within the simplest molecular junctions and the possible mechanisms responsible for it have been proposed.

7.1 Introduction to molecular junction measurements

Single molecular junction measurements can provide important insights to the physical phenomena at the atomic and molecular scale. There has been studies of molecular junctions with simple molecules such as oxygen, hydrogen, water and CO etc. [26, 267–272] using mechanically controllable break junctions (MCBJ). Most molecular electronic measurements involve MCBJ due to the inherent mechanical stability that the set-up provides. All these methods suffer from an inherent limitation regarding the definition of geometry of the metallic electrodes. The real time morphology of the metallic electrodes cannot be controlled in any set-up till date, which makes us rely on statistical approaches. Every time a junction is broken in presence or absence of molecules, there is a possibility of re-arrangements of atoms within the electrodes as well as of the interface. Re-arrangements within the electrode and the differences in molecule electrode interface geometries are the main reasons of fluctuations between measurements. IV measurements involve measurements of current w.r.t changing voltages. From IV sweeps, one can obtain an indication of such fluctuations, but cannot directly define or quantify the fluctuations. Understanding the changes in contact geometry and systematic investigation of the dynamic evolution of the electrode-molecule geometry requires more sophisticated measurements. Such information can be obtained by measuring the fluctuations of the current at constant voltages. Measurements involving faster response times helps to identify the metastable changes. Temperature is another important parameter in such measurements. Thermal drifts due to differences in temperature between the tip and the sample can cause misinterpretation of data, whereas temperature dependent phenomena are affected due to such drifts. Keeping such ideas in mind, the best way to understand the functionality of atomic junctions is by analysing simple molecules. Here, one of the simplest asymmetric molecules, CO, has been used for such studies on Ag atomic point contacts.

7.2 Experimental details

7.2.1 Fabrication of Ag atomic contacts with defined geometry

To reproducibly fabricate atomic point contacts, electromigration (EM) of elliptically patterned focused ion beam (FIB) structures was performed at 100 K (discussed in Chapter 6). The starting width of these FIB structures were below 20 nm ensuring locally that one single grain boundary exists at this constriction [258]. When these structures were electro-migrated, step-wise conductance plateaus up to the conductance quantum were observed. The process could be well controlled and the conductance value of $1.3 G_0$ was consistently observed even after repeated opening and closing cycles, which was assigned to the atomic point contact configuration [258]. Figure 7.1, shows one such breaking trace obtained during the EM of these structures. The inset of Figure 7.1 shows the conductance histogram of this measurement. Several metastable configurations that occur during the process of EM can be identified from the peaks in the histogram. For adsorption measurements, the contacts were not completely opened but during several opening and closing cycles, conductance dropped to zero suggesting even the adhesion layer was broken in such cases.

From the inset, the peak width at $1.3 G_0$ is the narrowest demonstrating the fluctuation at this value is significantly reduced compared to the other peaks. Another important feature

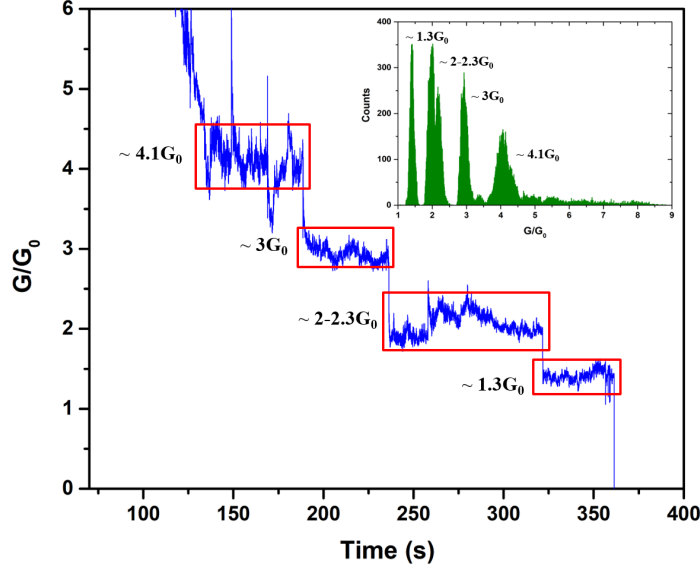


Figure 7.1: Breaking traces of a single Ag-Ag junction as obtained during EM. Inset: Conductance histogram corresponding to the different conductance values of this measurement.

that can be noticed in the histogram is the doublet peak at 2.1 and 2.3 G_0 showing that two distinct atomic configurations occur prior to the generation of atomic point contact. From the inset, it can be spotted that the fluctuations increase with increasing G/G_0 values as also seen in the conductance curve.

The non-integer values obtained in these experiments have close correlation to the theoretical simulation studies of conductance histograms published earlier [206]. In such simulation studies, two types of configurations were most likely responsible for the conductance values around $1 G_0$ for Ag [206]. The studies report that the exact conductance value depends on the situation whether a single-atom contact is more stable between two electrodes or a stable dimer configuration is formed prior to opening the contact. Pauly et al.[206] have shown both the situations (Figure 7.2) by simulations. A dimer configuration is referred to a geometry where both sides of the electrode have one Ag atom tip connected to each other by a single bond. The case of formation of an unstable dimer configuration ($<0.7 G_0$) is depicted in Figure 7.2(a). A single atomic contact bridging the two electrodes produces a conductance of $0.7 G_0$ (Figure 7.2(a)) in such a case. This single atomic contact is preceded by a double atomic configuration (conductance $1.7 G_0$). No stable conductance plateaus were observed from simulations in this particular case. On the other hand, stable plateaus of conductance were obtained in the EM measurements (Figure 7.1).

Therefore, the second case (Figure 7.2(b)) proposed by Pauly et al.[206] with stable conductance plateaus around $1 G_0$ depicts a scenario that is more closely related to the EM experiments reported here. In this case of formation of a stable dimer configuration (Figure 7.2(b)), the absolute values for each configuration are higher as compared to the unstable case (Figure 7.2(a)). Herein the conductance value for a dimer configuration corresponds to $0.7 G_0$ and a single atom contact corresponds to $1 G_0$ (similar to Au). In an analogous fashion, the conductance for a double atomic configuration was reported between 2-2.3 G_0 .

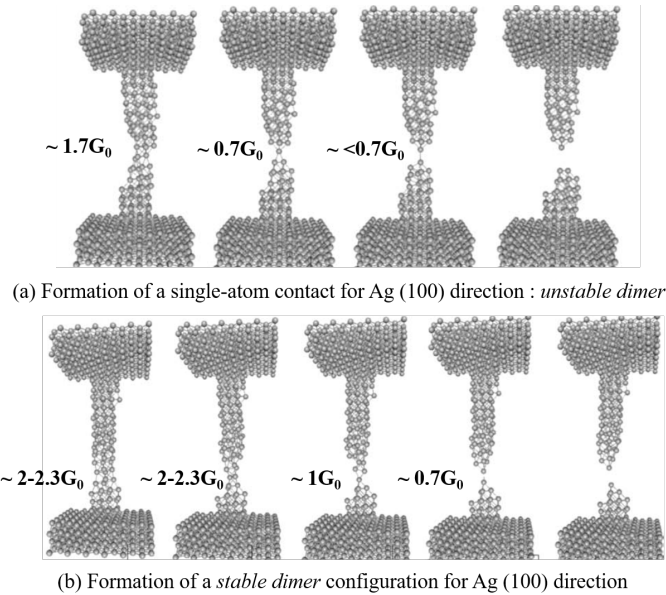


Figure 7.2: (a) Atomic configurations obtained from stretching simulations of Ag (100) with a single-atom contact formation. Here the dimer configuration having conductance $<0.7 G_0$ is not stable. (b) Atomic configurations obtained from stretching simulations of Ag (100) where a stable dimer configuration is obtained. Here the single-atom contact and dimer configurations are both stable. Geometries reproduced from [206].

For EM experiments reported here, stable plateaus at $2-2.3 G_0$ prior to the plateau at $1.3 G_0$ (Figure 7.1) have also been observed. Therefore, in view of the simulation studies it is likely that a single atomic contact (and not a dimer) is obtained in the present case. Nevertheless, as atomic contacts in this case is most likely produced at the grain boundaries, the deviation from the absolute values ($1 G_0$) reported in the simulations to non-integer values ($1.3 G_0$) is not unlikely (due to scattering at grain boundaries).

7.2.2 CO adsorption

Structures exhibiting conductance values between $1.1-1.3 G_0$ (atomic contacts) were used for further CO adsorption experiments. The contacts were not electro-migrated any further after this value was obtained. After atomic contacts were confirmed, the chamber was dosed with CO gas. The CO dosage experiments were performed at a background pressure of 2×10^{-9} mbar at 100 K. After approximately 200-300 s of opening the CO valve, while continuously monitoring the conductance of the structure in-situ, the conductance abruptly falls by one order of magnitude to values around $0.1 G_0$ (Figure 7.3). The impingement rate of CO (gas at 300 K) at this particular pressure can be estimated to be 5×10^{15} molecules per sq. metres per second. This rate corresponds to a CO concentration of 0.15 molecules per Ag atom area in 300 s on a flat surface. This estimated coverage needs to be multiplied by a factor 4 for a single atomic Ag point contact and by a factor 3 for a double atomic contact. As the present case is still on surfaces, factor 4 is un-realistic. Together with field focusing effects at the junction, the integrated probability that the Ag atomic contact is hit by one CO molecule

after 300 s is close to unity. The remaining structure is expected to have a sub mono-layer coverage of CO molecules with at least 4 times less concentration as the point contact after 300 s.

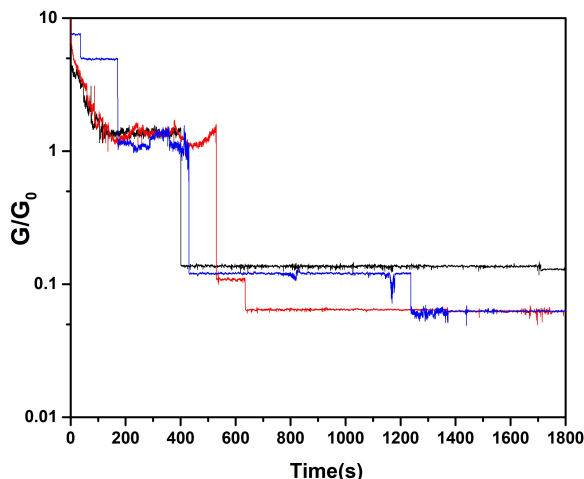


Figure 7.3: In situ conductance plateaus of metal-metal and metal molecule junction in logarithmic scale. The metal-molecule plateaus at approximately $0.1 G_0$ appears after CO adsorption. Conductance traces of 3 such structures are shown here in different colours.

To plot the metal metal vs metal molecule plateaus within one graph, the conductance is plotted on a logarithmic scale in Figure 7.3. It depicts the abrupt drop of conductance plateaus from $1.3 G_0$ to around $0.1 G_0$ for 3 different structures (marked in different colours). The fluctuations within the plateaus suggest a variation in the absolute conductance values between structures. This is attributed to the fact that the local atomic geometries differ from structure to structure while atomic junction formation as well as after adsorption. There is no direct correlation between the absolute conductance value obtained after CO adsorption and the conductance value of the atomic point contacts (before adsorption). It must be noted here that the contacts were not completely opened to form gaps before CO was adsorbed, meaning these sudden and highly reproducible drops in conductance values of point contacts (by a factor of 15) are due to the modification of local structure of the atomic point contacts after the adsorption process. Due to field enhancement effects within the electro-migrated junctions, the CO molecule(s) are most likely directed to the exact position of the atomic contact. This abrupt drop of conductance value was observed for more than 10 structures.

In the only reported study related to Ag-CO contacts (so far), Balogh et al. [264] tried an initial gap opening prior to inserting CO molecules. This is fundamentally and significantly different from the CO adsorption experiments on the Ag atomic contacts reported here (without opening a gap). In these experiments, a stable plateau between 1.1 - $1.3 G_0$ (attributed to an atomic point contact of Ag between grain boundaries) was obtained. This was the starting configuration on which CO was adsorbed which is remarkably different from the one reported by Balogh et al. [264]. They reported a Ag dimer configuration (conductance of $1 G_0$) as d1 (Figure 7.4) was obtained before an open contact (d2 in Figure 7.4). The conductance value of this dimer configuration (by [264]) is higher than the conductance value of the stable dimer ($0.7 G_0$) reported in simulation studies by Pauly et al.[206], again indicating that the

absolute conductance value depend on the local geometry (even in simulations).

For same inter-electrode distances, Balogh and group [264] (Figure 7.4) reported higher conductance values after CO adsorption as compared to the conductance of a bare Ag contact whereas lower conductance values were obtained after CO adsorption on point contacts in the present experiments (Figure 7.3). This leads us to conclude that the local geometries and the mechanism of contact formation have a direct impact on the conductance values obtained.

Having a closer look at the stable plateaus obtained after CO adsorption around $0.1 G_0$ (Figure 7.3) in the present experiments, blue and red curves especially show sequential jumps after the $0.1 G_0$ plateau. These further drops in conductance to lower conductance values might be due to a second CO molecule or configurational changes of one single molecule. Currently this is not clear and needs further clarification from simulations. From the conductance traces of Balogh and group [264] (Figure 7.4), conductance values of d1 (without CO) and b2 (with CO) are almost same - around $1 G_0$. This shows that there is no effect on conductance when one CO molecule is attached to a Ag-Ag dimer contact (b2) with similar inter-electrode distances. On the other hand, b1 and b2 geometries are quite similar (with slight inter-electrode difference), but even then a significant difference in the conductance values is observed (Figure 7.4) between the two.

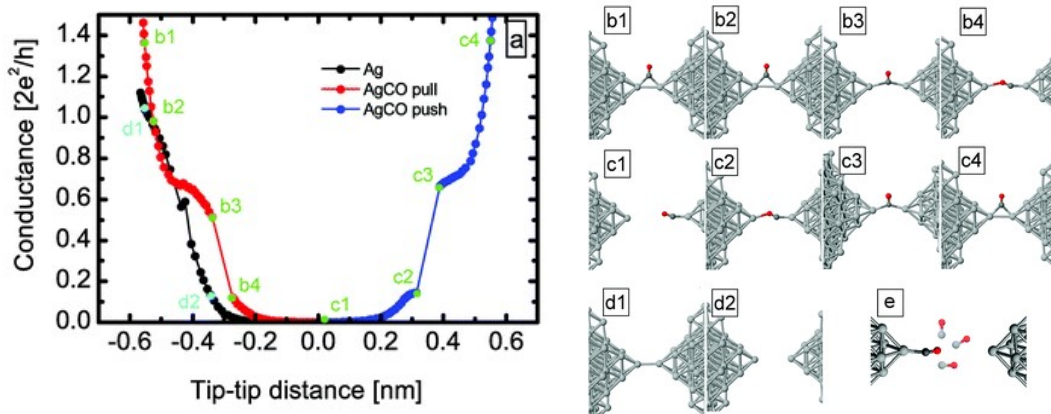


Figure 7.4: Reproduced from reference [264] (a) Simulated opening (red) and closing (blue) traces of a Ag-CO-Ag junction. (b) The cartoons depict the geometries corresponding to the different conductance values.

Another feature marking the difference between the experiments reported here and the one from Balogh et al. [264] is, no intermediate plateaus between $1.3 G_0$ and $0.1 G_0$ were observed here. The drastic drop in conductance by a factor of 15 was reproducible for more than 90 percent of the measured samples. This distinguishes the fact that this phenomenon is totally different from putting CO molecules in the open gap. On the contrary, from simulations of CO molecules inserted within the Ag gap (Figure 7.4(e)), pushing and pulling traces depict the conductance values of c2 and c3 geometries to be $0.1 G_0$ and $0.7 G_0$ and for b3, b4 geometries to be $0.7 G_0$ and $0.1 G_0$, respectively showing an intermediate value between $1 G_0$ and $0.1 G_0$ [264].

These configurations are unrealistic in the present case as the contact was not completely opened. Though the conductance value of $0.1 G_0$ matches quite well with these calculations,

it is very unlikely that configurations similar to b4 and c2 occur in these experiments. The reason lies on the fact that a Ag-CO bond cannot replace a Ag-Ag bond and the oxygen side of CO is a non-bonding side. Last but not the least, it is worth mentioning that, on reversing the direction of the current, the conductance value of the bare atomic contact remained unchanged. This suggests, it is less likely that the Ag atomic point contact is strained (after EM) prior to CO adsorption. In such a scenario, it also leaves minimal possibility that CO adsorption reduces the strain within the atomic contact. In order to better understand the dynamics of the junction, time resolved current measurements have been performed which is the topic of the next section.

7.2.3 Time resolved current measurements of Ag-CO junction: CO switch

To monitor the time evolution of the as-prepared molecular junctions, an in-house set-up was designed to perform the time resolved measurements of very small currents with a resolution of $5\mu\text{s}$. The working mechanism of this set-up is described in the Appendix. These time resolved measurements were performed to study the evolution of the current over time at fixed voltages. Measurements at constant voltages are carried out in order not to alter the distance between the electrodes, thereby keeping the junction conductance at $0.1 G_0$. Typical voltages needed for EM are 0.8 V, and these voltages are much below such values ensuring no migration occurs after a stable atomic point contact is generated. Fluctuations within the current helps to study the dynamics of such a molecular junction. Junctions with a stable conductance of $0.14 G_0$ at a 100 mV, exhibit unusual bi-stabilities between 0.1 V and 0.25 V.

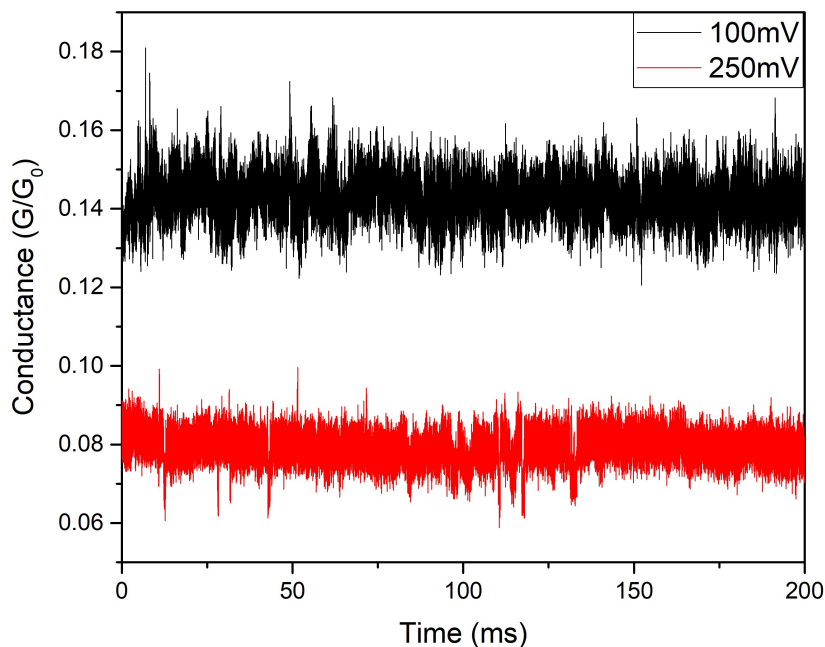


Figure 7.5: Average of conductance fluctuation measurements at 100 mV (black trace) and 250 mV (red). Each trace is an average of 10 measurements at the specified voltages.

Figure 7.5 shows the average of conductance fluctuation measurements at 0.1 V and 0.25 V.

In different measurements at 0.1V, the conductance fluctuates between $0.12 G_0$ and $0.16 G_0$ with an average value of $0.14 G_0$. On the other hand, at 0.25 V conductance fluctuations range between 0.07 and $0.09 G_0$, with a maximum probability at $0.08 G_0$. From Figure 7.5, it can be noticed that the relative fluctuations of both the conductance values are the same at two different voltages.

Measurements at intervals of 50 mV were performed between these two voltages. Figure 7.6 represents the conductance fluctuations obtained at 0.15 V. Here the conductance jumps essentially between two distinct levels $0.08 G_0$ and $0.14 G_0$. The main curve in Figure 7.6 shows a time span of 200 ms and the inset within the same figure portrays a time span of 20 ms. From the inset it is very clear that the higher conductance value is short lived as compared to the lower one. The maximum lifetime of the higher conductance state ($0.14 G_0$) is approximately 1 ms whereas maximum lifetime of the lower conductance state is approximately 4 ms. Similarly Figure 7.7 depicts the conductance fluctuations obtained at 0.2 V. This plot also shows a time span of 200 ms. Though all fluctuation measurements were performed for a much longer time span, a span of 200 ms is shown in order to observe the bi-stabilities. Figure 7.7 also depicts distinct bi-stabilities but with a lower frequency than the bi-stabilities at 0.15 V. The other difference between the fluctuations at 0.15 V and 0.2 V is that the higher conductance level is no longer at $0.14 G_0$ but around $0.11 G_0$. This shows that, as the voltage increases from 0.1 V to 0.25 V, the junction gradually moves towards a lower conductance value. Here, the maximum lifetime of the higher conductance state ($0.11 G_0$) is approximately 10 ms whereas maximum lifetime of the lower conductance state ($0.08 G_0$) is approximately 50 ms.

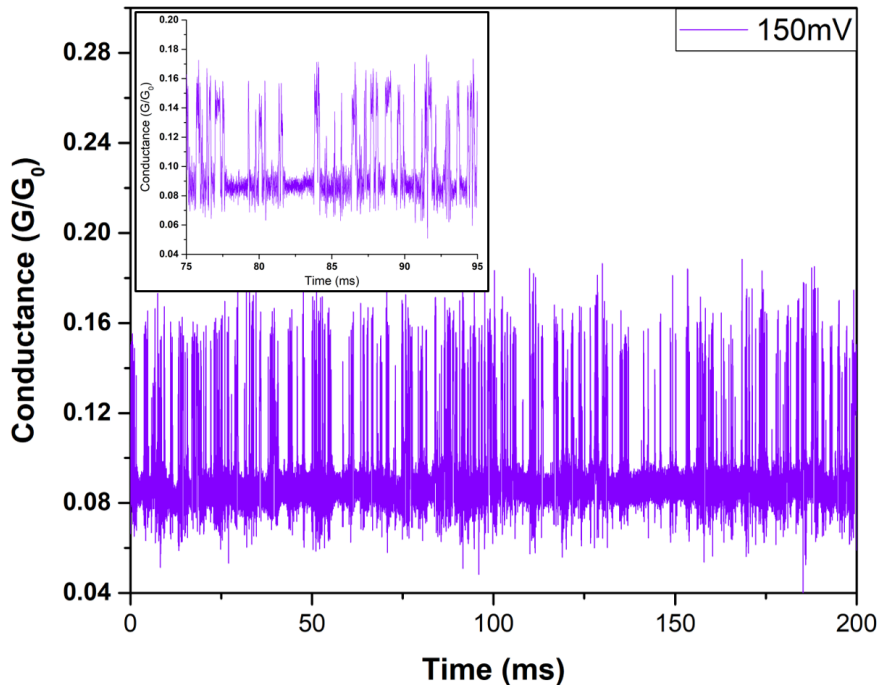


Figure 7.6: Conductance fluctuation measurements at 150 mV shown for a span of 200 ms. Inset is a zoomed in curve for a span of 20 ms in order to show the millisecond bi-stabilities of the junction at this voltage.

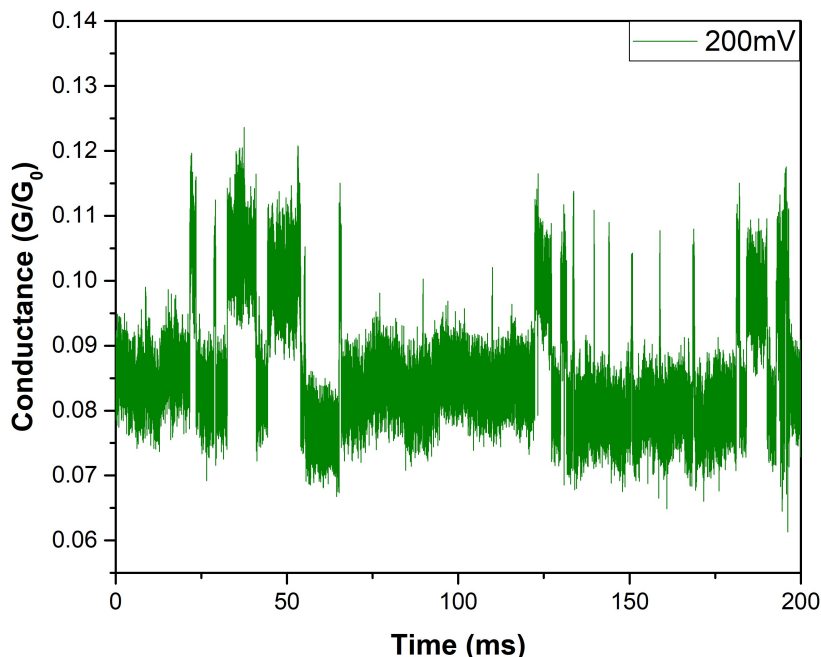


Figure 7.7: Conductance fluctuation measurements at 200 mV shown for a span of 200 ms. Two different conductance levels can be identified as $0.11 G_0$ and $0.08 G_0$.

The bi-stabilities in the conductance traces appear very clearly at intermediate voltages between 0.1V and 0.25V. The gradual transition of the higher conductance state at lower voltages to a lower conductance state at a higher voltages can be identified. When switching back from high voltages back to lower values, the conductance at $0.14 G_0$ is restored at 100 mV. This signifies that the presence of high fields introduces some metastable configurations which are released to the ground state in the absence of field.

Figure 7.8 shows conductance histograms of conductance values obtained at different voltages whose traces were shown before with same colour coding. The topmost figure shows the histogram at 100 mV (black), the second one at 150 mV (violet), the third one at 200 mV (green) and the bottom most at 250 mV (red). The two blue dashed lines represent the two conductance values $0.08 G_0$ and $0.14 G_0$. A slight shift from the exact values at different voltages can be noticed.

This drift in molecular junctions is not uncommon and has been observed by others as well [273, 274]. All molecular junctions are known to drift over time because of the re-arrangement of local atoms of the electrodes, molecules and charge distribution within the interface. The main message from this figure is the shift of higher conductance state ($0.14 G_0$) at low voltage (0.1 V) to a lower conductance state ($0.08 G_0$) at high voltage (0.25 V) and the intermediate switching levels in between. At 0.1 V, there is one peak at $0.14 G_0$. At 0.15 V, $0.14 G_0$ peak starts to decrease and the $0.09 G_0$ peak appears. At 0.2 V, these two levels slightly shift to the left having $0.11 G_0$ (high) and $0.08 G_0$ (low) states. Finally at 0.25 V the most stable value of conductance ($0.08 G_0$) appears. Only conductance values of $0.14 G_0$ at 100 mV could be switched to lower values at high fields.

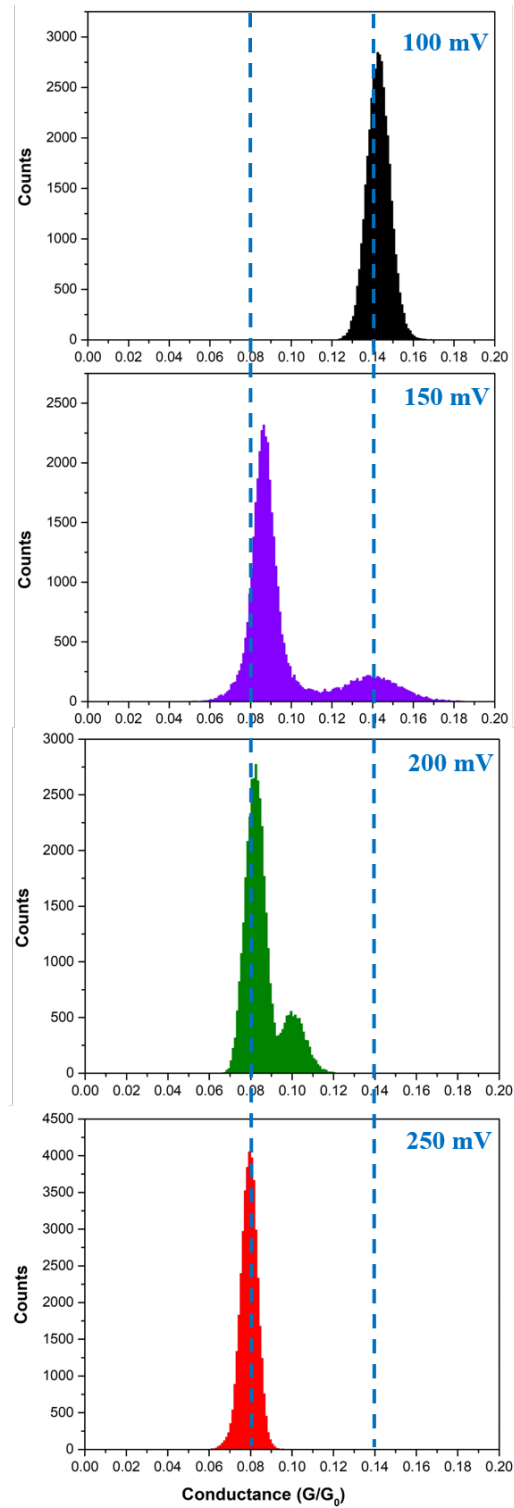


Figure 7.8: Conductance histograms at 100 mV (black), 150 mV (violet), 200 mV (green) and 250 mV (red). Two different conductance levels at $0.14 G_0$ and $0.08 G_0$ are marked by blue dashed lines.

7.3 Possible scenarios: CO switch

Conductance switching occurs when there is a change induced within the bonds between the molecule and the electrode. As voltage increases, there is a difference in charge transfer through the junction which can (i) induce switching between preferred bonding sites of Ag, (ii) change the number of molecules trapped close to the junction, (iii) change the local configuration of the molecule (bond angle etc.) modifying the electronic states participating in the transport.

7.3.1 Switching between adsorption sites

From the experience of experiments with larger Ag structure widths compared to the FIB structures it is pretty sure that only a single point contact is generated [258]. Field enhancement at this point contact would attract molecule(s) only near the single atom contact. The sudden drop of the conductance of atomic contact to values close to $0.1 G_0$ itself suggests that only this position is modified. On the other hand, the adsorption of CO on an on-top site of a Ag cluster is the most preferred site energetically as compared to bridge site [275]. From the DFT calculations of Zhou et al. [275], this result was found to be consistent irrespective of the charge state of the Ag cluster. This finding makes it unlikely that hopping between bonding sites or switching between Ag adsorption sites can take place due to field effects.

It has already been previously reported in case of thiol-terminated molecules, that variations in conductance can occur due to the blinking of the thiol bond [273]. Conductance switching was also postulated due to the change of bonding sites from top, bridge, hollow fcc, hollow hcp of Au with thiol groups [273]. Hopping of the molecule from one lattice position to the other can cause an increase or decrease of conductance depending on the stability of the new position and molecular orbital overlap. But in the present case, CO molecule changing its local position between different Ag sites does not seem likely because it is not possible to change adsorption sites by electric fields.

7.3.2 Local changes in bond angles thereby modifying electronic states

It is well known that CO chemisorbs on transition metal surfaces [276]. This metal carbonyl bonding has been extensively studied by chemists explaining the nature of the bond and its effect on CO stretching frequencies [276, 277]. CO always adsorbs in the on-top position [275, 276] on Ag flat surfaces as well as Ag clusters and it has been observed that the CO stretching frequency is often lowered after chemisorption. There are two contributions: metal to carbonyl π -back bonding and carbonyl to metal σ bonding. If electron transfer from the 5σ orbital of CO to the metal surface is the dominant effect, it results in an increase of bond strength between the metal and carbonyl thereby increasing the CO stretching frequency. Normally it has always been measured that CO vibration frequency gets reduced. This strongly proves that the back donation from the metallic d-orbital to the CO 2π anti-bonding orbital is an important effect. This effect leads to a bond weakening thereby lowering the frequency of CO stretching in the chemisorbed case as compared to free CO molecule.

In these experiments, a complete transition from one conductance state to the other takes place in presence of electric fields, with intermediate metastable configurations between them. To understand these meta-stable configurations, it is first useful to calculate the approxi-

mate energy available to observe a switching between the two states at 100 K. According to Boltzmann distribution, the occupation probability of one particular state is related to the temperature and energy of that state with an exponential dependence 7.3.1.

$$p \propto \exp\left(-\frac{\Delta E}{k_B T}\right) \quad (7.3.1)$$

At 100 K, the thermal energy ($k_B T$) is approximately 9 meV. Assuming less than one percent occupancy of the second state with respect to the first state, the energy available at this temperature is 5 times the thermal energy. Therefore, the estimates from Boltzmann probability distribution amounts to energy differences of 90 - 100 meV between low and high field states.

Now, looking for configurations that do not differ much in energies but can be switched by electric fields, it is important to first understand the different isomeric configurations that are possible as a result of bonding between Ag and CO and the most favourable configurations. This can be understood qualitatively by taking into account the two extreme cases: Ag surfaces and Ag clusters. Simulations on surfaces are not representative of atomic point contacts therefore comparison with such studies is not helpful. On the other hand, assuming isolated Ag clusters also exaggerates the effects and also do not serve as exact representatives of point contacts. Furthermore, due to the local point contact details, the binding energies may significantly differ from the energies of Ag clusters and flat surfaces. Nevertheless, as a point contact can be simulated as a cluster attached to a bulk surface, it is instructive to look at cluster simulations.

From the findings of cluster calculations [278], the CO molecule is not always aligned in a linear fashion with respect to the Ag-C bond. From the frontier orbital analysis, CO bonding with the cluster can be either bent or linear with respect to the Ag-C bond [278, 279]. An example of both the configurations is shown in Figure 7.9.

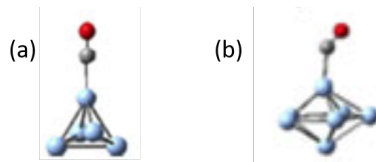


Figure 7.9: Geometries reproduced from [279]. (a) linear CO configuration to a 7 atom Ag cluster (b) bent CO attached to 7 atom Ag cluster. The cluster symmetry also changes significantly in this particular example.

On the other hand, a point contact can be visualised as a combination of two clusters tips pointed towards each other. This introduces a restriction to the adsorption sites available for CO as compared to isolated clusters shown in Figure 7.9.

The absolute binding energy of CO (per molecule) to a 4 atom Ag cluster is 0.829 eV [278]. For 5-7 atom cluster it is between 1-1.3 eV. Assuming a point contact as combination of two cluster tips, the absolute binding energies for point contacts must be lower than this value. Moreover, CO possesses an intrinsic dipole moment of its own that gets modified after the bonding. The estimated energy available for a free CO molecule attached to an isolated Ag atom at fields of 10^9 V/m is approximately 2-3 meV assuming the intrinsic dipole moment of CO (modified dipole moment not known). Also from the cluster calculations, only bond

angle changes exhibit binding energy differences of 2-3 meV, which is two orders of magnitude lower than the calculated value. This shows that apart from bond angle changes, the cluster geometry also needs to be taken into account.

Calculations of binding energy differences between cluster isomers are of the order of 20-30 meV [279] (still one order of magnitude lower than the calculated value of 100 meV). Therefore, this effect alone is also not sufficient. For 5 atom and 6 atom Ag clusters, binding energy difference to bring about symmetry changes and 20-30° changes in Ag-C-O angle is between 0.3 eV - 0.5 eV [279]. Thus the combined effect of bond angle changes and changes in cluster symmetry can exhibit binding energy differences of the same order of magnitude as calculated above. The values of 0.3 eV - 0.5 eV are reported for isolated clusters, hence binding energy differences of 100 meV for point contacts serves as a reasonable estimate. This can already introduce changes in CO bonding angles (between two configurations) with respect to Ag point contact geometry. Such a change in bond angle of CO is depicted in the illustration (Figure 7.10).

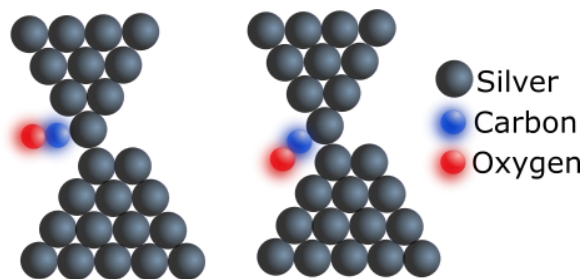


Figure 7.10: Model illustration of change in bond angles when present within an asymmetric contact. Many other possibilities may exist too.

Summarising the information obtained from cluster calculations, the two most important conclusions are: bond angle changes and variation in symmetry of the junction can introduce differences in binding energies. Extrapolation and simulation of such effects in the case of point contacts can provide information on the local geometries responsible for observance of switching. In the present case, as the junction is formed at the grain boundaries, the local atomic point contact configuration is most likely asymmetric. The local isomeric configuration whether bent CO or linear CO is preferred is also dependent on the geometry of the point contact here. The energy gain in presence of fields by the Ag-CO molecular entity as a whole (modified dipole moment and modified contact geometry) might be enough to tilt/bend the molecule by few degrees so that the orbital overlap between highest occupied molecular orbital (HOMO) of the Ag electrode and lowest unoccupied molecular orbital (LUMO) of CO molecule is increased. Increasing the field in steps introduces a bi-stability at intermediate voltages and finally when the molecule is already at an angle which reduces the asymmetry of the bare Ag contact, due to steric effects, the total conductance of the system goes to a minimum. This also explains why the conductance jumps back to high values in the absence of field. Adsorption at the point contact modifies the electron density of the local point contact and electric fields modify the local occupation of the HOMO. Both these effects together produces a change in conductance.

7.3.3 Number of molecules

In the present experiments, a second stable plateau below $0.1 G_0$ has already been observed. This is a clue that there might be this extra plateau due to an additional molecule. Moreover, the decrease in the absolute value of conductance with the increase in applied bias, depicts a modified configuration is established at the electrode molecule interface. Even though after the first jump only a sub-monolayer coverage of CO molecules is expected on the complete structure, but due the field focusing effects the integrated probability of finding one CO molecule close to the point contact can be close to unity.

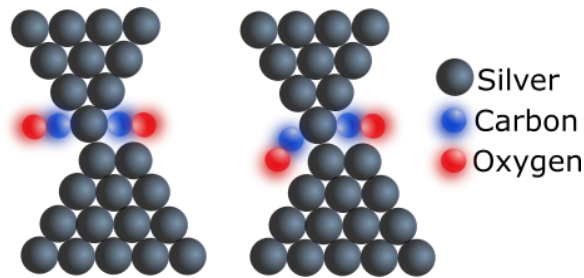


Figure 7.11: Model illustration of the relative orientation between two molecules when present within an asymmetric contact. Many other possibilities may exist too.

Assuming an atomic contact with a slight asymmetry between two sides of the electrode (contact at grain boundary), it can be possible that two CO molecules are attached at the narrowest neck in such a way that due to increasing voltages, the relative orientation of the two molecules can change. This offers a possibility to switch between two conductance states. An illustration (Figure 7.11) is shown to visualise the understanding. The external field can change the orbital overlap between the metal and the molecule(s) and provide extra energy to align it in a different configuration with respect to the electrode. Two molecules offer some symmetry to the contact which can explain why conductance values are restored to original values when lowering voltage to 100 mV.

Some groups reported that changes in conductance can occur due to additional trapping and de-trapping of molecules [37, 273]. Dulic et al. [273] suggested junction getting surrounded by additional molecules can take place due to field effects. They observed that conductance increased over time from $0.1 G_0$ to $0.2 G_0$ which did not return to the initial lower value. They assigned this irreversible change of conductance to the formation of multiple molecular junction (with molecules in parallel between electrodes). As in case of the present experiments, conductance can be reversed to the original values in the absence of field, therefore the presence of multiple molecules (more than two) is not very likely here.

7.4 Conclusion

The functionality of the Ag atomic contacts by adsorbing CO molecule in-situ and monitoring the conductance was tested here. A sudden drop of conductance values from $1.3 G_0$ to $0.1 G_0$ was observed which was the first proof of CO adsorbed atomic contacts being formed. Secondly, it was also observed from voltage dependent measurements, that conductance switches between two preferred values with higher conductance values at lower voltages and vice versa.

This was observed using time-resolved measurements of current at various constant voltages. The mechanism responsible for this bi-stability in conductance is not completely understood but the possible scenarios are listed. The probable mechanism that seems to be the most likely one is the local change in bond angles of CO with respect to Ag-C bond in order to maximise the local orbital overlap between HOMO of the Ag electrode and LUMO of CO molecule. Exact specifics needs to be clarified with simulations.

Summary and Outlook

8.1 Summary

With the help of a 4-tip-SEM/STM UHV set-up, a significantly different approach was used to conduct electromigration (EM) experiments on planar Ag nano-structures on Si. The tips served as robust electrical contacts which did not require additional wiring or chip carrier to connect individual nano-structures. In-situ imaging and electrical characterization was employed that facilitated easy navigation and probing of various structures.

Using Ag nano-structures on Si(100), as the model system, the role of geometry of the structure and temperature effects on EM process was systematically studied. In these systematic investigations, the main complications of using EM technique for fabrication of point contacts was understood. Often, EM led to a complex structure formation in bow-tie shaped structures where the central width was larger than the grain size of a single grain. This complication was overcome by producing structures with widths below the size of a single grain using the combination of e-beam lithography (EBL) and focused ion-beam (FIB) milling. This proved to be essential in order to ensure reliable Ag atomic point contacts by EM. In this thesis it was possible to reproducibly create atomic point contacts within Ag nano-structures using the process of EM. Using a robust statistical analysis based on conductance histograms, the different metastable pathways that occurred during the thinning process, before a stable atomic contact was generated, could be identified.

Interestingly, by chemisorption of CO molecules, the atomic contact conductance of Ag could be reduced by a factor of 15 and it was observed that this phenomenon was highly reproducible. Furthermore, voltage dependent measurements demonstrated that the conductance of CO adsorbed Ag contacts ($0.1 G_0$), could be switched between two different conductance states at specific voltage values. This serves as a basic platform for new switching/memory devices using simple molecules. These experimental findings show that a deeper insight into the dynamics of the junctions is crucial towards understanding the conductance values of molecular junctions.

8.2 Outlook

Based on the understanding of the behaviour of simplest junctions, future development of functionalities such as diodes, switches can be accessed by alteration of functional groups or electrode material. For example, this switching behaviour of CO molecules adsorbed on Ag contacts can be tested for different metals such as Au, Cu etc. for a better interpretation of

the underlying mechanism. Similarly, along with experimental trials, simulation studies also need to be performed by considering atomic geometries that best represent atomic contacts by EM at grain boundaries. These simulation results would shed light on the differences in the atomic structures produced by mechanical pulling as compared to the geometries produced by EM forces.

Another step forward with this technique developed within the 4-tip SEM/STM is that it offers several new dimensions to molecular electronic studies. Firstly, the additional tips can serve as molecule carriers which could be pre-functionalised with molecules and directed towards the junction using the SEM imaging. This would ensure a single molecule at the junction. Secondly, the additional tips could also be used for gating purposes. Direct imaging of atomic junctions using the in-situ STM is challenging, but this set-up possesses the capability of acquiring other important information from the molecular junctions, such as:

(a) Tip enhanced Raman spectroscopy (TERS) using an additional tip would provide optical information (b) Local Atomic Force Microscopy (AFM) of the junctions using an AFM tip would provide mechanical information (c) A tip made out of a thermocouple material (SThM) can be used to measure the thermal properties of the junction (d) Using tip made out of magnetic material can also be used to probe spin properties of the system.

Though all the above points are not simple and straight forward to implement, nevertheless this present set-up is capable to incorporate these ideas which are not possible in a normal break junction or scanning probe set-up. STM-MCBJ's exist and MCBJ-SERS/TERS also exists, but the entire process of MCBJ could be replaced by just controlling EM using two tips and the remaining two tips can be used for further imaging and characterisation purposes.

Part I

Appendix

Experimental Techniques

A.1 Electron Microscopy

An electron microscope is required to image objects on the nano-scale. Electron microscopes produce an image of the sample with the help of a beam of electrons. Due to the quantum mechanical nature of electrons, they exhibit a wave like behaviour. The wavelength of the electron (λ_e) accelerated with kinetic energy (E_{Kin}) is given by,

$$\lambda = \frac{hc}{\sqrt{2E_{Kin}m_0c^2}} \quad (\text{A.1.1})$$

where h is the Planck's constant and c is the velocity of light. For an electron with $E_{Kin} = 1 \text{ eV}$ and rest mass (m_0) 0.511 MeV , $hc = 1239.4 \text{ eVnm}$, the wavelength is around 1.23 nm . If the electron is excited by voltage of approximately 15 kV , which is the normal acceleration voltage used in case of a SEM imaging, the wavelength is around 10 pm . Therefore, the electron wavelength is not a limitation in case of an electron microscope.

When an electron beam of few kV, interacts with the surface of the sample, different processes occur that can be used for imaging purposes. Depending on the detector electronics, various types of information can be detected. The schematic shows the different types of interactions that take place when an electron beam hits the sample surface (Figure A.1). Most common interactions used for imaging purposes are secondary electrons and back-scattered electrons. Secondary electrons contain information only upto several nano-meters below the sample surface. As they have few eV energies, it is a very surface sensitive imaging technique. On the other hand, energies of back-scattered electrons can range upto few kV, thereby containing information from much longer depths (around few μm). Back-scattering electrons provide a strong material dependent contrast. Furthermore, deep down, detection of x-rays by energy dispersive x-ray (EDX) technique provides complete identification of material composition.

A.1.1 Scanning electron Microscope (SEM)

The SEM uses the above interactions discussed to create an image of the sample under investigation. The type of image acquired depends on the type of detector used to produce the image. Several detectors, in-lens, secondary electron as well as back-scattered electron detectors are available. The complete setup involves an electron-source, a combination of magnetic lenses in order to focus the electron beam, scanning coils to scan the beam over the

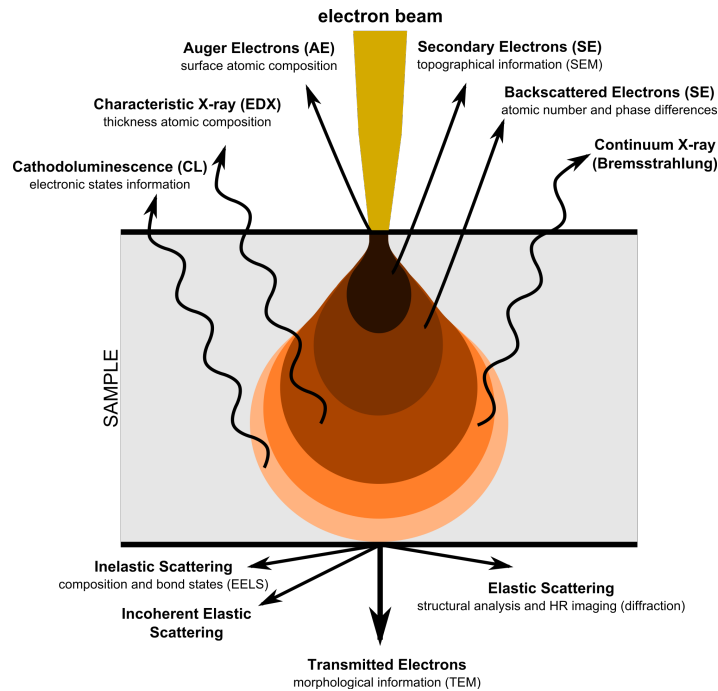


Figure A.1: Schematic showing the different processes that occur when an electron beam interacts with a sample surface.¹

sample and the detectors already mentioned. The position of the sample stage is controlled by laser interferometers. The resolution of the image depends on various factors such as the spot size, working distance between the sample and the electron beam. Electron beam within an SEM can not only perform imaging but the beam at high acceleration voltages can also be used for writing purposes (e-beam writing).

Components of SEM

Figure A.2 shows an illustration depicting the different parts of the SEM. It starts with an electron gun which is the source of electrons. This is followed by the anode that accelerates the electrons coming from the electron gun upto a several keV of energy. The beam of electrons then enters the electro-magnetic lenses which focuses the beam and prevents from scattering. The focused beam is then directed towards the scanning coils, responsible for scanning the beam over the sample area. The different types of detectors are located in order to process the different types of signals. The signals are amplified and finally the image development software processes the signals and creates a 2D image on the monitor.

Effect of acceleration voltage on image quality

A particular specimen imaged at an higher acceleration voltage produces a reduced resolution of surface intricacies as compared to the same specimen imaged at a lower acceleration voltage. This is because the high energy beam causes a stronger charging effect on the sample thereby

¹Source:https://en.wikipedia.org/wiki/Electron_microscope

leading to beam damage of the sample surface. On the other hand, a lower acceleration voltage has a reduced beam damage causing less charging effects. This leads to a better resolved image quality.

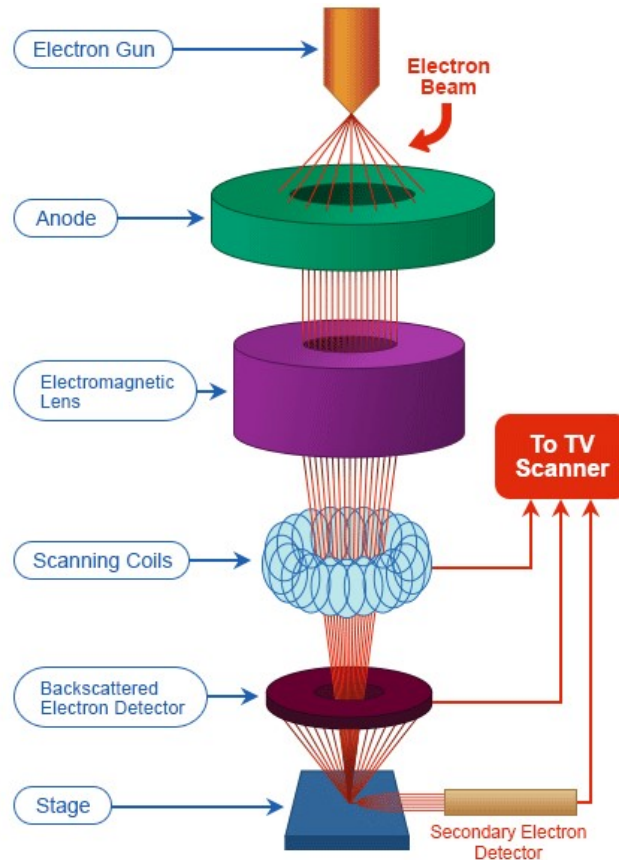


Figure A.2: Schematic showing the components of SEM column. The positions of the electron gun, magnetic lenses, scanning coils and the detector can be identified from the illustration.

²

Effect of secondary electron detector type on image quality

The Figure A.3 shows the image of the same structure captured using two different types of secondary electron detectors. In Figure A.3(a), the image is captured by a standard secondary electron detector depicting less sharpness in the image as compared to Figure A.3(b) showing an image captured by an in-lens secondary electron detector. The difference in the image quality appears due to the position of the secondary electron detector. An in-lens secondary electron detector is placed in the objective lens. Therefore, images acquired by this detector produces better resolution (short working distances).

The in-lens detector is able to capture sharp details (like grain boundaries here), which

²Source: <https://www.nanoimages.com/sem-technology-overview/>

was very essential in this case. It enabled local characterisation of the grain structure within the narrowest constriction.

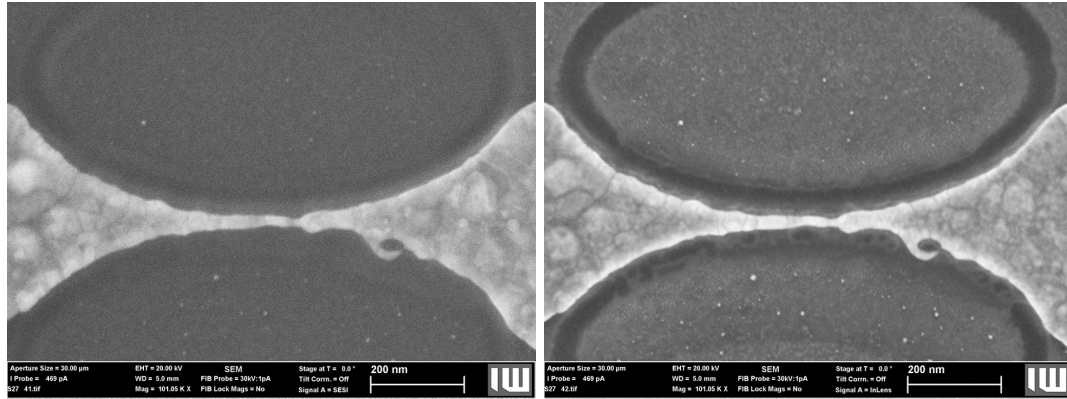


Figure A.3: (a) Image captured using a standard secondary electron detector (less sharpness) (b) Image captured using an in-lens secondary electron detector (the distinct grain boundaries can be very clearly observed).

A.1.2 Energy dispersive x-ray (EDX)

The EDX analysis as shortly discussed within the electron interaction with the sample surface, is an analysis technique to identify the chemical composition of the sample. The EDX detector characterises the energies obtained from the sample and identifies the elements present within the sample depending on the energies.

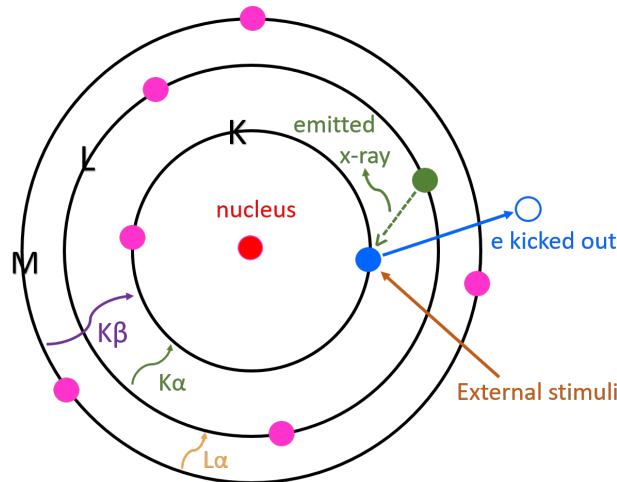


Figure A.4: Working principle of energy dispersive x-ray spectroscopy.

To obtain the EDX spectrum, an electron beam is focused on the sample. This stimulates the emission of energies characteristic to the specific atom. When an electron is excited by the incident electron beam, a hole is created at that position. A higher energy electron then

jumps to the lower energy hole to fill the position. The energy levels being discrete, this energy difference is emitted in the form of an x-ray emission which can be the characteristic of that particular element. A schematic shows the different x-ray emission characteristic to the shells (Figure A.4). During the emission of a characteristic x-ray, often this energy is transferred to another electron which takes up this energy and moves to higher energy shell. This electron is known as an Auger electron, and the whole created by this Auger electron can be occupied by another higher energy electron. This leads to emission of radiation as well that can be characterised by Auger electron spectroscopy.

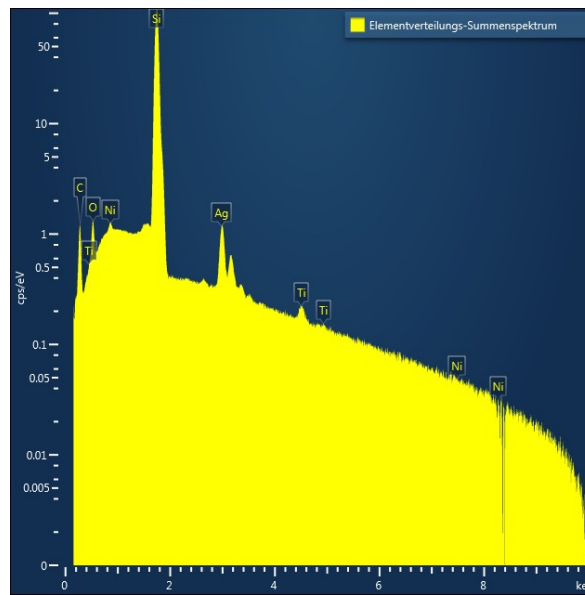


Figure A.5: Typical EDX spectrum of an e-beam fabricated Ag nano-structure on Si. The prominent signals within the spectrum shows contributions mostly from Si, and Ag. Traces of Ti, O and C was present in minorities, but was below the detection limit.

Figure A.5 shows a typical EDX scan of a Ag nano-structure on Si. The most dominant peak of Si provides signal from the substrate. The next dominant peak of Ag gives the contribution from the structure. Other elemental traces can also be spotted.

A.2 Finite element analysis

Here in this section a brief description of the theoretical simulation tool, ANSYS (type of finite element method (FEM) analysis) is discussed. This tool was used by Tianlin Bai from the group of Kirsten Weide Zaage for simulation of our nano-structures.

FEM is a widely accepted numerical method to solve boundary value problems using partial differential equations. FEM has high efficiency to calculate the partial differential equations. The main idea behind this method is subdividing a large complex model into simple regular elements. Here finite element program ANSYS has been used to create the nano-wire model and perform the model calculations [243].

A.2.1 Finite element method (FEM)

(1) Model idealisation: For FEM, the approximate model should be set up in first step. The geometry of model to be solved should be simplified to reduce the complexity of the model. On condition that calculation results are not affected, some non-ideal parts of the model can be ignored. The size of the model should be limited in an acceptable range.

(2) Meshing: Meshing process is an important procedure for finite element method. It has a strong effect on the calculation accuracy. Before the whole model is subdivided, the type of element should be first determined. Tetrahedron and hexahedron are often used as element in 3-dimensional parametric model. The element should be selected according to different electrical, thermal, mechanical properties of model. To reduce the calculation time and improve the calculation accuracy, the density of element varies with location. At the critical position, as far as possible, the mesh net should be homogeneous and fine as far as possible. At the non-critical position, the mesh net has less limited effect on the simulation.

(3) Function determination: The alternative function of every small element is determined depending on the material properties and the problem to deal with equation that has to be solved. Interpolation is utilized for numerical analysis.

(4) Establishing a system of equations: The functions of all small elements are linked together to build the system of simple functions with the limit of boundary value.

(5) Solution: In the end, the system of functions is calculated. All results are summarized and analysed with the help of finite element analysis software.

A.2.2 ANSYS

ANSYS Academic Research is published by American Computer-aided engineering software developer ANSYS, Inc. It is a finite element analysis, solver and simulation software. The principle of ANSYS is based on finite element analysis. The simulation flow can be briefly divided into 3 parts, shown as follows [243]:

(1) Preprocessing: In this step, the model to be simulated is set up in the first place. The dimension and geometry of the model should stay the same with original experimental parameters as far as possible. For small and simple model, meshing process can be done manually. For large and complex model, ANSYS provides free meshing function, which can mesh the model automatically according to default setting or user's setting. At last, boundary values are applied on the model and material properties need be assigned.

(2) Solution: In this step, a solver is selected for the simulation. There have been various solvers provided by ANSYS. Direct methods and iterative methods are utilized to solve system of function. Preconditioned Conjugate Gradient (PCG) and Incomplete Cholesky Conjugate Gradient (ICCG) solvers are most widely used iterative solvers, which cover 95% of all ANSYS applications. ICCG solver is typically used for asymmetric thermal analyses and electromagnetic analyses, which is also used for this work.

(3) General Postprocessing: Via postprocessing, the simulation results can be reviewed in many ways. Contour plot and vector plot are the most simple and intuitive method to show the distribution of temperature, current density, mass flux, etc. The simulation results can be displayed in several formats for the further application purposes.

A.2.3 Equations used in the simulation

The different differential equations used to solve the physical parameters such as temperature, flux, etc. are described [280].

Maxwell's equations are used to calculate the thermal electrical behaviour in the metallisation structure.

$$\vec{j} = \sigma \vec{E} \quad (\text{A.2.1})$$

where \vec{j} is the local current density, σ the electrical conductivity and \vec{E} the electric field.

$$\vec{E} = -\vec{\nabla}V \quad (\text{A.2.2})$$

where V is the electric potential.

Therefore it follows from eqs. A.2.1 and A.2.2

$$\vec{j} = -\sigma \vec{\nabla}V \quad (\text{A.2.3})$$

Similarly, the dissipated power density, p , is given by

$$p = \vec{j} \cdot \vec{E} \quad (\text{A.2.4})$$

From Equation A.2.1, A.2.4,

$$p = \sigma E^2 \quad (\text{A.2.5})$$

Similarly, the heat flow density \vec{h} is given by,

$$\vec{h} = -\kappa \vec{\nabla}T \quad (\text{A.2.6})$$

where κ is the thermal conductivity and T is the temperature.

the dissipated power density p , and heat flow density \vec{h} are related by

$$\text{div } \vec{h} = p \quad (\text{A.2.7})$$

Therefore from eqs. A.2.4 and A.2.7

$$\text{div } \vec{h} = \vec{j} \cdot \vec{E} \quad (\text{A.2.8})$$

As it is known,

$$\text{div } \vec{h} = \kappa \text{div}(\vec{\nabla}T) + \vec{\nabla}T \cdot \vec{\nabla}\kappa \quad (\text{A.2.9})$$

Therefore from eqs. A.2.2, A.2.3, A.2.8, and A.2.9, we get

$$\kappa \text{div}(\vec{\nabla}T) + \vec{\nabla}T \cdot \vec{\nabla}\kappa = \sigma [\vec{\nabla}V]^2 \quad (\text{A.2.10})$$

Eq. A.2.10 shows the relation between the heat flow density \vec{h} , and the electric potential V .

Electromigration

The electromigration (EM) mass flux \vec{J}_{EM} is given by:

$$\vec{J}_{EM} = \frac{N}{k_B T} e Z^* (\vec{j} - \vec{j}_{th}) \rho D_0 \exp\left(-\frac{E_A}{k_B T}\right) \quad (\text{A.2.11})$$

In eq. A.2.11, N is the atomic density, k_B the Boltzmann constant. eZ^* is the effective charge of an ion, \vec{j}_{th} the threshold current density, ρ the specific resistance, D_0 the diffusion co-efficient and E_A the activation energy.

To locate positions of voids and hillocks, the mass flux divergence was calculated. The value of mass flux divergence represents the difference between the net flow of metal into a region and the flow of metal out of a region. If the amount of flux leaving a certain point is more than the amount of flux entering a point, a void is generated. The mass flux divergence due to EM, $div \vec{J}_{EM}$, can be written as,

$$div \vec{J}_{EM} = \left(\frac{E_A}{k_B T^2} + \frac{\alpha_\rho}{1 + \alpha_\rho(T - T_0)} - \frac{1}{T} \right) \vec{J}_{EM} \cdot \vec{\nabla} T \quad (\text{A.2.12})$$

In eq. A.2.12 α_ρ is the thermal expansion coefficient.

Thermal migration

Thermal migration is the transport of material inside a structure caused by the temperature gradient. Due to the influence of geometry and material properties, the distribution of current density is not necessarily homogeneous within a metallic structure. Ohmic heating caused by current flow results in a temperature gradient at different regions which leads to the migration of material.

The mass flux due to thermal migration (TM) \vec{J}_{TM} is given by

$$\vec{J}_{TM} = -\frac{NQ}{k_B T^2} D_0 \exp\left(-\frac{E_A}{k_B T}\right) \vec{\nabla} T \quad (\text{A.2.13})$$

In eq. A.2.13, Q is the heat capacity per atom.

Similarly for TM, the mass flux divergence, $div \vec{J}_{TM}$, is given by

$$div \vec{J}_{TM} = \vec{\nabla} T \cdot \vec{\nabla} \left[\frac{A}{T^2} \exp\left(-\frac{E_A}{k_B T}\right) \right] + \frac{A}{T^2} \exp\left(-\frac{E_A}{k_B T}\right) div \vec{\nabla} T \quad (\text{A.2.14})$$

$$A = \frac{D_0 Q N}{k_B} \quad (\text{A.2.15})$$

The above mentioned equations are already defined within the program for calculation of parameters such as temperature, current density, flux etc. The program calculates once the material parameters, boundary values and geometry is specified by the user.

A.3 Fast current measurement (FCM) setup

This setup was integrated into the EM set-up in order to extract time resolved information from the current fluctuations (for very small currents) faster than LabVIEW response time-scales. This particular circuit was designed such that currents ranging from 8 mA to below

1 nA could be measured with a time resolution of $5 \mu\text{s}$. For this purpose, the main element of this circuit is a trans-impedance amplifier, OPA111 (available as NImyDAQ) which converts the input current to voltage with a sampling rate of 200kS/s. With the help of NImyDAQ, interfacing with the computer is easily possible by using NI LabVIEW programs. The current range can be selected depending on which feedback resistance is activated.

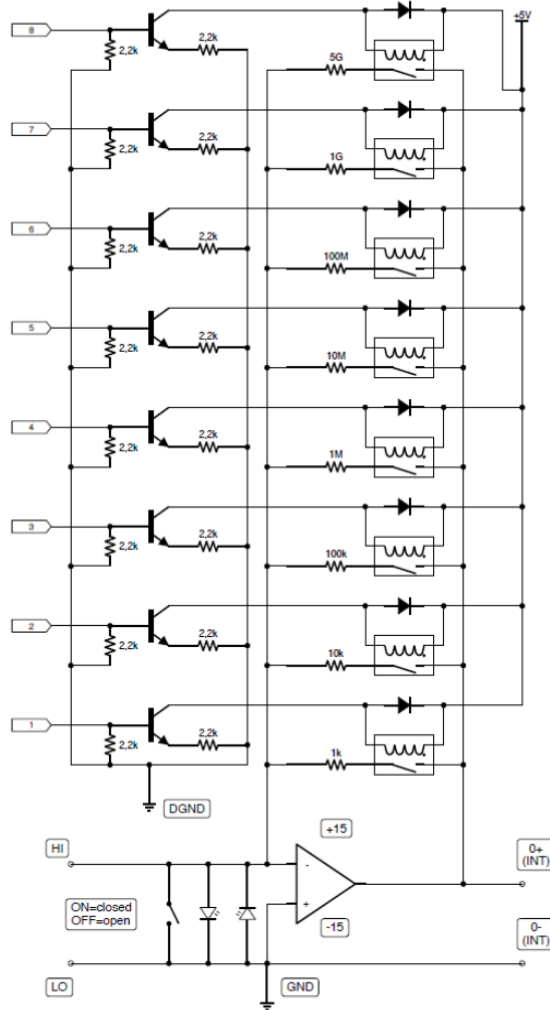


Figure A.6: FCM circuit diagram showing the connections.

Now the analog feedback circuit that was designed (Figure A.6) will be discussed. The analog circuit includes 8 different surface mounts resistors for switching sensitivity. All resistors can be activated as feedback resistances with individual reed switches (HE721A0500). In parallel to the reed switches, a high speed diode (1N4148) protects against inductive voltages during the reed shut down. The reed switches are driven by small signal npn transistors (2N3904) with a 5 V supply to maintain an stable operation. The NImyDAQ measurement card has 8 digital in/out terminals which are connected to the base of the transistors. The emitter of the transistors is connected to the digital ground (DGND) terminal of measure-

ment card. Two 2,2k resistors are connected from the base of the transistors and the emitter of the transistors each to the digital output of the measurement card (NImyDAQ) and DGND terminal of measurement card respectively.

The digital outputs can be controlled with the Digital Writer program from LabVIEW (Figure A.7). To switch to another resistance stage, the shift function has to be used. This ensures that there is always an active connection between the output and the inverting input of the chip. This software is a part of the NI ELVISmx package which includes basic measurement programs for the NImyDAQ. The maximum input of the measurement card is -10/+10 V. The data can be logged with the Continuous Input LabVIEW program (Figure A.8).

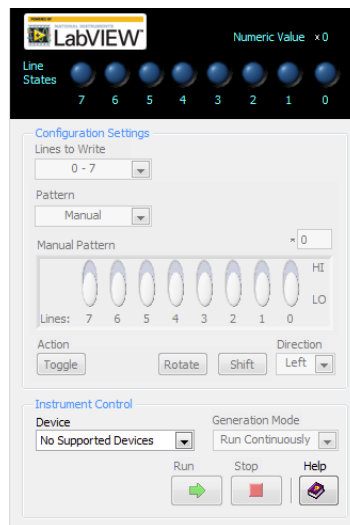


Figure A.7: Snapshot of the digital writer programme

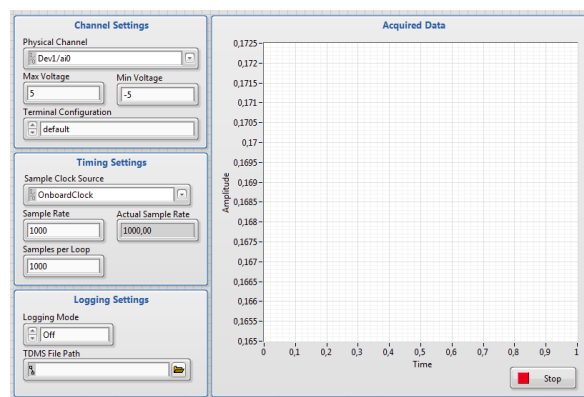


Figure A.8: Snapshot of continuous output programme

The input of the amplifier (OPA111) is protected by two red LEDs which are connected to ground. This complete circuit along with the NImyDAQ measurement card is integrated in an enclosed Al box with feed-throughs for power supplies, sample connection and USB connection of the computer with the measurement card. The circuit box has 2 terminals

(+5 V and DGND) for the 5 V digital power supply, 2 terminals (-15V and +15V) for the +15/-15V power supply and 2 terminals for the connecting of the sample.

For the sample connection the Hi terminal has to be connected to the I- port of the switch box of the scanning tunneling microscope (STM). Additionally the Keithley cable, which is usually connected to I- port of the switch box before, has to be connected to the LO/GND terminal. The LO/GND terminal also has to be connected to the ground terminal of the analog chip voltage supply (-15/+15V). The circuit box has one terminal for the USB connection to the computer. A switch between the input (HI) and ground (LO/GND) can be used to connect (switch label OFF) or disconnect (switch label ON) the chip to the experimental measurement circuit.

A.4 Data Treatment

The fast current measurements have 200k data points per second. This gives the $5\mu\text{s}$ time resolution between two data points. Before analysis of the bi-stabilities, and the absolute conductance values, the frequencies like 50 Hz and other unwanted frequencies should be filtered. If they are not properly filtered, there can be misleading results. From the frequency spectrum of the time resolved measurements, it was obvious that there is a significant contribution of 50 Hz signal within the data. Figure A.9 shows one conductance measurement at 100 mV, for a span of 200 ms. From the figure, the 50 Hz signal within the conductance data (black) can be clearly identified. The red scan shows the same signal after removal of this 50 Hz signal.

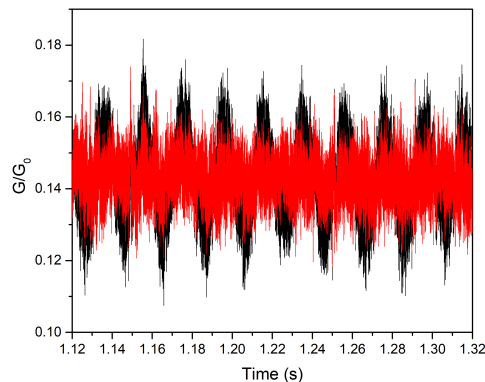


Figure A.9: Plot of a conductance measurement at 100 mV for 200 ms. The black scan shows the raw data with the 50 Hz cycles, whereas the red plot shows the filtered data.

Similarly, Figure A.10 shows the same conductance measurement at 100 mV, for a span of 100 ms. From the figure, the 50 Hz signal within the conductance data (black) can be clearly identified. The red scan shows the same signal after removal of this 50 Hz signal.

So far, the data treatment within the measurements at 100 mV was depicted. There were no bi-stabilities observed at 100 mV. At 150 mV the same data treatment was performed without affecting the the bi-stabilities. Figure A.11 shows one conductance measurement at

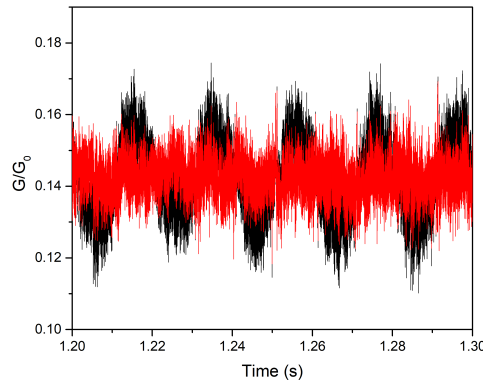


Figure A.10: Plot of a conductance measurement at 100 mV for 100 ms. The black scan shows the raw data with the 50 Hz cycles, whereas the red plot shows the filtered data.

150 mV, for a span of 200 ms. From the figure, the 50 Hz signal within the conductance data (black) can be clearly identified. The red scan shows the same signal after removal of this 50 Hz signal. It can be observed that the bi-stabilities remained un-affected after the filtering process.

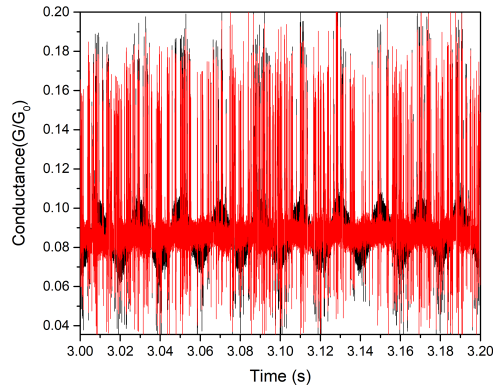


Figure A.11: Plot of a conductance measurement at 150 mV for 200 ms. The black scan shows the raw data with the 50 Hz cycles, whereas the red plot shows the filtered data. The bi-stabilities are intact after the filtering.

Similarly, Figure A.12 shows the same conductance measurement at 150 mV, for a span of 100 ms. From the figure, the 50 Hz signal within the conductance data (black) can be clearly identified. The red scan shows the same signal after removal of this 50 Hz signal.

To observe the bi-stabilities more clearly, the remaining frequencies were analysed. Even after removal of 50 Hz, another frequency band around 16 kHz was observed within the frequency spectrum. Figure A.13 shows the conductance measurement at 150 mV, for a span of 20 ms. From the figure, the 50 Hz signal within the conductance data (black) can be clearly

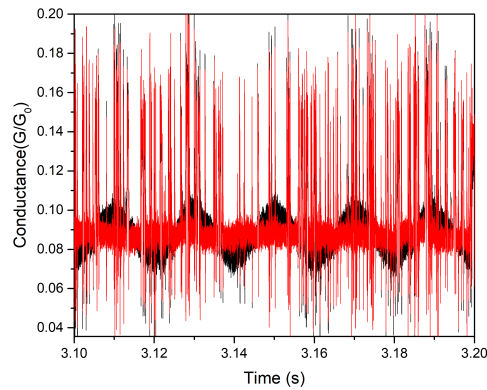


Figure A.12: Plot of a conductance measurement at 150 mV for 100 ms. The black scan shows the raw data with the 50 Hz cycles, whereas the red plot shows the filtered data. The bi-stabilities are not affected by the filtering.

identified. The red scan shows the same signal after removal of this 50 Hz signal. When looking at the data carefully, there are spikes which arise from this 16 kHz band.

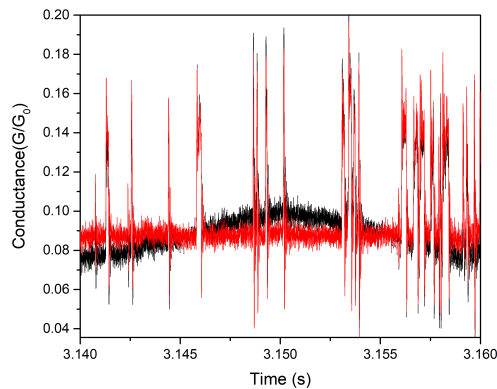


Figure A.13: Plot of a conductance measurement at 150 mV for 20 ms. The black scan shows the raw data with the 50 Hz cycles, whereas the red plot shows the filtered data. The bi-stabilities are intact after the filtering.

On filtering a frequency band of 13 kHz-19 kHz (broad bump obtained in frequency spectrum), the clean data with the bi-stabilities was obtained (Figure A.14). The yellow scan shows no spikes as seen in the black and red scans. From the figure, the 50 Hz signal within the conductance data (black) can be clearly identified. The red scan shows the same signal after removal of this 50 Hz signal. The yellow scan is the filtered data without the 50 Hz as well as the 16 kHz band.

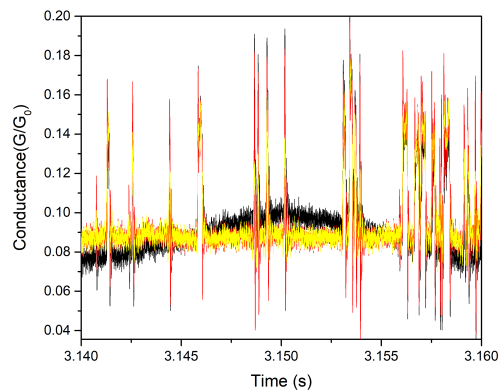


Figure A.14: Plot of a conductance measurement at 150 mV for 20 ms. black scan shows the raw data with the 50 Hz cycles, whereas the red plot shows the filtered data. The yellow plot shows the filtered data without 50 Hz and 16 kHz band.

Appendix *B*

Bibliography

- [1] E. LÖRTSCHER: Wiring molecules into circuits. *Nature Nanotechnology*, vol. 8 (June 2013), pp. 381–384 (cit. on p. 2).
DOI: 10.1038/nnano.2013.105.
- [2] J. WU et al.: A Nanotechnology Enhancement to Moore’s Law. *Applied Computational Intelligence and Soft Computing*, vol. 2013 (2013), pp. 1–13 (cit. on p. 2).
DOI: 10.1155/2013/426962.
- [3] A. AVIRAM and M. A. RATNER: Molecular rectifiers. *Chemical Physics Letters*, vol. 29(2) (Nov. 1974), pp. 277–283 (cit. on pp. 3, 15).
DOI: 10.1016/0009-2614(74)85031-1.
- [4] H. KUHN and D. MÖBIUS: Systems of Monomolecular Layers-Assembling and Physico-Chemical Behavior. *Angewandte Chemie International Edition in English*, vol. 10(9) (Sept. 1971), pp. 620–637 (cit. on p. 4).
DOI: 10.1002/anie.197106201.
- [5] M. A. REED: Conductance of a Molecular Junction. *Science*, vol. 278(5336) (Oct. 1997), pp. 252–254 (cit. on pp. 4, 6).
DOI: 10.1126/science.278.5336.252.
- [6] M. RATNER: A brief history of molecular electronics. *Nature Nanotechnology*, vol. 8(6) (June 2013), pp. 378–381 (cit. on p. 4).
DOI: 10.1038/nnano.2013.110.
- [7] H. SONG, M. A. REED, and T. LEE: Single Molecule Electronic Devices. *Advanced Materials*, vol. 23(14) (Feb. 2011), pp. 1583–1608 (cit. on p. 4).
DOI: 10.1002/adma.201004291.
- [8] M. TSUTSUI and M. TANIGUCHI: Single Molecule Electronics and Devices. *Sensors*, vol. 12(12) (May 2012), pp. 7259–7298 (cit. on p. 4).
DOI: 10.3390/s120607259.

- [9] L. SUN et al.: Single-molecule electronics: from chemical design to functional devices. *Chem. Soc. Rev.* Vol. 43(21) (2014), pp. 7378–7411 (cit. on pp. 4, 5).
DOI: 10.1039/c4cs00143e.
- [10] K. WANG and B. XU: Modulation and Control of Charge Transport Through Single-Molecule Junctions. *Topics in Current Chemistry*, vol. 375(1) (Jan. 2017), p. 17 (cit. on p. 4).
DOI: 10.1007/s41061-017-0105-z.
- [11] T. WEIMANN et al.: Four-angle evaporation method for the preparation of single electron tunneling devices. *Microelectronic Engineering*, vol. 57-58 (Sept. 2001), pp. 915–918 (cit. on p. 4).
DOI: 10.1016/s0167-9317(01)00456-7.
- [12] A. KANDA, M. WADA, Y. HAMAMOTO, and Y. OOTUKA: Simple and controlled fabrication of nanoscale gaps using double-angle evaporation. *Physica E: Low-dimensional Systems and Nanostructures*, vol. 29(3-4) (Nov. 2005), pp. 707–711 (cit. on p. 4).
DOI: 10.1016/j.physe.2005.06.065.
- [13] Y. NAITOH et al.: Self-Aligned Formation of Sub 1 nm Gaps Utilizing Electromigration during Metal Deposition. *ACS Applied Materials & Interfaces*, vol. 5(24) (Dec. 2013), pp. 12869–12875 (cit. on p. 4).
DOI: 10.1021/am403115m.
- [14] Y. NAITOH, Q. WEI, M. MUKAIDA, and T. ISHIDA: Formation of accurate 1-nm gaps using the electromigration method during metal deposition. *Applied Physics Express*, vol. 9(3) (Feb. 2016), p. 035201 (cit. on p. 4).
DOI: 10.7567/apex.9.035201.
- [15] F. CHEN et al.: Electrochemical approach for fabricating nanogap electrodes with well controllable separation. *Appl. Phys. Lett.* Vol. 86(12) (Mar. 2005), p. 123105 (cit. on p. 4).
DOI: 10.1063/1.1871361.
- [16] N. V. HOANG, S. KUMAR, and G.-H. KIM: Growth of segmented gold nanorods with nanogaps by the electrochemical wet etching technique for single-electron transistor applications. *Nanotechnology*, vol. 20(12) (Mar. 2009), p. 125607 (cit. on p. 4).
DOI: 10.1088/0957-4484/20/12/125607.
- [17] G. PHILIPP et al.: Shadow evaporation method for fabrication of sub 10 nm gaps between metal electrodes. *Microelectronic Engineering*, vol. 46(1-4) (May 1999), pp. 157–160 (cit. on p. 4).
DOI: 10.1016/s0167-9317(99)00052-0.
- [18] H. SPELTHAHN, A. POGHOSSIAN, and M. SCHÖNING: Self-aligned nanogaps and

- nanochannels via conventional photolithography and pattern-size reduction technique. *Electrochimica Acta*, vol. 54(25) (Oct. 2009), pp. 6010–6014 (cit. on p. 4).
DOI: 10.1016/j.electacta.2009.03.029.
- [19] M. AUSTIN and S. Y. CHOU: Fabrication of nanocontacts for molecular devices using nanoimprint lithography. *Journal of Vacuum Science & Technology B: Microelectronics and Nanometer Structures*, vol. 20(2) (2002), p. 665 (cit. on p. 4).
DOI: 10.1116/1.1463068.
- [20] D. J. BEESLEY et al.: Sub-15-nm patterning of asymmetric metal electrodes and devices by adhesion lithography. *Nature Communications*, vol. 5(1) (May 2014), p. 3933 (cit. on p. 4).
DOI: 10.1038/ncomms4933.
- [21] Y.-C. LIN, J. BAI, and Y. HUANG: Self-Aligned Nanolithography in a Nanogap. *Nano Letters*, vol. 9(6) (June 2009), pp. 2234–2238 (cit. on p. 4).
DOI: 10.1021/nl9000597.
- [22] T. NAGASE, T. KUBOTA, and S. MASHIKO: Fabrication of nano-gap electrodes for measuring electrical properties of organic molecules using a focused ion beam. *Thin Sol. Films*, vol. 438-439 (Aug. 2003), pp. 374–377 (cit. on p. 4).
DOI: 10.1016/s0040-6090(03)00772-7.
- [23] T. BLOM et al.: Fabrication and characterization of highly reproducible, high resistance nanogaps made by focused ion beam milling. *Nanotechnology*, vol. 18(28) (June 2007), p. 285301 (cit. on p. 4).
DOI: 10.1088/0957-4484/18/28/285301.
- [24] W. ASGHAR et al.: Rapid Nanomanufacturing of Metallic Break Junctions Using Focused Ion Beam Scratching and Electromigration. *J. Manufact. Sci. Engin.* Vol. 132(3) (2010), p. 030911 (cit. on p. 4).
DOI: 10.1115/1.4001664.
- [25] A. CUI et al.: Single Grain Boundary Break Junction for Suspended Nanogap Electrodes with Gapwidth Down to 1-2 nm by Focused Ion Beam Milling. *Adv. Mat.* Vol. 27(19) (Apr. 2015), pp. 3002–3006 (cit. on p. 4).
DOI: 10.1002/adma.201500527.
- [26] H. LI et al.: Fabrication of reproducible sub-5 nm nanogaps by a focused ion beam and observation of Fowler-Nordheim tunneling. *Appl. Phys. Lett.* Vol. 107(10) (Sept. 2015), p. 103108 (cit. on pp. 4, 104).
DOI: 10.1063/1.4930821.
- [27] M. MANHELLER, S. TRELLENKAMP, R. WASER, and S. KARTHÄUSER: Reliable fabri-

- cation of 3 nm gaps between nanoelectrodes by electron-beam lithography. *Nanotechnology*, vol. 23(12) (Mar. 2012), p. 125302 (cit. on p. 4).
DOI: 10.1088/0957-4484/23/12/125302.
- [28] T. WEIMANN, H. SCHERER, P. HINZE, and J. NIEMEYER: Fabrication of metallic multilayer single electron tunneling devices using low-energy e-beam lithography. *Microelectronic Engineering*, vol. 53(1-4) (June 2000), pp. 225–228 (cit. on p. 4).
DOI: 10.1016/s0167-9317(00)00302-6.
- [29] X. D. CUI: Reproducible Measurement of Single-Molecule Conductivity. *Science*, vol. 294(5542) (Oct. 2001), pp. 571–574 (cit. on p. 4).
DOI: 10.1126/science.1064354.
- [30] B. XU: Measurement of Single-Molecule Resistance by Repeated Formation of Molecular Junctions. *Science*, vol. 301(5637) (Aug. 2003), pp. 1221–1223 (cit. on pp. 4, 5).
DOI: 10.1126/science.1087481.
- [31] Z. J. DONHAUSER: Conductance Switching in Single Molecules Through Conformational Changes. *Science*, vol. 292(5525) (June 2001), pp. 2303–2307 (cit. on p. 4).
DOI: 10.1126/science.1060294.
- [32] M. FREI et al.: Mechanics and Chemistry: Single Molecule Bond Rupture Forces Correlate with Molecular Backbone Structure. *Nano Letters*, vol. 11(4) (Apr. 2011), pp. 1518–1523 (cit. on pp. 4, 5).
DOI: 10.1021/nl11042903.
- [33] D. J. WOLD and C. D. FRISBIE: Formation of Metal-Molecule-Metal Tunnel Junctions: Microcontacts to Alkanethiol Monolayers with a Conducting AFM Tip. *Journal of the American Chemical Society*, vol. 122(12) (Mar. 2000), pp. 2970–2971 (cit. on p. 4).
DOI: 10.1021/ja994468h.
- [34] M. L. PERRIN et al.: Large tunable image-charge effects in single-molecule junctions. *Nature Nanotechnology*, vol. 8(4) (Mar. 2013), pp. 282–287 (cit. on p. 6).
DOI: 10.1038/nnano.2013.26.
- [35] J. MORELAND and J. W. EKIN: Electron tunneling experiments using Nb-Sn “break” junctions. *Journal of Applied Physics*, vol. 58(10) (Nov. 1985), pp. 3888–3895 (cit. on p. 6).
DOI: 10.1063/1.335608.
- [36] C. MULLER, J. van RUITENBEEK, and L. de JONGH: Experimental observation of the transition from weak link to tunnel junction. *Physica C: Superconductivity*, vol. 191(3-4) (Feb. 1992), pp. 485–504 (cit. on p. 6).
DOI: 10.1016/0921-4534(92)90947-b.

-
- [37] M. TSUTSUI et al.: Single-molecule sensing electrode embedded in-plane nanopore. *Scientific Reports*, vol. 1(1) (July 2011), p. 46 (cit. on pp. 7, 116).
DOI: 10.1038/srep00046.
- [38] D. E. JOHNSTON, D. R. STRACHAN, and A. T. C. JOHNSON: Parallel Fabrication of Nanogap Electrodes. *Nano Letters*, vol. 7(9) (Sept. 2007), pp. 2774–2777 (cit. on pp. 7, 29).
DOI: 10.1021/nl0713169.
- [39] S. L. JOHNSON et al.: High-Throughput Nanogap Formation Using Single Ramp Feedback Control. *IEEE Transactions on Nanotechnology*, vol. 10(4) (July 2011), pp. 806–809 (cit. on pp. 7, 29).
DOI: 10.1109/tnano.2010.2080283.
- [40] H. S. J. van der ZANT et al.: Molecular three-terminal devices: fabrication and measurements. *Faraday Discuss.* Vol. 131 (2006), pp. 347–356 (cit. on pp. 7, 29).
DOI: 10.1039/b506240n.
- [41] H. PARK et al.: Fabrication of metallic electrodes with nanometer separation by electromigration. *Appl. Phys. Lett.* Vol. 75(2) (July 1999), pp. 301–303 (cit. on pp. 7, 27, 28, 62).
DOI: 10.1063/1.124354.
- [42] D. R. STRACHAN et al.: Controlled fabrication of nanogaps in ambient environment for molecular electronics. *Appl. Phys. Lett.* Vol. 86(4) (Jan. 2005), p. 043109 (cit. on pp. 7, 27, 28, 58, 62, 84).
DOI: 10.1063/1.1857095.
- [43] P. MOTTO et al.: Nanogap structures for molecular nanoelectronics. *Nanoscale Res. Lett.* Vol. 7(1) (2012), p. 113 (cit. on pp. 7, 27, 29, 58, 62, 71, 73, 84).
DOI: 10.1186/1556-276x-7-113.
- [44] G. ESEN: “Formation of Molecular-Scale Gold Nanogap Junctions via Controlled Electromigration”. *AIP Conference Proceedings*. AIP, 2005, pp. 534–537 (cit. on pp. 7, 27, 28).
DOI: 10.1063/1.2103925.
- [45] J. M. CAMPBELL and R. G. KNOBEL: Feedback-controlled electromigration for the fabrication of point contacts. *Applied Physics Letters*, vol. 102(2) (Jan. 2013), p. 023105 (cit. on pp. 7, 27, 29).
DOI: 10.1063/1.4775695.
- [46] V.-Y. SHIH, S. ZHENG, A. CHANG, and Y.-C. TAI: “Nanometer gaps by feedback-controlled electromigration”. *TRANSDUCERS '03. 12th International Conference on*

- Solid-State Sensors, Actuators and Microsystems. Digest of Technical Papers (Cat. No.03TH8664)*. IEEE, 2003, pp. 1530–1533 (cit. on pp. 7, 27, 29).
DOI: 10.1109/sensor.2003.1217069.
- [47] Y. KANAMARU, M. ANDO, and J.-i. SHIRAKASHI: Ultrafast feedback-controlled electromigration using a field-programmable gate array. *Journal of Vacuum Science & Technology B, Nanotechnology and Microelectronics: Materials, Processing, Measurement, and Phenomena*, vol. 33(2) (Mar. 2015), 02B106 (cit. on p. 7).
DOI: 10.1116/1.4903929.
- [48] J. DONG and B. A. PARVIZ: Using noise for controlled disassembly of nanoscale gold wires. *Nanotechnology*, vol. 17(20) (Sept. 2006), pp. 5124–5130 (cit. on pp. 7, 29).
DOI: 10.1088/0957-4484/17/20/014.
- [49] Z. M. WU et al.: Feedback controlled electromigration in four-terminal nanojunctions. *Applied Physics Letters*, vol. 91(5) (July 2007), p. 053118 (cit. on pp. 8, 29).
DOI: 10.1063/1.2760150.
- [50] Y. TOMODA et al.: Fabrication of nanogap electrodes by field-emission-induced electromigration. *Journal of Vacuum Science and Technology B*, vol. 27 (2009), pp. 813–816 (cit. on p. 8).
DOI: 10.1116/1.3039683.
- [51] S. KAYASHIMA, K. TAKAHASHI, M. MOTOYAMA, and J.-i. SHIRAKASHI: Control of Tunnel Resistance of Nanogaps by Field-Emission-Induced Electromigration. *Japanese Journal of Applied Physics*, vol. 46(No. 37) (Sept. 2007), pp. L907–L909 (cit. on p. 8).
DOI: 10.1143/jjap.46.1907.
- [52] T. WATANABE, K. TAKIYA, and J.-i. SHIRAKASHI: Fabrication of planar-type Ni/vacuum/Ni tunnel junctions based on ferromagnetic nanogaps using field-emission-induced electromigration. *Journal of Applied Physics*, vol. 109(7) (Apr. 2011), p. 07C919 (cit. on p. 8).
DOI: 10.1063/1.3565198.
- [53] S. UENO et al.: Field-emission-induced electromigration method for the integration of single-electron transistors. *Applied Surface Science*, vol. 258(6) (Jan. 2012), pp. 2153–2156 (cit. on p. 8).
DOI: 10.1016/j.apsusc.2011.03.016.
- [54] M. YAGI, M. ITO, and J.-i. SHIRAKASHI: Structural tuning of nanogaps using electromigration induced by field emission current with bipolar biasing. *Journal of Applied Physics*, vol. 118(1) (July 2015), p. 014306 (cit. on p. 8).
DOI: 10.1063/1.4923347.
- [55] M. ITO, M. YAGI, K. MORIHARA, and J.-i. SHIRAKASHI: Simultaneous fabrication of

- nanogap electrodes using field-emission-induced electromigration. *Journal of Applied Physics*, vol. 118(1) (July 2015), p. 014301 (cit. on p. 8).
DOI: 10.1063/1.4923411.
- [56] M. ITO et al.: High-throughput nanogap formation by field-emission-induced electromigration. *Journal of Vacuum Science & Technology B, Nanotechnology and Microelectronics: Materials, Processing, Measurement, and Phenomena*, vol. 33(5) (Sept. 2015), p. 051801 (cit. on p. 8).
DOI: 10.1116/1.4927443.
- [57] T. TOYONAKA et al.: Controlling the tunnel resistance of suspended Ni nanogaps using field-emission-induced electromigration. *Journal of Vacuum Science and Technology B*, vol. 33 (2015), 02B107 (cit. on p. 8).
DOI: 10.1116/1.4904731.
- [58] M. L. TROUWBORST, S. J. van der MOLEN, and B. J. van WEES: The role of Joule heating in the formation of nanogaps by electromigration. *Journal of Applied Physics*, vol. 99(11) (June 2006), p. 114316 (cit. on pp. 8, 27, 28).
DOI: 10.1063/1.2203410.
- [59] W. JEONG et al.: Characterization of nanoscale temperature fields during electromigration of nanowires. *Scientific Reports*, vol. 4(1) (May 2014), p. 4975 (cit. on pp. 8–10, 27, 29).
DOI: 10.1038/srep04975.
- [60] G. ESEN and M. S. FUHRER: Temperature control of electromigration to form gold nanogap junctions. *Applied Physics Letters*, vol. 87(26) (Dec. 2005), p. 263101 (cit. on pp. 8, 27, 28).
DOI: 10.1063/1.2149174.
- [61] T. TAYCHATANAPAT, K. I. BOLOTIN, F. KUEMMETH, and D. C. RALPH: Imaging Electromigration during the Formation of Break Junctions. *Nano Letters*, vol. 7(3) (Mar. 2007), pp. 652–656 (cit. on pp. 8, 16, 27, 29).
DOI: 10.1021/nl1062631i.
- [62] D. R. STRACHAN et al.: Clean Electromigrated Nanogaps Imaged by Transmission Electron Microscopy. *Nano Letters*, vol. 6(3) (Mar. 2006), pp. 441–444 (cit. on pp. 8, 16).
DOI: 10.1021/nl1052302a.
- [63] M. RUDNEVA et al.: In Situ Transmission Electron Microscopy Imaging of Electromigration in Platinum Nanowires. *Microscopy and Microanalysis*, vol. 19(S5) (Aug. 2013), pp. 43–48 (cit. on pp. 8, 16).
DOI: 10.1017/s1431927613012300.
- [64] H. B. HEERSCHE et al.: In situ imaging of electromigration-induced nanogap formation

- by transmission electron microscopy. *Applied Physics Letters*, vol. 91(7) (Aug. 2007), p. 072107 (cit. on pp. 8, 16).
DOI: 10.1063/1.2767149.
- [65] D. R. STRACHAN et al.: Real-Time TEM Imaging of the Formation of Crystalline Nanoscale Gaps. *Physical Review Letters*, vol. 100(5) (Feb. 2008), p. 056805 (cit. on pp. 8, 16).
DOI: 10.1103/physrevlett.100.056805.
- [66] M. RUDNEVA, T. KOZLOVA, and H. W. ZANDBERGEN: The use of STEM imaging to analyze thickness variations due to electromigration-induced mass transport in thin polycrystalline nanobridges. *Ultramicroscopy*, vol. 134 (Nov. 2013), pp. 155–159 (cit. on pp. 8, 16).
DOI: 10.1016/j.ultramicro.2013.05.022.
- [67] B. GAO, E. A. OSORIO, K. B. GAVEN, and H. S. J. van der ZANT: Three-terminal electric transport measurements on gold nano-particles combined with ex situ TEM inspection. *Nanotechnology*, vol. 20(41) (Sept. 2009), p. 415207 (cit. on p. 8).
DOI: 10.1088/0957-4484/20/41/415207.
- [68] T. KIZUKA, S. KODAMA, and T. MATSUDA: Verification of unzipping models of electromigration in gold nanocontacts by in situ high-resolution transmission electron microscopy. *Nanotechnology*, vol. 21(49) (Nov. 2010), p. 495706 (cit. on pp. 8, 16).
DOI: 10.1088/0957-4484/21/49/495706.
- [69] S. V. ARADHYA and L. VENKATARAMAN: Single-molecule junctions beyond electronic transport. *Nature Nanotechnology*, vol. 8(6) (June 2013), pp. 399–410 (cit. on pp. 8–10, 12).
DOI: 10.1038/nnano.2013.91.
- [70] H. OHNISHI, Y. KONDO, and K. TAKAYANAGI: Quantized conductance through individual rows of suspended gold atoms. *Nature*, vol. 395(6704) (Oct. 1998), pp. 780–783 (cit. on pp. 9, 38, 85, 97).
DOI: 10.1038/27399.
- [71] N. AGRAÏT: Quantum properties of atomic-sized conductors. *Physics Reports*, vol. 377(2-3) (Apr. 2003), pp. 81–279 (cit. on pp. 9, 31–38, 42, 88).
DOI: 10.1016/s0370-1573(02)00633-6.
- [72] G. RUBIO, N. AGRAÏT, and S. VIEIRA: Atomic-Sized Metallic Contacts: Mechanical Properties and Electronic Transport. *Physical Review Letters*, vol. 76(13) (Mar. 1996), pp. 2302–2305 (cit. on p. 9).
DOI: 10.1103/physrevlett.76.2302.
- [73] B. XU, X. XIAO, and N. J. TAO: Measurements of Single-Molecule Electromechani-

- cal Properties. *Journal of the American Chemical Society*, vol. 125(52) (Dec. 2003), pp. 16164–16165 (cit. on p. 9).
DOI: 10.1021/ja038949j.
- [74] M. TERNES et al.: Interplay of Conductance, Force, and Structural Change in Metallic Point Contacts. *Physical Review Letters*, vol. 106(1) (Jan. 2011), p. 016802 (cit. on p. 9).
DOI: 10.1103/physrevlett.106.016802.
- [75] C. WAGNER, N. FOURNIER, F. S. TAUTZ, and R. TEMIROV: Measurement of the Binding Energies of the Organic-Metal Perylene-Teracarboxylic-Dianhydride/Au(111) Bonds by Molecular Manipulation Using an Atomic Force Microscope. *Physical Review Letters*, vol. 109(7) (Aug. 2012), p. 076102 (cit. on p. 9).
DOI: 10.1103/physrevlett.109.076102.
- [76] S. V. ARADHYA, M. FREI, M. S. HYBERTSEN, and L. VENKATARAMAN: Van der Waals interactions at metal/organic interfaces at the single-molecule level. *Nature Materials*, vol. 11(10) (Aug. 2012), pp. 872–876 (cit. on p. 9).
DOI: 10.1038/nmat3403.
- [77] Y. KIM et al.: Electrostatic control of thermoelectricity in molecular junctions. *Nature Nanotechnology*, vol. 9(11) (Oct. 2014), pp. 881–885 (cit. on p. 9).
DOI: 10.1038/nnano.2014.209.
- [78] K. KIM, W. JEONG, W. LEE, and P. REDDY: Ultra-High Vacuum Scanning Thermal Microscopy for Nanometer Resolution Quantitative Thermometry. *ACS Nano*, vol. 6(5) (May 2012), pp. 4248–4257 (cit. on p. 9).
DOI: 10.1021/nn300774n.
- [79] B. LUDOPH and J. M. van RUITENBEEK: Thermopower of atomic-size metallic contacts. *Physical Review B*, vol. 59(19) (May 1999), pp. 12290–12293 (cit. on p. 10).
DOI: 10.1103/physrevb.59.12290.
- [80] P. REDDY, S.-Y. JANG, R. A. SEGALMAN, and A. MAJUMDAR: Thermoelectricity in Molecular Junctions. *Science*, vol. 315(5818) (Mar. 2007), pp. 1568–1571 (cit. on p. 10).
DOI: 10.1126/science.1137149.
- [81] J. R. WIDAWSKY, P. DARANCET, J. B. NEATON, and L. VENKATARAMAN: Simultaneous Determination of Conductance and Thermopower of Single Molecule Junctions. *Nano Letters*, vol. 12(1) (Dec. 2011), pp. 354–358 (cit. on p. 10).
DOI: 10.1021/nl203634m.
- [82] K. BAHETI et al.: Probing the Chemistry of Molecular Heterojunctions Using Thermoelectricity. *Nano Letters*, vol. 8(2) (Feb. 2008), pp. 715–719 (cit. on p. 10).
DOI: 10.1021/nl0727381.

- [83] J. A. MALEN et al.: Identifying the Length Dependence of Orbital Alignment and Contact Coupling in Molecular Heterojunctions. *Nano Letters*, vol. 9(3) (Mar. 2009), pp. 1164–1169 (cit. on p. 10).
DOI: 10.1021/nl803814f.
- [84] J. A. MALEN, S. K. YEE, A. MAJUMDAR, and R. A. SEGALMAN: Fundamentals of energy transport, energy conversion, and thermal properties in organic-inorganic heterojunctions. *Chemical Physics Letters*, vol. 491(4-6) (May 2010), pp. 109–122 (cit. on p. 10).
DOI: 10.1016/j.cplett.2010.03.028.
- [85] S. K. YEE, J. A. MALEN, A. MAJUMDAR, and R. A. SEGALMAN: Thermoelectricity in Fullerene-Metal Heterojunctions. *Nano Letters*, vol. 11(10) (Oct. 2011), pp. 4089–4094 (cit. on p. 10).
DOI: 10.1021/nl2014839.
- [86] X. CHEN et al.: Split-Wedge Antennas with Sub-5 nm Gaps for Plasmonic Nanofocusing. *Nano Letters*, vol. 16(12) (Nov. 2016), pp. 7849–7856 (cit. on p. 10).
DOI: 10.1021/acs.nanolett.6b04113.
- [87] Y. WANG et al.: Rapidly fabricating large-scale plasmonic silver nanosphere arrays with sub-20 nm gap on Si-pyramids by inverted annealing for highly sensitive SERS detection. *RSC Advances*, vol. 7(19) (2017), pp. 11578–11584 (cit. on p. 10).
DOI: 10.1039/c6ra28517a.
- [88] T. KONISHI et al.: Single Molecule Dynamics at a Mechanically Controllable Break Junction in Solution at Room Temperature. *Journal of the American Chemical Society*, vol. 135(3) (Oct. 2012), pp. 1009–1014 (cit. on p. 10).
DOI: 10.1021/ja307821u.
- [89] S. KANEKO et al.: Site-Selection in Single-Molecule Junction for Highly Reproducible Molecular Electronics. *Journal of the American Chemical Society*, vol. 138(4) (Jan. 2016), pp. 1294–1300 (cit. on p. 10).
DOI: 10.1021/jacs.5b11559.
- [90] Z. IOFFE et al.: Detection of heating in current-carrying molecular junctions by Raman scattering. *Nature Nanotechnology*, vol. 3(12) (Oct. 2008), pp. 727–732 (cit. on p. 10).
DOI: 10.1038/nnano.2008.304.
- [91] Y. LI et al.: Interplay of Bias-Driven Charging and the Vibrational Stark Effect in Molecular Junctions. *Nano Letters*, vol. 16(2) (Feb. 2016), pp. 1104–1109 (cit. on p. 10).
DOI: 10.1021/acs.nanolett.5b04340.
- [92] D. R. WARD et al.: Simultaneous Measurements of Electronic Conduction and Raman

- Response in Molecular Junctions. *Nano Letters*, vol. 8(3) (Mar. 2008), pp. 919–924 (cit. on p. 10).
DOI: 10.1021/nl1073346h.
- [93] D. R. WARD et al.: Electromigrated Nanoscale Gaps for Surface-Enhanced Raman Spectroscopy. *Nano Letters*, vol. 7(5) (May 2007), pp. 1396–1400 (cit. on p. 11).
DOI: 10.1021/nl1070625w.
- [94] D. R. WARD et al.: Electronic and optical properties of electromigrated molecular junctions. *Journal of Physics: Condensed Matter*, vol. 20(37) (Aug. 2008), p. 374118 (cit. on p. 11).
DOI: 10.1088/0953-8984/20/37/374118.
- [95] D. R. WARD, D. A. CORLEY, J. M. TOUR, and D. NATELSON: Vibrational and electronic heating in nanoscale junctions. *Nature Nanotechnology*, vol. 6(1) (Dec. 2010), pp. 33–38 (cit. on pp. 11, 62).
DOI: 10.1038/nnano.2010.240.
- [96] Z. LIU et al.: Revealing the molecular structure of single-molecule junctions in different conductance states by fishing-mode tip-enhanced Raman spectroscopy. *Nature Communications*, vol. 2(1) (May 2011), p. 305 (cit. on p. 11).
DOI: 10.1038/ncomms1310.
- [97] N. JIANG et al.: Observation of Multiple Vibrational Modes in Ultrahigh Vacuum Tip-Enhanced Raman Spectroscopy Combined with Molecular-Resolution Scanning Tunneling Microscopy. *Nano Letters*, vol. 12(10) (Jan. 2012), pp. 5061–5067 (cit. on p. 11).
DOI: 10.1021/nl2039925.
- [98] Y. LI et al.: Voltage tuning of vibrational mode energies in single-molecule junctions. *Proceedings of the National Academy of Sciences*, vol. 111(4) (Jan. 2014), pp. 1282–1287 (cit. on p. 11).
DOI: 10.1073/pnas.1320210111.
- [99] R. MATSUSHITA and M. KIGUCHI: Surface enhanced Raman scattering of a single molecular junction. *Physical Chemistry Chemical Physics*, vol. 17(33) (2015), pp. 21254–21260 (cit. on p. 11).
DOI: 10.1039/c4cp04906c.
- [100] S. F. MADOKA IWANE and M. KIGUCHI: Surface-Enhanced Raman Scattering in Molecular Junctions. *Sensors*, vol. 17(8) (Aug. 2017), p. 1901 (cit. on p. 11).
DOI: 10.3390/s17081901.
- [101] J.-H. TIAN et al.: Study of Molecular Junctions with a Combined Surface-Enhanced

- Raman and Mechanically Controllable Break Junction Method. *Journal of the American Chemical Society*, vol. 128(46) (Nov. 2006), pp. 14748–14749 (cit. on p. 11).
DOI: 10.1021/ja0648615.
- [102] J. M. BAIK, S. J. LEE, and M. MOSKOVITS: Polarized Surface-Enhanced Raman Spectroscopy from Molecules Adsorbed in Nano-Gaps Produced by Electromigration in Silver Nanowires. *Nano Letters*, vol. 9(2) (Feb. 2009), pp. 672–676 (cit. on p. 11).
DOI: 10.1021/nl803145d.
- [103] X. H. QIU: Vibrationally Resolved Fluorescence Excited with Submolecular Precision. *Science*, vol. 299(5606) (Jan. 2003), pp. 542–546 (cit. on p. 11).
DOI: 10.1126/science.1078675.
- [104] S. W. WU, G. V. NAZIN, and W. HO: Intramolecular photon emission from a single molecule in a scanning tunneling microscope. *Physical Review B*, vol. 77(20) (May 2008), p. 205430 (cit. on p. 11).
DOI: 10.1103/physrevb.77.205430.
- [105] R. BERNDT et al.: Photon Emission at Molecular Resolution Induced by a Scanning Tunneling Microscope. *Science*, vol. 262(5138) (Nov. 1993), pp. 1425–1427 (cit. on p. 11).
DOI: 10.1126/science.262.5138.1425.
- [106] J. HE et al.: Switching of a photochromic molecule on gold electrodes: single-molecule measurements. *Nanotechnology*, vol. 16(6) (Apr. 2005), pp. 695–702 (cit. on p. 12).
DOI: 10.1088/0957-4484/16/6/012.
- [107] K. MATSUDA and M. IRIE: Effective photoswitching of intramolecular magnetic interaction by diarylethene: Backgrounds and applications. *Polyhedron*, vol. 24(16-17) (Nov. 2005), pp. 2477–2483 (cit. on p. 12).
DOI: 10.1016/j.poly.2005.03.050.
- [108] S. J. van der MOLEN and P. LILJEROTH: Charge transport through molecular switches. *Journal of Physics: Condensed Matter*, vol. 22(13) (Mar. 2010), p. 133001 (cit. on p. 12).
DOI: 10.1088/0953-8984/22/13/133001.
- [109] N. YU et al.: Bowtie plasmonic quantum cascade laser antenna. *Optics Express*, vol. 15(20) (2007), p. 13272 (cit. on p. 12).
DOI: 10.1364/oe.15.013272.
- [110] A. STOLZ et al.: Nonlinear Photon-Assisted Tunneling Transport in Optical Gap Antennas. *Nano Letters*, vol. 14(5) (Apr. 2014), pp. 2330–2338 (cit. on p. 12).
DOI: 10.1021/nl404707t.

-
- [111] W. ZHU et al.: Quantum mechanical effects in plasmonic structures with subnanometre gaps. *Nature Communications*, vol. 7 (June 2016), p. 11495 (cit. on p. 12).
DOI: 10.1038/ncomms11495.
- [112] J. PARK et al.: Coulomb blockade and the Kondo effect in single-atom transistors. *Nature*, vol. 417(6890) (June 2002), pp. 722–725 (cit. on p. 12).
DOI: 10.1038/nature00791.
- [113] W. LIANG et al.: Kondo resonance in a single-molecule transistor. *Nature*, vol. 417(6890) (June 2002), pp. 725–729 (cit. on p. 12).
DOI: 10.1038/nature00790.
- [114] L. H. YU and D. NATELSON: The Kondo Effect in C60Single-Molecule Transistors. *Nano Letters*, vol. 4(1) (Jan. 2004), pp. 79–83 (cit. on p. 12).
DOI: 10.1021/nl1034893f.
- [115] L. H. YU et al.: Kondo Resonances and Anomalous Gate Dependence in the Electrical Conductivity of Single-Molecule Transistors. *Physical Review Letters*, vol. 95(25) (Dec. 2005), p. 256803 (cit. on p. 12).
DOI: 10.1103/physrevlett.95.256803.
- [116] A. A. HOUCK et al.: Kondo Effect in Electromigrated Gold Break Junctions. *Nano Letters*, vol. 5(9) (Sept. 2005), pp. 1685–1688 (cit. on p. 12).
DOI: 10.1021/nl1050799i.
- [117] A. N. PASUPATHY: The Kondo Effect in the Presence of Ferromagnetism. *Science*, vol. 306(5693) (Oct. 2004), pp. 86–89 (cit. on p. 12).
DOI: 10.1126/science.1102068.
- [118] R. SORDAN, K. BALASUBRAMANIAN, M. BURGHARD, and K. KERN: Coulomb blockade phenomena in electromigration break junctions. *Applied Physics Letters*, vol. 87(1) (July 2005), p. 013106 (cit. on p. 12).
DOI: 10.1063/1.1991988.
- [119] L. BOGANI and W. WERNSDORFER: Molecular spintronics using single-molecule magnets. *Nature Materials*, vol. 7(3) (Mar. 2008), pp. 179–186 (cit. on p. 12).
DOI: 10.1038/nmat2133.
- [120] R. VINCENT et al.: Electronic read-out of a single nuclear spin using a molecular spin transistor. *Nature*, vol. 488(7411) (Aug. 2012), pp. 357–360 (cit. on p. 12).
DOI: 10.1038/nature11341.
- [121] R. BAER and D. NEUHAUSER: Phase Coherent Electronics: A Molecular Switch Based on Quantum Interference. *Journal of the American Chemical Society*, vol. 124(16) (Apr. 2002), pp. 4200–4201 (cit. on p. 12).
DOI: 10.1021/ja016605s.

- [122] K. WALCZAK: The role of quantum interference in determining transport properties of molecular bridges. *Open Chemistry*, vol. 2(3) (Jan. 2004), pp. 524–533 (cit. on p. 12). DOI: 10.2478/bf02476205.
- [123] D. WALTER, D. NEUHAUSER, and R. BAER: Quantum interference in polycyclic hydrocarbon molecular wires. *Chemical Physics*, vol. 299(1) (Mar. 2004), pp. 139–145 (cit. on p. 12). DOI: 10.1016/j.chemphys.2003.12.015.
- [124] D. Q. ANDREWS et al.: Quantum Interference: The Structural Dependence of Electron Transmission through Model Systems and Cross-Conjugated Molecules. *The Journal of Physical Chemistry C*, vol. 112(43) (Oct. 2008), pp. 16991–16998 (cit. on p. 12). DOI: 10.1021/jp805588m.
- [125] G. C. SOLOMON, D. Q. ANDREWS, R. P. V. DUYNÉ, and M. A. RATNER: When Things Are Not as They Seem: Quantum Interference Turns Molecular Electron Transfer "Rules" Upside Down. *Journal of the American Chemical Society*, vol. 130(25) (June 2008), pp. 7788–7789 (cit. on p. 12). DOI: 10.1021/ja801379b.
- [126] G. C. SOLOMON et al.: Exploring local currents in molecular junctions. *Nature Chemistry*, vol. 2(3) (Feb. 2010), pp. 223–228 (cit. on p. 12). DOI: 10.1038/nchem.546.
- [127] R. HÄRTLE, M. BUTZIN, O. RUBIO-PONS, and M. THOSS: Quantum Interference and Decoherence in Single-Molecule Junctions: How Vibrations Induce Electrical Current. *Physical Review Letters*, vol. 107(4) (July 2011), p. 046802 (cit. on p. 12). DOI: 10.1103/physrevlett.107.046802.
- [128] S. V. ARADHYA et al.: Dissecting Contact Mechanics from Quantum Interference in Single-Molecule Junctions of Stilbene Derivatives. *Nano Letters*, vol. 12(3) (Feb. 2012), pp. 1643–1647 (cit. on p. 12). DOI: 10.1021/nl2045815.
- [129] C. R. ARROYO et al.: Quantum interference effects at room temperature in OPV-based single-molecule junctions. *Nanoscale Research Letters*, vol. 8(1) (2013), p. 234 (cit. on p. 12). DOI: 10.1186/1556-276x-8-234.
- [130] H. VAZQUEZ et al.: Probing the conductance superposition law in single-molecule circuits with parallel paths. *Nature Nanotechnology*, vol. 7(10) (Sept. 2012), pp. 663–667 (cit. on p. 12). DOI: 10.1038/nnano.2012.147.

-
- [131] D. XIANG et al.: Molecular-Scale Electronics: From Concept to Function. *Chemical Reviews*, vol. 116(7) (Mar. 2016), pp. 4318–4440 (cit. on p. 13).
DOI: 10.1021/acs.chemrev.5b00680.
- [132] Y. KIM et al.: Charge Transport Characteristics of Diarylethene Photoswitching Single-Molecule Junctions. *Nano Letters*, vol. 12(7) (June 2012), pp. 3736–3742 (cit. on p. 14).
DOI: 10.1021/nl3015523.
- [133] D. DULIĆ et al.: One-Way Optoelectronic Switching of Photochromic Molecules on Gold. *Physical Review Letters*, vol. 91(20) (Nov. 2003), p. 207402 (cit. on p. 14).
DOI: 10.1103/physrevlett.91.207402.
- [134] S. MARTIN, W. HAISS, S. J. HIGGINS, and R. J. NICHOLS: The Impact of E-Z Photo-Isomerization on Single Molecular Conductance. *Nano Letters*, vol. 10(6) (June 2010), pp. 2019–2023 (cit. on p. 14).
DOI: 10.1021/nl9042455.
- [135] M. KIGUCHI et al.: Single Molecular Resistive Switch Obtained via Sliding Multiple Anchoring Points and Varying Effective Wire Length. *Journal of the American Chemical Society*, vol. 136(20) (Mar. 2014), pp. 7327–7332 (cit. on p. 14).
DOI: 10.1021/ja413104g.
- [136] M. KIGUCHI et al.: Highly Conductive Molecular Junctions Based on Direct Binding of Benzene to Platinum Electrodes. *Physical Review Letters*, vol. 101(4) (July 2008), p. 046801 (cit. on p. 14).
DOI: 10.1103/physrevlett.101.046801.
- [137] T. A. SU et al.: Stereoelectronic switching in single-molecule junctions. *Nature Chemistry*, vol. 7(3) (Feb. 2015), pp. 215–220 (cit. on p. 14).
DOI: 10.1038/nchem.2180.
- [138] S. Y. QUEK et al.: Mechanically controlled binary conductance switching of a single-molecule junction. *Nature Nanotechnology*, vol. 4(4) (Mar. 2009), pp. 230–234 (cit. on p. 14).
DOI: 10.1038/nnano.2009.10.
- [139] S. KANEKO, C. MOTTA, G. P. BRIVIO, and M. KIGUCHI: Mechanically controllable bi-stable states in a highly conductive single pyrazine molecular junction. *Nanotechnology*, vol. 24(31) (July 2013), p. 315201 (cit. on p. 14).
DOI: 10.1088/0957-4484/24/31/315201.
- [140] D. MIGUEL et al.: Toward Multiple Conductance Pathways with Heterocycle-Based Oligo(phenyleneethynylene) Derivatives. *Journal of the American Chemical Society*, vol. 137(43) (Oct. 2015), pp. 13818–13826 (cit. on p. 14).
DOI: 10.1021/jacs.5b05637.

- [141] C. HUANG et al.: Controlling Electrical Conductance through a π -Conjugated Cruciform Molecule by Selective Anchoring to Gold Electrodes. *Angewandte Chemie International Edition*, vol. 54(48) (Oct. 2015), pp. 14304–14307 (cit. on p. 15). DOI: 10.1002/anie.201506026.
- [142] I. DIEZ-PEREZ et al.: Rectification and stability of a single molecular diode with controlled orientation. *Nature Chemistry*, vol. 1(8) (Oct. 2009), pp. 635–641 (cit. on pp. 15, 16). DOI: 10.1038/nchem.392.
- [143] R. M. METZGER et al.: Unimolecular Electrical Rectification in Hexadecylquinolinium Tricyanoquinodimethanide. *Journal of the American Chemical Society*, vol. 119(43) (Oct. 1997), pp. 10455–10466 (cit. on p. 15). DOI: 10.1021/ja971811e.
- [144] J. HIHATH et al.: Inelastic Transport and Low-Bias Rectification in a Single-Molecule Diode. *ACS Nano*, vol. 5(10) (Sept. 2011), pp. 8331–8339 (cit. on p. 15). DOI: 10.1021/nn2030644.
- [145] C. JOACHIM, J. K. GIMZEWSKI, and A. AVIRAM. *Nature*, vol. 408(6812) (Nov. 2000), pp. 541–548 (cit. on p. 15). DOI: 10.1038/35046000.
- [146] A. AVIRAM, C. JOACHIM, and M. POMERANTZ: Evidence of switching and rectification by a single molecule effected with a scanning tunneling microscope. *Chemical Physics Letters*, vol. 146(6) (May 1988), pp. 490–495 (cit. on pp. 15, 16). DOI: 10.1016/0009-2614(88)87486-4.
- [147] K. WANG, J. ZHOU, J. M. HAMILL, and B. XU: Measurement and understanding of single-molecule break junction rectification caused by asymmetric contacts. *The Journal of Chemical Physics*, vol. 141(5) (Aug. 2014), p. 054712 (cit. on p. 15). DOI: 10.1063/1.4891862.
- [148] C. A. NIJHUIS, W. F. REUS, and G. M. WHITESIDES: Mechanism of Rectification in Tunneling Junctions Based on Molecules with Asymmetric Potential Drops. *Journal of the American Chemical Society*, vol. 132(51) (Dec. 2010), pp. 18386–18401 (cit. on p. 15). DOI: 10.1021/ja108311j.
- [149] E. LÖRTSCHER et al.: Transport Properties of a Single-Molecule Diode. *ACS Nano*, vol. 6(6) (May 2012), pp. 4931–4939 (cit. on p. 16). DOI: 10.1021/nn300438h.
- [150] C. GUO et al.: Molecular rectifier composed of DNA with high rectification ratio

- enabled by intercalation. *Nature Chemistry*, vol. 8(5) (Apr. 2016), pp. 484–490 (cit. on p. 16).
DOI: 10.1038/nchem.2480.
- [151] M. POMERANTZ et al.: Rectification of STM Current to Graphite Covered with Phthalocyanine Molecules. *Science*, vol. 255(5048) (Feb. 1992), pp. 1115–1118 (cit. on p. 16).
DOI: 10.1126/science.255.5048.1115.
- [152] B. CAPOZZI et al.: Single-molecule diodes with high rectification ratios through environmental control. *Nature Nanotechnology*, vol. 10(6) (May 2015), pp. 522–527 (cit. on p. 16).
DOI: 10.1038/nnano.2015.97.
- [153] G. J. ASHWELL, W. D. TYRRELL, and A. J. WHITTAM: Molecular Rectification: Self-Assembled Monolayers in Which Donor-(π -Bridge)-Acceptor Moieties Are Centrally Located and Symmetrically Coupled to Both Gold Electrodes. *Journal of the American Chemical Society*, vol. 126(22) (June 2004), pp. 7102–7110 (cit. on p. 16).
DOI: 10.1021/ja049633u.
- [154] Y. KIM et al.: Charge Transport in Azobenzene-Based Single-Molecule Junctions. *Physical Review Letters*, vol. 109(22) (Nov. 2012), p. 226801 (cit. on p. 16).
DOI: 10.1103/physrevlett.109.226801.
- [155] H. HUNTINGTON and A. GRONE: Current-induced marker motion in gold wires. *Journal of Physics and Chemistry of Solids*, vol. 20(1-2) (June 1961), pp. 76–87 (cit. on p. 22).
DOI: 10.1016/0022-3697(61)90138-x.
- [156] C. BOSVIEUX and J. FRIEDEL: Sur l’electrolyse des alliages metalliques. *Journal of Physics and Chemistry of Solids*, vol. 23(1-2) (Jan. 1962), pp. 123–136 (cit. on p. 22).
DOI: 10.1016/0022-3697(62)90066-5.
- [157] R. SORBELLO: A pseudopotential based theory of the driving forces for electromigration in metals. *Journal of Physics and Chemistry of Solids*, vol. 34(6) (June 1973), pp. 937–950 (cit. on p. 22).
DOI: 10.1016/s0022-3697(73)80002-2.
- [158] A. H. VERBRUGGEN and R. GRIESSEN: Experimental evidence for nonintegral direct-force valence in electromigration. *Physical Review B*, vol. 32(2) (July 1985), pp. 1426–1429 (cit. on p. 22).
DOI: 10.1103/physrevb.32.1426.
- [159] J. LIENIG: “Interconnect and current density stress”. *Proceedings of the 2005 interna-*

- tional workshop on System level interconnect prediction - SLIP '05*. ACM Press, 2005, pp. 81–88 (cit. on pp. 22–25).
DOI: 10.1145/1053355.1053374.
- [160] I. A. BLECH and C. HERRING: Stress generation by electromigration. *Appl. Phys. Lett.* Vol. 29(3) (1976), pp. 131–133 (cit. on pp. 23, 67).
DOI: 10.1063/1.89024.
- [161] J. LIENIG: “Electromigration and its impact on physical design in future technologies”. *Proceedings of the 2013 international symposium on International symposium on physical design*. ACM Press, 2013, pp. 33–40 (cit. on p. 24).
DOI: 10.1145/2451916.2451925.
- [162] J. R. BLACK. *Proceedings 6th Annual International Reliability Physics Symposium (1967)*. 1967, p. 148 (cit. on pp. 24, 67).
DOI: 10.1109/IRPS.1967.362408.
- [163] D. O. BELLISARIO, Z. ULISSI, and M. S. STRANO: A Quantitative and Predictive Model of Electromigration-Induced Breakdown of Metal Nanowires. *The Journal of Physical Chemistry C*, vol. 117(23) (June 2013), pp. 12373–12378 (cit. on p. 27).
DOI: 10.1021/jp4035776.
- [164] I. RATTALINO, P. MOTTO, G. PICCININI, and D. DEMARCHI: A new validation method for modeling nanogap fabrication by electromigration, based on the Resistance-Voltage (R-V) curve analysis. *Physics Letters A*, vol. 376(30-31) (June 2012), pp. 2134–2140 (cit. on pp. 27, 29).
DOI: 10.1016/j.physleta.2012.05.020.
- [165] J. JING, L. LIANG, and G. MENG: Electromigration Simulation for Metal Lines. *Journal of Electronic Packaging*, vol. 132(1) (2010), p. 011002 (cit. on pp. 27, 62, 71).
DOI: 10.1115/1.4000716.
- [166] T. OHKUBO, Y. HIROTSU, and K. NIKAWA: Molecular Dynamics Simulation of Electromigration in Nano-sized Metal Lines. *Materials Transactions, JIM*, vol. 37(3) (1996), pp. 454–457 (cit. on p. 27).
DOI: 10.2320/matertrans1989.37.454.
- [167] D. DEMARCHI et al.: Electrothermal modelling for EIBJ nanogap fabrication. *Electrochimica Acta*, vol. 54(25) (Oct. 2009), pp. 6003–6009 (cit. on pp. 27, 29).
DOI: 10.1016/j.electacta.2009.02.070.
- [168] C. DURKAN, M. A. SCHNEIDER, and M. E. WELLAND: Analysis of failure mechanisms in electrically stressed Au nanowires. *Journal of Applied Physics*, vol. 86(3) (Aug. 1999), pp. 1280–1286 (cit. on p. 28).
DOI: 10.1063/1.370882.

-
- [169] S. I. KHONDAKER and Z. YAO: Fabrication of nanometer-spaced electrodes using gold nanoparticles. *Applied Physics Letters*, vol. 81(24) (Dec. 2002), pp. 4613–4615 (cit. on p. 28).
DOI: 10.1063/1.1528285.
- [170] A. UMENO and K. HIRAKAWA: Nonthermal origin of electromigration at gold nanojunctions in the ballistic regime. *Applied Physics Letters*, vol. 94(16) (Apr. 2009), p. 162103 (cit. on p. 28).
DOI: 10.1063/1.3124654.
- [171] F. O. HADEED and C. DURKAN: Controlled fabrication of 1-2nm nanogaps by electromigration in gold and gold-palladium nanowires. *Applied Physics Letters*, vol. 91(12) (Sept. 2007), p. 123120 (cit. on p. 28).
DOI: 10.1063/1.2785982.
- [172] G. GARDINOWSKI et al.: Switchable nanometer contacts: Ultrathin Ag nanostructures on Si(100). *Appl. Phys. Lett.* Vol. 89(6) (Aug. 2006), p. 063120 (cit. on pp. 28, 48, 66).
DOI: 10.1063/1.2336650.
- [173] R. HOFFMANN, D. WEISSENBERGER, J. HAWECKER, and D. STÖFFLER: Conductance of gold nanojunctions thinned by electromigration. *Applied Physics Letters*, vol. 93(4) (July 2008), p. 043118 (cit. on p. 28).
DOI: 10.1063/1.2965121.
- [174] H. S. J. van der ZANT, E. A. OSORIO, M. POOT, and K. O’NEILL: Electromigrated molecular junctions. *physica status solidi (b)*, vol. 243(13) (Nov. 2006), pp. 3408–3412 (cit. on p. 29).
DOI: 10.1002/pssb.200669185.
- [175] M. TROUWBORST: “Electron Transport through single gold atoms and hydrogen molecules switching on the the atomic scale”. PhD thesis. University of Groningen, 2009 (cit. on pp. 30, 31, 33, 35, 37, 45, 46).
- [176] S. WU: “Electrical conductance of single conjugated oligomers”. PhD thesis. University of Basel, 2010 (cit. on pp. 30, 31, 37).
DOI: 10.5451/unibas-005285471.
- [177] J. C. MAXWELL: *A Treatise on Electricity and Magnetism*. Clarendon Press, Oxford, 1873 (cit. on pp. 31, 32).
- [178] Y. V. SHARVIN: A POSSIBLE METHOD FOR STUDYING FERMI SURFACES. *Journal of Experimental and Theoretical Physics*, vol. (1965), p. 655 (cit. on pp. 31, 33, 34).

- [179] R. LANDAUER: Electrical resistance of disordered one-dimensional lattices. *Philosophical Magazine*, vol. 21(172) (Apr. 1970), pp. 863–867 (cit. on pp. 31, 35, 36, 38).
DOI: 10.1080/14786437008238472.
- [180] D. ERTS et al.: Maxwell and Sharvin conductance in gold point contacts investigated using TEM-STM. *Physical Review B*, vol. 61(19) (May 2000), pp. 12725–12727 (cit. on p. 33).
DOI: 10.1103/physrevb.61.12725.
- [181] G. WEXLER: The non-local Boltzmann transport equation in orifice and disk geometry: The absorbing disk. *Proceedings of the Physical Society*, vol. 92(1) (Sept. 1967), pp. 165–176 (cit. on p. 33).
DOI: 10.1088/0370-1328/92/1/323.
- [182] M. KAMENETSKA: “SINGLE MOLECULE JUNCTION CONDUCTANCE AND BINDING GEOMETRY”. PhD thesis. Columbia University, 2012 (cit. on pp. 37, 44).
DOI: 10.7916/D82N587J.
- [183] A. I. YANSON et al.: Formation and manipulation of a metallic wire of single gold atoms. *Nature*, vol. 395(6704) (Oct. 1998), pp. 783–785 (cit. on p. 38).
DOI: 10.1038/27405.
- [184] A. HALBRITTER et al.: Connective neck evolution and conductance steps in hot point contacts. *Physical Review B*, vol. 65(4) (Jan. 2002), p. 045413 (cit. on p. 38).
DOI: 10.1103/physrevb.65.045413.
- [185] F.-Q. XIE et al.: Preselectable integer quantum conductance of electrochemically fabricated silver point contacts. *Appl. Phys. Lett.* Vol. 93(4) (July 2008), p. 043103 (cit. on pp. 38, 101).
DOI: 10.1063/1.2955521.
- [186] C. Z. LI, A. BOGOZI, W. HUANG, and N. J. TAO: Fabrication of stable metallic nanowires with quantized conductance. *Nanotechnology*, vol. 10(2) (Jan. 1999), pp. 221–223 (cit. on p. 38).
DOI: 10.1088/0957-4484/10/2/320.
- [187] W. H. A. THIJSSSEN, M. STRANGE, J. M. J. aan de BRUGH, and J. M. van RUITENBEEK: Formation and properties of metal-oxygen atomic chains. *New Journal of Physics*, vol. 10(3) (Mar. 2008), p. 033005 (cit. on p. 39).
DOI: 10.1088/1367-2630/10/3/033005.
- [188] R. H. M. SMIT, C. UNTIEDT, A. I. YANSON, and J. M. van RUITENBEEK: Common Origin for Surface Reconstruction and the Formation of Chains of Metal Atoms. *Phys. Rev. Lett.* Vol. 87(26) (Dec. 2001), p. 266102 (cit. on pp. 39, 98, 101).
DOI: 10.1103/physrevlett.87.266102.

- [189] S. V. ARADHYA, M. FREI, A. HALBRITTER, and L. VENKATARAMAN: Correlating Structure, Conductance, and Mechanics of Silver Atomic-Scale Contacts. *ACS Nano*, vol. 7(4) (Apr. 2013), pp. 3706–3712 (cit. on pp. 39, 98).
DOI: 10.1021/nn4007187.
- [190] Y. KONDO and K. TAKAYANAGI: Gold Nanobridge Stabilized by Surface Structure. *Physical Review Letters*, vol. 79(18) (Nov. 1997), pp. 3455–3458 (cit. on p. 40).
DOI: 10.1103/physrevlett.79.3455.
- [191] V. RODRIGUES, T. FUHRER, and D. UGARTE: Signature of Atomic Structure in the Quantum Conductance of Gold Nanowires. *Phys. Rev. Lett.* Vol. 85(19) (Nov. 2000), pp. 4124–4127 (cit. on pp. 40, 41, 85, 99).
DOI: 10.1103/physrevlett.85.4124.
- [192] V. RODRIGUES et al.: Quantum conductance in silver nanowires: Correlation between atomic structure and transport properties. *Phys. Rev. B*, vol. 65(15) (Mar. 2002), p. 153402 (cit. on pp. 40, 41, 89, 101).
DOI: 10.1103/physrevb.65.153402.
- [193] V. RODRIGUES and D. UGARTE: Quantum conductance properties of metal nanowires. *Materials Science and Engineering: B*, vol. 96(2) (Nov. 2002), pp. 188–192 (cit. on p. 40).
DOI: 10.1016/s0921-5107(02)00316-1.
- [194] V. RODRIGUES and D. UGARTE: Metal nanowires: atomic arrangement and electrical transport properties. *Nanotechnology*, vol. 13(3) (May 2002), pp. 404–408 (cit. on p. 40).
DOI: 10.1088/0957-4484/13/3/332.
- [195] V. RODRIGUES and D. UGARTE: Atomic Arrangement and Conductance of Metal Nanowires. *Physica Status Solidi B: Basic Solid State Physics*, vol. 230(2) (2002), pp. 475–480 (cit. on p. 40).
DOI: 10.1002/1521-3951(200204)230:2<475::AID-PSSB475>3.0.CO;2-A.
- [196] H. MASUDA: “Combined Transmission Electron Microscopy - In situ Observation of the Formation Process and Measurement of Physical Properties for Single Atomic-Sized Metallic Wires”. *Modern Electron Microscopy in Physical and Life Sciences*. InTech, Feb. 2016. Chap. 5, pp. 107–119 (cit. on p. 40).
DOI: 10.5772/62288.
- [197] J. BETTINI, V. RODRIGUES, J. GONZÁLEZ, and D. UGARTE: Real-time atomic resolution study of metal nanowires. *Appl. Phys. A*, vol. 81(8) (Nov. 2005), pp. 1513–1518 (cit. on pp. 40, 101).
DOI: 10.1007/s00339-005-3388-9.

- [198] E. TOSATTI: Nanowire formation at metal-metal contacts. *Solid State Communications*, vol. 135(9-10) (Sept. 2005), pp. 610–617 (cit. on p. 40).
DOI: 10.1016/j.ssc.2005.04.045.
- [199] C.A.STAFFORD: Metal Nanowires: Quantum Transport, Cohesion, and Stability. *Physica Status Solidi B: Basic Solid State Physics*, vol. 230(2) (2002), pp. 481–489 (cit. on p. 40).
DOI: 10.1002/1521-3951(200204)230:2<481::AID-PSSB481>3.0.CO;2-M.
- [200] A. L. KLAUSYUK and A. M. SALETSKY: Formation and properties of metallic atomic contacts. *Uspekhi Fizicheskikh Nauk*, vol. 185(10) (2015), pp. 1009–1030 (cit. on pp. 40, 41, 43).
DOI: 10.3367/ufnr.0185.201510a.1009.
- [201] T. NAKAZUMI, Y. WADA, and M. KIGUCHI: The self-breaking mechanism of atomic scale Au nanocontacts. *Nanotechnology*, vol. 23(40) (Sept. 2012), p. 405702 (cit. on p. 41).
DOI: 10.1088/0957-4484/23/40/405702.
- [202] A. I. YANSON, I. K. YANSON, and J. M. van RUITENBEEK: Observation of shell structure in sodium nanowires. *Nature*, vol. 400(6740) (July 1999), pp. 144–146 (cit. on p. 41).
DOI: 10.1038/22074.
- [203] A. I. MARES and J. M. van RUITENBEEK: Observation of shell effects in nanowires for the noble metals Cu, Ag, and Au. *Physical Review B*, vol. 72(20) (Nov. 2005), p. 205402 (cit. on pp. 41, 89, 90).
DOI: 10.1103/physrevb.72.205402.
- [204] C. OBERMAIR, H. KUHN, and T. SCHIMMEL: Lifetime analysis of individual-atom contacts and crossover to geometric-shell structures in unstrained silver nanowires. *Beilstein Journal of Nanotechnology*, vol. 2 (Nov. 2011), pp. 740–745 (cit. on p. 41).
DOI: 10.3762/bjnano.2.81.
- [205] A. I. YANSON, I. K. YANSON, and J. M. van RUITENBEEK: Crossover from Electronic to Atomic Shell Structure in Alkali Metal Nanowires. *Physical Review Letters*, vol. 87(21) (Nov. 2001), p. 216805 (cit. on p. 41).
DOI: 10.1103/physrevlett.87.216805.
- [206] F. PAULY et al.: Theoretical analysis of the conductance histograms and structural properties of Ag, Pt, and Ni nanocontacts. *Physical Review B*, vol. 74(23) (Dec. 2006), p. 235106 (cit. on pp. 42, 87, 101, 105–107).
DOI: 10.1103/physrevb.74.235106.
- [207] A. HASMY, E. MEDINA, and P. A. SERENA: From Favorable Atomic Configurations

- to Supershell Structures: A New Interpretation of Conductance Histograms. *Physical Review Letters*, vol. 86(24) (June 2001), pp. 5574–5577 (cit. on pp. 42, 87, 89).
DOI: 10.1103/physrevlett.86.5574.
- [208] M. DREHER et al.: Structure and conductance histogram of atomic-sized Au contacts. *Physical Review B*, vol. 72(7) (Aug. 2005), p. 075435 (cit. on pp. 42, 87).
DOI: 10.1103/physrevb.72.075435.
- [209] V. S. STEPANYUK et al.: Structure and quantum effects in atomic-sized contacts. *Physical Review B*, vol. 69(3) (Jan. 2004), p. 033302 (cit. on p. 43).
DOI: 10.1103/physrevb.69.033302.
- [210] A. CHATTERJEE et al.: Electromigration and morphological changes in Ag nanostructures. *J.Phys.: Condensed Matter*, vol. 30 (Jan. 2018), p. 084002 (cit. on pp. 47, 61, 82, 92).
DOI: 10.1088/1361-648x/aaa80a.
- [211] M. H.-v. HOEGEN et al.: Epitaxial layer growth of Ag(111)-films on Si(100). *Surf. Sci.* Vol. 331-333 (July 1995), pp. 575–579 (cit. on pp. 48, 101).
DOI: 10.1016/0039-6028(95)00320-7.
- [212] H. H. WEITERING et al.: Inhomogeneous Schottky barriers at Ag/Si(111) and Ag/Si(100) interfaces. *Journal of Applied Physics*, vol. 79(10) (May 1996), pp. 7820–7829 (cit. on p. 48).
DOI: 10.1063/1.362390.
- [213] J. P. VERMEULEN: 12 Years Zeiss Gemini FESEM Technology. *Imaging & Microscopy*, vol. 4 (2004), pp. 34–35 (cit. on p. 56).
- [214] OMICRON NANOTECHNOLOGY GMBH: *Ultimate Nanoprobng with Four Independent Scanning Probe Microscopes - Further Details* (cit. on p. 56).
URL: <http://www.omicron.de/en/products/uhv-nanoprobe/further-details> (visited on 04/10/2012).
- [215] J. P. IBE et al.: On the electrochemical etching of tips for scanning tunneling microscopy. *Journal of Vacuum Science & Technology A: Vacuum, Surfaces, and Films*, vol. 8(4) (1990), pp. 3570–3575 (cit. on p. 57).
DOI: 10.1116/1.576509.
- [216] E. OLSEN: “Controlled Electromigration to Create Sub-Nanometer Gaps for Molecular Electronic Applications”. Bachelor Thesis, University of Hannover. 2016 (cit. on pp. 58, 60).
- [217] P. S. HO and T. KWOK: Electromigration in metals. *Rep. Prog. Phys.* Vol. 52(3) (Mar. 1989), pp. 301–348 (cit. on p. 62).
DOI: 10.1088/0034-4885/52/3/002.

- [218] D. PIERCE and P. BRUSIUS: Electromigration: A review. *Microelectr. Reliab.* Vol. 37(7) (July 1997), pp. 1053–1072 (cit. on p. 62).
DOI: 10.1016/s0026-2714(96)00268-5.
- [219] K. N. TU: Recent advances on electromigration in very-large-scale-integration of interconnects. *J. Appl. Phys.* Vol. 94(9) (Nov. 2003), pp. 5451–5473 (cit. on p. 62).
DOI: 10.1063/1.1611263.
- [220] K. N. TU, Y. LIU, and M. LI: Effect of Joule heating and current crowding on electro-migration in mobile technology. *Appl. Phys. Rev.* Vol. 4(1) (2017), p. 011101 (cit. on p. 62).
DOI: 10.1063/1.4974168.
- [221] D. NATELSON, Y. LI, and J. B. HERZOG: Nanogap structures: combining enhanced Raman spectroscopy and electronic transport. *Physical Chemistry Chemical Physics*, vol. 15(15) (2013), p. 5262 (cit. on p. 62).
DOI: 10.1039/c3cp44142c.
- [222] J. B. HERZOG et al.: Dark Plasmons in Hot Spot Generation and Polarization in Interelectrode Nanoscale Junctions. *Nano Letters*, vol. 13(3) (Mar. 2013), pp. 1359–1364 (cit. on p. 62).
DOI: 10.1021/nl400363d.
- [223] J. MERTENS et al.: How Light Is Emitted by Plasmonic Metals. *Nano Letters*, vol. 17(4) (Mar. 2017), pp. 2568–2574 (cit. on p. 62).
DOI: 10.1021/acs.nanolett.7b00332.
- [224] J. PERUMAL et al.: Development of optimized nanogap plasmonic substrate for improved SERS enhancement. *AIP Advances*, vol. 7(5) (May 2017), p. 055017 (cit. on p. 62).
DOI: 10.1063/1.4984769.
- [225] P. ZOLOTAVIN, C. EVANS, and D. NATELSON: Photothermoelectric Effects and Large Photovoltages in Plasmonic Au Nanowires with Nanogaps. *The Journal of Physical Chemistry Letters*, vol. 8(8) (Apr. 2017), pp. 1739–1744 (cit. on p. 62).
DOI: 10.1021/acs.jpcllett.7b00507.
- [226] J.-S. CHO et al.: Pd effect on reliability of Ag bonding wires in microelectronic devices in high-humidity environments. *Metals and Materials International*, vol. 18(5) (Oct. 2012), pp. 881–885 (cit. on p. 62).
DOI: 10.1007/s12540-012-5021-8.
- [227] H.-W. HSUEH, F.-Y. HUNG, T.-S. LUI, and L.-H. CHEN: Effect of the direct current on microstructure, tensile property and bonding strength of pure silver wires. *Microelectronics Reliability*, vol. 53(8) (Aug. 2013), pp. 1159–1163 (cit. on p. 62).
DOI: 10.1016/j.microrel.2013.04.004.

-
- [228] H.-W. HSUEH, F.-Y. HUNG, and T.-S. LUI: A study on electromigration-inducing intergranular fracture of fine silver alloy wires. *Applied Physics Letters*, vol. 110(3) (Jan. 2017), p. 031902 (cit. on p. 62).
DOI: 10.1063/1.4974154.
- [229] P. HO and H. HUNTINGTON: Electromigration and void observation in silver. *J. Phys. Chem. Solids*, vol. 27(8) (Aug. 1966), pp. 1319–1329 (cit. on p. 62).
DOI: 10.1016/0022-3697(66)90016-3.
- [230] E. MISRA, N. THEODORE, J. MAYER, and T. ALFORD: Failure mechanisms of pure silver, pure aluminum and silver-aluminum alloy under high current stress. *Microelectronics Reliability*, vol. 46(12) (Dec. 2006), pp. 2096–2103 (cit. on p. 62).
DOI: 10.1016/j.microrel.2006.01.011.
- [231] E. ARZT, O. KRAFT, W. D. NIX, and J. E. SANCHEZ: Electromigration failure by shape change of voids in bamboo lines. *Journal of Applied Physics*, vol. 76(3) (Aug. 1994), pp. 1563–1571 (cit. on p. 62).
DOI: 10.1063/1.357734.
- [232] R. HOFFMANN-VOGEL: Electromigration and the structure of metallic nanocontacts. *Appl. Phys. Rev.* Vol. 4(3) (Sept. 2017), p. 031302 (cit. on pp. 62, 66).
DOI: 10.1063/1.4994691.
- [233] M. BRANDBYGE et al.: Origin of current-induced forces in an atomic gold wire: A first-principles study. *Phys. Rev. B*, vol. 67 (Aug. 19, May 2003), p. 193104 (cit. on p. 62).
DOI: 10.1103/PhysRevB.67.193104.
- [234] K. DOI, K. IGUCHI, K. NAKAMURA, and A. TACHIBANA: First-principle dynamical electronic characteristics of Al electromigration in the bulk, surface, and grain boundary. *Phys. Rev. B*, vol. 67 (Aug. 11, Mar. 2003), p. 115124 (cit. on p. 62).
DOI: 10.1103/PhysRevB.67.115124.
- [235] B. CUNNINGHAM, T. N. TODOROV, and D. DUNDAS: Nonconservative dynamics in long atomic wires. *Phys. Rev. B*, vol. 90 (Aug. 11, Sept. 2014), p. 115430 (cit. on p. 62).
DOI: 10.1103/PhysRevB.90.115430.
- [236] L. J. FERNÁNDEZ-ALCÁZAR, R. A. BUSTOS-MARÚN, and H. M. PASTAWSKI: Decoherence in current induced forces: Application to adiabatic quantum motors. *Phys. Rev. B*, vol. 92 (Aug. 7, Aug. 2015), p. 075406 (cit. on p. 62).
DOI: 10.1103/PhysRevB.92.075406.
- [237] M. R. KASPERS, A. M. BERNHART, C. A. BOBISCH, and R. MÖLLER: Current induced

- surface diffusion on a single-crystalline silver nanowire. *Nanotechnology*, vol. 23(20) (Apr. 2012), p. 205706 (cit. on p. 62).
DOI: 10.1088/0957-4484/23/20/205706.
- [238] M. R. KASPERS et al.: Electromigration and potentiometry measurements of single-crystalline Ag nanowires under UHV conditions. *J. Phys.: Condensed Matter*, vol. 21(26) (June 2009), p. 265601 (cit. on p. 62).
DOI: 10.1088/0953-8984/21/26/265601.
- [239] B. STAHLMECKE, L. I. CHELARU, F.-J. M. zu HERINGDORF, and G. DUMPICH: Electromigration in Gold and Single Crystalline Silver Nanowires. *AIP Conference Proceedings*, vol. 817(1) (2006), pp. 65–70 (cit. on p. 62).
DOI: 10.1063/1.2173533.
- [240] D. STÖFFLER, S. FOSTNER, P. GRÜTTER, and R. HOFFMANN-VOGEL: Scanning probe microscopy imaging of metallic nanocontacts. *Phys. Rev. B*, vol. 85(3) (Jan. 2012), p. 033404 (cit. on pp. 63, 83).
DOI: 10.1103/physrevb.85.033404.
- [241] D. STÖFFLER et al.: Resistance-voltage dependence of nanojunctions during electromigration in ultrahigh vacuum. *Physical Review B*, vol. 90(11) (Sept. 2014), p. 115406 (cit. on p. 63).
DOI: 10.1103/physrevb.90.115406.
- [242] K. WEIDE-ZAAGE, F. KASHANCHI, and O. AUBEL: Simulation of migration effects in nanoscaled copper metallizations. *Microelectronics Reliability*, vol. 48(8-9) (Aug. 2008), pp. 1398–1402 (cit. on pp. 67, 69, 70).
DOI: 10.1016/j.microrel.2008.06.025.
- [243] T. BAI: “Simulation of Metallization Structures of Different Materials and Geometry”. MA thesis. Leibniz University Hannover, 2016 (cit. on pp. 67, 68, 70, 71, 127, 128).
- [244] R. W. POWELL, C. Y. HO, and P. E. LILEY: *Thermal conductivity of selected materials*. Tech. rep. 1966 (cit. on p. 69).
DOI: 10.6028/nbs.nsrds.8.
- [245] R. A. MATULA: Electrical resistivity of copper, gold, palladium, and silver. *Journal of Physical and Chemical Reference Data*, vol. 8(4) (Oct. 1979), pp. 1147–1298 (cit. on p. 70).
DOI: 10.1063/1.555614.
- [246] N. PAPANICOLAOU, G. EVANGELAKIS, and G. KALLINTERIS: Molecular dynamics description of silver adatom diffusion on Ag(100) and Ag(111) surfaces. *Comput. Mater. Sci.* Vol. 10(1) (1998). Computational Modelling of Issues in Materials Science, pp. 105–110. ISSN: 0927-0256 (cit. on p. 81).
DOI: 10.1016/S0927-0256(97)00089-X.

-
- [247] J. SCHMEIDEL, H. PFNÜR, and C. TEGENKAMP: Coulomb blockade effects in Ag/Si(111): The role of the wetting layer. *Phys. Rev. B*, vol. 80 (Ausc. 11, Sept. 2009), p. 115304 (cit. on p. 82).
DOI: 10.1103/PhysRevB.80.115304.
- [248] Z. YANG et al.: Role of heating and current-induced forces in the stability of atomic wires. *Phys. Rev. B*, vol. 71(4) (Jan. 2005), p. 041402 (cit. on p. 84).
DOI: 10.1103/physrevb.71.041402.
- [249] N. AGRAIT, J. G. RODRIGO, and S. VIEIRA: Conductance steps and quantization in atomic-size contacts. *Phys. Rev. B*, vol. 47(18) (May 1993), pp. 12345–12348 (cit. on pp. 85, 97).
DOI: 10.1103/physrevb.47.12345.
- [250] W. H. A. THIJSEN: “Molecule-assisted atomic chain formation: mechanisms and properties of new one-dimensional conductors”. PhD thesis. University Leiden, The Netherlands, 2007 (cit. on p. 85).
- [251] R. PFENDER-SIEDLE, J. HAUSER, and R. HOFFMANN-VOGEL: Atomic discreteness and the nature of structural equilibrium in conductance histograms of electromigrated Cu nanocontacts. *Phys. Rev. B*, vol. 95(23) (June 2017), p. 235418 (cit. on pp. 85–87, 89, 99, 100).
DOI: 10.1103/physrevb.95.235418.
- [252] O. I. SHKLYAREVSKII and I. K. YANSON: Effect of cold working of the metal on the conductance of platinum, copper, and silver nanocontacts. *Low Temperature Physics*, vol. 39(3) (Mar. 2013), pp. 285–288 (cit. on p. 85).
DOI: 10.1063/1.4795200.
- [253] N. ITTAH, I. YUTSIS, and Y. SELZER: Fabrication of Highly Stable Configurable Metal Quantum Point Contacts. *Nano Letters*, vol. 8(11) (Nov. 2008), pp. 3922–3927 (cit. on p. 85).
DOI: 10.1021/nl802372t.
- [254] I. K. YANSON et al.: Atomic-Size Oscillations in Conductance Histograms for Gold Nanowires and the Influence of Work Hardening. *Physical Review Letters*, vol. 95(25) (Dec. 2005), p. 256806 (cit. on pp. 87–89).
DOI: 10.1103/physrevlett.95.256806.
- [255] I. K. YANSON, O. I. SHKLYAREVSKII, J. M. van RUITENBEEK, and S. SPELLER: Aluminum nanowires: Influence of work hardening on conductance histograms. *Physical Review B*, vol. 77(3) (Jan. 2008), p. 033411 (cit. on pp. 87, 89).
DOI: 10.1103/physrevb.77.033411.

- [256] B. WANG et al.: Novel Structures and Properties of Gold Nanowires. *Physical Review Letters*, vol. 86(10) (Mar. 2001), pp. 2046–2049 (cit. on p. 89).
DOI: 10.1103/physrevlett.86.2046.
- [257] A. I. YANSON, I. K. YANSON, and J. M. van RUITENBEEK: Supershell Structure in Alkali Metal Nanowires. *Physical Review Letters*, vol. 84(25) (June 2000), pp. 5832–5835 (cit. on p. 89).
DOI: 10.1103/physrevlett.84.5832.
- [258] A. CHATTERJEE et al.: Shaping single atomic junctions in ultra-thin Ag structures by electromigration. *Applied Physics Letters*, vol. 113(1) (July 2018), p. 013106 (cit. on pp. 91, 104, 113).
DOI: 10.1063/1.5040405.
- [259] T. KIM, H. VÁZQUEZ, M. S. HYBERTSEN, and L. VENKATARAMAN: Conductance of Molecular Junctions Formed with Silver Electrodes. *Nano Lett.* Vol. 13(7) (July 2013), pp. 3358–3364 (cit. on p. 98).
DOI: 10.1021/nl401654s.
- [260] M. P. DAS and F. GREEN: Conductance anomalies in quantum point contacts and 1D wires. *Advances in Natural Sciences: Nanoscience and Nanotechnology*, vol. 8(2) (May 2017), p. 023001 (cit. on p. 98).
DOI: 10.1088/2043-6254/aa5e17.
- [261] D. S. GALVÃO, V. RODRIGUES, D. UGARTE, and S. B. LEGOAS: The role of carbon contamination in metallic nanowires. *Materials Research*, vol. 7(2) (June 2004), pp. 339–342 (cit. on p. 98).
DOI: 10.1590/s1516-14392004000200020.
- [262] N. MOSSO et al.: Heat transport through atomic contacts. *Nat. Nanotech.* Vol. 12(5) (Feb. 2017), pp. 430–433 (cit. on p. 98).
DOI: 10.1038/nnano.2016.302.
- [263] T. KIM: Reducing Gap Distance of Ag Electrodes by Oxygen Atomic Junction Formation. *The Journal of Physical Chemistry C*, vol. 119(22) (May 2015), pp. 12703–12707 (cit. on p. 100).
DOI: 10.1021/acs.jpcc.5b02399.
- [264] Z. BALOGH et al.: Precursor configurations and post-rupture evolution of Ag-CO-Ag single-molecule junctions. *Nanoscale*, vol. 6 (Aug. 24, 2014), pp. 14784–14791 (cit. on pp. 101, 107, 108).
DOI: 10.1039/C4NR04645E.
- [265] J. BETTINI et al.: Experimental realization of suspended atomic chains composed of

- different atomic species. *Nature Nanotechnology*, vol. 1(3) (Nov. 2006), pp. 182–185 (cit. on p. 101).
DOI: 10.1038/nnano.2006.132.
- [266] M. J. LAGOS, P. A. S. AUTRETO, D. S. GALVAO, and D. UGARTE: Correlation between quantum conductance and atomic arrangement of atomic-size silver nanowires. *J. Appl. Phys.* Vol. 111(12) (June 2012), p. 124316 (cit. on p. 101).
DOI: 10.1063/1.4729805.
- [267] Y. LI et al.: Atomic and Electronic Structures of a Single Oxygen Molecular Junction with Au, Ag, and Cu Electrodes. *The Journal of Physical Chemistry C*, vol. 120(29) (June 2016), pp. 16254–16258 (cit. on p. 104).
DOI: 10.1021/acs.jpcc.6b04862.
- [268] Y. LI et al.: Atomic structure of water/Au, Ag, Cu and Pt atomic junctions. *Physical Chemistry Chemical Physics*, vol. 19(6) (2017), pp. 4673–4677 (cit. on p. 104).
DOI: 10.1039/c6cp07549e.
- [269] W. H. A. THIJSSSEN, D. MARJENBURGH, R. H. BREMMER, and J. M. VAN RUITENBEEK: Oxygen-Enhanced Atomic Chain Formation. *Physical Review Letters*, vol. 96(2) (Jan. 2006), p. 026806 (cit. on p. 104).
DOI: 10.1103/physrevlett.96.026806.
- [270] O. TAL et al.: Molecular signature of highly conductive metal-molecule-metal junctions. *Physical Review B*, vol. 80(8) (Aug. 2009), p. 085427 (cit. on p. 104).
DOI: 10.1103/physrevb.80.085427.
- [271] M. KIGUCHI, D. DJUKIC, and J. M. van RUITENBEEK: The effect of bonding of a CO molecule on the conductance of atomic metal wires. *Nanotechnology*, vol. 18(3) (Jan. 2007), p. 035205 (cit. on p. 104).
DOI: 10.1088/0957-4484/18/3/035205.
- [272] W. H. A. THIJSSSEN et al.: Vibrationally Induced Two-Level Systems in Single-Molecule Junctions. *Physical Review Letters*, vol. 97(22) (Dec. 2006), p. 226806 (cit. on p. 104).
DOI: 10.1103/physrevlett.97.226806.
- [273] D. DULIC et al.: Controlled Stability of Molecular Junctions. *Angewandte Chemie International Edition*, vol. 48(44) (Sept. 2009), pp. 8273–8276 (cit. on pp. 111, 113, 116).
DOI: 10.1002/anie.200902168.
- [274] A. SPERL, J. KRÖGER, and R. BERNDT: Direct observation of conductance fluctuations of a single-atom tunneling contact. *Physical Review B*, vol. 81(3) (Jan. 2010), p. 035406 (cit. on p. 111).
DOI: 10.1103/physrevb.81.035406.

- [275] J. ZHOU, Z.-H. LI, W.-N. WANG, and K.-N. FAN: Density Functional Study of the Interaction of Carbon Monoxide with Small Neutral and Charged Silver Clusters. *The Journal of Physical Chemistry A*, vol. 110(22) (June 2006), pp. 7167–7172 (cit. on p. 113).
DOI: 10.1021/jp0609961.
- [276] C. M. MARIAN: Stability and the CO stretching vibrational frequency of molecular AgCo. *Chemical Physics Letters*, vol. 215(6) (Dec. 1993), pp. 582–586 (cit. on p. 113).
DOI: 10.1016/0009-2614(93)89359-p.
- [277] A. S. GOLDMAN and K. KROGH-JESPERSEN: Why Do Cationic Carbon Monoxide Complexes Have High C-O Stretching Force Constants and Short C-O Bonds? Electrostatic Effects, Not σ -Bonding. *Journal of the American Chemical Society*, vol. 118(48) (Jan. 1996), pp. 12159–12166 (cit. on p. 113).
DOI: 10.1021/ja960876z.
- [278] P. H. ACIOLI, N. RATANAHADE, M. R. CLINE, and S. SRINIVAS: “Density Functional Theory Study of Ag-Cluster/CO Interactions”. *Lecture Notes in Computer Science*. Springer Berlin Heidelberg, 2009, pp. 203–210 (cit. on p. 114).
DOI: 10.1007/978-3-642-01973-9{_}23.
- [279] P. H. ACIOLI, S. BURKLAND, and S. SRINIVAS: An exploration of the potential energy surface of the seven atom silver cluster and a carbon monoxide ligand. *The European Physical Journal D*, vol. 66(8) (Aug. 2012), p. 215 (cit. on pp. 114, 115).
DOI: 10.1140/epjd/e2012-30136-y.
- [280] K. W. ZAAGE: “Untersuchungen von Stromdichte-, Temperatur und Massenflussverteilung in Viastrukturen integrierter Schaltungen”. PhD thesis. University Hannover, 1994 (cit. on p. 129).

Publications

- [P1] A. CHATTERJEE, T. BAI, F. EDLER, C. TEGENKAMP, K. WEIDE-ZAAGE, and H. PFNÜR: Electromigration and morphological changes in Ag nanostructures. *Journal of Physics: Condensed Matter*, vol. 30 (Jan. 2018), p. 084002.
DOI: 10.1088/1361-648x/aaa80a.
- [P2] A. CHATTERJEE, T. HEIDENBLUT, F. EDLER, E. OLSEN, J. P. STÖCKMANN, C. TEGENKAMP, and H. PFNÜR: Shaping single atomic junctions in ultra-thin Ag structures by electromigration. *Applied Physics Letters*, vol. 113(1) (July 2018), p. 013106.
DOI: 10.1063/1.5040405.
- [P3] A. CHATTERJEE, C. TEGENKAMP, and H. PFNÜR: Anisotropic nanocontact formation by electromigration. *Submitted to Phys. Rev B*, vol. (Sept. 2019).
- [P4] A. CHATTERJEE, F. EDLER, C. TEGENKAMP, and H. PFNÜR: Modification of Ag atomic point contacts by CO adsorption. *Manuscript in preparation*, vol. (2019).

Curriculum Vitae

PERSONAL INFORMATION:

NAME Atasi Chatterjee
DATE OF BIRTH 03.11.1987 in Durgapur, India

EDUCATION:

Since Oct. 2013 Doctorate at Institut für Festkörperphysik, Gottfried Wilhelm Leibniz Universität Hannover

2012-2013 Research Engineer, Research and Development Center, SNAM Alloys Pvt. Ltd., Hosur, India

2010-2012 Master of Technology, Advanced Material Science and Technology, Department of Physics, National Institute of Technology, Durgapur, India
Thesis: *Carbon-nanotube and Graphene based Polymer nanocomposites*

2006-2010 Bachelor of Technology, Electronic and Instrumentation Engineering, Dr. B.C Roy Engineering College, Durgapur, India
Thesis: *Design of factorial circuit using software simulation and hardware elements*

2004-2006 Higher Secondary School, DAV Model School, Durgapur, India

1992-2004 Secondary School, Carmel Convent School, Durgapur, India

Acknowledgements

I thank **Prof. Dr. Herbert Pfnür** for being an excellent supervisor throughout my doctoral thesis years. He was always there for discussions and providing me with new ideas whenever I sought suggestions. Without his encouragement, I would not be able to accomplish this to the end.

I also thank **Prof. Dr. Christoph Tegenkamp** for his help and co-operation during integration of the measurement setup with the 4-tip scanning electron microscope (SEM)/scanning tunneling microscope (STM). Apart from this, he was actively involved in the scientific discussions related to presentations, manuscript submissions and his suggestions regarding those were of great help.

I express my regards to **Prof. Dr. Peter Lemmens** for agreeing to be my co-referee and evaluating my thesis as well as **Prof. Dr. Eric Jeckelmann** for being a part of the exam committee.

With great pleasure I would like to thank **Dr. Ing Torsten Heidenblut** from Institute of Werkstoffkunde, for helping me with the focused ion beam (FIB) structuring. My sincere thanks to **Dr. Ing Kirsten Weide Zaage** and her student **Tianlin Bai** from the Institute of Microelectronic Systems for carrying out the theoretical simulations.

I also thank **Ejvind Olsen** and **Priscilla Kochanski**, my bachelor students, **Detlef Zech** from the department of MBE for deposition and **Oliver Kerker**, LNQE for assistance in the clean room. My heartiest thanks to **Dr. Frederik Edler** for helping me regarding 4-tip SEM/STM and LaTeX. I also express my gratitude to my office colleagues **Dr. Jens Baringhaus**, **Julian Koch**, **Monika Jäger** and **Johannes Aprojanz** as well as other colleagues from ATMOS and my friends in Hannover for their help and support.

Last but not least, I thank my family for their unconditional support and faith in me. I thank my mother **Anubrata Chatterjee** for motivating me throughout my life and making me eligible so that I could pursue my PhD. It goes without saying that my husband **Dr. Souvik Chakraborty** was always there for support and inspiration. Without his love, patience and encouragement, it would not have been possible for me to stay alone and finish my thesis.

Declaration of originality

I hereby declare that this work reported here in the form of a doctoral thesis was entirely performed by me. Information reported from the published and unpublished work of other research items have been cited properly in the text and their references are given in the list of references. This work in any form has not been submitted for any other degree at any other university.

Hannover, September 24, 2019

Atasi Chatterjee